

OXIDE FORMATION INSIDE A CYCLICALLY LOADED CRACK AND
ITS EFFECT ON ENVIRONMENTAL ENHANCED CRACK
GROWTH RATE IN 93°C WATER

G. Gabetta, C. Fossati

Paper presented at the IAEA Specialists'
Meeting on Subcritical Crack Growth,
Freiburg (F.R.G.), May 13-15, 1981

Work performed in the frame of the
CISE-ENEL "ISMAT 900" Contract

TABLE OF CONTENTS

ABSTRACT

1. INTRODUCTION

2. EXPERIMENTAL FACILITY (WATER CELL)

3. DATA ACQUISITION AND REDUCTION

4. EXPERIMENTAL

5. RESULTS AND DISCUSSION

6. CONCLUSIONS

ACKNOWLEDGEMENTS

REFERENCES

TABLE

FIGURES

ABSTRACT

As a part of a main program in environmental fatigue on pressure vessel steel at 288 °C, tests have been performed in demineralized water at 93 °C on these materials with the purpose of obtaining crack growth rate data and information on the environmental mechanisms at two different temperatures.

The effect of the oxygen content in water was studied, two oxygen concentrations were chosen:

- a) ~ 0.01 ppm (de-oxygenated water)
- b) 5.6 ppm (oxygen saturated water)

The obtained results show that an oxide layer forms inside the crack at the higher oxygen concentration; that oxide layer causes a kind of "crack closure", which is responsible of an increase of K_{MIN} and R ratio. It is therefore necessary to correct the applied K value with a calculated "effective K".

Because of the imposed loading wave form (ramp with fast reset), the presence of the oxide can easily be detected by a double slope in the specimen mouth opening vs time.

A few thousand cycles are necessary for the formation of a detectable oxide layer. The oxide formation is probably related to the deformation rate at the crack tip: at high deformation rates (end of tests, higher frequencies), the oxide effect is less apparent. At higher R ratio (0.7) the oxide stills forms, however its effect is less detectable.

1. INTRODUCTION

The measurement of fatigue crack growth rates on pressure vessel steels is an important part of water reactor safety research. Environmental fatigue tests are performed at CISE in both simulated LWR environment and low-temperature (93 °C), low pressure (.01 - .015 MPa) demineralized water, which also simulates transient conditions for a nuclear reactor.

In the second environment, a set of tests was made, aimed at to outline the effect of oxygen content in water, at different loading rates and R-ratios.

The obtained data show that an high oxygen content causes the formation of an oxide layer on the fracture surface. The main effect of the oxide layer seems to be a modification of the loading parameters at the crack tip, causing a phenomenon similar to crack closure.

This paper describes the tests and the results; moreover, the real meaning of the observed modification in the data is analyzed.

2. EXPERIMENTAL FACILITY (WATER CELL)

The water cell is a testing device aimed at to perform tests at a temperature under 100 °C and pressures below .05 MPa.

A picture of the water cell is shown in Fig. 1. The flow-sheet of the hydraulic plant is shown in Fig. 2.

The pressure in the plant is maintained by a gas blanket in the feeding tank. The blanket is maintained by bubbling continuously the gas, namely oxygen when the tests are in oxygen saturated water, or Nitrogen when the tests are in de-oxygenated water.

The environmental chamber for a 2T CT specimen is shown in Fig. 3.

It consists of two shells where the water is forced to circulate through the notch of the specimen.

Two glass windows allow the optical reading of the crack length during the test. An LVDT is mounted on the specimen mouth and gi

ves a measure of the crack opening during the test.

The load is applied to the specimen by an MTS 50 tons servo-hydraulic machine that may be controlled in load, stroke or strain. The loading wave form can be chosen between sine and ramp, with or without hold time.

3. DATA ACQUISITION AND REDUCTION

During the test, the crack mouth opening is continuously recorded and plotted together with the applied load. After the test is completed, the specimen is open broken at liquid nitrogen temperature, and the value of the elastic modulus E is calculated from the final crack length (measured value). The values of crack length (a) as a function of the elapsed cycles (N) are calculated by means of the polynomial method proposed by Saxena and Hudak [1], with coefficients corresponding to the LVDT location on the specimen mouth. The values of da/dN vs ΔK are calculated with the "incremental polynomial" method [2].

4. EXPERIMENTAL

A summary of test conditions is shown in table 1. Tests were made in de-mineralized water on 2T CT specimens of A533 grade B pressure vessel steel.

A couple of tests was performed for each set of loading parameters, at two different oxygen content in water:

- a) low concentration (~ 10 ppb);
- b) high concentration (5-6 ppm).

It was pointed out [3] that the environmental effect on the crack growth rate is more pronounced at loading frequencies of around 1 cycle per minute; for this reason frequencies were chosen in this order of magnitude (1 to 2 c.p.m.).

The loading wave form was a ramp (which has a constant derivative with respect to time) followed by a fast reset. The im-

portance of the deformation rate at the crack tip was pointed out by Scott [4] and Törrönen and al. [5] also if its role needs to be better clarified.

The pH and conductivity of water were measured during the test, by periodic sampling. A chemical analysis of water was made at the end of each test.

5. RESULTS AND DISCUSSION

The obtained data are shown as a vs N curves in Fig. 4-5-6, moreover da/dN vs ΔK curves are given in Fig. 7-8-9. For each couple of data, a vs N curves are compared starting at the same values of a, so that the loading conditions of the crack tip are consistent. The general trend of the data is that the crack growth rate is higher for low oxygen conditions. In the a vs N graphs, a change in the slope of the curve is observed after a few thousand cycles for the specimens tested at high O_2 level. For a high oxygen test, plots of load and mouth opening as a function of time are shown in Fig. 10; the mouth opening shows a double slope, which does not appear during the low oxygen tests.

This anomalous behavior may be due to the oxide which forms inside the crack; the oxide layer fills the crack, so that the loading parameters at the crack tip are altered, with the mechanism shown in Fig. 11a and 11b: when the load approaches maximum, the crack is open with no effect of the oxide; when the load decreases, and the contact between the surfaces is reached, the inside of the crack tip begins to feel a compressive load. The value of K_{min} is increased by the superimposed traction load due to the reaction force at the crack tip. The difference, in terms of ΔK , is shown in Fig. 12: it is possible to calculate the effective ΔK value by means of the effective R measured from the LVDT output. The correction has been applied to the da/dN vs ΔK curves, and the difference between "low oxygen" and "high oxygen" data has become smaller (see Fig. 13, 14, 15). It is of interest a discussion of the obtained data with

reference to the theories about crack closure. Richtie did find a similar effect [6] during environmental fatigue test at higher temperature, and reports it as a bare crack closure. However, several authors (see f.e. Elber, 7) indicate more properly that crack closure is a phenomenon due to the variation of plastic zone size around the crack tip, which causes a residual compressive stress at the crack tip.

For the specimens here examined, the oxide effect is detectable only after a few thousand cycles. At that point, the crack growth (see a vs N and da/dN vs ΔK plots) slows down and the observed effective value of R begins to increase; the value of R reaches a maximum, and decreases very slowly at the end of the test. This behavior suggests that:

- a) a time several times greater than a single cycle is requested to build up an oxide layer thick enough to provoke the phenomenon;
- b) as an increase in frequency results in a higher value of da/dt for the 2 c.p.m. test the oxide layer is active after a number of cycles greater than for the 1 c.p.m. test;
- c) the increase of R as the crack grows shows that the position of the contact point between the fracture surfaces moves together with the crack tip;
- d) as R decreases at the end of tests, the influence of the oxide-free, new surface created became more evident, because the crack grows faster than the oxide is built up.

A first test has been completed at high R ratio (0.7). The effect of the oxide is there less noticeable, because the minimum applied load is quite high.

6. CONCLUSIONS

Both data and discussions shows that it is necessary to have a grate care in observing all aspect of row data in environmental fatigue test. The true effect of oxygen on the crack growth mechanisms at the crack tip, seems in effect to be almost comple-

tely masked by the macroscopic one due to the oxide.

At the environmental conditions examined in these tests, the oxide formed is very thick. At the service temperature of water reactor pressure vessels (288 °C) the oxide formed is compact and thin. It is possible to assume that in LWR simulated condition the oxide effect would be different. A set of tests in these conditions is necessary to verify the hypothesis.

ACKNOWLEDGEMENTS

The authors express their gratitude to ENEL-DSR (Ente Nazionale per l'Energia Elettrica - Direzione Studi e Ricerche) which supported this work under the contract ISMAT 900. Thanks are also due to Mr. G. Gritti for the experimental work.

REFERENCES

- 1 Ashok Saxena and S.J. Hudak, Jr
Westinghouse Scientific Paper
77-9E7-AFCGR-P1
- 2 ASTM 647-78T appeared in 1978 Book of ASTM Standards,
Vol. 10
- 3 J.D. Atkinson and T.C. Lindley
I Mech E conference, London, May 1977
- 4 P.M. Scott,
Conference on "Defects and crack initiation in environment
sensitive fracture" University of Newcastle upon Tyne (U.K.),
12/14 January 1981.
- 5 Törrönen and al. Technical Research Center of Finland, Metals
Laboratory, Report 69 Espoo, March 1980
- 6 Robert O. Ritchie
Proceeding of the Int. Conf. on Analytical and Experimental
Fracture Mechanics, Rome, Italy, June 1980
- 7 W. Elber, Eng. Fracture Mech., vol. 2, 37 (1970)

TABLE 1

SPECIMEN NAME	WAVE FORM	FREQUENCY	R	O ₂ level
W3-1		1 c.p.m.	0.2	Low
W3-2	"	1 c.p.m.	0.2	High
X1B1	"	1 c.p.m.	0.2	High
X1B2	"	1 c.p.m.	0.7	High
X1B3	"	2 c.p.m.	0.2	Low
X1B4	"	2 c.p.m.	0.2	High
X1B5	"	1 c.p.m.	0.2	Low

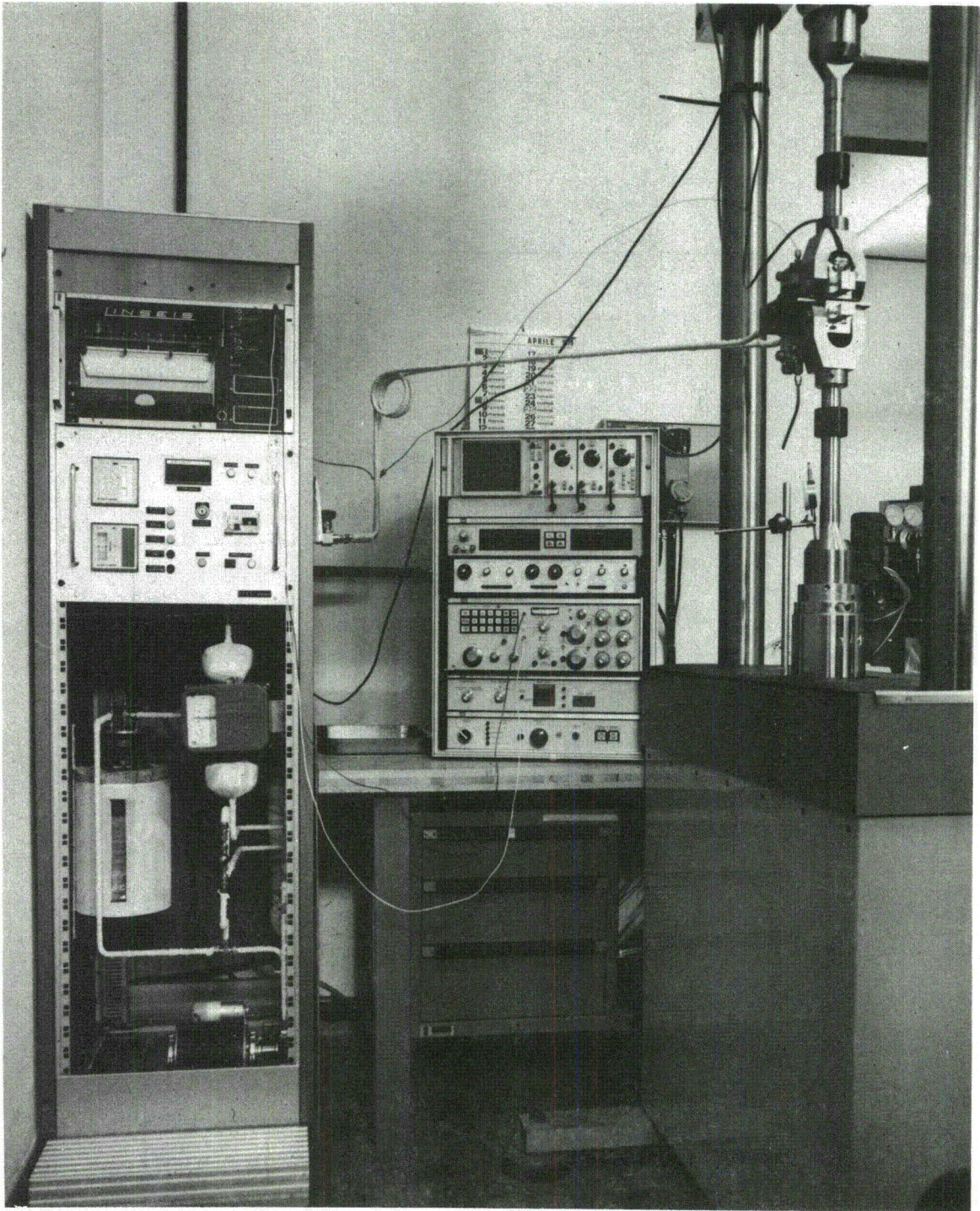


Fig. 1 - The water cell. Complete plant.

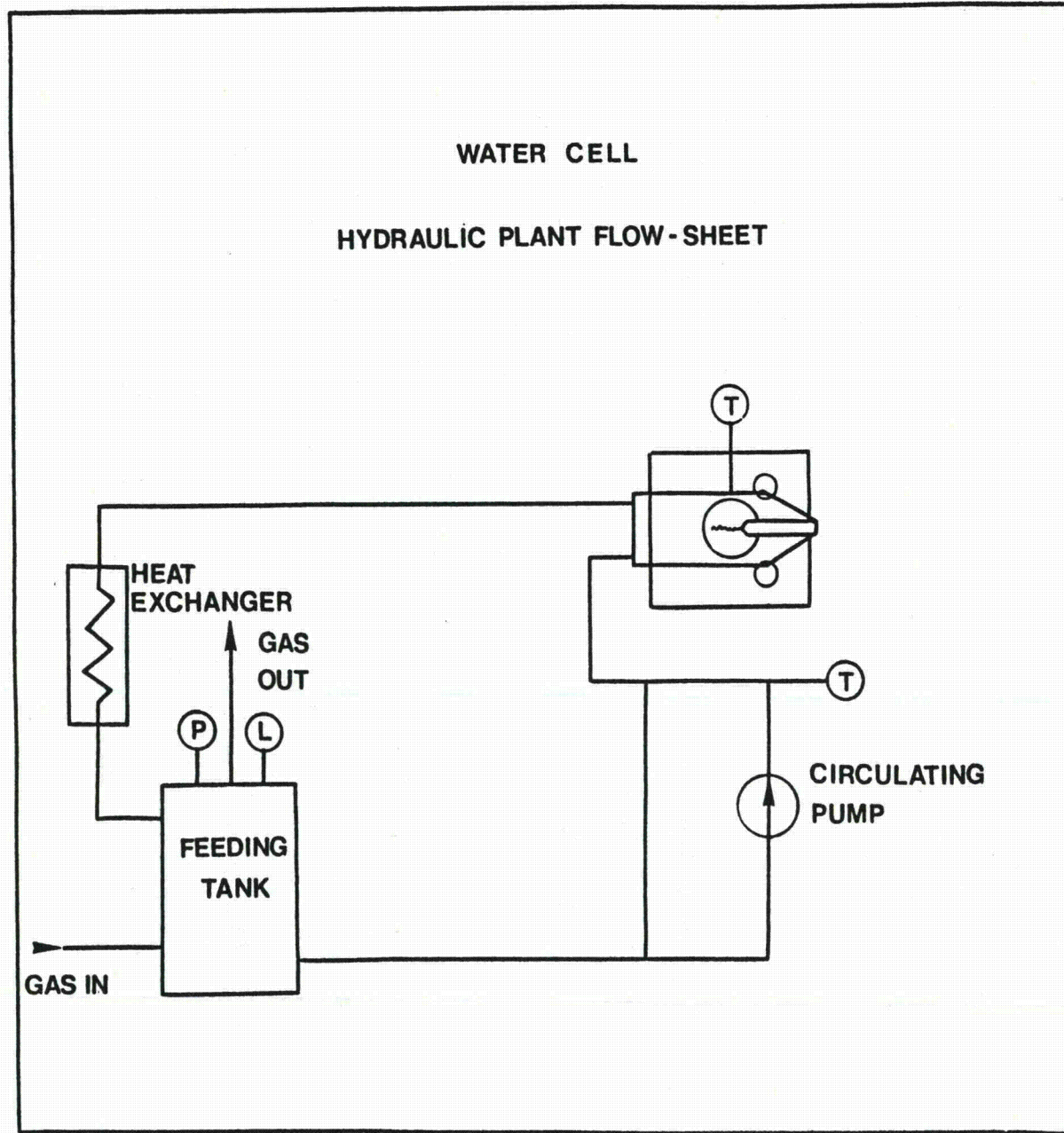


Fig. 2 - Flow-sheet of the water cell hydraulic plant.

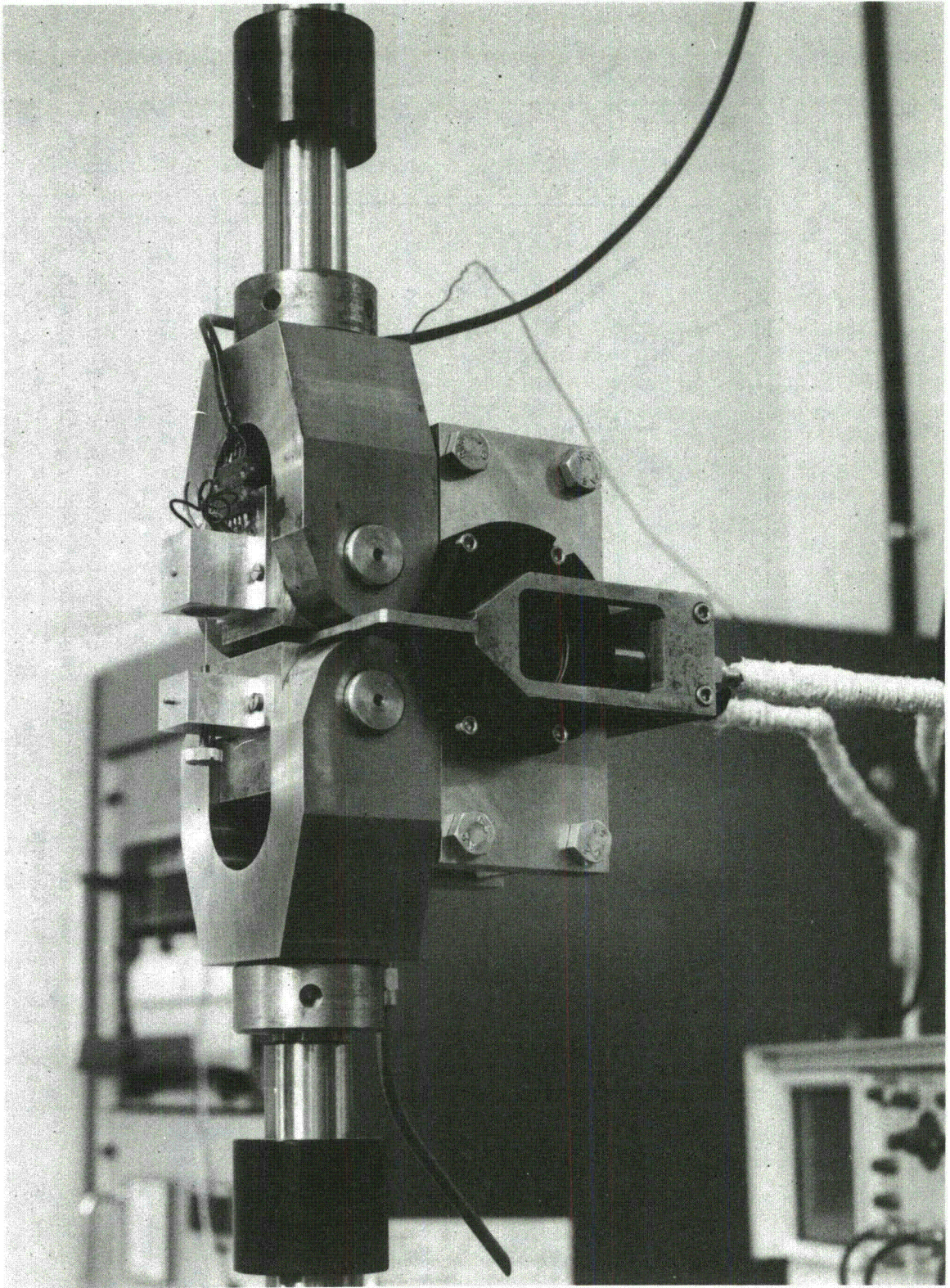


Fig. 3 -The water cell. Environmental chamber.

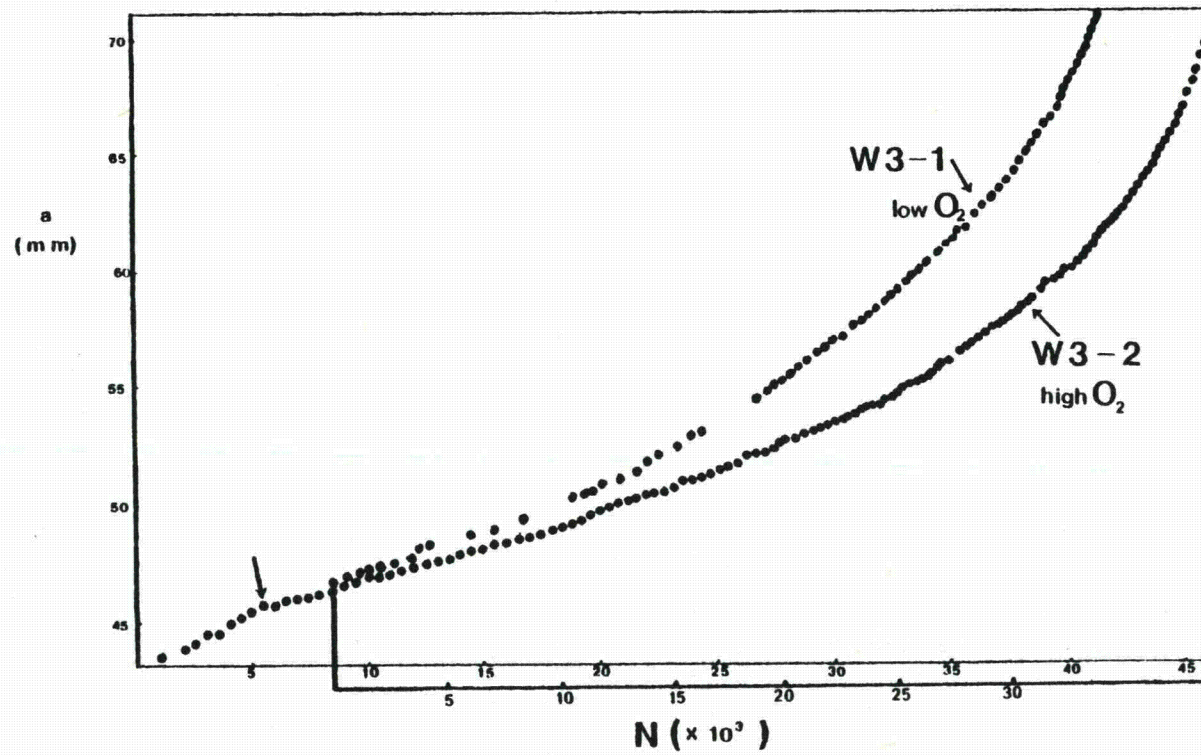


Fig. 4 - a vs N curves for the specimens W3-1 and W3-2. The arrow indicates the point where the growth rate decreases.

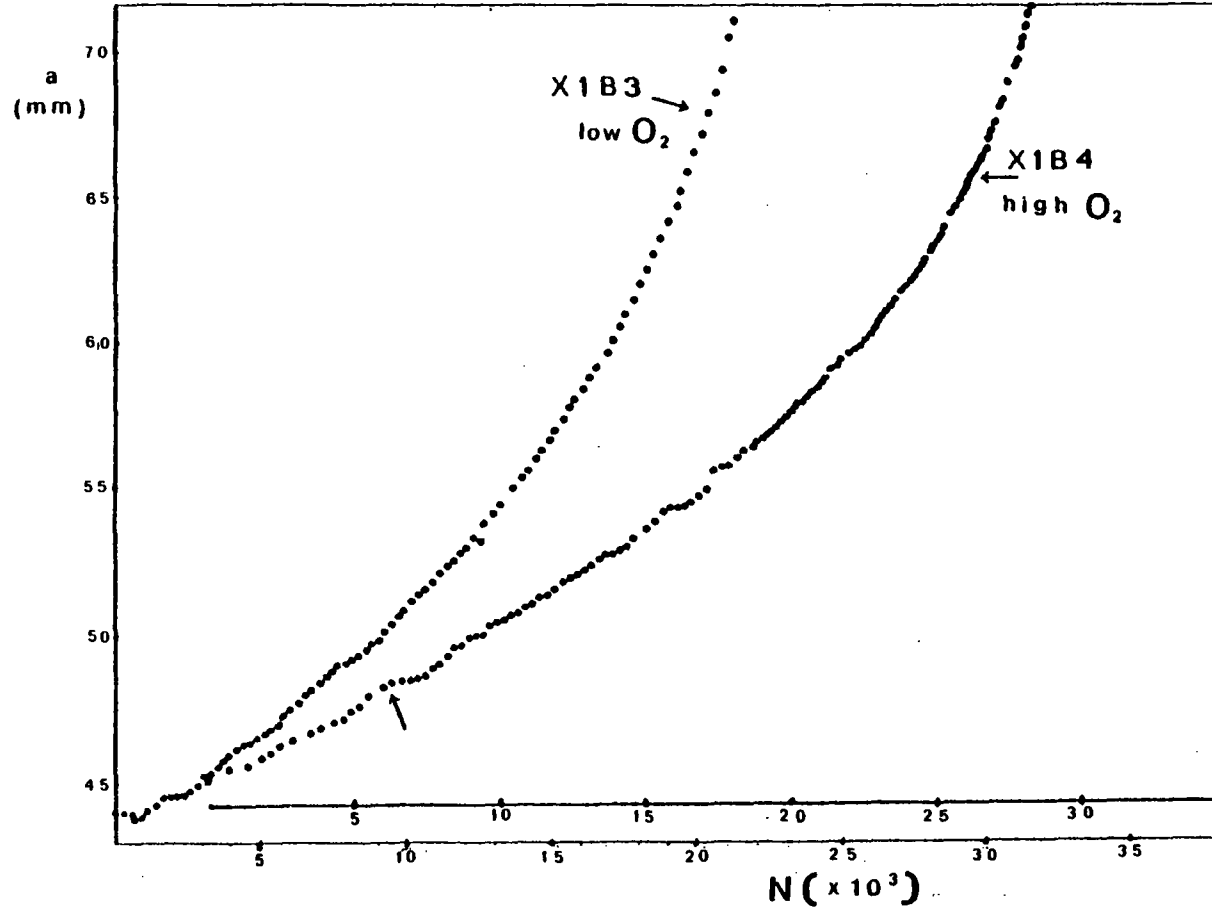


Fig. 5 - a vs N curves for the specimens X1B3 and X1B4. The arrow indicates the point where the growth rate decreases.

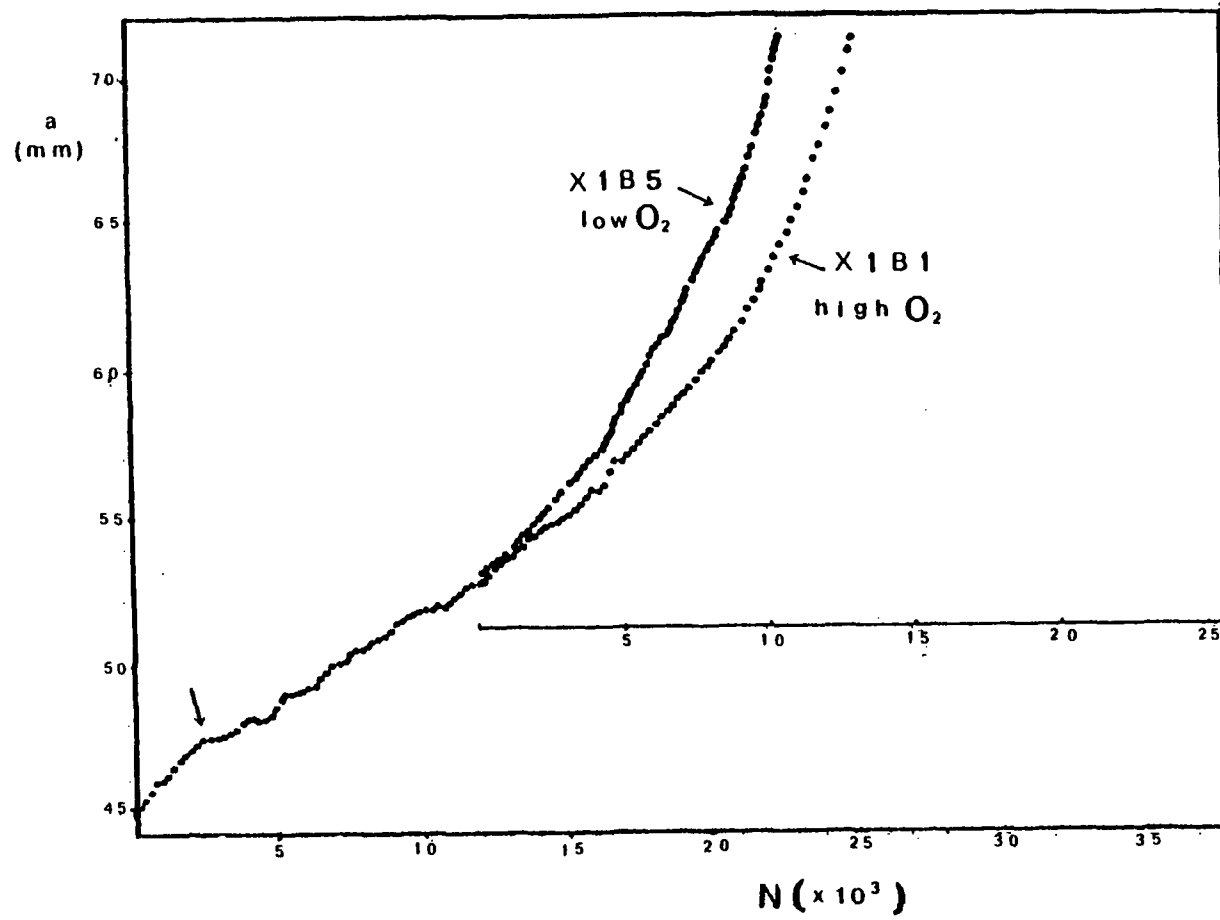


Fig. 6 - a vs N curves for the specimens X1B1 and X1B5. The arrow indicates the point where the growth rate decreases.

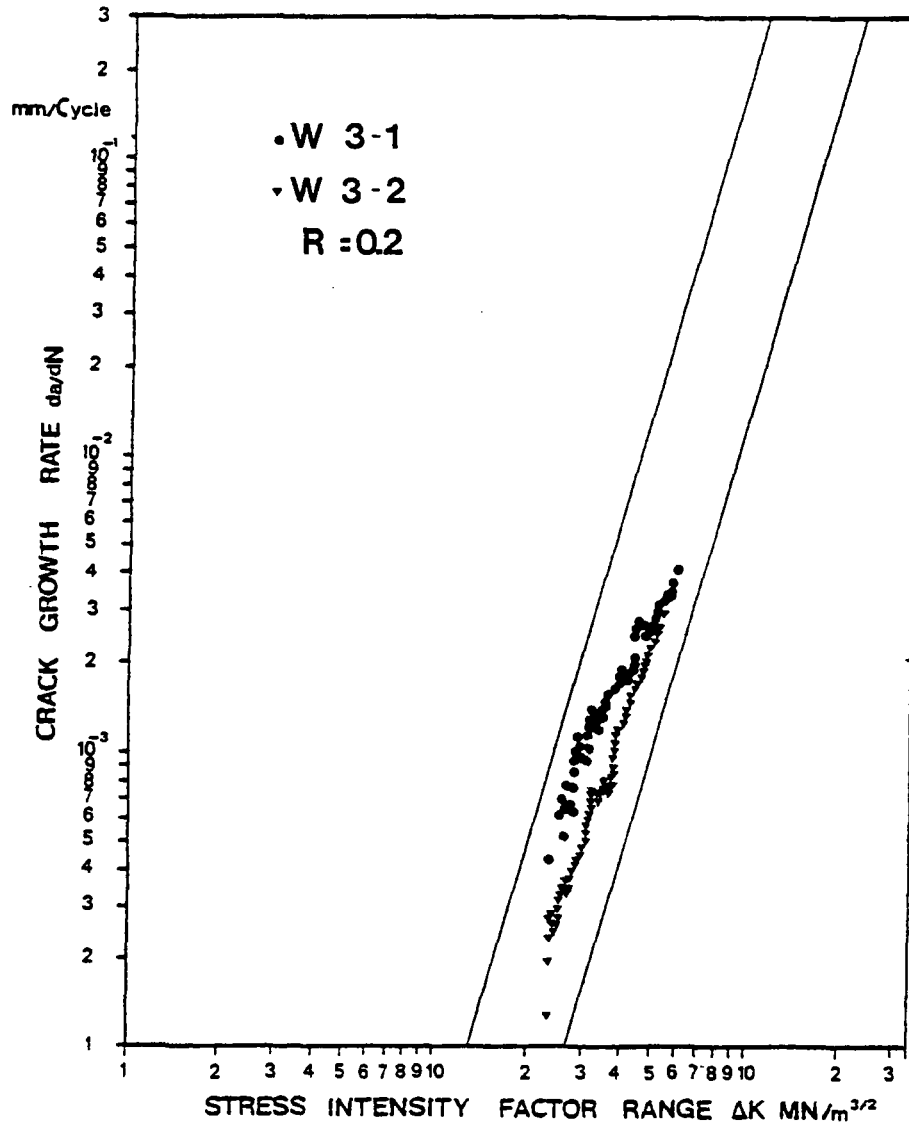


Fig. 7 - da/dN vs ΔK for the specimens W3-1 and W3-2.

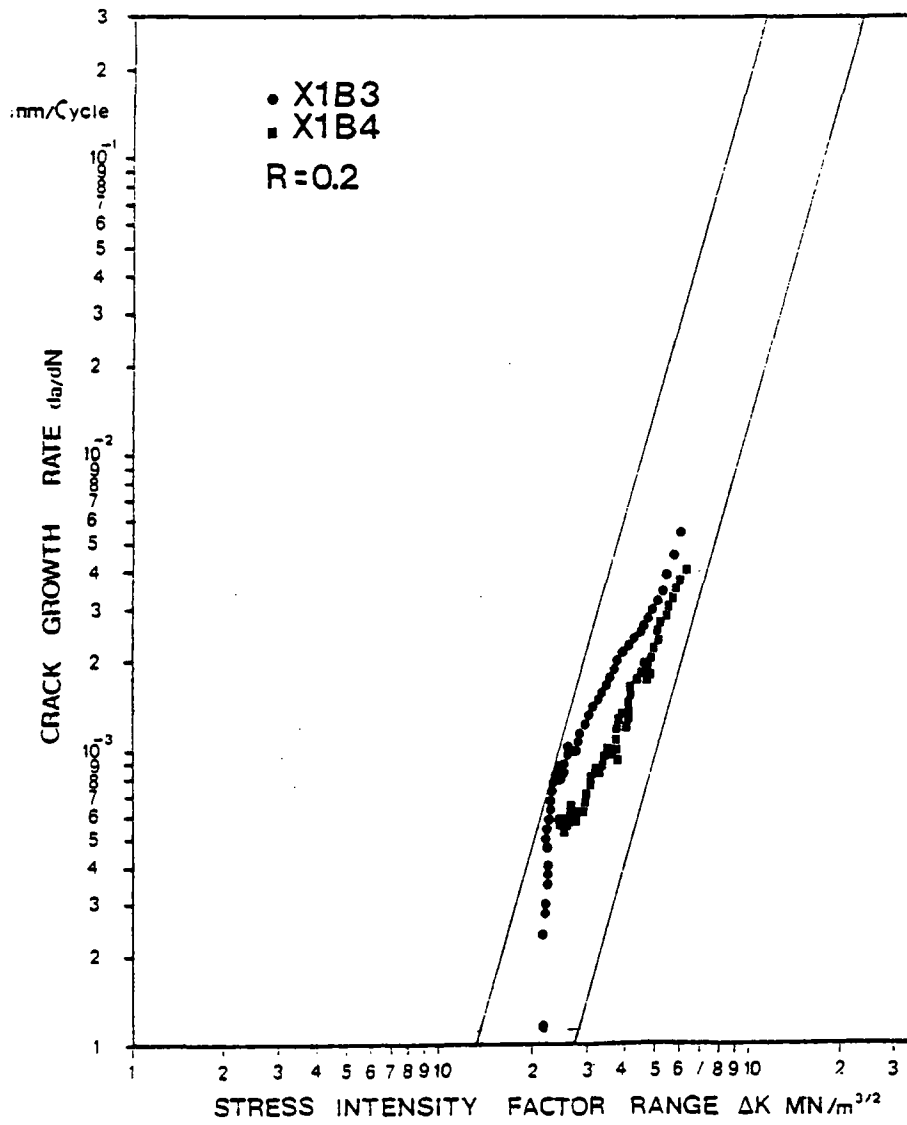


Fig. 8 - da/dN vs ΔK for the specimens X1B3 and X1B4.

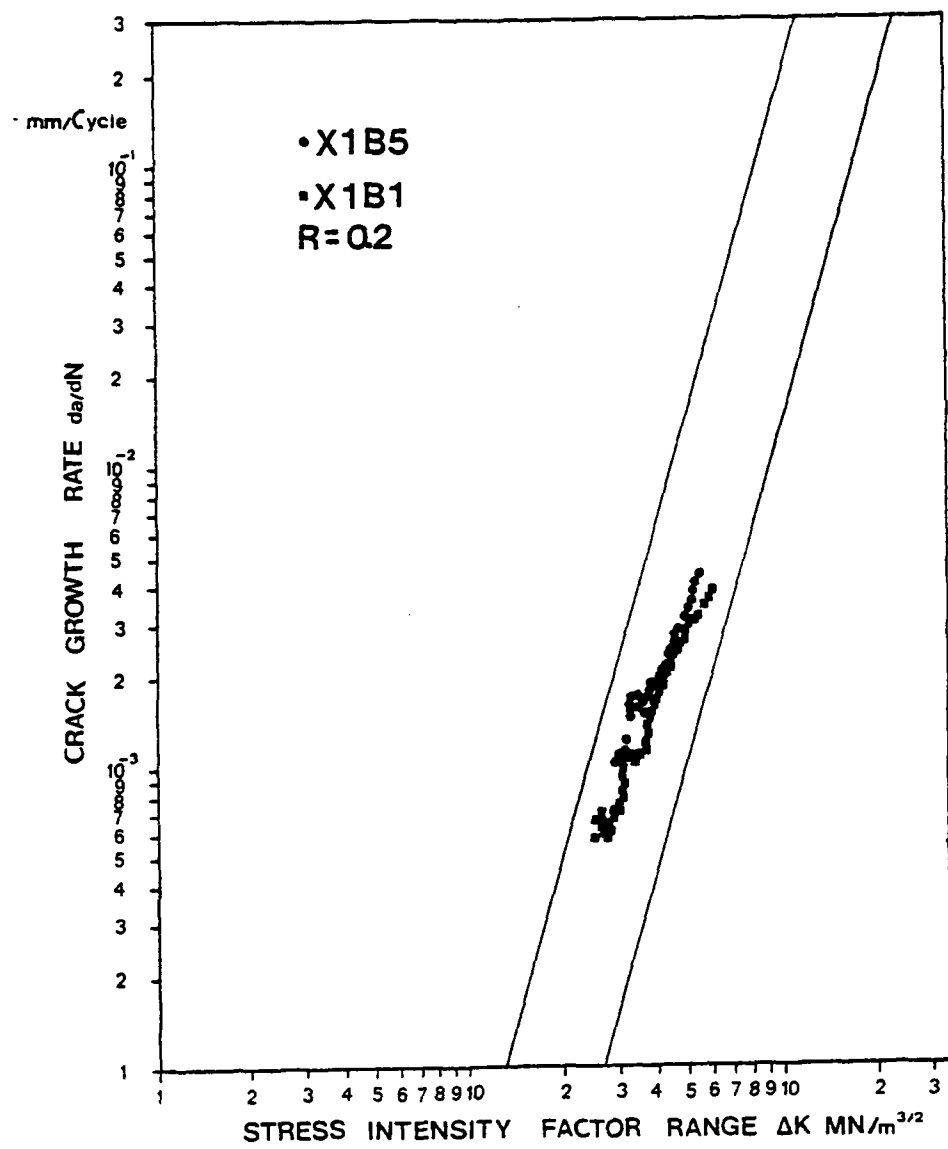


Fig. 9 - da/dN vs ΔK for the specimens X1B1 and X1B5.

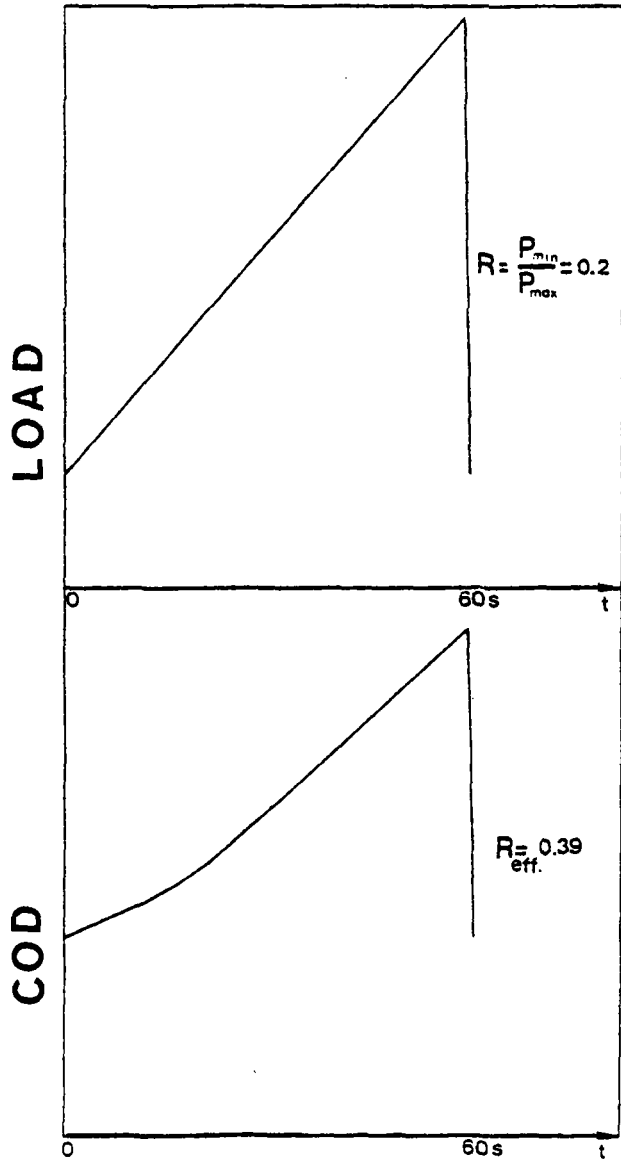


Fig. 10 - Applied load and COD for a specimen tested with high oxygen content in water.

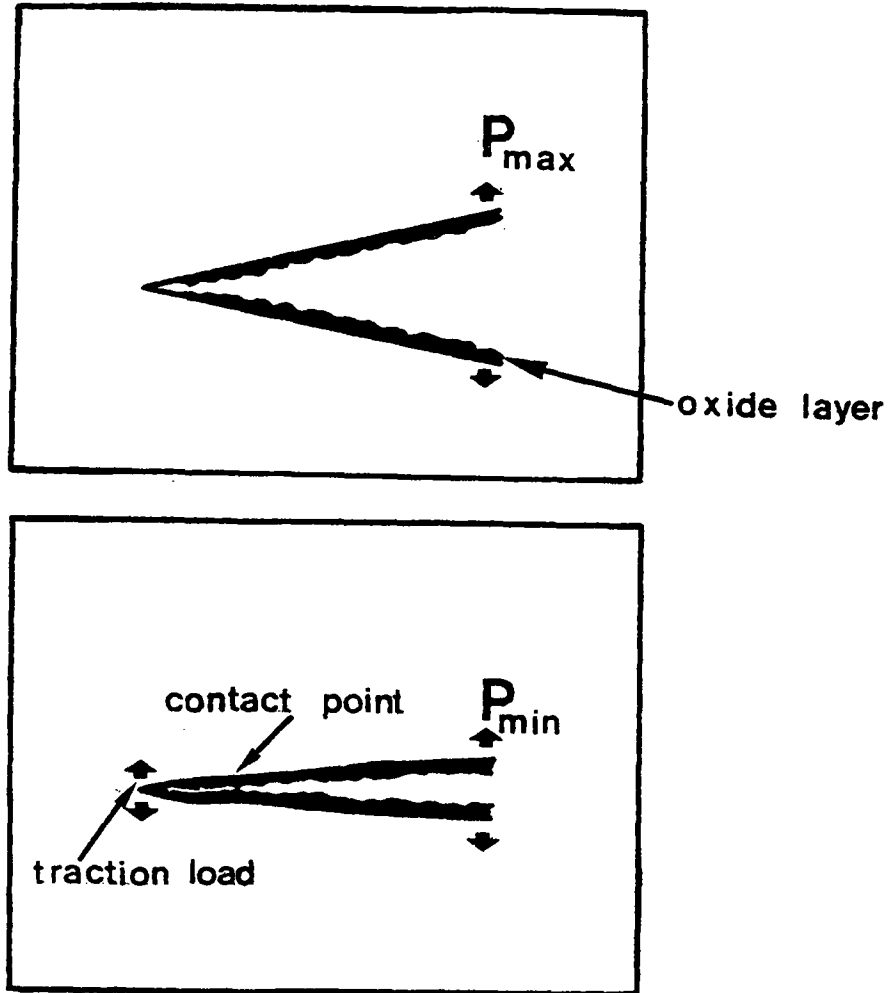


Fig. 11a-11b - The proposed mechanism for the action of the oxide layer.

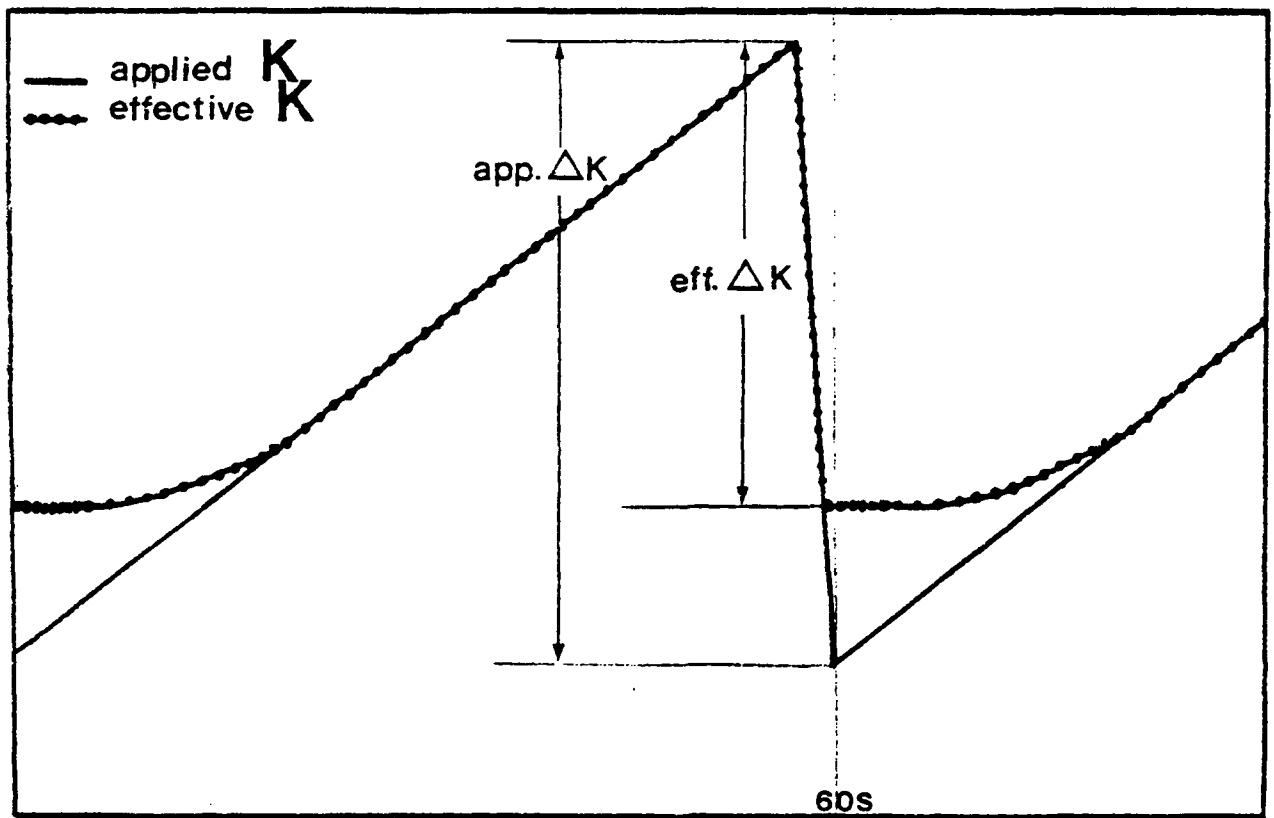


Fig. 12 - Effective ΔK vs applied ΔK at the crack tip.

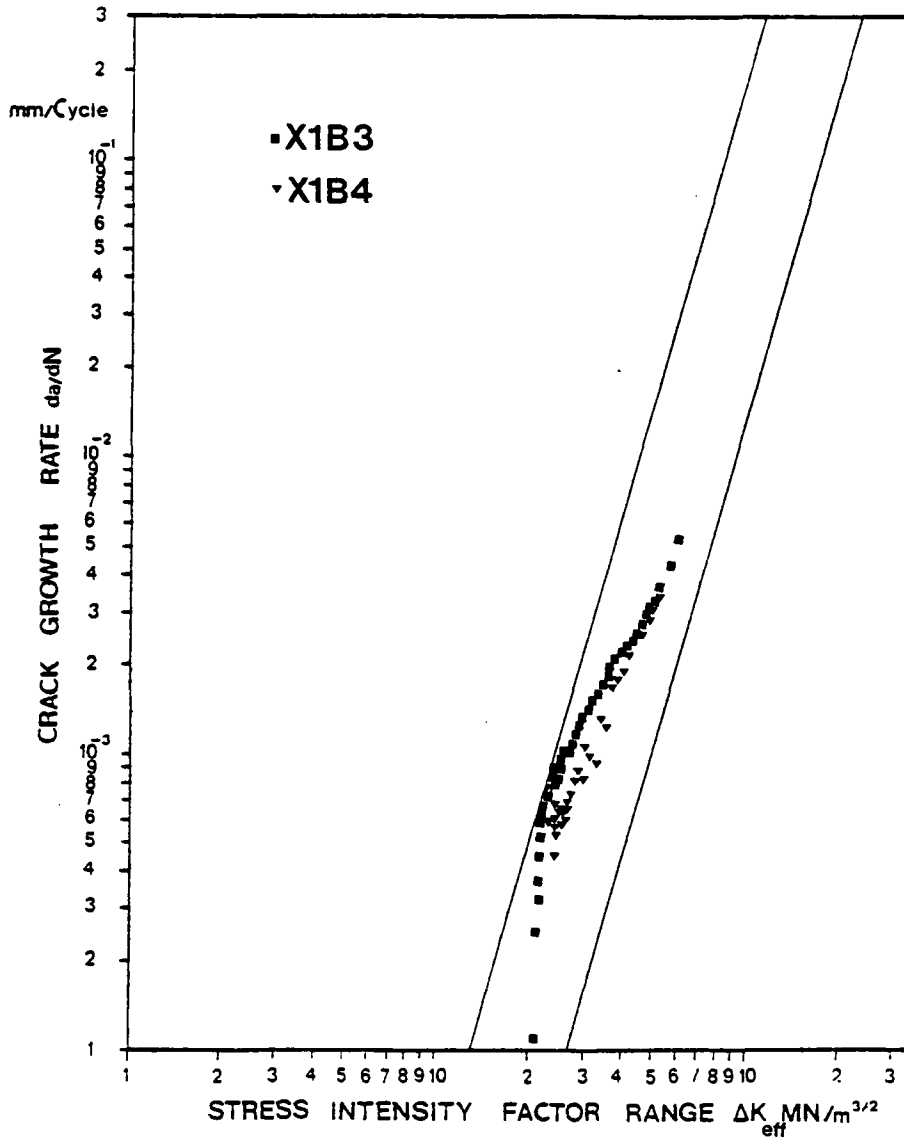


Fig. 13 - da/dN vs ΔK after the correction with ΔK effective.
 Specimen W3-1 - W3-2.

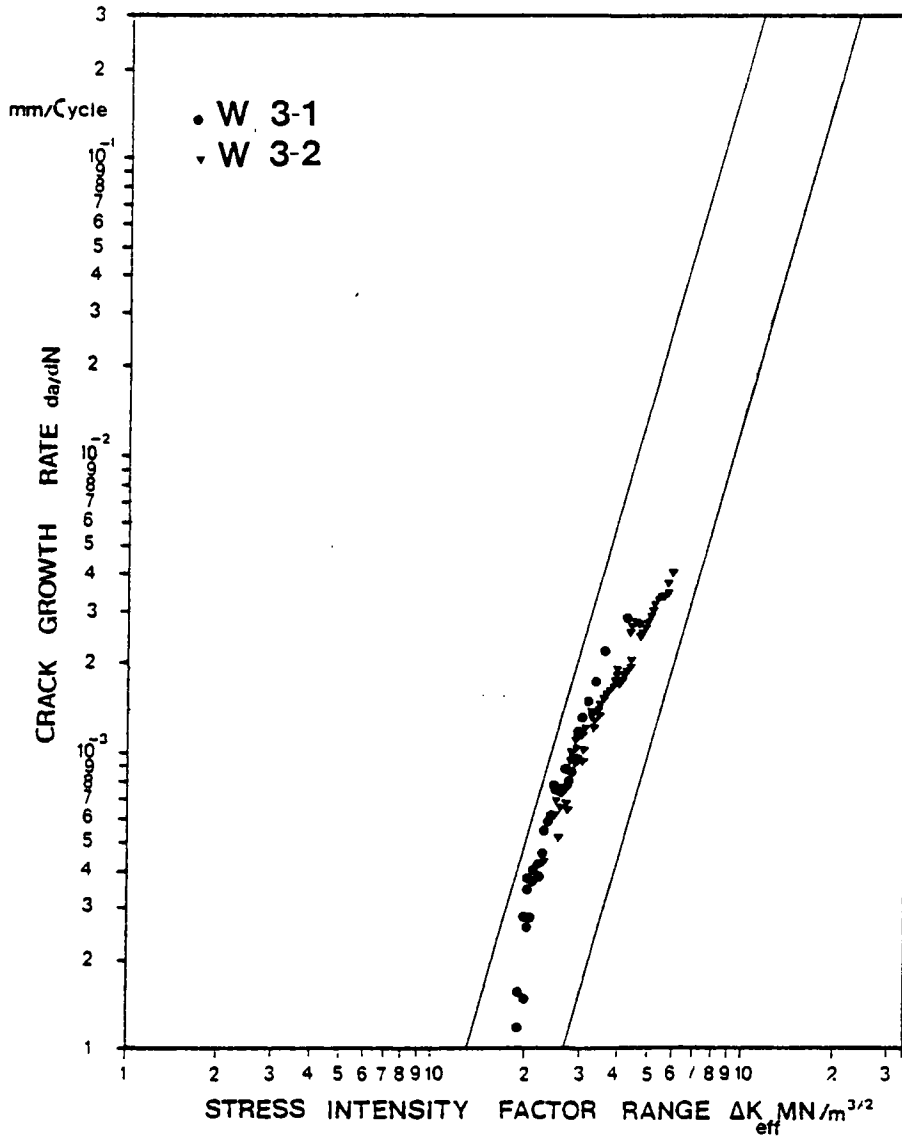


Fig. 14 - da/dN vs ΔK after the correction with ΔK effective. Specimen X1B3 - X1B4.

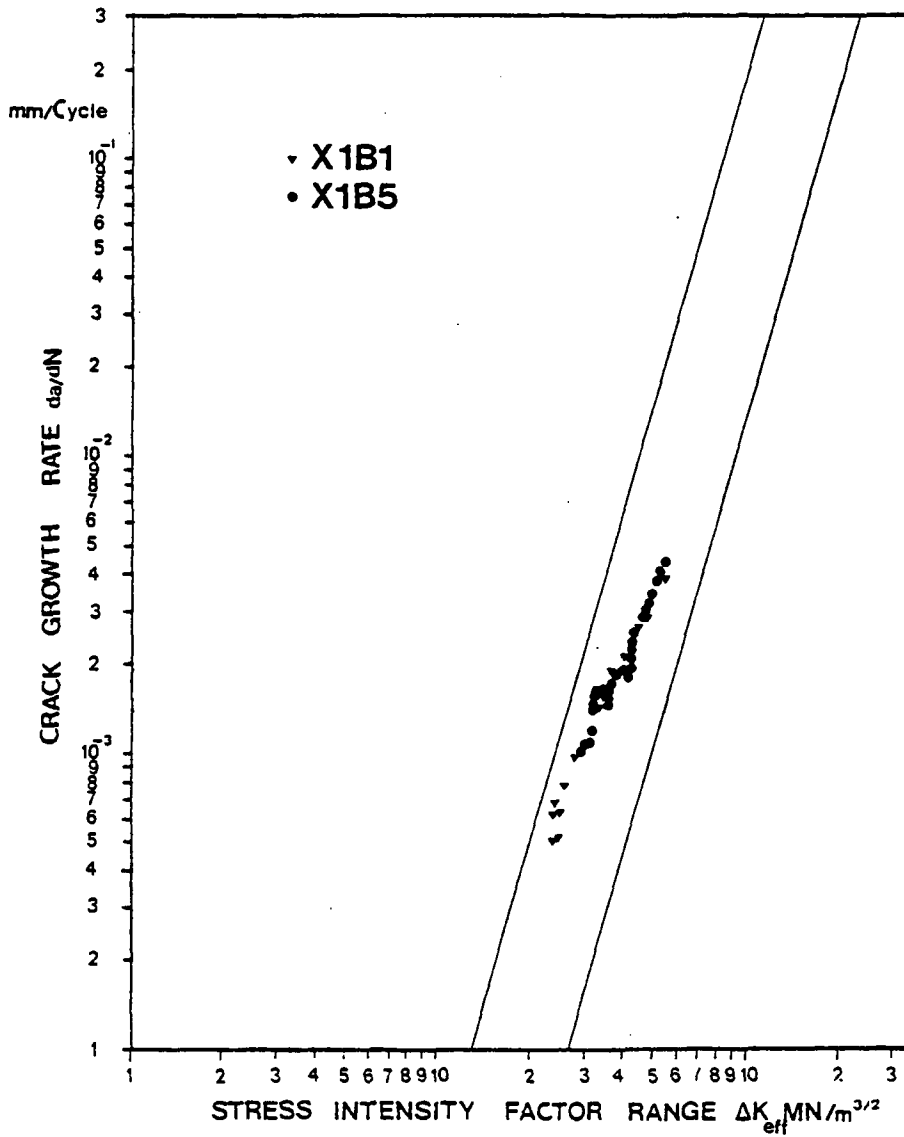


Fig. 15 - da/dN vs ΔK after the correction with ΔK effective. Specimen X1B1 - X1B5.

A MECHANISM OF ENVIRONMENTALLY-CONTROLLED CRACK-GROWTH OF STRUCTURAL STEELS IN HIGH-TEMPERATURE WATER

F.P. Ford

General Electric Corporate Research and Development

Schenectady, New York 12301 USA

Abstract

The slip dissolution model is used as a working hypothesis to explain the variations in environmentally-controlled cracking susceptibility of 304 stainless steel and SA333Gr6 carbon-steel in water as a function of oxygen, temperature, and strain rate. It is shown that the model is able to predict quantitatively the observed crack morphology and propagation rate of sensitized 304 stainless steel in H₂O/O₂ mixtures at 100 °C, and the blunting kinetics of SA333Gr6 carbon steel in the same environment. The variation in crack-morphology in the spectrum of straining modes covering static through high-frequency loading is also understandable. The model is able to explain qualitatively both the anomalously high cracking susceptibility of various iron-based alloys that is noted around 200 °C in water with low oxygen contents (e.g., $\sim \leq 0.2$ ppm O₂), and the relative crack propagation rates of carbon steel and stainless steel in water at 288 °C.

INTRODUCTION

It has been amply demonstrated in laboratory experiments that sensitized type 304 stainless steel is susceptible to intergranular stress corrosion (I/GSCC) both in high temperature oxygenated water (288 °C);⁽¹⁻¹¹⁾ and in lower temperature (≤ 100 °C) water,^(11-14,19) provided the oxygen content is in a specific range. It has also been experimentally observed that transgranular stress corrosion cracking (T/GSCC) can occur in both sensitized stainless steel^(8,11,16,17) and in carbon steels⁽¹⁸⁾ under specific environmental and loading conditions in high temperature water.

The object of this paper is to present recent constant extension rate data on the variation of stress

corrosion susceptibility for both sensitized 304 stainless steel and SA333Gr6 carbon steel in water as a function of oxygen, temperature, and strain rate, and to evaluate whether the slip-dissolution model of cracking can explain *quantitatively* the changes in cracking susceptibility and morphology in these alloys with different environmental and stressing conditions.

EXPERIMENTAL DETAILS

The line diagram of the water loop (Figure 1) used in these experiments indicates the flow pattern of solution to and from the test autoclaves. Deionized water (conductivity $< 0.4 \mu\text{mhos cm}^{-1}$) was delivered from a mixed resin bed to a 450 liter stainless steel reservoir. Aeration or controlled deaeration was accomplished by saturating the solution in the tank with either synthetic air (21% O_2 , 79% N_2) or argon/oxygen mixtures. The solutions were pressurized by a Pulsafeeder pump to 10.3 MNm^{-2} and delivered through a primary header system of stainless steel to the various testing stations, where the solution was introduced to each 1 liter 316 stainless steel autoclave at 20 cc min^{-1} via a coaxial heat exchanger. Automatic analytical facilities for pH (Beckman model 940B), conductivity (Beckman Solumeter) and oxygen (Beckman models 7001 and 7002) were used, via appropriate valving for both inlet and outlet solutions; the oxygen content was double-checked by colorimetric methods.

The 304 stainless steel used in the experiments had a composition 18.38% Cr, 8.6% Ni, 1.68% Mn, 0.6% Si, 0.22% Mo, 0.18% Cu, 0.12% Co, 0.017% S, 0.025% P, 0.07% C, and balance Fe. Tensile specimens were centerless ground from solution annealed ($1100 \text{ }^\circ\text{C} \times \frac{1}{2} \text{ hour}$, WQ) stock to $0.635 \text{ cm diameter} \times 3.81 \text{ cm gage-length}$ bars. These were then encapsulated in quartz tubes, evacuated to 10^{-6} torr and furnace-sensitized $600 \text{ }^\circ\text{C}$ for 24 hours.

Following the furnace sensitization treatment, the gage length of each bar was shot peened with size 550 ceramic shot at $0.012 \text{ } \text{Å}$ intensity to give a hardened surface layer. The objective of this shot peening was to lessen the initiation time for stress-corrosion cracking during the subsequent tensile test. Previous experiments have shown that when the shot peened samples were strained $\leq 3\%$, the hardened surface layer mechanically failed to give shear cracks of $\sim 50 \mu\text{m}$ depth; these cracks may then act as nucleii for subsequent propagation of I/G stress-corrosion cracks which are superficially observable at $\times 50$ magnification by 6-8% elongation.⁽¹⁹⁾

The SA333Gr6 carbon steel used in the experiments had the composition 0.22% C, 0.8% Mn, 0.009% P, 0.015% S, 0.18% Si, and balance Fe. Tensile bar specimens were centerless ground (0.317 cm diameter \times 3.175 cm gage length) from the wall of the as-received pipe, with the tensile axis parallel to the pipe-length; as with the stainless-steel specimens, the gage-lengths were shot-peened with 550 ceramic shot at 0.012 A intensity.

The specimens were mounted in the autoclave and were strained at between 2.1 and $2.7 \times 10^{-7} \text{ s}^{-1}$ in either an Instron model 1131 or 1125 tensile machine.

RESULTS

The effect of oxygen on the crack-growth rate in sensitized 304 stainless steel at 288 °C is shown in Figure 2. The propagation rate is defined as an *average* crack propagation rate, calculated from the largest observed crack penetration and the time from the attainment of 3% strain in the tensile test to final fracture. The present results are compared in Figure 2 with other data⁽²⁰⁾ obtained under faster extension rate conditions ($\dot{\epsilon} = 2.1 \times 10^{-6} \text{ s}^{-1}$) on a different heat of sensitized 304 stainless steel (0.063% C). Although all the cracks in the present work were intergranular, there is an indication from other work^(16,17,20) that at lower oxygen contents and higher strain rates, the cracks may be transgranular. Also shown in Figure 2 are the results^(15,21) for specimens under constant load either at 25 ksi or the prevalent stresses in pipes which failed in service.

The relationship between the average crack propagation rates observed in sensitized 304 stainless steel in $\text{H}_2\text{O}/\text{O}_2$ ppm O_2 at 288 °C under constant load,⁽²²⁾ constant extension rate or under cyclic loading⁽²²⁾ conditions are shown in Figure 3. These data are shown as a function of the crack-tip opening displacement rate which (for the constant extension rate and cyclic loading conditions) may be calculated from knowledge of the applied strain rates or the ΔK , frequency, and R values. Note that this crack-tip opening displacement rate is *not* known for constant load conditions, and the data points in Figure 3 for these conditions are plotted at values which *might* correspond to creep rates. It is seen that the crack propagation rates under these loading conditions are comparable, with the rate decreasing monotonically with decreasing crack-tip opening displacement rate. At the same time that the propagation rate decreases, so the fracture mode changes from 100% T/G under high frequency cyclic loading

to 100% I/G under static load.⁽²²⁾ Similar transitions in morphology and crack propagation rate under static, constant extension rate, and cyclic loading conditions have been observed⁽¹³⁾ on sensitized 304 stainless steel in H₂O/1.5-2.0 ppm O₂ at 98 °C.

The effect of different oxygen/temperature combinations on the I/GSCC susceptibility of sensitized 304 stainless steel in a constant extension rate test are reported in Figure 4; the superscripts beside each symbol indicate the average crack propagation rate in cm s⁻¹ ($\times 10^{-7}$). (It should be noted that because the length of the test is limited ultimately by ductile fracture of the remaining load-bearing area of the tensile specimens, the slowest crack propagation rate that can be detected by this testing technique is $\sim 5.8 \times 10^{-9}$ cm s⁻¹). The high cracking susceptibility in the temperature range 150-200 °C in low-oxygen water has been observed in other work on stainless steel,⁽²³⁾ low-alloy pressure vessel steel,⁽²⁴⁾ and carbon,⁽²⁷⁾ and turbine^(25,26) steels under a variety of loading conditions (Figure 5). It should also be noted, however, that although other workers^(11-14,19) have observed the high cracking susceptibility range at 100 °C in water within a specific oxygen range, the precise definition of that range in stainless steel is in debate and the magnitude of the susceptibility is strongly dependent on the degree of grain boundary sensitization.⁽²⁸⁾

The constant extension rate data obtained on SA333Gr6 carbon steel indicated that a degradation of tensile properties occurred at specific O₂/T combinations similar to those observed on 304 stainless steel. However, metallographic examination showed that, although at higher temperatures the ductility degradation is primarily due to T/GSCC, the degradation at lower temperatures is due to a combination of severe pitting and T/GSCC. The relative roles of cracking and pitting (in terms of the maximum penetrations) are recorded in Figure 6. Although in some incidences cracks were observed emanating from the base of pits, the pitting was not a necessary condition for crack initiation. Indeed at temperatures less than 200 °C, transgranular cracks became *blunted* due to subsequent pitting—at least at oxygen contents $> \sim 0.2$ ppm (Figure 7).

The average crack propagation rates at various O₂/T combinations are shown in Figure 8, for both SA333Gr6 carbon steel and (for comparative purposes) 304 sensitized stainless steel. The values with an asterisk (*) in Figure 8 indicate pit propagation in carbon steel rather than crack penetration (cf. Fig-

ure 7). Note that at a given O_2/T combination, the average crack propagation rate for SA333Gr6 is generally lower than that for sensitized 304 stainless steel under the specific constant extension rate conditions used.

DISCUSSION

The objective of the discussion is to determine whether the slip-dissolution model for crack-propagation is capable of explaining *quantitatively* the effects of different O_2/T combinations on the cracking susceptibilities of sensitized 304 stainless and SA333Gr6 carbon steels in high-purity water (Figures 4 and 8), the strain-rate effects on cracking (Figure 3), and the abnormally high cracking susceptibility at the temperature range 150-200 °C in low-oxygen water (Figure 5).

The salient features of the slip-dissolution model of stress-corrosion crack propagation, its applicability to corrosion-fatigue,^(29,30) and its relation to other propagation mechanisms (e.g., hydrogen embrittlement) have been described in detail in other documents.⁽³¹⁻³⁹⁾ In brief, the advancement mechanism relates faradaically the propagation rate to the total oxidation rate at the crack-tip, where the normally protective oxide is being mechanically ruptured by changes in the strain-field concentrated there. Thus the crack-propagation rate will depend on the bare-surface dissolution rate, the rate of passivation at the oxide-ruptured crack-tip surface, the periodicity of oxide-rupture and, finally, on the mass-transport rate of solvating water molecules to the dissolving surface and the flux of solvated metal cations away from that surface (Figures 9 and 10).

The average crack-propagation rate, V , may be predicted therefore (Figure 10), if the oxidation charge-density is known as a function of time following an oxide-rupture event, and provided the periodicity of oxide rupture is also known.

i.e., by applying Faraday's Laws

$$V = \frac{M}{\rho F \eta} \cdot \frac{Q_f}{t_f} \quad (1)$$

where

M, ρ = atomic weight and density of metal at the crack tip being oxidized.

η = the valence change during the overall oxidation process, which will involve both dissolution

and oxide-growth reactions.

F = Faraday constant (= 96,500 coulombs)

Q_f = the oxidation charge-density passed in t_f , following the oxide rupture event

t_f = the periodicity of oxide rupture.

Calculation of the latter parameter, t_f , will involve knowledge of the local crack-tip strain rate, $\dot{\epsilon}$, and the fracture strain of the surface oxide, ϵ_f , (i.e., $t_f = \epsilon_f / \dot{\epsilon}$) provided it is assumed that the strain changes in the matrix are transferred to the adherant oxide.

The variation in oxidation charge density with time, Q_t , values may be experimentally determined by a variety of techniques which involve either chemically or mechanically⁽⁴⁰⁻⁵¹⁾ removing the surface oxide and measuring, under potentiostatic control, the resultant oxidation charge density transients. Such experiments⁽¹²⁾ have been performed in dilute sulphate solutions on alloys of Fe 12% Cr 10% Ni or Fe 18% Cr 8% Ni nominal compositions which simulate⁽⁵²⁾ a range of chromium and nickel contents expected at the tip of a grain-boundary crack in sensitized 304 stainless steel. By applying Faraday's Laws, the penetration down the vector corresponding to Fe 12% Cr 10% Ni, i.e., the grain boundary, may be compared with that down a vector corresponding to Fe 18% Cr 8% Ni i.e., the grain matrix. Such a comparison⁽¹²⁾ is shown in Figure 11 as a function of electrode potential in 0.01 M Na_2SO_4 (pH 5.8) at 98 °C. It is observed that in certain potential ranges the penetration down the sensitized grain-boundary is calculated to be significantly greater than into the grain matrix; in these regions, therefore, deep intergranular cracks would be predicted. In other potential regions there is no significant difference in calculated penetrations in the two directions and the morphology prediction is for relatively blunt and shallow intergranular notches. Such predictions are, in fact, confirmed metallographically (Figure 12); the salient point being that deep I/GSCC is predicted in the potential range that would correspond to the corrosion-potential in water containing ~ 2 ppm O_2 at 100 °C. Thus it is not surprising that I/GSCC in water at 100 °C is observed in the range 0.8-4 ppm O_2 (Figure 4).

The crack propagation *rate* in the low temperature water, or dilute sulphate solution, may be predicted by the slip-dissolution model from the $Q_{(t)}$ characteristics, provided the periodicity of oxide rupture, t_f , is known. This may be calculated (crudely) in a constant-extension rate test by combining

the measured⁽⁵³⁾ fracture strain of the oxide, 10^{-3} , and the applied strain rate during the test, e.g., for an applied strain rate of $2.1 \times 10^{-6} \text{ s}^{-1}$, the periodicity of oxide rupture is 476 s ($= 10^{-3}/2.1 \times 10^{-6}$). A comparison between the predicted and observed crack propagation rates is shown in Figure 13 for sensitized 304 stainless steel, strained at $2.1 \times 10^{-6} \text{ s}^{-1}$ in 0.01 M Na_2SO_4 at 98 °C at various potentials; a reasonable agreement is observed, the major discrepancy between prediction and observation occurring at the more positive potentials where the *observed* cracks are blunted by pitting (Figure 12a).

The predicted and observed crack propagation rate variations with strain rate are shown in Figure 14 for the case of sensitized 304 stainless steel in 0.01 M Na_2SO_4 (controlled at +193 mV she) and in $\text{H}_2\text{O}/1.8 \text{ ppm O}_2$ at 98 °C. The theoretical values have been calculated from equation 1 with t_f values corresponding to the applied strain rate ($t_f = 10^{-3}\dot{\epsilon}^{-1}$). As expected, the theoretical rate increases monotonically with strain rate (i.e., oxide rupture rate) when an asymptotic value is reached, symptomatic of the creation of a *continuously* bare surface at the crack-tip and the associated bare-surface dissolution rate in a *stagnant* solution. (At higher strain rates, crack blunting can theoretically occur⁽⁵⁴⁾ due to plastic deformation under constant extension rate conditions, and the observed crack propagation rate should decrease from the maximum theoretical value.) It is seen that there is again a reasonable correlation between theory and the observed average crack propagation rate on wire samples under applied strain rate conditions.

Under constant load conditions, the crack-tip strain rate may be correlated with a creep rate, and indeed the observed crack-propagation rates under constant-load do correspond to the rate expected in the appropriate creep strain-rate range.⁽⁵⁵⁾ However these latter correlations must be questionable since uniaxial creep data on relatively unconstrained wire specimens are not necessarily accurate for the situation at a plastically-constrained crack-tip, where matrix/environment interactions may well affect the *local* creep rate due to surface dissolution,⁽⁵⁶⁻⁵⁸⁾ adsorption,⁽⁵⁹⁾ surface film formation,^(60,61) and periodic stress relaxation as the dislocations rupture the oxide film.⁽⁶²⁾ Further, data obtained in uniaxial creep tests on smooth specimens do not account for the fact that, in the case of a propagating crack, the mobile dislocation spectrum at the triaxially stressed crack-tip is continually changing because of the increasing stress field at any given dislocation source.

Subsequently, prime importance has been attached to the fact that the stress field at a fixed point in front of the crack-tip is changing as the crack propagates, and this has led to suggestions by Newman,^(63,64) Scully,⁽⁶⁵⁾ and Vermilyea⁽⁶⁶⁾ that the requirement for *continued* oxide rupture is a specific amount of crack advance, L^* , between oxide rupture events (Figure 15). Although the *precise* metallurgical reasoning behind such a criterion is unclear, the logic⁽⁵³⁾ is that L^* may be related to a stress-dependent increase in an athermal strain increment and a time-dependent creep strain increment at the crack tip. Since the critical penetration distance, L^* , may be faradaically related to an oxidation charge-density, Q^* , (i.e., $L^* = \frac{M}{n\rho F} \cdot Q^*$), the same formulation may be used (i.e., equation 1) to predict the crack propagation rate from the $Q(t)$ characteristics as was used in the prediction of propagation rates for constant extension rate conditions. The only difference is that, now, Q^* is a metallurgically-fixed constant and t_f is dependent on the $Q(t)$ characteristics which vary with the environmental conditions (Figure 15).

The difficulty in applying such a constant-charge criterion for crack-propagation under constant-load conditions is the uncertainty in ascribing, from first principles, a value of Q^* . It can be argued that Q^* should be related to a dislocation-source spacing—and, indeed, it has been shown⁽¹²⁾ that L^* values of 0.5-1 μm , which correspond to dislocation cell diameters, do give a reasonable fit between observed and theoretical crack-propagation rates in the 304 stainless-steel/ Na_2SO_4 system. Values of Q^* may also be predicted⁽⁵³⁾ to within a factor of two by employing an energy-balance argument which states that changes in the elastic, surface, and chemical energies of the system as the crack moves forward by a distance, L^* , must be balanced by appropriate changes in the plastic energy concentrated at the crack-tip. Alternatively, a very simplistic linear-elastic fracture mechanics argument⁽⁵³⁾ (based on the assumption that, in order to have creep at a required rate, the activation stress for dislocation glide⁽⁶⁷⁾ must be decreased by a specific amount) leads to the conclusion that

$$Q^* = AK^{-1} \quad (2)$$

where A is a constant that is dependent on crack length and the dislocation-source spacing, and K is the stress-intensity. Indeed, such a relationship as equation 2 has been demonstrated for turbine steels in caustic environments.⁽⁵³⁾ In order to evaluate A in equation 2 for the present stainless steel/water sys-

tem, a forced fit between theory and observation is required at one data point. Using such a procedure leads to a good prediction of the crack propagation rate/stress-intensity relationship⁽⁵³⁾ for 304 sensitized stainless steel in H₂O/1.5 ppm O₂ at 98 °C, as shown in Figure 16. In this example the Q(t) data in 0.01 M Na₂SO₄ at an appropriate potential (+193 mV she) corresponding to the corrosion potential in H₂O/1.5 ppm O₂ has been used in conjunction with equations 1 and 2. (Force fitting observation and theory at $K = 27 \text{ MNm}^{-3/2}$ yields a value of $A = 1.6 \times 10^2 \text{ C cm}^{-2} \text{ MNm}^{-3/2}$). It is seen in Figure 16 that the theory has not taken into account the decelerating effect of crack-branching, but presumably this may be accounted for by substituting K in equation 2 for K_{eff} .

The intermediate conclusions concerning the present theoretical prediction capabilities for stress-corrosion cracking in the systems considered in this paper are, that the slip dissolution model is capable of quantitatively defining the potential, strain rate, and stress-intensity dependence of both crack propagation rate and morphology for sensitized 304 stainless steel in water and dilute sulphate solutions at 98-100 °C. Therefore in *extrapolating* these predictive capabilities to higher temperatures and to carbon-steels, importance must be attached to the effect that these environmental and compositional changes may have on the controlling parameters in the slip-dissolution model, i.e., total oxidation rates, liquid diffusion rates, and oxide rupture rates.

Since the slip-dissolution model is basically an electrochemical mechanism, the data in Figure 4 has been replotted in Figure 17 in terms of the average crack propagation rate and corrosion potential, where the corrosion potential values for various oxygen/temperature combinations have been taken from the work of Indig.^(68,69) Note that in the following arguments it is tacitly assumed that there is a minimal potential drop down the crack-length under open-circuit conditions and that, therefore, the potential at the crack-tip is approximately equal to the corrosion-potential at the exposed specimen-surface. The narrow potential range for high IGSCC susceptibility, predicted⁽¹¹⁾ for 100 °C, is observed, but it is also noted that as the temperature increases so the potential dependence for crack propagation changes. (It is also apparent that at 150 °C the crack propagation rate dependence on potential may be either high or low, presumably mirroring a transitional behavior in rate-determining steps for crack propagation; the shaded regions in Figure 4 correspond to this particular region of uncertainty in Figure 17.) A preliminary activation enthalpy analysis⁽⁵³⁾ on these (sparse) data indicates that,

in general, the activation enthalpy is low (~ 4 Kcals gm-mol⁻¹) at higher temperatures and faster crack propagation rates, but is much higher (> 20 Kcals gm-mol⁻¹) at lower temperatures. The inference is, therefore, that *at a given potential*, the propagation rate is determined at lower temperatures by reaction rates on the crack tip surface which are controlled by oxidation rate/oxide rupture rate interactions, but as the temperature increases above ~ 150 °C and the crack-propagation rates $> 10^{-7}$ cms⁻¹, liquid diffusion processes remote from the crack tip surface become rate-determining. On this basis, one would expect the crack propagation rates *at a given potential*, to increase with temperature according to the dashed lines in Figure 18. In fact, it is observed that *under open-circuit conditions*, the propagation rate in an environment having a given oxygen content follows the expected relationship at low temperatures, but deviates at higher temperatures—especially in lower oxygen-content solutions. The explanation for this deviation could be that the open-circuit corrosion-potential does not remain constant with increasing temperature,⁽⁶⁹⁾ and this is especially the case in lower oxygen-content solutions—as shown in the inset diagram in Figure 18. Thus, the ‘anomolously’ high cracking susceptibility noted ~ 150 - 200 °C in low oxygen environments is caused by competing effects of an increase in propagation rate with temperature under high activation enthalpy conditions at lower temperatures, and a decrease in propagation rate as the corrosion potential moves in the negative direction with further increase in temperature (and thereby slows down the oxidation kinetics). Similar arguments can be made, based on the $E_{corr}/O_2/T$ relationships of Indig,⁽⁷⁰⁾ for the ‘anomolous temperature’ effects noted in carbon-steel and pressure-vessel steels (Figure 5).

The slip-dissolution model for crack propagation may also be applied in principle to the carbon steel/water system. In this case, however, there is compositionally no preferred crack propagation path, as in the sensitized grain boundaries in 304 stainless steel. Thus crack propagation would be expected to be transgranular since it is the matrix vector that the oxide-rupture rates will be highest. A major factor that will differentiate between the carbon steel/water and stainless steel/water systems, however, is the propensity for crack blunting in the former system due to general corrosion on the crack-sides, Figure 19. In situations where V_r , the penetration rate at the crack-tip, is much greater than V_s , the penetration rate on the crack sides, then sharp transgranular cracks should be observed. Such situations are noted in high temperature water where V_s is relatively low because of the protective magnetite on

the crack sides, and under constant extension rate or corrosion fatigue conditions where the high applied strain rates ensure a high V_i value. Indeed it can be argued that, under these high V_i conditions at high temperatures, the crack propagation will be under diffusion control similar to that observed in stainless steel. Consequently the crack propagation rates in the carbon steel/water and stainless steel/water systems should be similar. (That is, provided the basic requirements for crack propagation are met by protected crack sides and a high oxidation charge density at the crack tip, then the propagation rate is not *material*-dependent but is limited by solution hydrodynamics.) Such a similarity in propagation rate/potential dependence between the two systems is, in fact, observed (Figure 20) under these *required* testing conditions. Note that, since the E_{corr} value for carbon-steel tends to be slightly more negative than that for stainless steel at a given oxygen content, this would explain why, at 288 °C in Figure 8, carbon steels exhibit lower average crack propagation rates than stainless steel.

At low temperatures and high oxygen conditions, where V_s is high for carbon-steel and pitting occurs, or under loading conditions such as constant-load, or low frequency cyclic loading, where V_i is low due to the lower oxide-rupture rates, then progressive crack blunting will occur and crack arrest may be expected with time. This is in fact observed⁽⁷¹⁾ on SA333Gr6 in H₂O/1.5 ppm O₂ at 98 °C, and has also been noted under similar environmental conditions in other carbon and low alloy steels;⁽⁷²⁻⁷⁵⁾ by contrast, in environmental situations such as H₂O/0.1 ppm O₂ where the V_s value for carbon steel is reduced, or with different alloys such as 304 stainless steel where V_s is inherently low in water, no such crack arrest is noted (Figure 21). There is some debate whether the arresting effect under cyclic loading is due to the effect of chemical blunting on the *actual* stress-intensity value, or on the effect that corrosion debris has on the extent of crack tip closure;⁽⁷⁵⁾ since both of these effects are associated with the same phenomenon (i.e., corrosion on the crack sides) it is difficult to devise an experiment which unambiguously differentiates between the two models. However, in Figure 22 the applicability of the chemical-blunting model is suggested, at least for the low-temperature environments by the reasonable prediction of the decrease in da/dN values, for an observed range of V_s values.⁽⁷¹⁾

It follows from the above analysis that the frequency, ΔK and R values during cyclic loading or the applied strain rate during constant extension rate testing should all have an effect on the time dependent blunting of cracks in the carbon steel/water system, since these parameters all control V_i , and

hence the relative values of V_s and V_f . For instance the observed⁽⁷¹⁾ values of the environmentally controlled da/dN values for SA333Gr6 are shown in Figure 23 as a function of frequency (for $K_{max} = 22 \text{ MNm}^{-3/2}$ and $R = 0.1$ in $\text{H}_2\text{O}/1.5 \text{ ppm O}_2$ at $98 \text{ }^\circ\text{C}$). It is seen that, in common with many other observations on iron-based alloys, the $(da/dN)_{\Delta K}$ value increases with decreasing frequency. However, unlike observations⁽¹³⁾ on 304 stainless steel in the same low-temperature environment, the $(da/dN)_{\Delta K}$ values decrease with lowering frequency for $V < 1 \text{ Hz}$. This decrease can be explained however by the fact that, at these slow frequencies, the *time*-dependent crack growth rate is lowered to the extent that, at the prevalent V_s values, blunting occurs. The *predicted* variations⁽⁵³⁾ in the $(da/dN)_{\Delta K}$ values are shown in Figure 23 as a function of exposure time and frequency. It is seen that the predicted and observed values (after the exposure times indicated by each data point) are in reasonable agreement. It is interesting to note that, with current crack following techniques, it needs at least 45 hours exposure under low frequency loading to make a reliable crack increment measurement; hence the measured $da/dN_{\Delta K} \nu$ relationships for these steels under these environmental conditions will always have an inverted U-shape, since crack blunting and deceleration will occur during the measurement time at low frequencies. It is not surprising therefore that at very low frequency loading, or ultimately under constant load situations, that no detrimental environmental effects are observed in carbon steels (at least under the environmental conditions of $\text{H}_2\text{O}/1.5 \text{ ppm O}_2$ at $98 \text{ }^\circ\text{C}$), since any cracks which may inherently be liable to propagate will blunt and arrest in a comparatively short time period.

Although these latter observations and theories relating to crack blunting have been applied primarily to carbon-steel in $\text{H}_2\text{O}/1.5 \text{ ppm O}_2$ at $98 \text{ }^\circ\text{C}$, the general logic should be applicable to the situation at higher temperatures, where very similar $da/dt \nu \epsilon$ and $(da/dN) \nu$ responses are noted.

CONCLUSIONS

- The slip dissolution model for environmentally-controlled propagation is able to predict quantitatively the crack morphology and crack propagation rate for sensitized 304 stainless steel in $0.01 \text{ M Na}_2\text{SO}_4$ and in water at $98\text{-}100 \text{ }^\circ\text{C}$, as a function of potential and strain rate.
- The model may be used to quantitatively explain the blunting kinetics of carbon-steel and offers an explanation as to why carbon-steel does not crack under the low strain rates associated with

static loading.

- The slip dissolution model gives a qualitative insight into the reason behind the anomalously high cracking susceptibility of various iron-base alloys in low-oxygen/water circa 150-200 °C. The model also defines the experimental conditions where the cracking rates of carbon steel and 304 stainless steel are similar.

ACKNOWLEDGMENTS

Grateful acknowledgment is given to D. Broecker, P. Emigh and M. Silverman who performed many of the experiments and to the many colleagues who offered advice. Acknowledgment is also extended to EPRI who sponsored some of the work reported in this paper under projects RP1332-1 and RP1248-1.

REFERENCES

1. S. Szklarska-Smialowska and G. Cragolino, *Corrosion* 36, 653 (1980).
2. R.L. Cowan and G.M. Gordon, "Stress-Corrosion Cracking and Hydrogen-Embrittlement of Iron-Base Alloys," *NACE*, p. 1023 (1978).
3. J.S. Armijo, *Corrosion* 24, 319 (1968).
4. B.E. Wilde and J.E. Weber, *Br. Corrosion J.* 4, 42 (1969).
5. W. Hübner, B. Johansson, and M. de Pourbaix, *Aktiebolaget Atomenergi*, AE-437, Sweden (1971).
6. W.L. Clarke and G.M. Gordon, 5th International Congress on Metallic Corrosion, Tokyo 1972, *NACE*, p. 884 (1974).
7. W.E. Berry, E.L. White, and W.K. Boyd, *Corrosion* 29, 451 (1973).
8. G.A. Welch, PhD Dissertation, The Ohio State University (1978).
9. M. Hishida and H. Nakada, *Corrosion* 33, 332 (1977).
10. E.L. White, W.E. Berry, and W.K. Boyd, Third Quarterly Progress Report, EPRI RP-1311-3, November 1977.
11. F.P. Ford and M.J. Povich, *Corrosion* 35, 569 (1979).
12. F.P. Ford and M. Silverman, *Corrosion* 36, 558 (1980).
13. F.P. Ford and M. Silverman, *Corrosion* 36, 597 (1980).
14. H.S. Isaacs, "Intergranular Stress Corrosion of Sensitized Stainless Steel," *BWR Water Chemistry Projects Review*, EPRI, Palo Alto, May 13/14, 1980.
15. H.H. Klepfer et al., "Investigation of Cause of Cracking in Austenitic Stainless Steel Piping," General Electric Report NEDO2100-1, July 1975.
16. A.K. Agrawal et al., "SCC of Sensitized and Quench Annealed Type 304 Stainless Steel in High Purity Water," paper 187, Corrosion-78 Conference, Houston, March 6/10, 1978.
17. G.A. Welch et al., "SCC of Sensitized Type 304 Stainless Steel in High Purity Water," paper 48, Corrosion-79 Conference, Atlanta, March 12/16, 1979.
18. Various papers given at EPRI Workshop on Carbon-Steel Cracking, Palo Alto, May 1979.
19. P.L. Andresen, paper submitted to *Corrosion*, NACE.; GE Corporate Research and Development Report 81CRD042.

20. F.P. Ford, Final report on Dept. of Energy Contract EY-76-C02-2985, "Alternate Water Chemistry Studies for Sensitized 304 Stainless Steel," December 1978.
21. W.L. Clarke and G.M. Gordon, *Corrosion* 29, 1 (1973).
22. R.M. Horn, et al., "Crack Growth Behavior of Sensitized Stainless Steel in High-temperature High-purity Water." IAEA Specialist Meeting on Environmental Cracking, Freiburg, Germany, May 1981.
23. E.L. White, W.E. Berry, and W.K. Boyd, "Influence of Combined Environmental Effects on Stress-Corrosion Cracking of Welded Stainless Steel Piping," EPRI contract RP311-3, 3rd Quarterly report, July-September, 1977.
24. T. Kondo et al., "Corrosion-Fatigue of ASTM302-B Steel in High-Temperature Water, the Simulated Nuclear Reactor Environment," International Conference on Corrosion-Fatigue, *Stress Corr.* June 1971. (Pub. NACE)
25. J.M. Hodge and I.L. Mogford, *Proc. Inst. Mech. Eng.* 193, 93 (1979).
26. F.P. Ford, J.D. Atkinson, and P.J. Worthington, unpublished CEGB data.
27. M. Indig, EPRI contract 1248-1, "BWR Environmental Cracking Margins for Carbon Steel Piping," pp. 4-23, 3rd Semiannual Progress Report, January 1980.
28. M. Indig, private communication.
29. R.N. Parkins and B.S. Greenwell, *Metal Sci.* 465, August 1977.
30. F.P. Ford, "Corrosion-Fatigue Crack Propagation," Proceedings of the 27th Sagamore Army Materials Conf., Bolton Landing, NY, July 1980.
31. H.L. Logan, *J. Research NBS*, 48 99 (1952).
32. R.W. Staehle, "Theory of Stress Corrosion Cracking," *Ericiera Portugal*, March 1971, (ed. J.C. Scully; NATO, Brussels (pub.), p. 223.
33. T.R. Beck, *Corrosion* 30, 408 (1974).
34. J.C. Scully, *Corrosion Sci.* 7, 197 (1967).
35. J.C. Scully, *ibid.* 8, 513 (1968).
36. J.C. Scully, *ibid.* 8, 771 (1968).
37. T.P. Hoar, as ref. 36, p. 106.

38. D.A. Vermilyea, *J. Electrochem Soc.* 119, 405 (1972).
39. F.P. Ford, "Stress Corrosion Cracking," Chapter in *Advances in Corrosion Sci-I*, R.N. Parkins (ed.), Applied Science Publishers.
40. N.D. Tomashou and L.P. Verastinina, *Electrochimica Acta* 15, 501 (1976).
41. J.R. Ambrose and J. Kruger, *Corrosion* 28, 30 (1972).
42. D.J. Lees and T.P. Hoar, "European Federation of Corrosion Electrochemical Methods for Stress-Corrosion Cracking," *Firminy France*, September 1978.
43. F.P. Ford, G.T. Burstein and T.P. Hoar, *J. Electrochemical Soc.* 127, 1325 (1980).
44. T. Hagyard and W. B. Earl, *ibid.* 114, 694 (1967).
45. J.F. Rimbart and J. Pagetti, *Corrosion Sci.* 20, 189 (1980).
46. T.P. Hoar and R.W. Jones, *Corrosion Sci.* 13, 725 (1973).
47. T.P. Hoar and J.R. Galvele, *ibid.* 10, 211 (1970).
48. T.P. Hoar and F.P. Ford, *J. Electrochemical Soc.* 120, 1013 (1973).
49. T.P. Hoar and J.C. Scully, *ibid.* 111, 348 (1964).
50. T.R. Beck, *ibid.* 115, 880 (1968).
51. R.B. Diegle and D.A. Vermilyea, *ibid.* 122, 180 (1975).
52. P. Rao, "Microstructural and Microchemical Studies in Sensitized 8 Stainless Steel," ASTM-STP 672; also presented at Micom-78, Houston, April 1978.
53. F.P. Ford, Final report on EPRI contract RP1332-1, "Mechanisms of Environment-Controlled Cracking in Systems Peculiar to the Power Generation Industry," 1981.
54. D.A. Vermilyea and R.M. Diegle, *Corrosion* 32, 26 (1976).
55. D. Dejardins et al., *Corrosion Sci.* 20, 177 (1980).
56. H.H. Uhlig, *J. Electrochemical Soc.* 123, 1699 (1976).
57. R.W. Revie and H.H. Uhlig, *Acta Met* 22, 619 (1974); *Scripta Met* 8, 1231 (1974).
58. D.J. Duquette, H. Hahn, and P. Andresen, "Surface Effects in Crystal Plasticity," Hohegeiss, Germany, September 1975. (R.M. Latanision and J.T. Fourie, eds., Noordhoj-Leyden 1977 pub.)
59. A. Pfitzenkeuter and G. Mazing, *Z. Metallk* 42, 361 (1951).
60. G.E. Ruddle and H.G.F. Wilsdorf, *Appl Phys Letters* 12, 271 (1968).

61. V.K. Sethi and R. Gibala, *Scripta Met.* 9, 527 (1975).
62. J.T. Evans and R.N. Parkins, *Acta Met* 24, 511 (1976).
63. J.F. Newman, "On the Mechanism of the Stress-Corrosion of a 3%CrMo Steel in Sodium Hydroxide in the Potential Range -900 to -650 mV Hg/HgO," Central Electricity Research Lab Report RD/L/N78/75, August 1975.
64. J.F. Newman, "The Application of a Film-Rupture Mechanism to the Stress-Corrosion of a 3%CrMo Steel in Sodium Hydroxide in the Potential Range -900 to -650 mV Hg/HgO," Proceedings of conference "Mechanisms of Environment Sensitive Cracking of Materials," University of Surrey, April 4-7, 1977, p. 19. (P.R. Swann, F.P. Ford, and A.R.C. Westwood, eds.; The Metals Soc., London, pub.)
65. J.C. Scully, *Corrosion Sci* 15, 207 (1975).
66. D.A. Vermilyea, "Stress Corrosion Cracking and Hydrogen Embrittlement of Iron-Based Alloys," Firminy, France, June 1973, p. 208. (R.W. Straehle, J. Hochmann, R.D. McCright, and J.E. Slater, eds., NACE-Houston, 1977, pub.)
67. J. Gittus, "Creep, Viscoelasticity, and Creep Fracture in Solids," Applied Science Publishers, 1975.
68. M.E. Indig and A.R. McIlree, *Corrosion* 35, 288 (1979).
69. M.E. Indig, private communication.
70. M.E. Indig, as ref. 31, First Semiannual Report, July-December, 1978, pp. 4-53.
71. F.P. Ford, "Crack Blunting During Corrosion-Fatigue Crack Propagation in the SA333Gr6 Carbon-Steel/Water System at 208 °F," Final report on EPRI Contract 1248-1, 'BWR Environmental Cracking Margins for Carbon Steel Piping,' January 1981.
72. J.D. Atkinson and T.C. Lindley, "The Effect of Frequency and Temperature on Environmentally Assisted Fatigue Crack Growth Below K_{ISCC} in Steels," Central Electricity Research Lab report RD/L/N40/77, July 1977.
73. J.C. Radon, C.M. Branco, and L.E. Culver, "Crack Blunting and Arrest in Corrosion-Fatigue of Mild-Steel," *Int. J. of Fracture* 12, 467 (1976).
74. P.C. Paris, R.J. Bucci, et al., *ASTM STP* 513, 141 (1972).
75. R.O. Ritchie, S. Suresh, and C.M. Moss, *J. Eng Mats. and Tech.* 102, 293 (1980).

76. H. Neuber, "Theoretical Determination of Fatigue Strength at Stress Concentration," Technical report AFML-TR 68-20 (1968).
77. M. Creager and P.C. Paris, "Elastic Field Equations for Blunt Cracks with Reference to Stress Corrosion Cracking," *Int'l. Fracture Mechanics* 3, 247 (1967).

Figure Captions

- Figure 1. Water loop.
- Figure 2. Variation in the average crack propagation rate in sensitized 304 stainless-steel in water at 288 °C with oxygen content. Data from both constant extension rate tests,⁽²⁰⁾ constant load,^(15,21) and field observations on BWR piping.⁽¹⁵⁾ Open data points denote transgranular cracking, closed data points denote intergranular cracking.
- Figure 3. Variation in environmentally-controlled crack propagation rate (ECPR) with crack-tip opening displacement rate (CTOD) for constant extension rate and cyclic loading⁽²²⁾ conditions. The CTOD for cyclic load tests was calculated from the change in CTOD per cycle divided by the rise time; in the case of the multiple cracked tensile bar specimens in the constant extension rate test, the CTOD was equated with the macroscopically applied strain rate divided by the number of deep cracks noted metallographically. Observe that the CTOD is *not* known for the constant-load tests.⁽²²⁾ Note also the change in crack morphology based on the data in Figure 2 and ref. 22.
- Figure 4. Variation in average crack-propagation rate with oxygen/temperature combinations for the sensitized 304 stainless steel/water system. Data obtained under constant extension rate conditions on shot-peened specimens ($\dot{\epsilon} = 2.1 - 2.4 \times 10^{-7} \text{ s}^{-1}$). Crack propagation rates given in units of $\text{cm s}^{-1} \times 10^{-7}$.
- Figure 5. Illustration of the high cracking susceptibility noted circa 150-200 °C in water/low-oxygen environment for a variety of iron-base alloys in a variety of testing modes.⁽²³⁻²⁶⁾
- Figure 6. Comparison between pit and crack penetration on SA333Gr6 carbon steel after a constant extension rate test in water at different oxygen/temperature combinations. Note that at higher temperatures, the crack penetration predominates; whereas, at lower temperatures, crack and pit depths are comparable. Units in $\text{cms} \times 10^{-2}$
- Figure 7. Transgranular cracking/pitting in SA333Gr6 carbon steel; water/ 1.8 ppm O₂, 150 °C.
- Figure 8. Comparison between the average crack propagation rate for sensitized 304 stainless steel

(I/GSCC) and SA333Gr6 carbon steel (T/GSCC) observed under constant extension rate conditions in water at various oxygen/temperature combinations. ($\dot{\epsilon} = 2.1\text{-}2.7 \times 10^{-7} \text{ s}^{-1}$, shot-peened surfaces.) Data points marked (*) denote 'cracking' was predominantly pit penetration (cf. Figure 7). Crack propagation rates given in units of $\text{cm s}^{-1} \times 10^{-7}$.

Figure 9. Parameters of importance in the slip-dissolution (and hydrogen-embrittlement) model of crack-propagation.⁽³⁹⁾ Solid lines denote primary interactions with dotted lines denoting secondary interactions.

Figure 10. Schematic variation of oxidation charge-density with time during crack propagation illustrating the parameters relevant to the slip-dissolution model of crack-propagation.

Figure 11. Predicted penetration down the grain-boundary (of composition Fe 12% Cr 10% Ni) and into the grain matrix (of composition Fe 18% Cr 8% Ni) following the rupture of oxide at a crack tip in the 304 stainless steel/0.01 M Na_2SO_4 system at 98 °C.⁽¹²⁾ The penetrations have been calculated for 4 seconds after the rupture event; this choice of time is arbitrary, but the conclusions do not alter substantially for times greater than ~ 10 ms. At shorter rupture times than 10 ms, i.e., high crack tip strain rates, there is no significant difference between the penetrations and I/GSCC would not be predicted over T/GSCC.

Figure 12. Observed crack propagation morphologies following constant-extension rate testing of sensitized 304 stainless steel in 0.01 M Na_2SO_4 at 98 °C, $\dot{\epsilon} = 2.6 \times 10^{-6} \text{ s}^{-1}$. (a) +343 mVshe; (b) +218 mVshe; (c) +193 mVshe; (d) +143 mVshe; (e) +43 mVshe. Note the correlation between the observed morphologies and those predicted in Figure 11.

Figure 13. Comparison between observed and calculated crack-propagation rates for sensitized 304 stainless steel in 0.01 M Na_2SO_4 at 98 °C.⁽¹²⁾ Observed data obtained at $\dot{\epsilon} = 2.1 \times 10^{-6} \text{ s}^{-1}$; theoretical data based on slip-dissolution model with $t_f = 475$ s. Note that the large discrepancy between observation and theory at +340 mVshe may be related to the fact that the observed failure is due primarily to *pitting* rather than cracking; i.e., the crack propagation rate will be slowed down by chemical blunting.

- Figure 14. Variation of observed^(12,13) and theoretical crack propagation rates for sensitized 304 stainless steel in either 0.01 M Na₂SO₄ or H₂O/1.8 ppm O₂ at 98 °C. Note that the crack tip strain rates under constant-load conditions are *not* known; in this figure the data points for constant-load have been placed at a crack tip strain rate corresponding to the steady state creep rate observed on unconstrained wire samples in an inert environment.⁽⁵⁵⁾
- Figure 15. Parameters of importance in constant-charge criterion for crack-propagation.⁽⁵³⁾
- Figure 16. Comparison between theoretical and observed⁽¹³⁾ crack propagation rate/stress-intensity relationship for sensitized 304 stainless-steel in H₂O/1.5 ppm O₂ at 98 °C.⁽⁵³⁾ Theoretical values have been calculated on basis of constant-charge density criterion with $Q^* = 1.6 \times 10^2 \text{K}^{-1} \text{ } ^\circ\text{C cm}^{-2}$ and the $Q(t)$ relationship observed in 0.01 M Na₂SO₄ at +193 mVshe. Note the fact that the theory does not account for the effect that macro-branching has on the crack propagation rate.
- Figure 17. Data from Figure 4 replotted in terms of crack propagation rate and corrosion potential. The latter values have been taken from work by Indig^(68,69) on stainless steel in water at various oxygen/temperature combinations.
- Figure 18. Variation of crack propagation rate in sensitized 304 stainless steel/water system for different temperatures and oxygen contents (potentials). Constant extension rate conditions at $2.1 \times 10^{-7} \text{ s}^{-1}$.
- Figure 19. Elastic stress function at an elliptical crack tip with major and minor axes, c and b , and crack tip radius, ρ .^(76,77) Note that the maximum surface tensile stress $\sigma_{y_{\max}}$ will change with time as the crack tip radius increases according to the relative values of V_s and V_t .⁽⁷²⁾
- Figure 20. Variation in the average crack propagation rate for sensitized 304 stainless steel and SA333Gr6 carbon-steel in water, with corrosion potential at 288 °C. The corrosion-potential has been varied by altering the oxygen content between 0.08 ppm and 8 ppm. Constant extension rate conditions: $2.1\text{-}2.6 \times 10^{-7} \text{ s}^{-1}$.
- Figure 21. Variation^(71,53) in (da/dN) with time for SA333Gr6 carbon steel in argon and wa-

ter/oxygen mixtures at 98 °C. $K_{\max} = 7.7 \text{ MNm}^{-3/2}$, $R = 0.1$, 10 Hz. Note the crack arrest in $\text{H}_2\text{O}/1.5 \text{ ppm O}_2$, an environment where considerable general corrosion is observed, and the lack of such arrest when the environment is inert or relatively benign ($\text{H}_2\text{O}/0.1 \text{ ppm O}_2$).

Figure 22. Comparison⁽⁷¹⁾ between observed and predicted crack arrest of SA333Gr6 carbon steel during corrosion fatigue in $\text{H}_2\text{O}/1.5 \text{ ppm O}_2$. Predicted values based on assumption that crack sides are being corroded at a rate between 1.46 and $2.9 \times 10^{-8} \text{ cm s}^{-1}$, and that this leads to crack blunting at the prevalent crack tip propagation rates.

Figure 23. Variation^(53,71) of theoretical and observed (da/dN) values with frequency for SA333Gr6 carbon steel in $\text{H}_2\text{O}/1.5 \text{ ppm O}_2$ at 98 °C; $K_{\max} = 22 \text{ MNm}^{-3/2}$, $R = 0.1$. The superscript numbers beside each experimental data point denote the corresponding exposure time. The theoretical $da/dN \nu$ relationships are also shown as a function of the exposure time, the decrease in da/dN values at slower frequencies being associated with chemical blunting of the crack. (The V_s value used in the calculated curves was $1.46 \times 10^{-8} \text{ cm s}^{-1}$.)

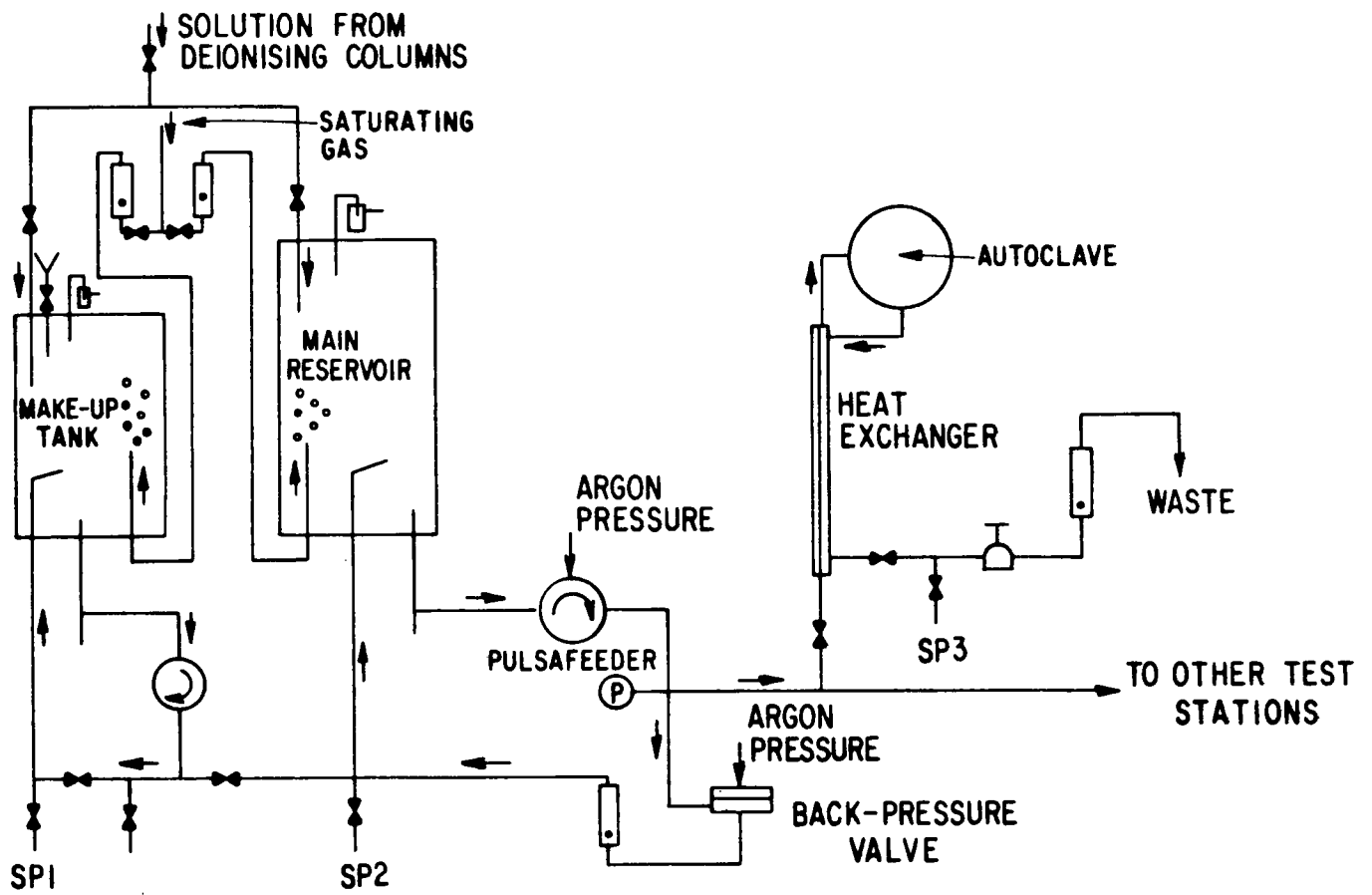


Figure 1. Water loop.

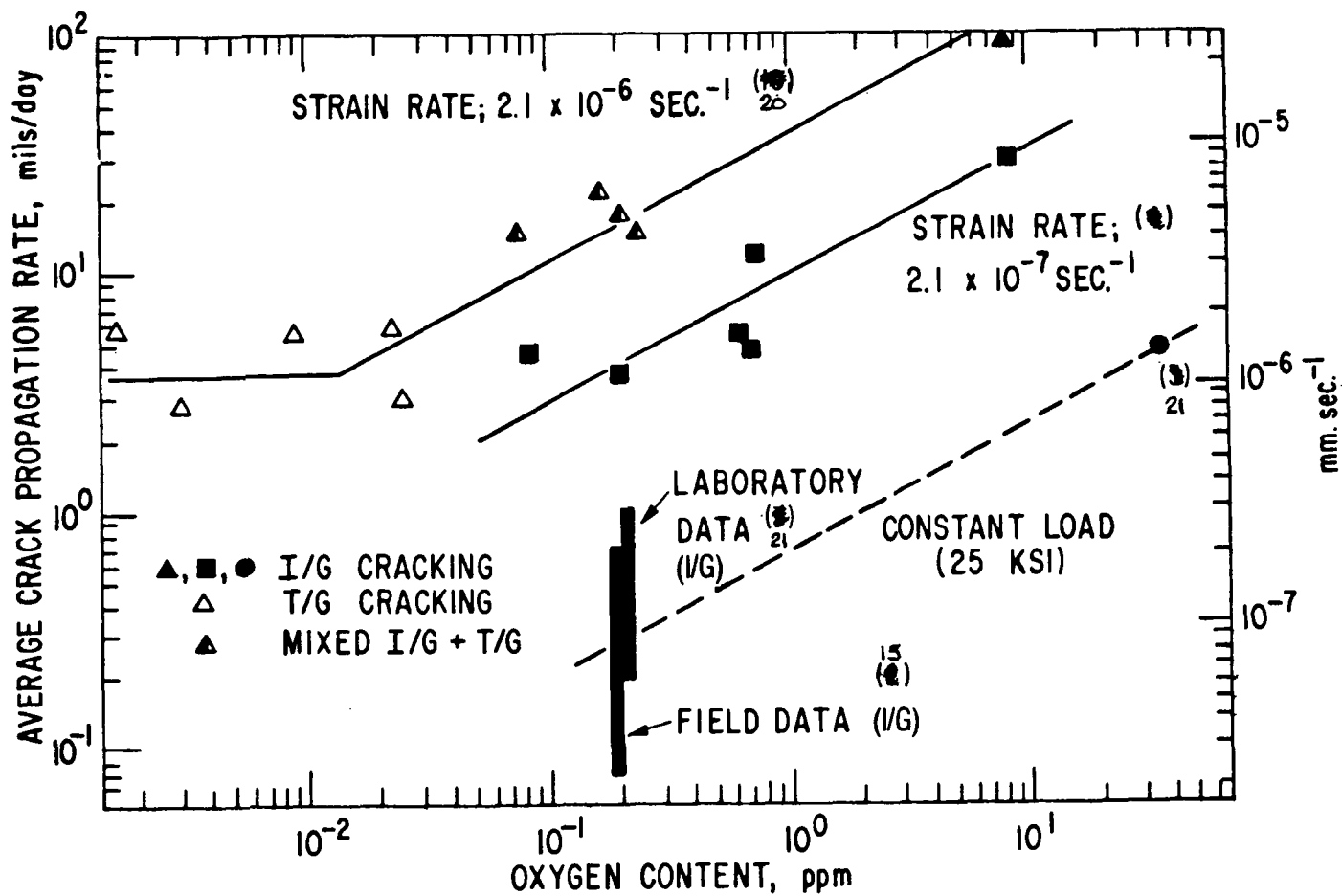


Figure 2. Variation in the average crack propagation rate in sensitized 304 stainless-steel in water at 288 °C with oxygen content. Data from both constant extension rate tests;⁽²⁰⁾ constant load,^(15,21) and field observations on BWR piping.⁽¹⁵⁾ Open data points denote transgranular cracking, closed data points denote intergranular cracking.

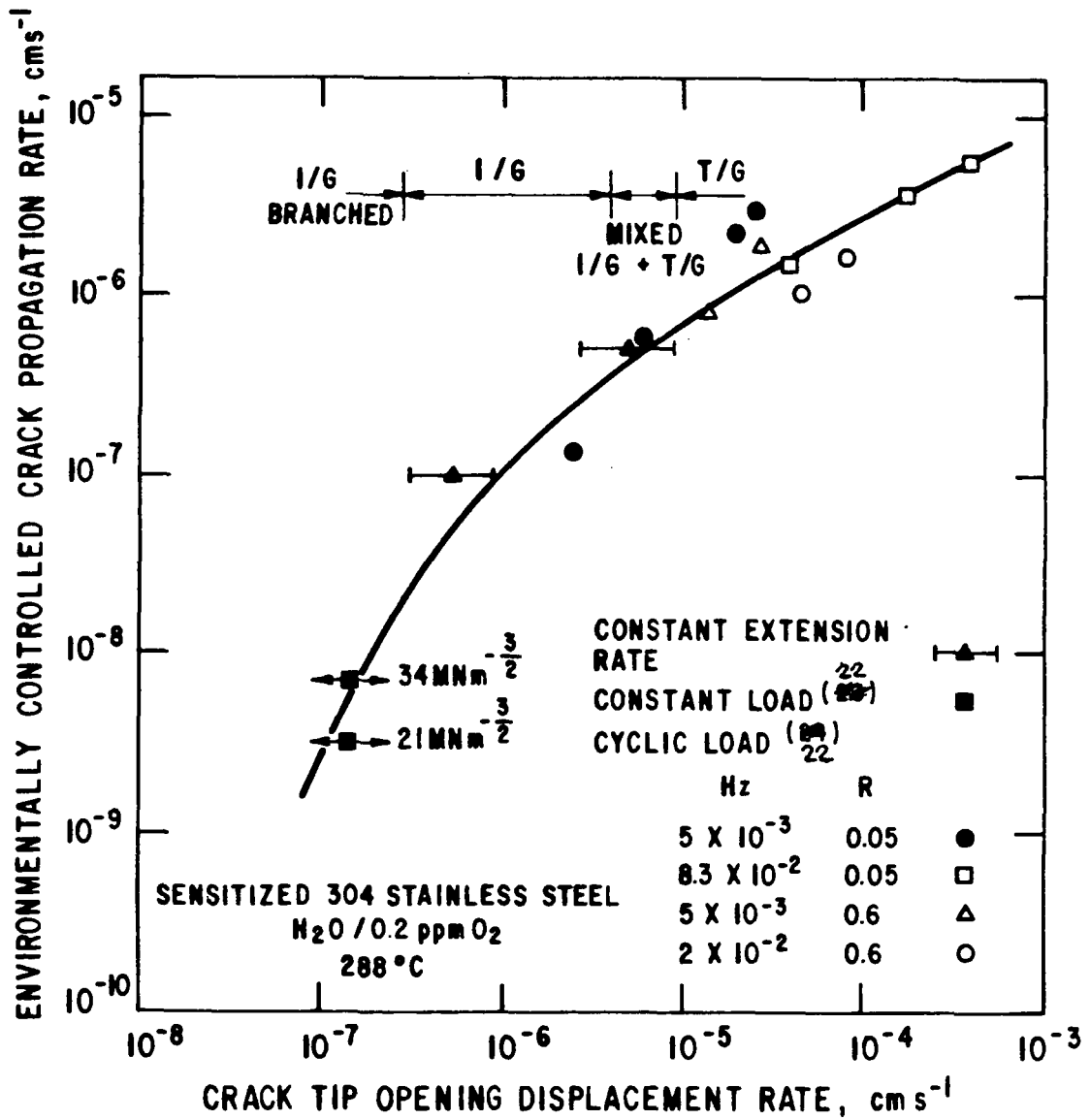


Figure 3. Variation in environmentally-controlled crack propagation rate (ECPR) with crack-tip opening displacement rate (CTOD) for constant extension rate and cyclic loading⁽²²⁾ conditions. The CTOD for cyclic load tests was calculated from the change in CTOD per cycle divided by the rise time; in the case of the multiple cracked tensile bar specimens in the constant extension rate test, the CTOD was equated with the macroscopically applied strain rate divided by the number of deep cracks noted metallographically. Observe that the CTOD is *not* known for the constant-load tests.⁽²²⁾ Note also the change in crack morphology based on the data in Figure 2 and ref. 22.

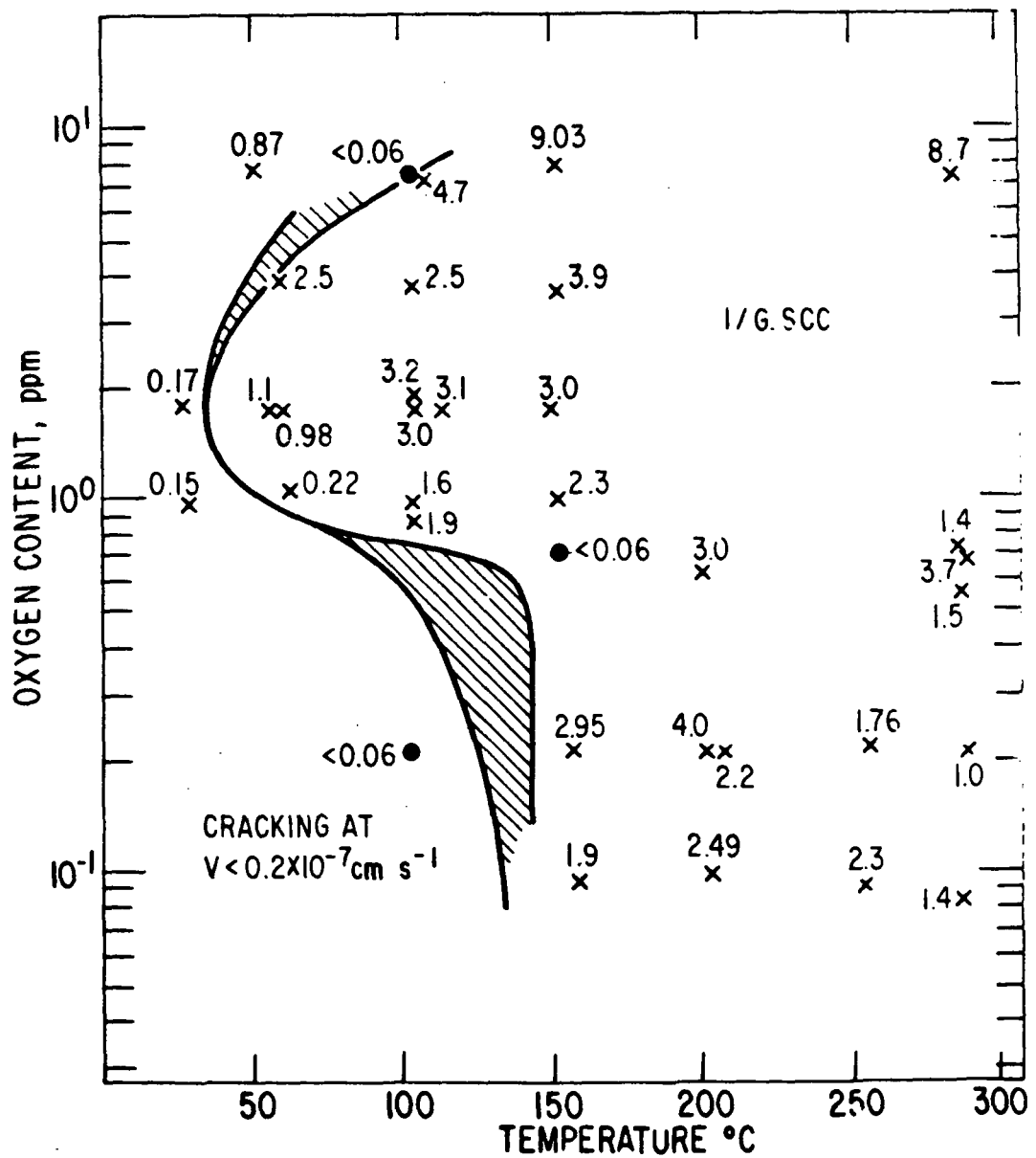


Figure 4. Variation in average crack-propagation rate with oxygen/temperature combinations for the sensitized 304 stainless steel/water system. Data obtained under constant extension rate conditions on shot-peened specimens ($\dot{\epsilon} = 2.1 - 2.4 \times 10^{-7} \text{ s}^{-1}$). Crack propagation rates given in units of $\text{cm s}^{-1} \times 10^{-7}$.

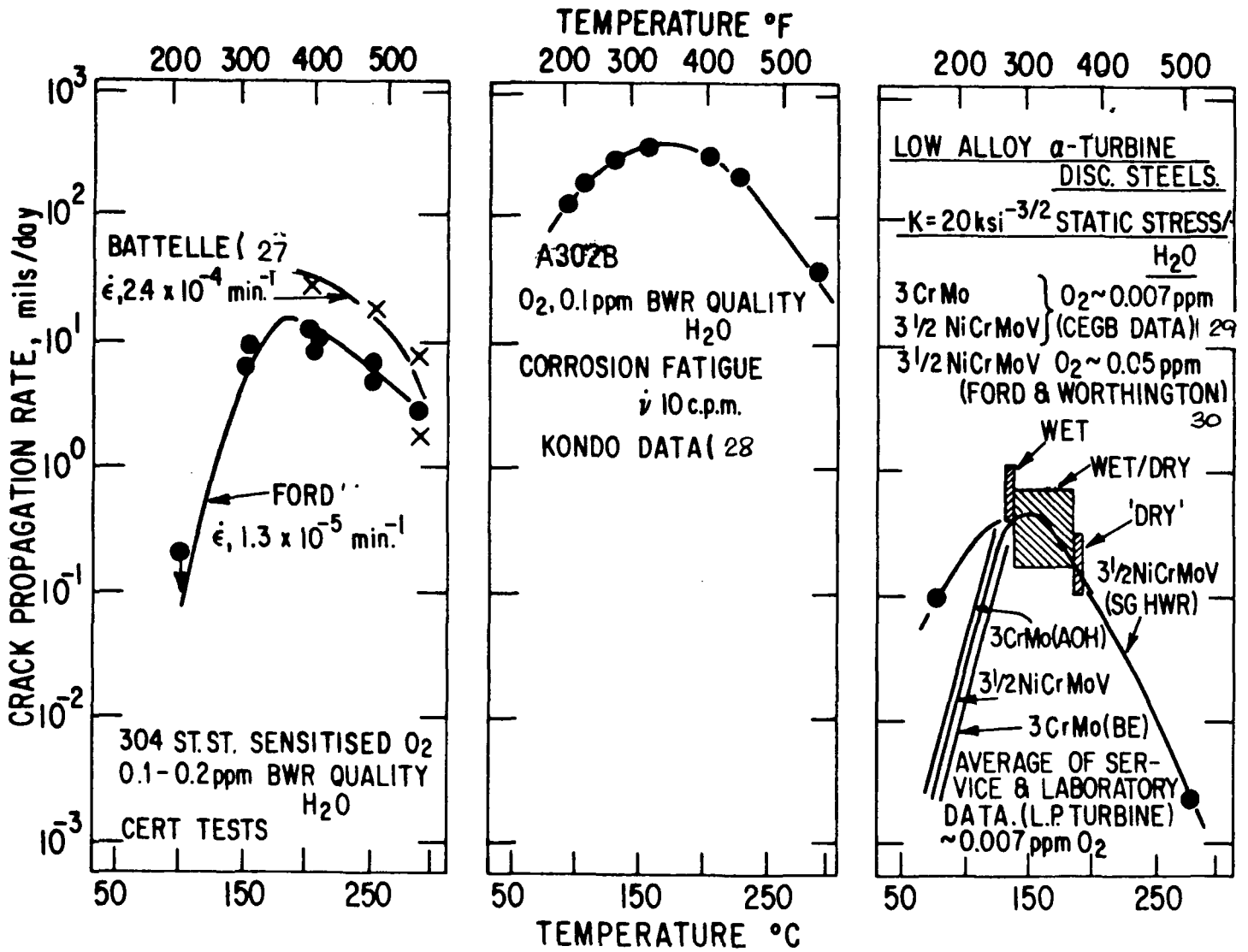


Figure 5. Illustration of the high cracking susceptibility noted circa 150-200 °C in water/low-oxygen environment for a variety of iron-base alloys in a variety of testing modes. (27-30)

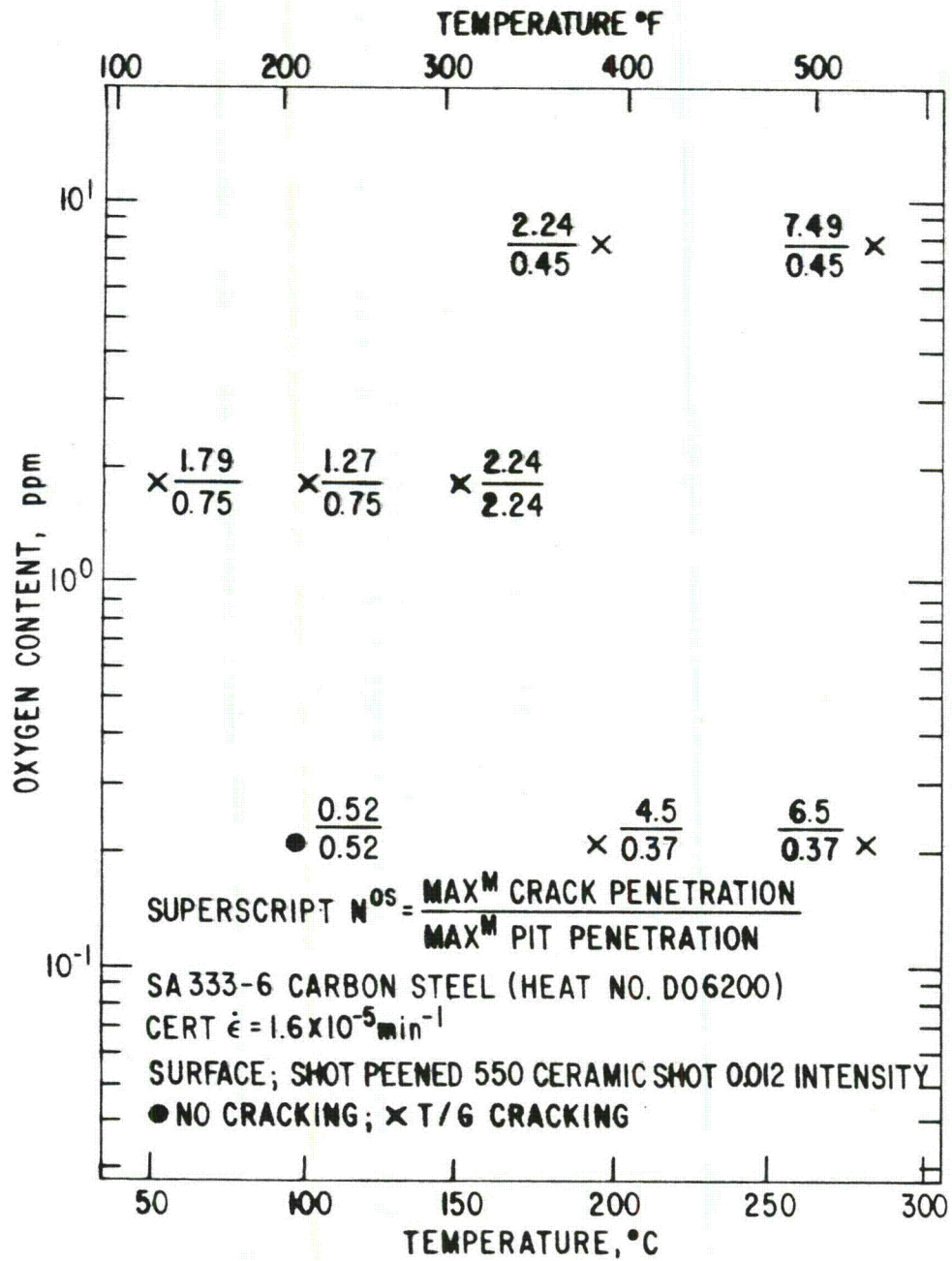


Figure 6. Comparison between pit and crack penetration on SA333Gr6 carbon steel after a constant extension rate test in water at different oxygen/temperature combinations. Note that at higher temperatures, the crack penetration predominates; whereas, at lower temperatures, crack and pit depths are comparable. Units in $\text{cms} \times 10^{-2}$.

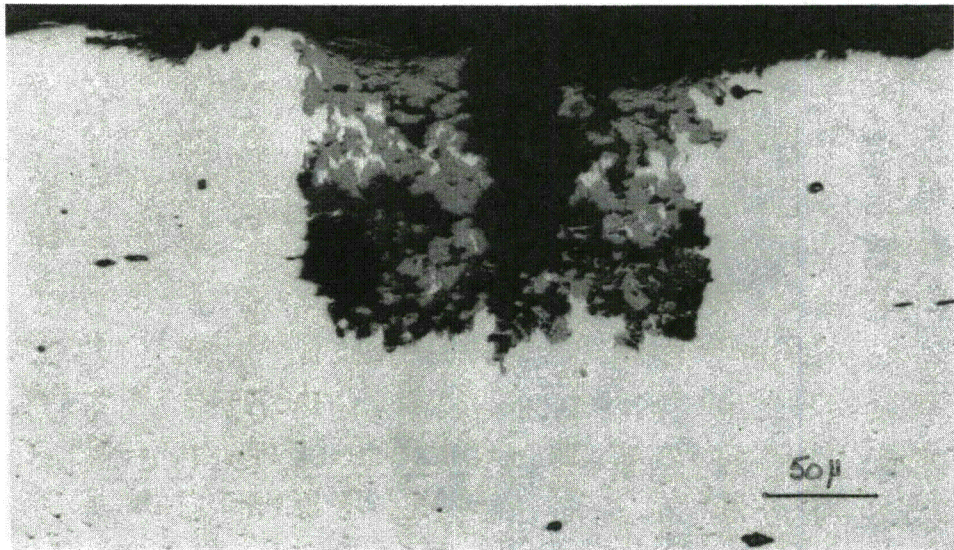
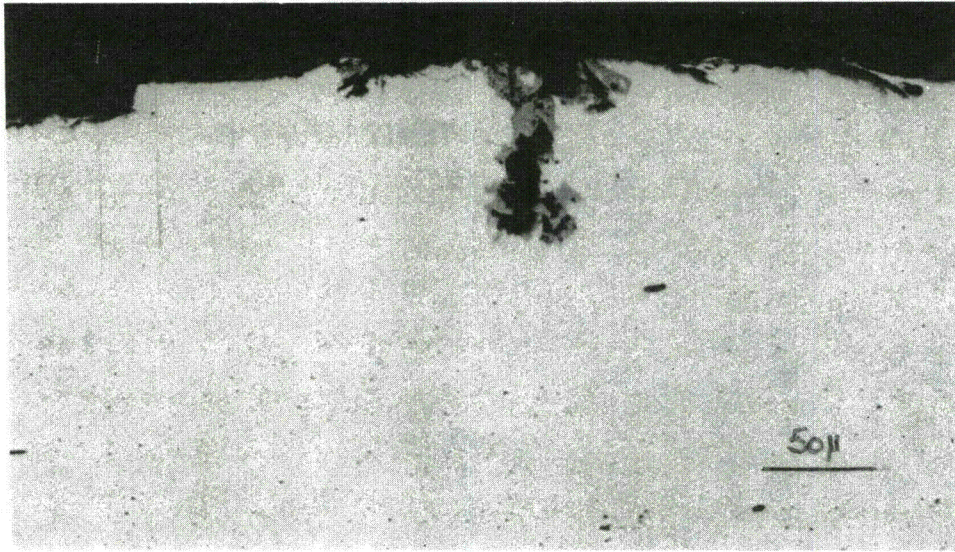


Figure 7. Transgranular cracking/pitting in SA333Gr6 carbon steel; water/ 1.8 ppm O₂, 150 °C.

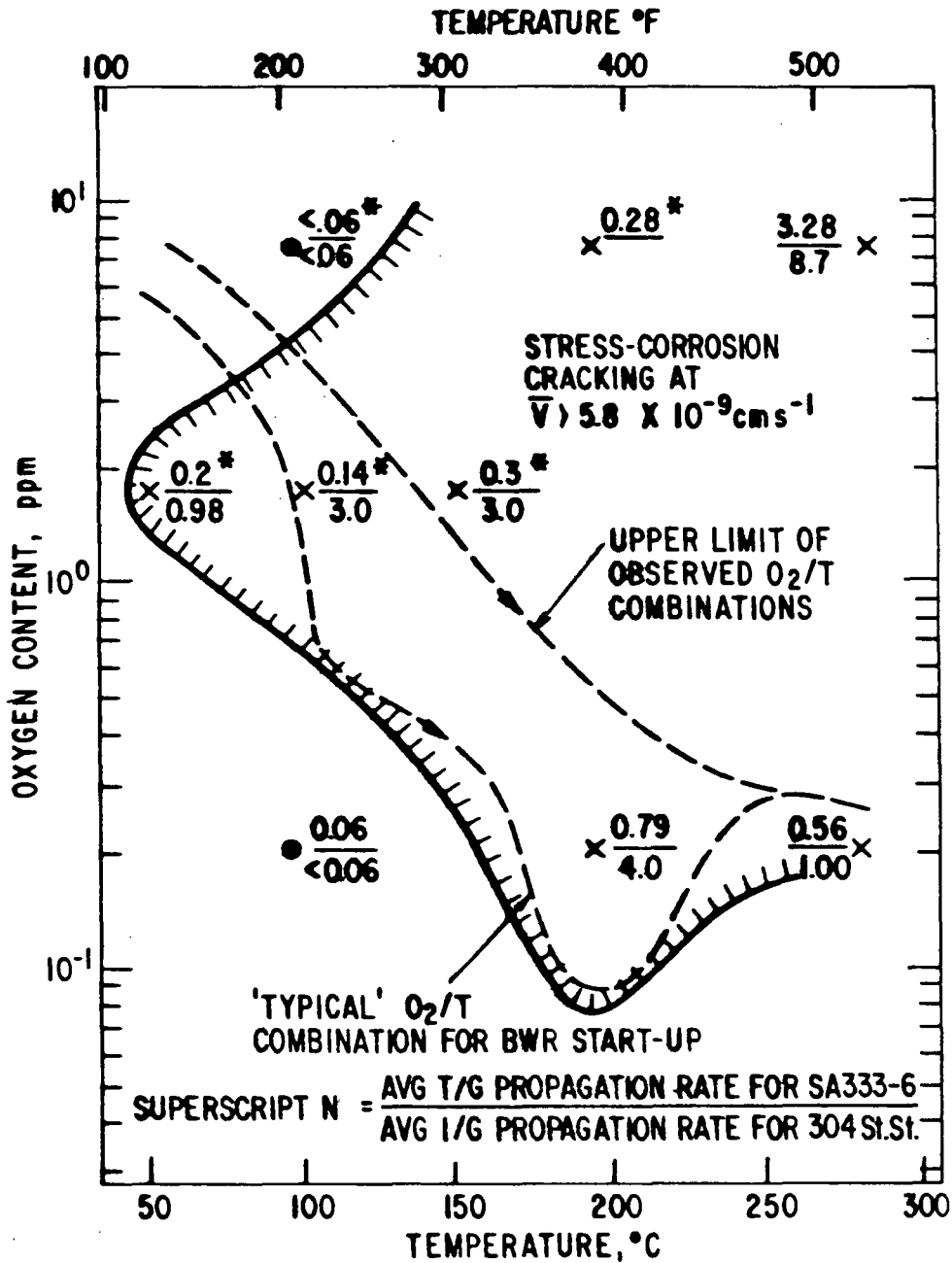


Figure 8. Comparison between the average crack propagation rate for sensitized 304 stainless steel (I/GSCC) and SA333Gr6 carbon steel (T/GSCC) observed under constant extension rate conditions in water at various oxygen/temperature combinations. ($\dot{\epsilon} = 2.1\text{-}2.7 \times 10^{-7} \text{ s}^{-1}$, shot-peened surfaces.) Data points marked (*) denote 'cracking' was predominantly pit penetration (cf. Figure 7). Crack propagation rates given in units of $\text{cm s}^{-1} \times 10^{-7}$.

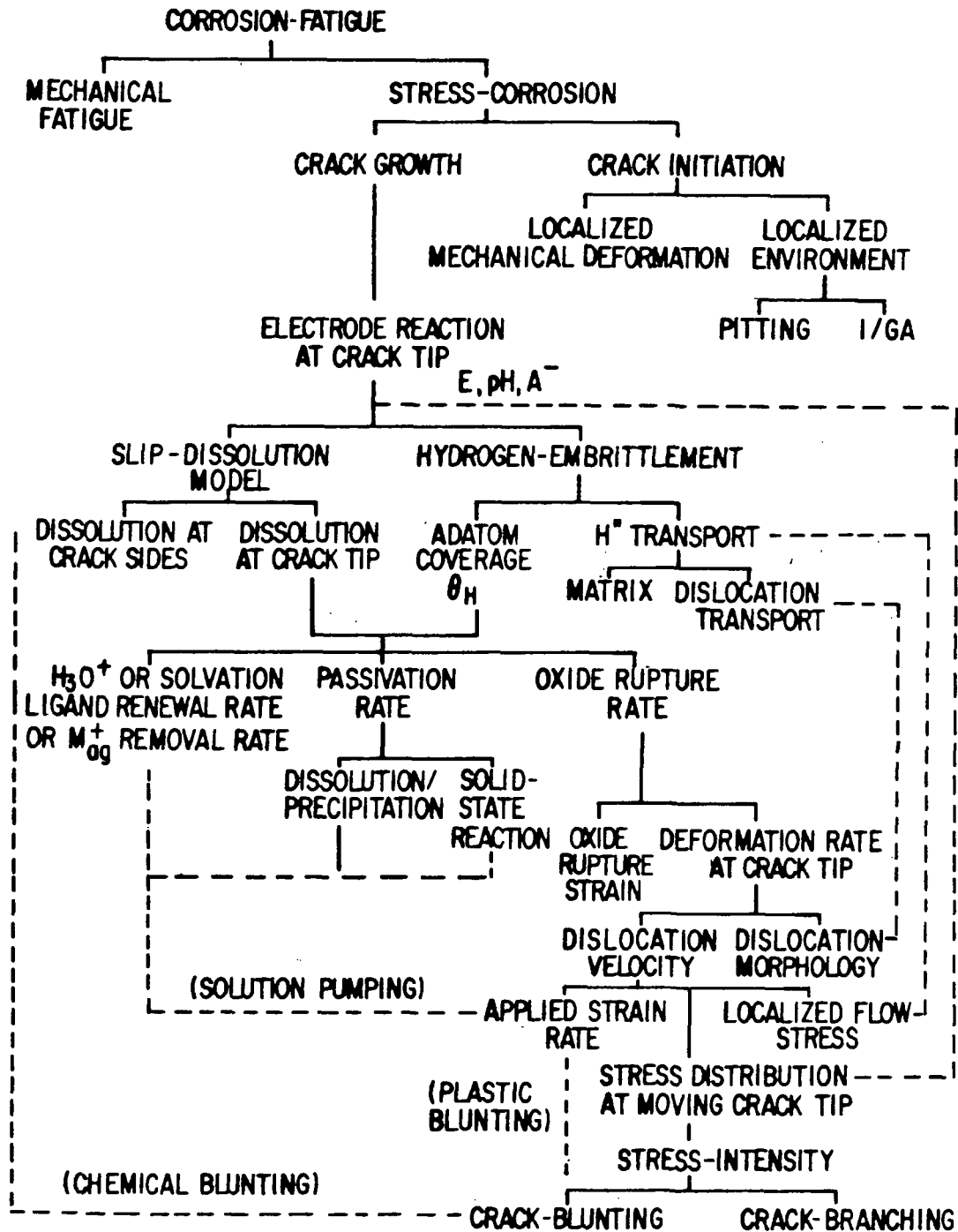


Figure 9. Parameters of importance in the slip-dissolution (and hydrogen-embrittlement) model of crack-propagation.⁽³⁹⁾ Solid lines denote primary interactions with dotted lines denoting secondary interactions.

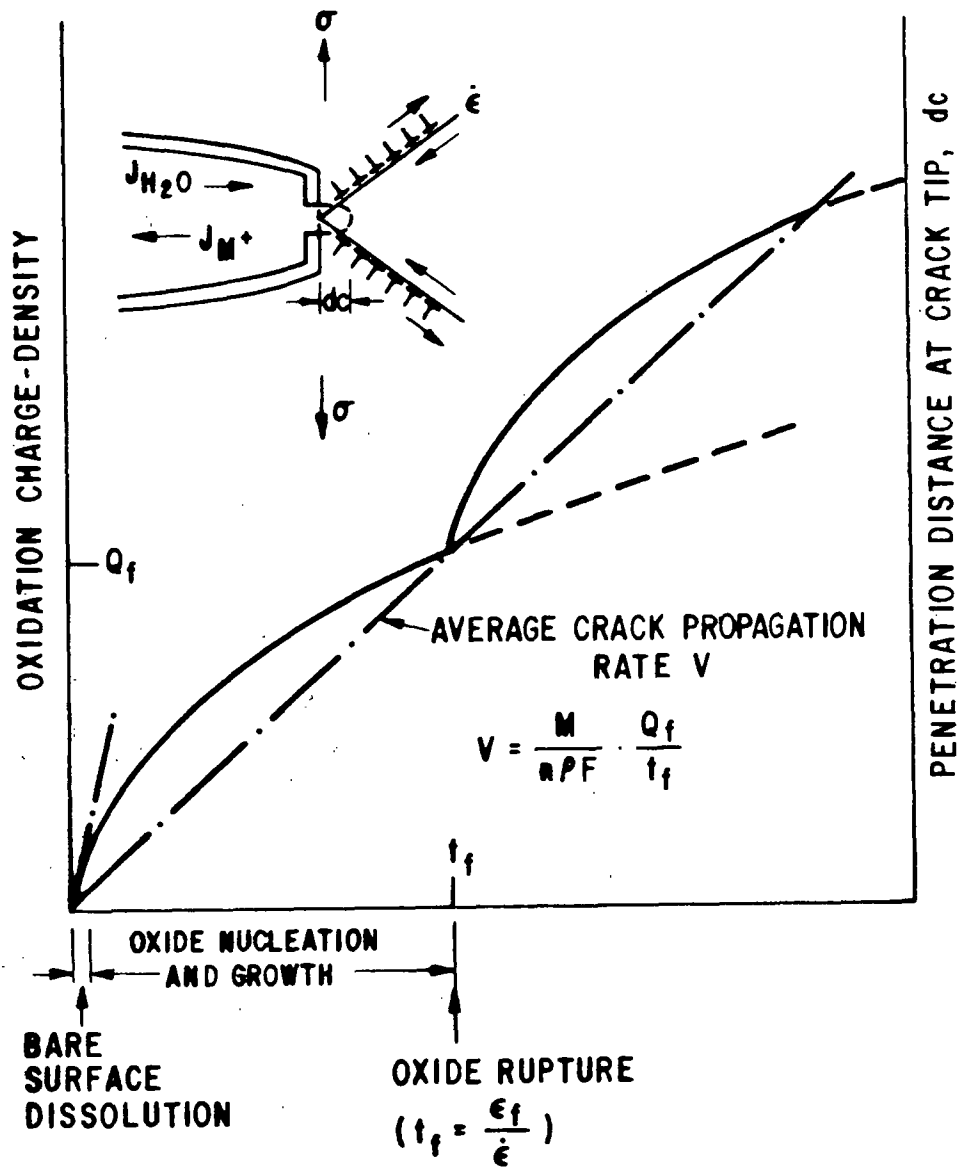


Figure 10. Schematic variation of oxidation charge-density with time during crack propagation illustrating the parameters relevant to the slip-dissolution model of crack-propagation.

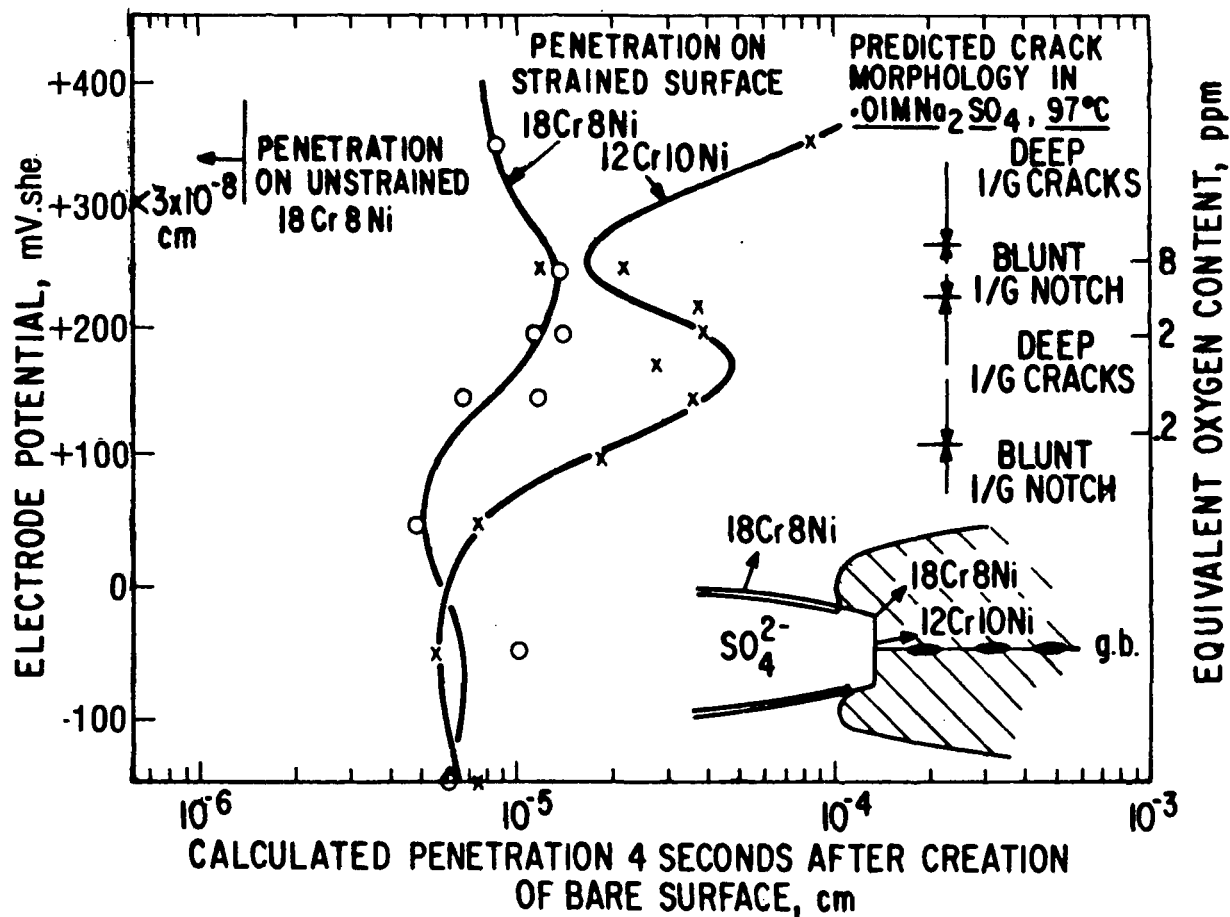


Figure 11. Predicted penetration down the grain-boundary (of composition Fe 12% Cr 10% Ni) and into the grain matrix (of composition Fe 18% Cr 8% Ni) following the rupture of oxide at a crack tip in the 304 stainless steel/0.01 M Na₂SO₄ system at 98 °C.⁽¹²⁾ The penetrations have been calculated for 4 seconds after the rupture event; this choice of time is arbitrary, but the conclusions do not alter substantially for times greater than ~10 ms. At shorter rupture times than 10 ms, i.e., high crack tip strain rates, there is no significant difference between the penetrations and I/GSCC would not be predicted over T/GSCC.

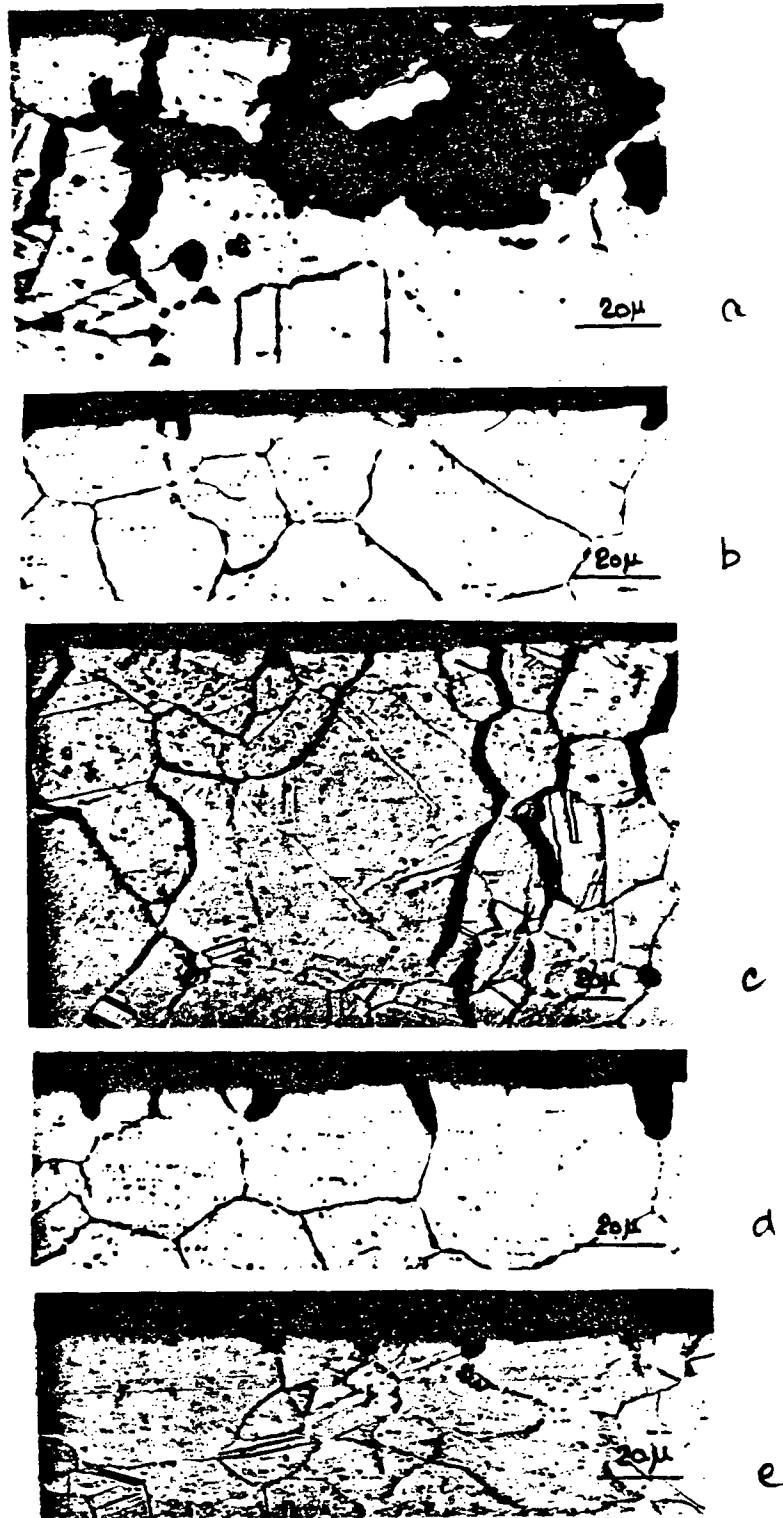


Figure 12. Observed crack propagation morphologies following constant-extension rate testing of sensitized 304 stainless steel in 0.01 M Na₂SO₄ at 98 °C, $\dot{\epsilon} = 2.6 \times 10^{-6} \text{ s}^{-1}$. (a) +343 mVshe; (b) +218 mVshe; (c) +193 mVshe; (d) +143 mVshe; (e) +43 mVshe. Note the correlation between the observed morphologies and those edicted in Figure 11.

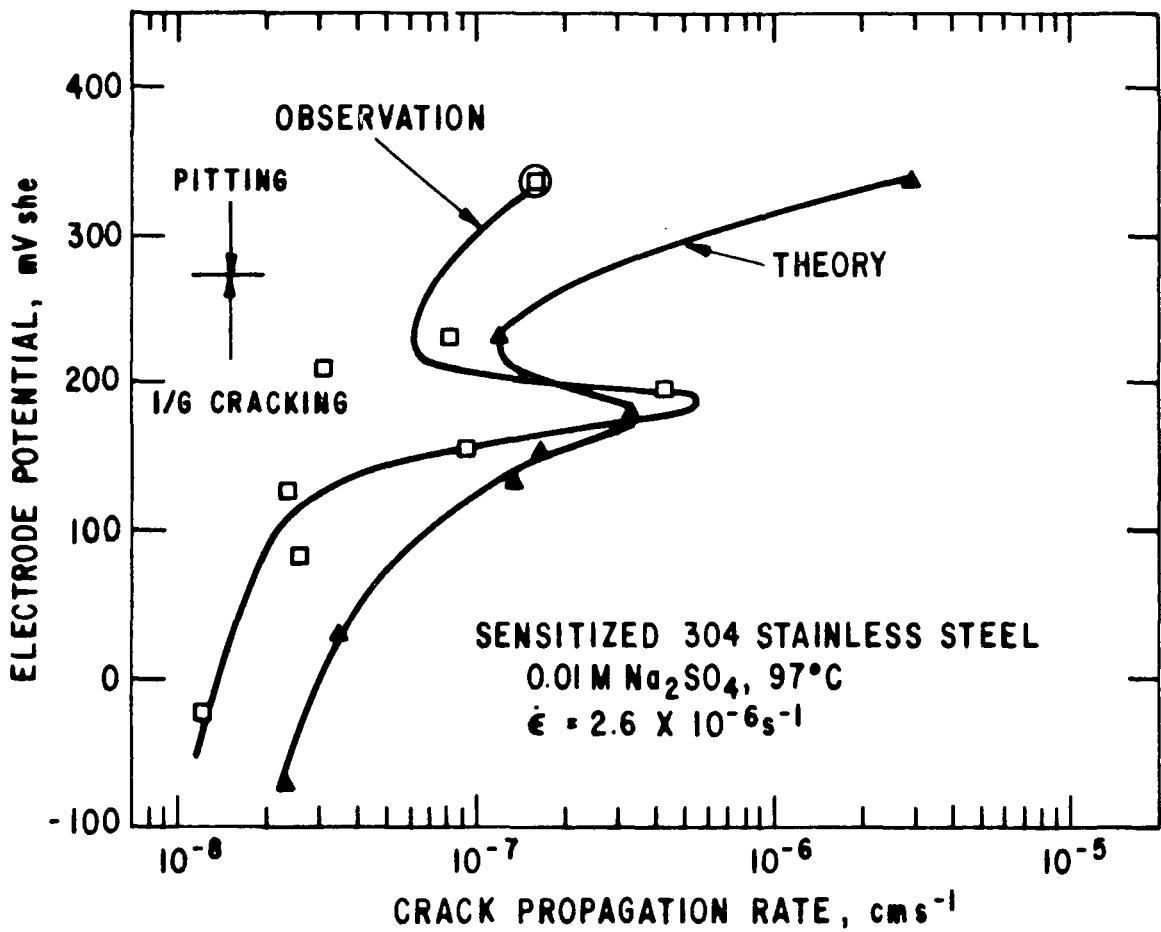


Figure 13. Comparison between observed and calculated crack-propagation rates for sensitized 304 stainless steel in 0.01 M Na₂SO₄ at 98 °C.⁽¹²⁾ Observed data obtained at $\dot{\epsilon} = 2.1 \times 10^{-6} \text{ s}^{-1}$; theoretical data based on slip-dissolution model with $t_f = 475 \text{ s}$. Note that the large discrepancy between observation and theory at +340 mVshe may be related to the fact that the observed failure is due primarily to *pitting* rather than cracking; i.e., the crack propagation rate will be slowed down by chemical blunting.

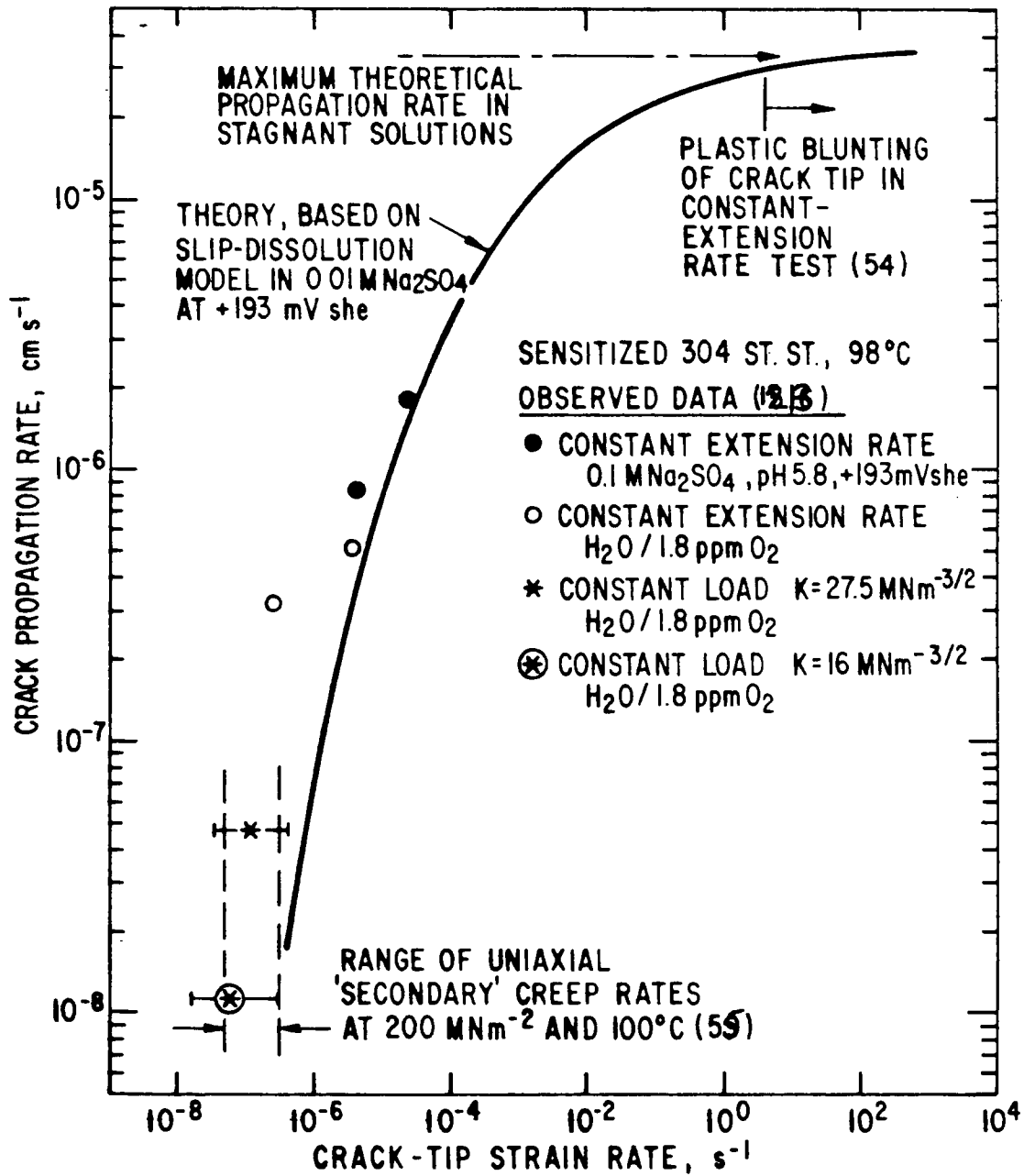


Figure 14. Variation of observed^(12,13) and theoretical crack propagation rates for sensitized 304 stainless steel in either 0.01 M Na₂SO₄ or H₂O/1.8 ppm O₂ at 98 °C. Note that the crack tip strain rates under constant-load conditions are *not* known; in this figure the data points for constant-load have been placed at a crack tip strain rate corresponding to the steady state creep rate observed on unconstrained wire samples in an inert environment.⁽⁵⁵⁾

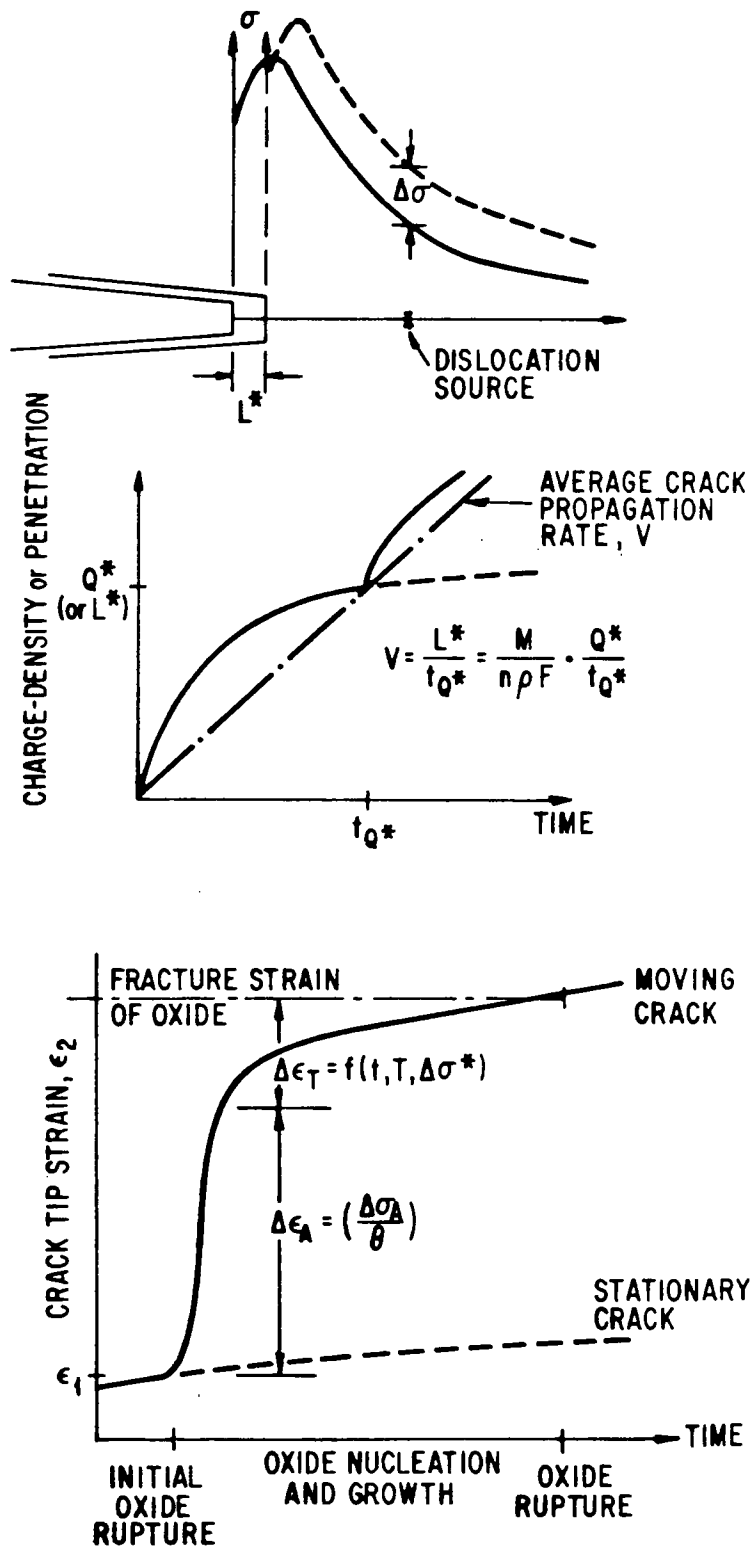


Figure 15. Parameters of importance in constant-charge criterion for crack-propagation.⁽⁵³⁾

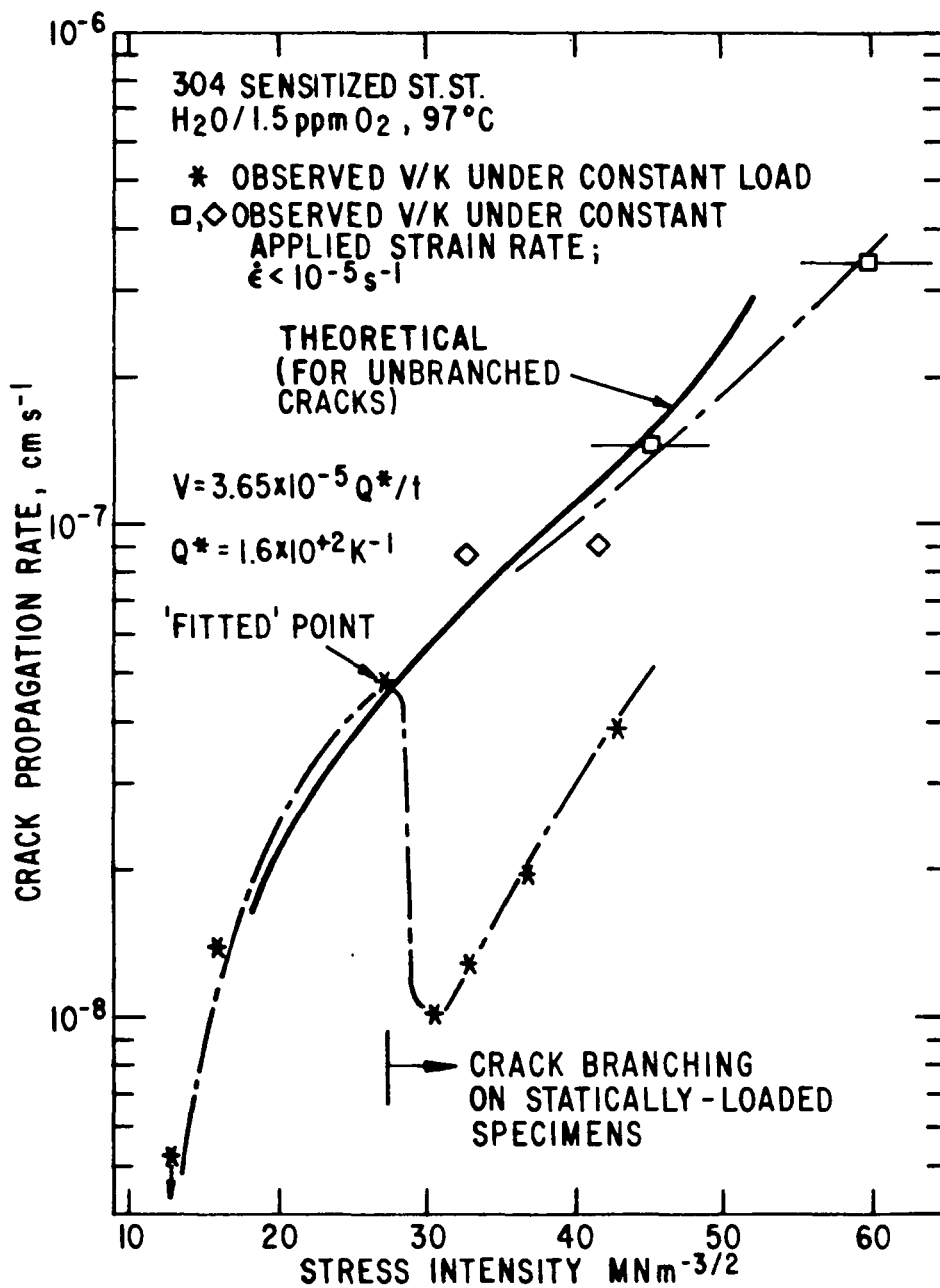


Figure 16. Comparison between theoretical and observed⁽¹³⁾ crack propagation rate/stress-intensity relationship for sensitized 304 stainless-steel in H₂O/1.5 ppm O₂ at 98 °C.⁽⁵³⁾ Theoretical values have been calculated on basis of constant-charge density criterion with $Q^* = 1.6 \times 10^2 K^{-1} \text{ } ^\circ C \text{ cm}^{-2}$ and the $Q(t)$ relationship observed in 0.01 M Na₂SO₄ at +193 mVshe. Note the fact that the theory does not account for the effect that macro-branching has on the crack propagation rate.

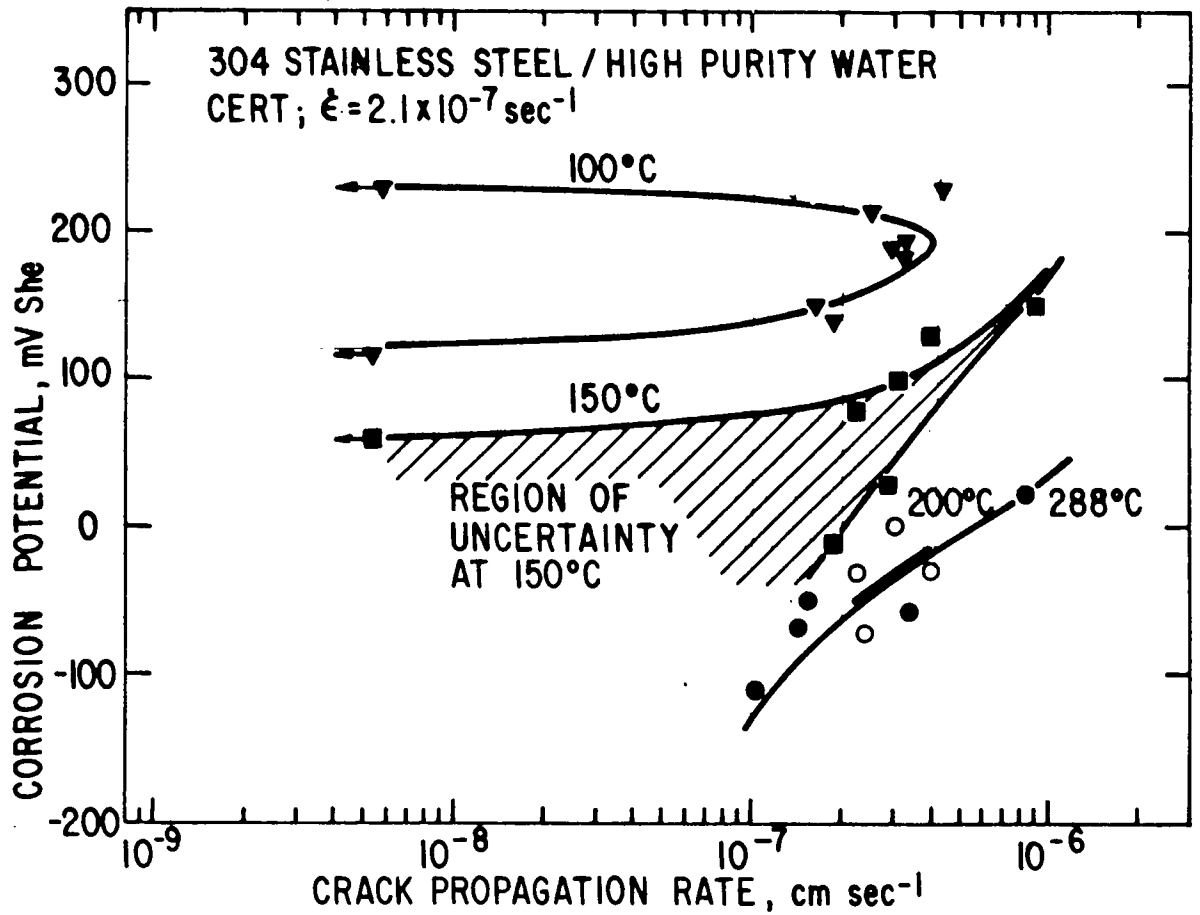


Figure 17. Data from Figure 4 replotted in terms of crack propagation rate and corrosion potential. The latter values have been taken from work by Indig^(68,69) on stainless steel in water at various oxygen/temperature combinations.

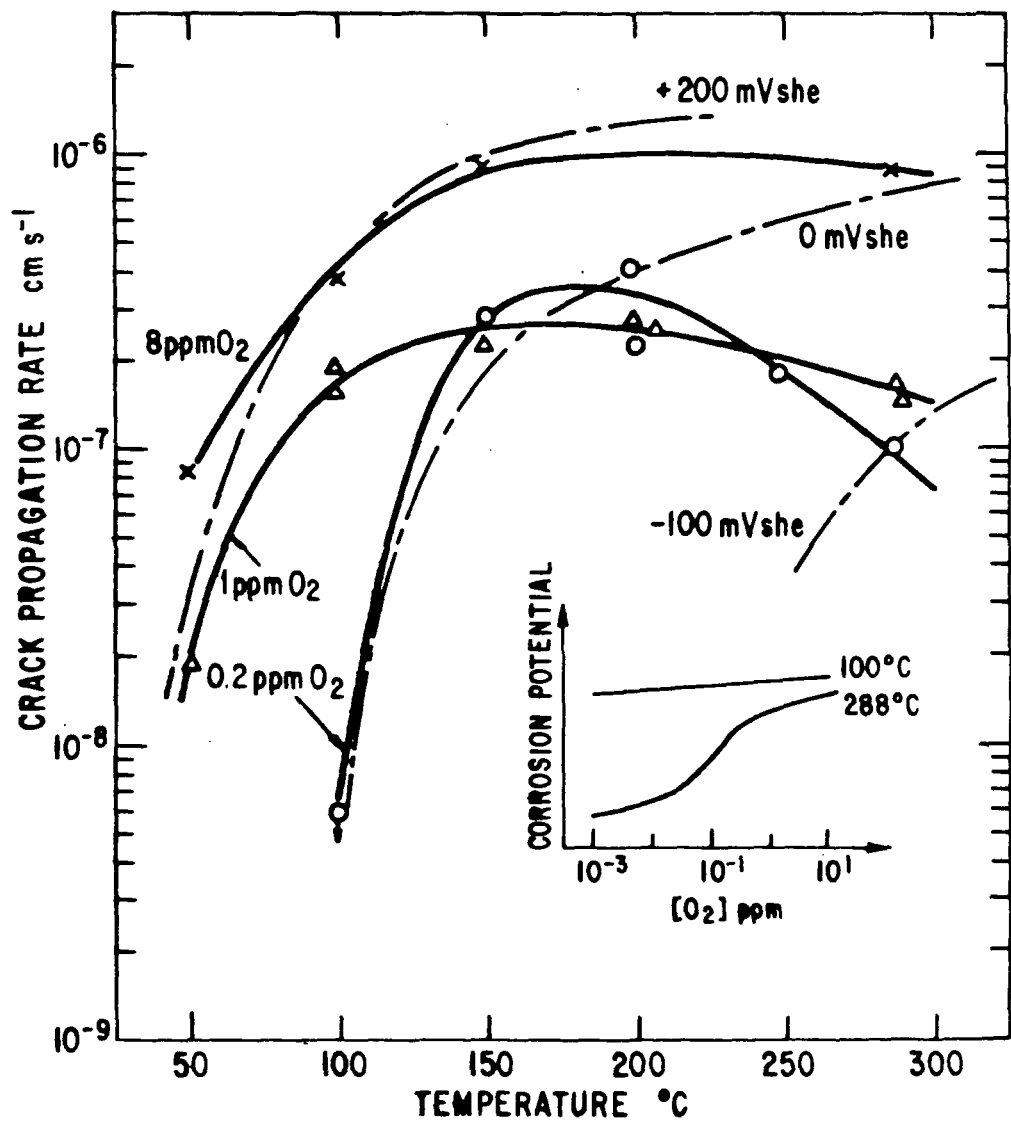
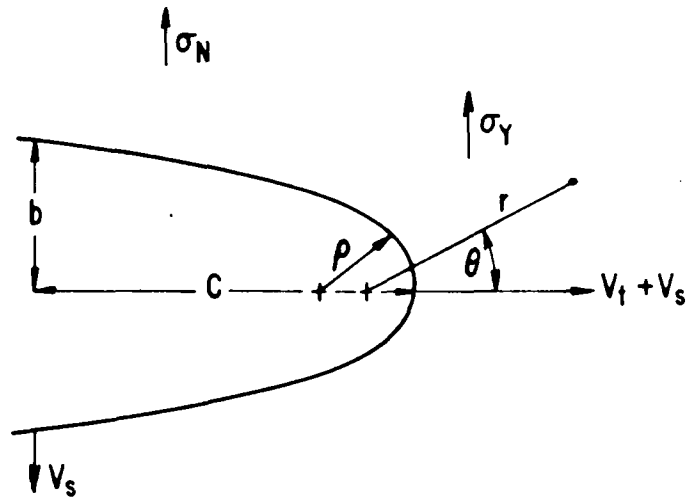


Figure 18. Variation of crack propagation rate in sensitized 304 stainless steel/water system for different temperatures and oxygen contents (potentials). Constant extension rate conditions at $2.1 \times 10^{-7} \text{ s}^{-1}$.



$$\sigma_Y = \frac{K}{\sqrt{2\pi r}} \cos \frac{\theta}{2} \left(1 + \sin \frac{\theta}{2} \cos \frac{3\theta}{2} \right) + \frac{K}{\sqrt{2\pi r}} \cdot \frac{\rho}{2r} \cos 3\theta$$

$$\sigma_{Y_{\max}} = \frac{2K_I}{\sqrt{\pi\rho}} \text{ AT } \theta=0 \text{ AND } r = \frac{\rho}{2}$$

$$\dot{\rho} = \frac{V_s^2}{V_s + V_t}$$

Figure 19. Elastic stress function at an elliptical crack tip with major and minor axes, c and b , and crack tip radius, ρ .^(76,77) Note that the maximum surface tensile stress $\sigma_{Y_{\max}}$ will change with time as the crack tip radius increases according to the relative values of V_s and V_t .⁽⁷²⁾

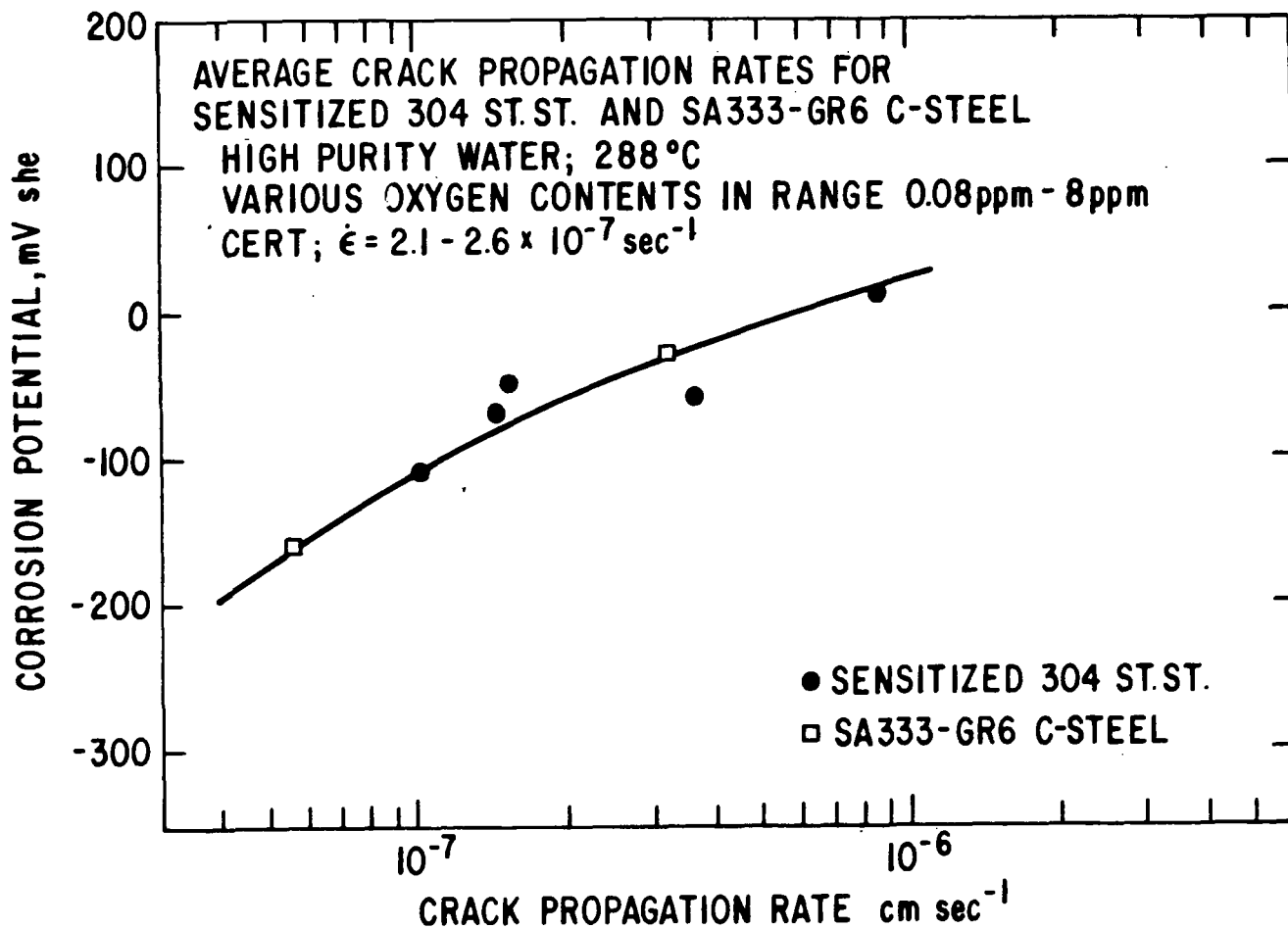


Figure 20. Variation in the average crack propagation rate for sensitized 304 stainless steel and SA333Gr6 carbon-steel in water, with corrosion potential at 288 °C. The corrosion-potential has been varied by altering the oxygen content between 0.08 ppm and 8 ppm. Constant extension rate conditions: $2.1-2.6 \times 10^{-7} \text{ s}^{-1}$.

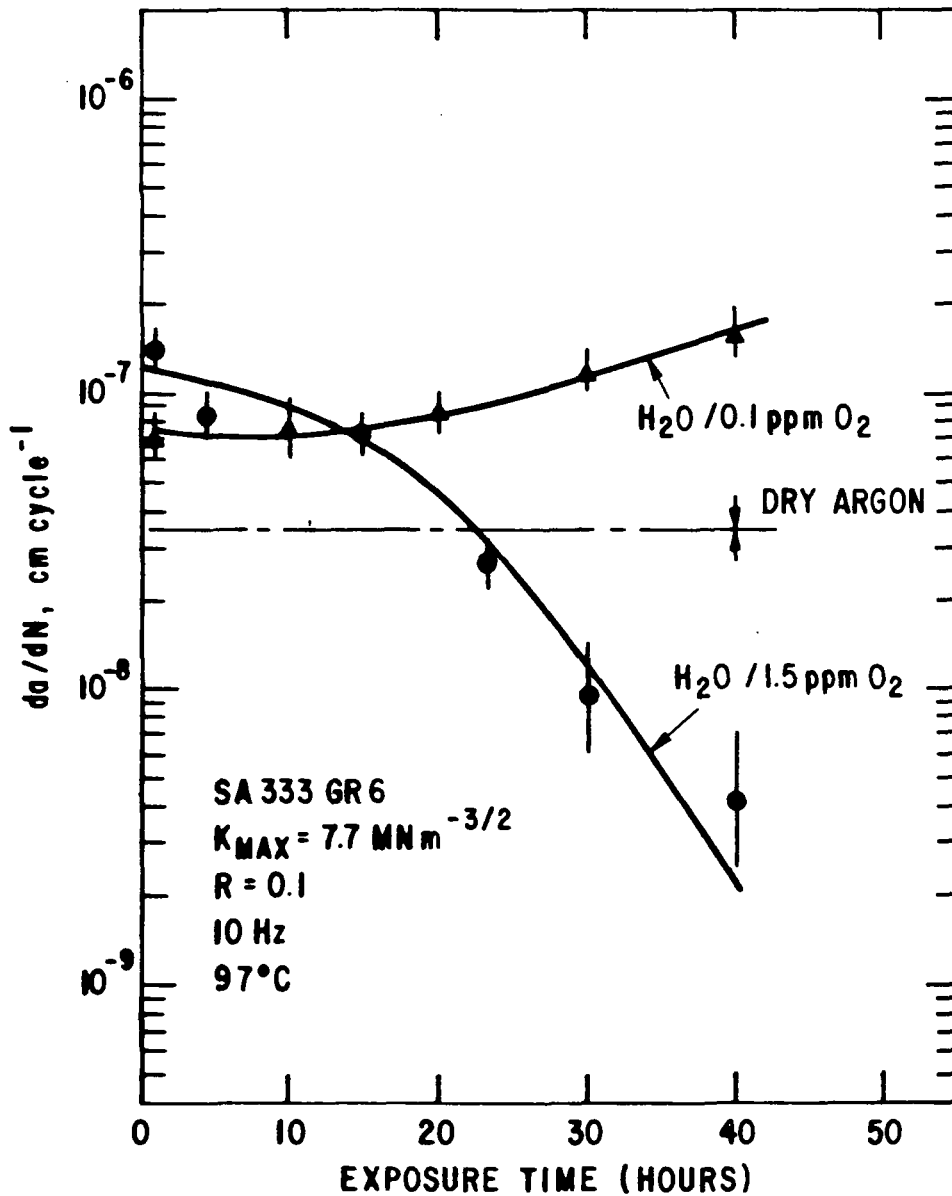


Figure 21. Variation^(71,53) in (da/dN) with time for SA333Gr6 carbon steel in argon and water/oxygen mixtures at 98 °C. $K_{max} = 7.7 \text{ MNm}^{-3/2}$, $R = 0.1$, 10 Hz. Note the crack arrest in H₂O/1.5 ppm O₂, an environment where considerable general corrosion is observed, and the lack of such arrest when the environment is inert or relatively benign (H₂O/0.1 ppm O₂).

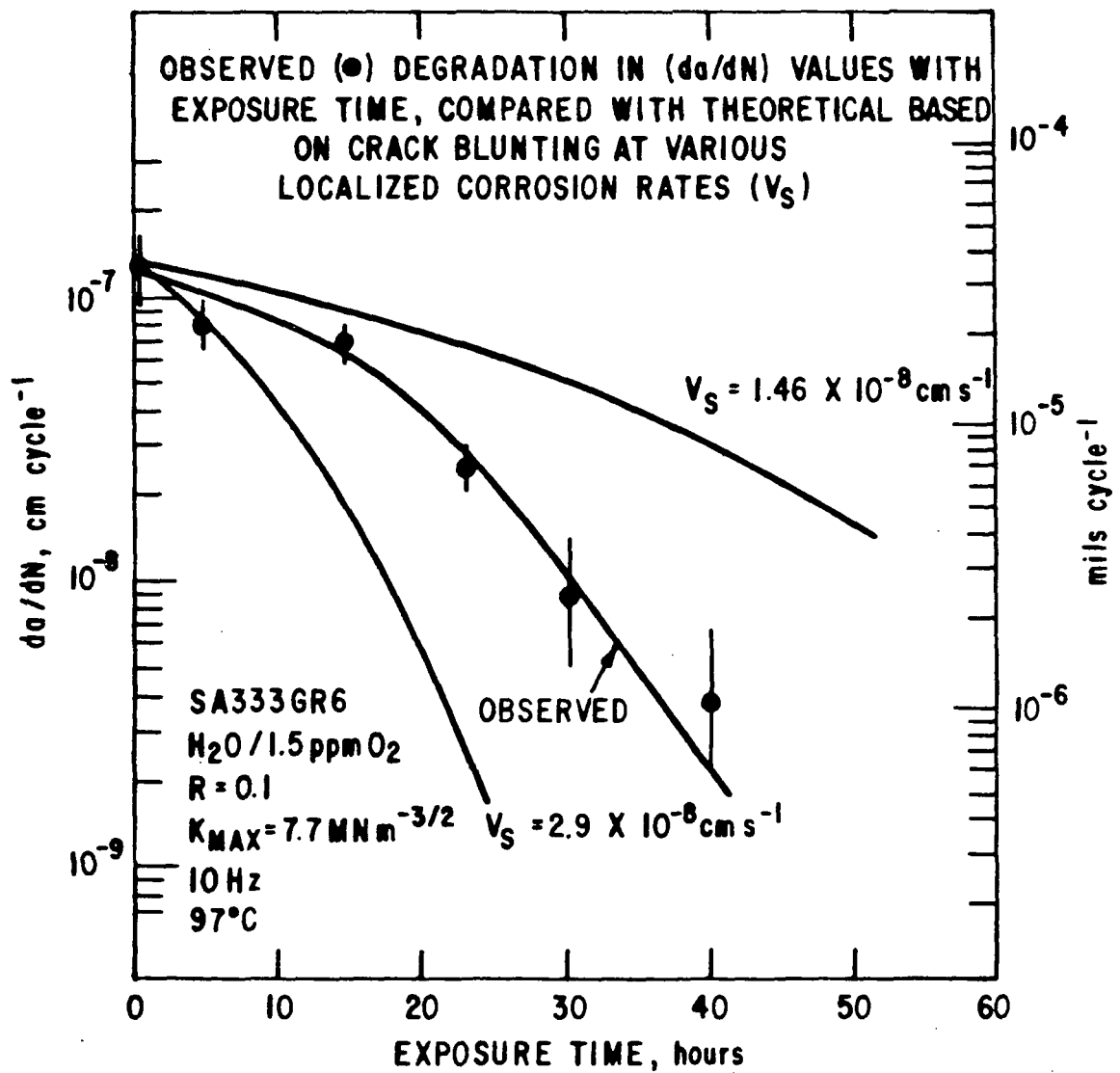


Figure 22. Comparison⁽⁷¹⁾ between observed and predicted crack arrest of SA333Gr6 carbon steel during corrosion fatigue in H₂O/1.5 ppm O₂. Predicted values based on assumption that crack sides are being corroded at a rate between 1.46 and 2.9×10⁻⁸ cm s⁻¹, and that this leads to crack blunting at the prevalent crack tip propagation rates.

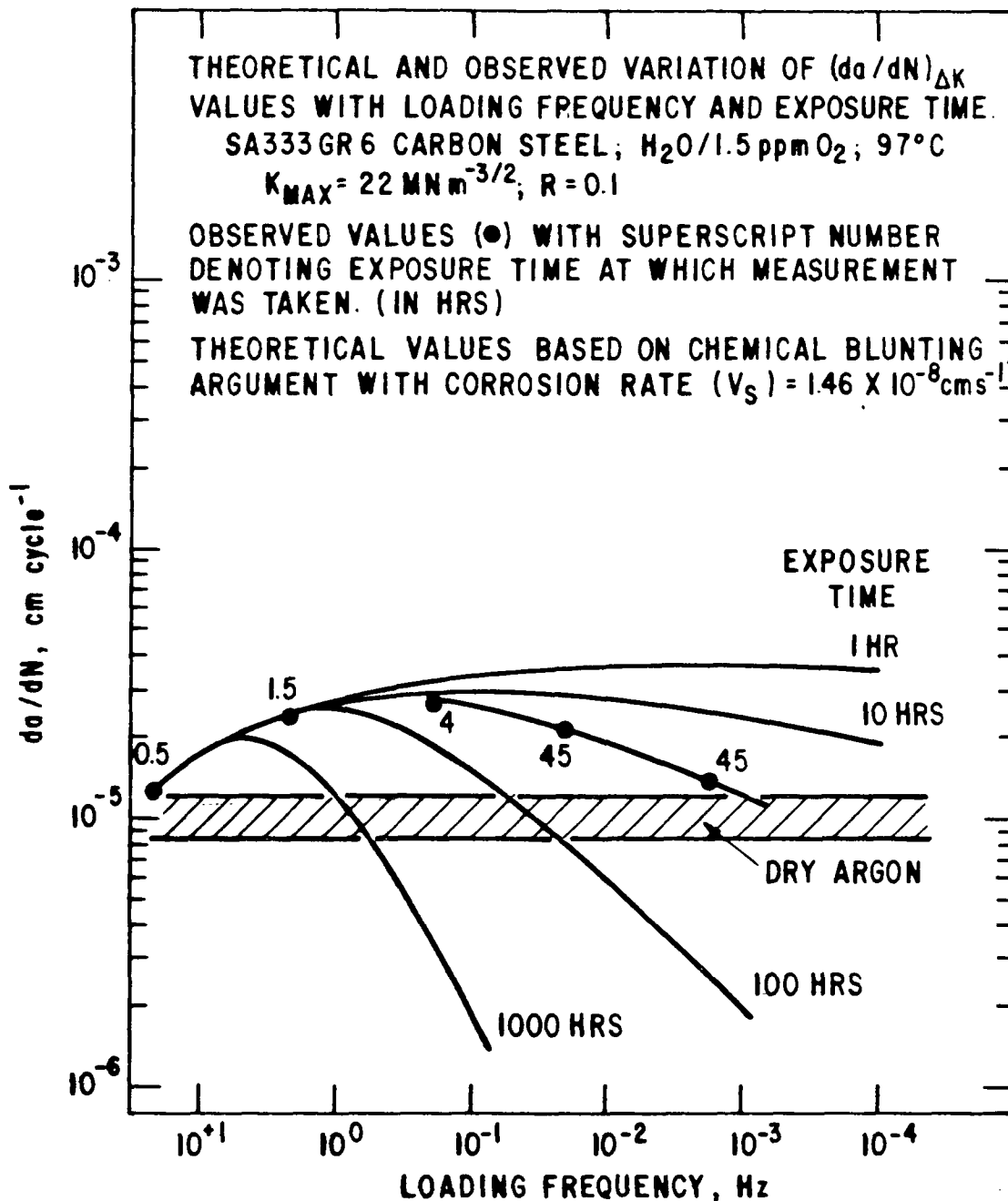


Figure 23. Variation^(53,71) of theoretical and observed (da/dN) values with frequency for SA333Gr6 carbon steel in H₂O/1.5 ppm O₂ at 98 °C; $K_{max} = 22 \text{ MNm}^{-3/2}$, $R = 0.1$. The superscript numbers beside each experimental data point denote the corresponding exposure time. The theoretical $da/dN \nu$ relationships are also shown as a function of the exposure time, the decrease in da/dN values at slower frequencies being associated with chemical blunting of the crack. (The V_s value used in the calculated curves was $1.46 \times 10^{-8} \text{ cm s}^{-1}$).

Device for Investigating Subcritical Crack Growth

of RPV Steel Specimens under BWR Conditions

(To be presented at the IAEA Specialists' Meeting on
"Subcritical Crack Growth" in Freiburg from 13 to 15 May 1981)

D. Anders, J. Ahlf

GKSS-Forschungszentrum Geesthacht, Federal Republic of Germany

Abstract

An experiment is being prepared to investigate the subcritical crack growth of RPV steel specimens under cyclic load and under the environmental conditions of a BWR with regard to primary water and irradiation.

The experiment will be carried out in the VAK reactor* Kahl which is a boiling water reactor operating at 71 bar, 286°C and generating 16 MW_e.

The experimental setup is composed of an open frame to which a string consisting of five compact tension specimens (40 mm thickness) and connecting links is fixed. The specimen chain is set under cyclic load by a pneumatically actuated bellows unit which is attached to the frame top. Specimen strain and crack opening are measured by linear differential transformers; for temperature distribution measurements in the specimens thermocouples are applied.

*Versuchsatomkraftwerk

1. Introduction

For the design of reactor pressure vessels the crack growth behaviour of the steel selected for the vessel, of welds and heat affected zones is of great importance. To characterize the material in that respect crack growth rate $\frac{da}{dN}$ is measured against cyclic stress intensity ΔK in a fatigue test.

Crack growth rate is dependent on temperature, water chemistry, form and frequency of load and -possibly- on neutron and gamma radiation. The combined action of these environmental conditions may result in synergetic effects. To study this, an irradiation experiment on compact tension specimens set under cyclic load is prepared, which will be inserted into the boiling water reactor VAK ("Versuchsatomkraftwerk Kahl").

2. Experimental setup

The irradiation rig will be placed at the core periphery inside the core shroud (s. fig. 1).

The outer dimensions and accordingly the maximum size of the specimens are determined by the place available at that position.

The design of the rig is shown in a simplified manner in figure 2. A string composed of five compact tension specimens of thickness 40 mm which are linked together by yokes is fixed to a tractive mechanism at the top and a lower fixture. Auxiliary yokes confine the crack opening to a maximum value; by this measure the experiment can be continued even if one of the specimens fails before the scheduled total number of load cycles has been reached.

The tractive force F is applied by a piston on the one side of which the reactor pressure is acting; the other side is set under the working pressure which is controlled according to the specified load sequence. A bellows system separates the reactor medium from the

working medium of the loading device in an elastic manner.

To measure the loading force a ring is built into the specimens string, the deformation of which is measured by a linear differential transformer.

Differential transformers are also used for measuring the crack opening δ . Two gages are fixed to the front of each specimen. From the readings of the gages the crack length a can be inferred from the compliance curve $\delta/F = f(a)$, which will be measured at specimens similar to the irradiation specimens.

Specimen temperature is measured by sheathed thermocouples. Iron-nickel wires are attached to the rig to monitor the fast fluence.

The electric cables and the pressure line for the controlling medium penetrate the pressure vessel of the reactor via a measurement port.

The auxiliary systems are shown schematically in figure 3.

The pressure bellows V_R of the loading assembly is connected to the control cylinder V_Z by a pressure line; both together make up a closed system that is filled with helium of high purity. The pressure within this system which defines the loading force on the specimen string is controlled by the piston position in the control cylinder. For control the load signal of the measuring ring F is compared to the command variable signal delivered from a programmer in a controller. The controller acts via a disc armature motor on a worm drive that is coupled rigidly to the control cylinder.

The relevant experimental data - these are

- crack opening δ
- loading force F
- specimen temperature T
- number of load cycles N
- pressure in the loading system P_s
- reactor pressure P_R
- pressure difference ΔP

are continuously measured and recorded.

3. Anticipated experimental conditions

The following experimental conditions are specified

- stress intensity (at the beginning)	$K_{I\max} = 1053 \text{ Nmm}^{-3/2}$
	$K_{I\min} = 737 \text{ Nmm}^{-3/2}$
	$\Delta K = 316 \text{ Nmm}^{-3/2}$
- stress intensity ratio	$R = 0,7$
- load form	saw tooth without holdtime
- load frequency	$f = 1 \text{ min}^{-1}$
- fluence ($E > 1\text{MeV}$)	$\Phi_f = 2 \cdot 10^{19} \text{ cm}^{-2}$
- number of load cycles	$N = 1,4 \cdot 10^5$

4. Pre-experiments

to verify the design considerations two major pre-experiments are in progress.

Firstly a simplified irradiation rig will be inserted into VAK to measure the temperature gradients in the specimen which result from gamma heating, to measure the neutron field in the irradiation position and lastly to get experience in handling the whole device.

Secondly an autoclave is under construction in which the environmental conditions of VAK can be simulated without radiation. In this autoclave the original irradiation rig will be outpile tested intensively.

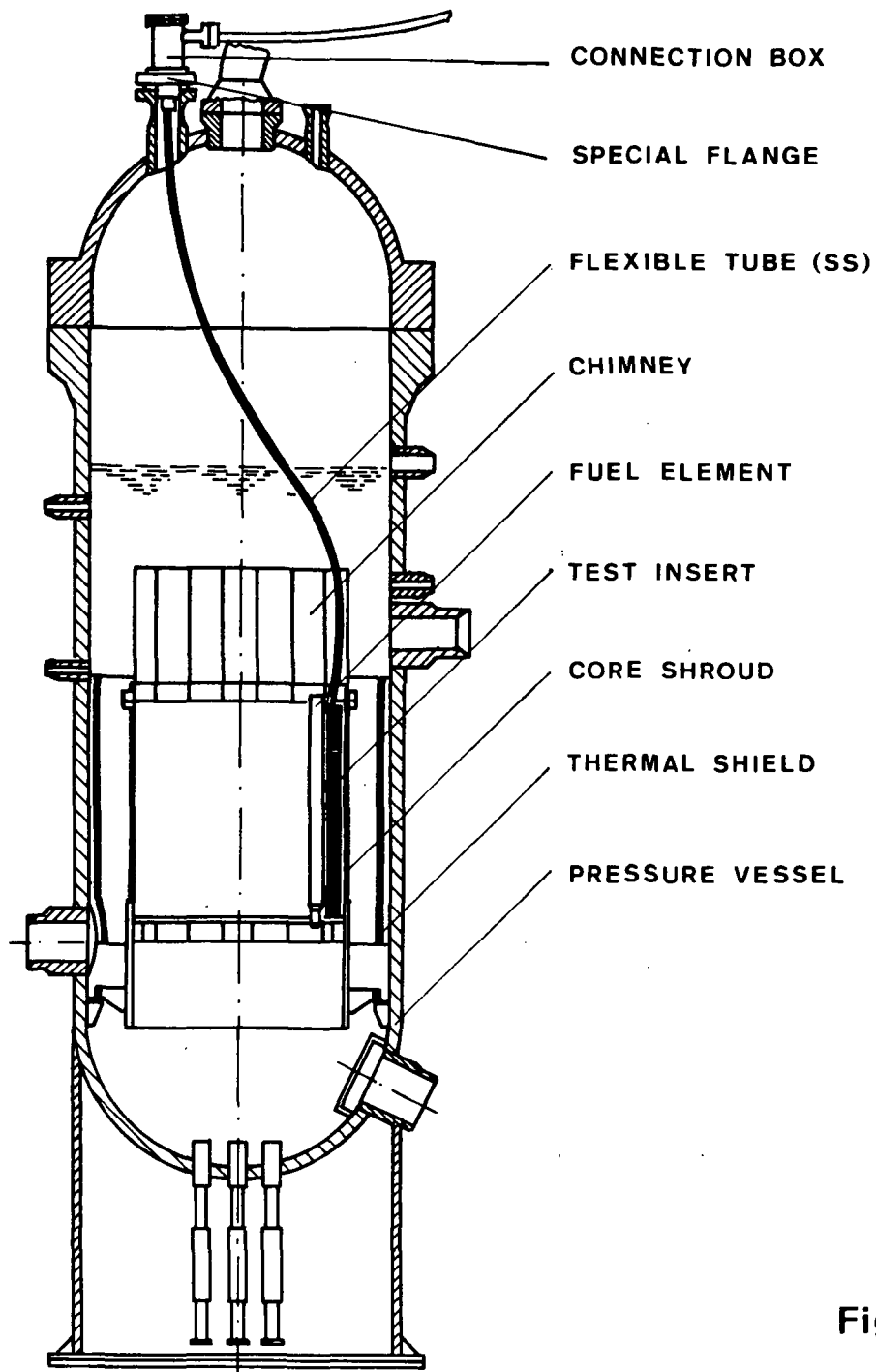


Fig.1

EXPERIMENT FOR CRACK GROWTH INVESTIGATIONS, ARRANGEMENT
IN THE REACTOR (VAK KAHL)

IfW / WV

GKSS
FORSCHUNGSZENTRUM GEESTHACHT GMBH

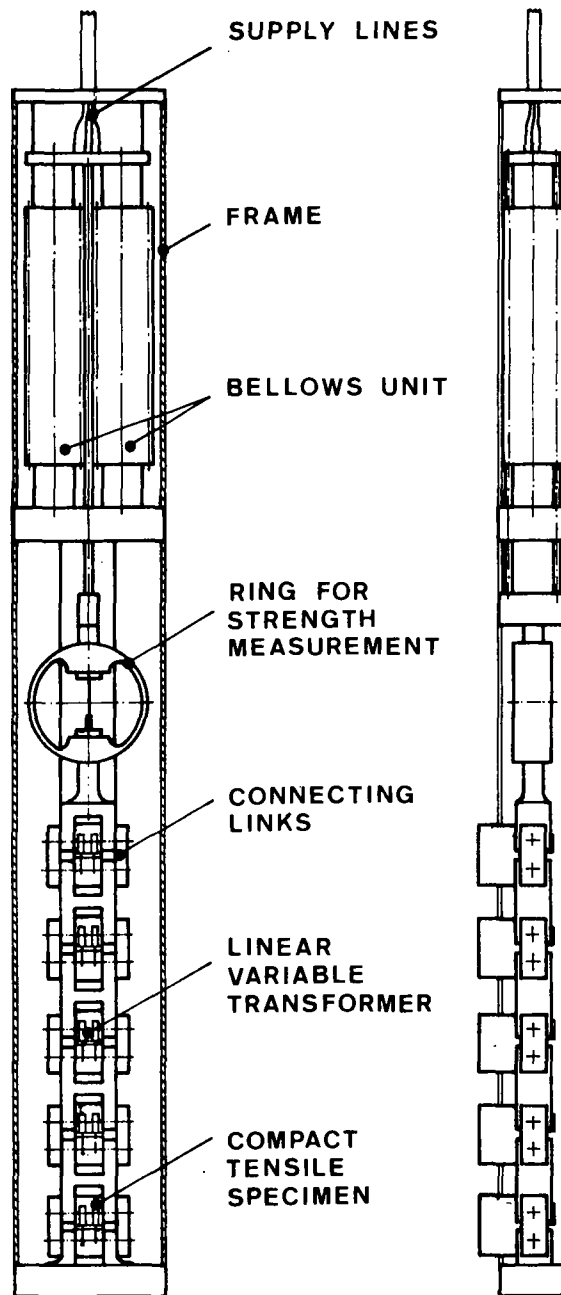


Fig. 2

IRRADIATION RIG FOR CRACK GROWTH INVESTIGATIONS

IfW / WV

GKSS
 FORSCHUNGSZENTRUM GEESTHACHT GMBH

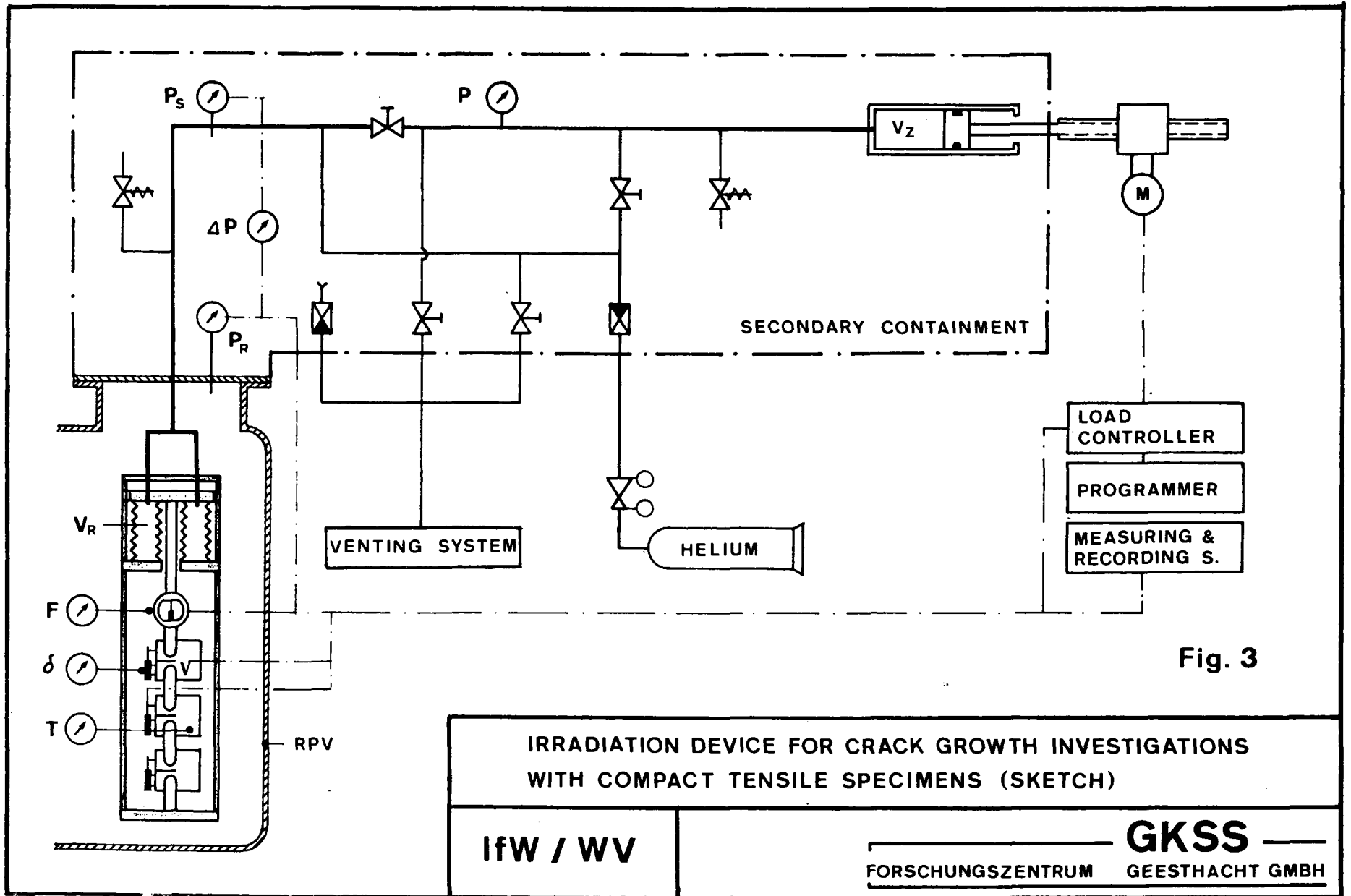


Fig. 3

IRRADIATION DEVICE FOR CRACK GROWTH INVESTIGATIONS
WITH COMPACT TENSILE SPECIMENS (SKETCH)

IfW / WV

GKSS
FORSCHUNGSZENTRUM GEESTHACHT GMBH

Harada¹⁾, Kussmaul²⁾, Schwab²⁾

1) Dept. Mech. Eng., Kyushu Institute of Technology,
Tobata Kitakyushu, Japan

2) Staatliche Materialprüfungsanstalt, University of Stuttgart (MPA)
Federal Republic of Germany

Directionality Effect on Fatigue Crack Growth Rate
for Forged 20 MnMoNi55 (A 508 Cl 3) Material

Abstract

In order to better understand directionality effect mainly related to MnS inclusions on fatigue crack growth rate, fatigue tests were carried out using CT specimens removed from two differently forged plates 3300 x 1500 x 250 mm and 1500 x 200 x 120 mm with a sulphur content of 0.011 %. Specimen orientations were varied as L-S, L-T, T-S, T-L, S-L and S-T for the first plate and as L-T and T-L for the second plate, where, L, T and S indicate longitudinal, transverse and short transverse direction, respectively. Anisotropy was characterized by metallographic investigations and tensile and impact toughness tests. Low and high cyclic stress amplitudes were selected for the evaluation of stress amplitude dependency at room temperature. Cyclic crack growth rate was measured by microscopic observation on both edges of the crack front. Although both plates showed a strong toughness directionality effect of about 4 : 1 in C_V -impact strength, no effect in fatigue crack growth rate resulted at low ΔK values. Directionality became efficient, only when ΔK was significantly above 800 N/mm^{-3/2} (maximum acceleration factor about 2).

INTRODUCTION

It is well known that plastic working such as rolling and forging induces anisotropy in static mechanical properties as well as fatigue properties of metallic materials. In general, this anisotropy is strongly intensified in the thickness direction of the materials. The causes of this anisotropy are usually attributed to the rolling- or forging-induced fibering (1)-(4). Former studies by one of the present authors were related to a fairly clean rolled steel plate for boiler and pressure vessel use (5), (6).

The primary interest of this paper is aimed to characterize microscopically as well as macroscopically the MnS inclusion-induced directionality effect on fatigue crack growth rate of two forged structural steel plates with a sulphur content of 0.011 %. The second objective of this paper is the evaluation of the stress amplitude dependency.

As the sulphur content plays an important role in environmentally assisted crack growth (in high-temperature, pressurized water), (7), the aim of these results is to contribute to a better understanding of corrosion fatigue in anisotropic steels.

MATERIAL AND EXPERIMENTAL PROCEDURES

The supplied material 20 MnMoNi 55 (A508 C1 3) with a comparatively high sulphur content of 0.011 % (chemical composition in Table 1) and a purity degree of $K_{SS}0 = 250$ according to the German "Stahl-Eisen-Prüfblatt" was forged in two different ways to produce different kinds of MnS inclusions.

Plate I was mainly forged in one direction, which produced board-shaped inclusions, Fig. 1. The dimensions of plate I were 3300 x 1500 x 250 mm, the forging ratio was 10. The heat treatment after forging was 9 hrs 900 °C/water quenched/9 hrs 640 °C/air cooling which produced a bainite structure (see also Fig. 7). The static mechanical properties in the three reference directions were checked at room temperature and the results are tabulated in Table 2. The material shows a definite trend in the three directions: the tensile properties are rather isotropic, whilst those relating to ductility are anisotropic. Charpy V-notch impact tests were conducted at different temperatures using standard specimens (specimen orientation, see Fig. 4). The results, Fig. 2, indicate a strong anisotropy of about 4 : 1 at 100 °C (LS- and SL-oriented specimens).

Plate II was forged in two directions (forging ratio 30) thus inducing fiber-like inclusions, Fig. 10. The dimensions of plate II were 1500 x 200 x 120 mm. The heat treatment after forging was 6 hrs 900 °C/water-quenched/9 hrs 640 °C/air cooling/9 hrs 600 °C/furnace cooling and produced a typical microstructure (Fig. 15). The static mechanical properties were checked in the L and T direction (Table 3) and showed no anisotropy with respect to $R_{p0,2}$ and R_m , and little anisotropy with regard to A_5 and Z. Obviously, the fiber-like inclusions do not affect the static ductility values as much as the board-shaped ones. However, the Charpy V-notch impact values, which are

shown in Fig. 11, (orientation see Fig. 12), indicate a strong anisotropy of 4 : 1 at 100 °C.

The fatigue tests were carried out with standard CT specimens, Fig. 3. For plate I all the possible orthogonal specimen orientations, i.e. L-T, L-S, T-L, T-S, S-L and S-T, were selected as shown in Fig. 4. The specimen orientations are designated as follows: for example, L-S: the first letter (L) indicates a precracked plane (or a loading axis) and the second letter (S) indicates the direction of fatigue crack growth. For plate II, which had fiber-like inclusions, just two orientations were selected as shown in Fig. 12.

In order to microscopically observe fatigue crack growth behaviour, the specimen surfaces were polished with an electric surface finisher and one of two specimen surfaces was slightly etched with picric acid prior to fatigue. The test frequency was 1600 to 1900 cpm (Schenck push-pull machine). The fatigue crack growth was observed using an optical microscope.

Low and high levels of the cyclic load range ΔP ($=P_{\max}-P_{\min}$) applied to the specimens were selected as $\Delta P = 17\text{ kN}$ ($P_{\max} = 19\text{ kN}$ and $P_{\min} = 2\text{ kN}$) and $\Delta P = 30\text{ kN}$ ($P_{\max} = 33\text{ kN}$ and $P_{\min} = 3\text{ kN}$), respectively. Only in the case of $\Delta P = 17\text{ kN}$ a higher repeated load of $\Delta P = 25\text{ kN}$ ($P_{\max} = 27\text{ kN}$ and $P_{\min} = 2\text{ kN}$) was initially applied to the specimens until the crack initiated and reached a length of about $a = 14\text{ mm}$ (about 1 mm crack growth), then the load level was lowered to the definite level of $\Delta P = 17\text{ kN}$. In order to exclude the influences of an initial slit-affected zone and the initial overload cycling, the crack growth data before the crack reached a length of $a = 15\text{ mm}$ were ignored in both cyclic load levels. Through the experiments it was found that almost all the specimens showed a difference in the crack length of both sides of the specimen surfaces during fatigue crack growth. This difference was mostly within a length of 0.5 to 1.0 mm. Therefore, an average crack length of both sides of the specimen surfaces was adopted.

EXPERIMENTAL RESULTS

PLATE I

Macroscopic crack growth rates

Figs. 5 (a) and (b) show macroscopic crack growth curves in each specimen orientation under the low and the high cyclic load range, respectively. In Fig. 5

(a) the results of the L-T specimen, showing the fastest crack growth, is one exception in which a intermediate cyclic load range of $\Delta P = 25$ kN ($P_{\max} = 27$ kN and $P_{\min} = 2$ kN) was used. The number of the load cycles during precracking under the higher cyclic load range of $\Delta P = 25$ kN was about 2×10^5 cycles in each specimen. The L-S, S-T and T-S specimens in Fig. 5 (a) show almost the same crack growth curves, whilst the T-L and the S-L specimens indicate a shorter crack propagation life than other specimens. In the case of the high cyclic load range shown in Fig. 5 (b), the S-L and the T-S specimens show the shortest and the longest crack propagation life, respectively, whilst the crack propagation lives of the other specimens are almost the same. In both figures no definite trend of the crack growth curves in all the specimens is noticed except that the S-L specimen indicates a slightly shorter crack propagation life.

Figure 6 illustrates the log-log relationship between cyclic stress intensity factor range, ΔK and crack growth rate da/dN , for the low and the high cyclic load range, respectively, where the ΔK -value was evaluated by the series expansion formula (8). The least square method was applied in order to determine each $da/dN - \Delta K$ relation. In the case of the low cyclic load range it is found that the crack growth rate of each specimen is only slightly anisotropic and that the S-L and T-S specimens indicate the fastest and the slowest crack growth rate respectively. It is, however, noticed that although each $da/dN - \Delta K$ relation indicates a slightly different slope, the crack growth rate of all the specimens falls on a narrow scatter band. Observing them closer, it is understood that anisotropy in crack growth rate is slightly amplified as ΔK becomes larger. This trend becomes clearer when the cyclic load range is higher, where the S-L specimen shows the fastest crack growth rate. The trend of anisotropy in the crack growth rate found in Fig. 6 is in agreement with that found in the literature (2) - (4). The anisotropy found in the macroscopic crack growth of the specimens is considered to be caused by the directionality effect of the elongated inclusions, as will be shown in the metallographic and fractographic examinations.

Metallographic examination

Through the observation of the microscopic crack growth behaviour it was found that the MnS inclusions produce different types of crack growth mechanisms, depending on the specimen orientation. These differences can be roughly classi-

fied as being caused by two factors: the plane of the crack growth, i.e. LT-, TS-, and SL-planes and the crack direction of the macroscopic crack growth.

Figures 7 (a) - (e) indicate typical examples of the microscopic crack growth behaviour observed on each specimen. In the case of the observed TS-plane, the T-S and the S-T specimens showed rather zigzag-like crack growth as shown in Fig. 7 (a), whilst the L-T, T-L, S-L and L-S specimens in the LT- and SL-observed planes indicated relatively straightforward crack growth as exemplified in Fig. 7 (b). The shape of the MnS inclusions in the TS-plane is more or less elliptic. The major axis of the ellipse is located vertically to the direction of the crack growth of the T-S specimen. The linking of the main crack with the inclusions in Fig. 7 (c) was often observed to be zigzag-type with branches in the T-S specimen. This might retard the main crack growth shown in Fig. 5 (b). Figure 7 (d) shows another example of the zigzag or lamellar tearing-like crack growth observed in the S-T specimen. In this case, the major axis of the ellipse of MnS inclusions is parallel to the direction in which the main crack runs. It was observed that the main crack grew up by linking with preceding "subcracks" originated at the inclusions which locate in the different planes from the premature crack plane.

In the case of the L-T and L-S specimens, the crack runs perpendicular to the pattern of the elongated inclusions. The main crack tip lamellar branching and the change in the crack growth path, as shown in Fig 7 (e), were rarely observed. The MnS inclusions in this case apparently gave little effect. The elongated inclusions might be too long to affect the crack path. This might be the reason why the L-T and L-S specimens showed rather straightforward crack growth.

Macro- and microfractographies

The macro- and microfractographic examinations were only done in the case of $\Delta P = 30$ kN. Fatigue tests were interrupted in the course of the crack growth, except the S-T and T-S specimens.

The macrofractography is shown in Fig. 8 for each specimen. Characteristic features of the fracture surfaces can be classified into following three prints: (i) the fracture surfaces of the S-T and S-L specimens are rough, which becomes remarkable as the crack grows, whilst the other specimens show a comparatively flat fracture surface.

- (ii) In the case of the T-S specimen, tongues or submacrocracks located perpendicular to the direction of the main crack growth can be observed in the wide area of the fracture surface.
- (iii) On the fracture surfaces of the T-L and S-L specimens, in which the main crack ran parallel to the elongated MnS inclusions, stripes along the direction of the crack growth are seen. Especially closely spaced stripes can be observed in the case of the S-L specimen.

Concerning the first point (i), the rough fracture surface observed in the S-T specimen may correspond to the zigzag-like crack growth seen on the specimen surface. This might be induced by the effect of the elliptic-form MnS inclusions, as described in the foregoing paragraph. In the case of the L-S and L-T specimens, the flat fracture surface observed can be interpreted that the main crack ran perpendicularly to cut the elongated MnS inclusions and as the result, the inclusions gave no effect to change crack growth pattern and the flat fracture surface was formed. The second point (ii) may correspond to the result observed on the specimen surface; the tongues on the submacrocracks may indicate steps which appear when the main crack changes its growth path through the linking with the MnS inclusions. These phenomena might retard the main crack growth rate. Concerning the third point (iii), it is obvious that the stripes indicate the elongated MnS inclusions. Their appearances, however, differ depending on the specimen orientation. The stripes observed in the S-L specimen are rather wide because the flat inclusions lie on the crack plane, whilst the fine stripes observed in the T-L specimen are due to the perpendicular crossing of the crack plane and the flat inclusions.

Through the observation of the fracture surfaces with the aid of a scanning electron microscope, it was found that the effect of the MnS inclusions on the crack growth differed depending on the specimen orientation and the stage of the crack growth.

Figures 9 (a) - (f) show examples of the microfractographs. In the case of the L-S and L-T specimens in which the crack ran to intersect perpendicularly the elongated MnS inclusions, the wide portion of the fracture surface was covered with a typical striation pattern. Some amount of inclusions of which shapes were elliptic or circular, as shown in Fig. 9 (a), were observed at the final stage of the crack growth. In this case subcracks running perpendicularly to the main crack and parallel to the inclusions were originated. These subcracks might retard the main crack. This mechanism was more evident in plate II and is discussed later.

In the case of the specimens in which the crack ran parallel to the elongated inclusions, i.e. T-L, S-L and S-T specimens, the entire fracture surface was covered with the MnS inclusions. Figure 9 (b) indicates an example of the elongated flat inclusions observed at the initial stage of the crack growth in the S-L specimen, in which the crack plane coincides with that of the flat inclusions. At the final stage of the crack growth in the S-L specimen, elongated MnS inclusions were found broken into pieces due to plastic deformation at the crack tip, as shown in Fig. 9 (c). On the whole fracture surface of the S-T specimen, a coarse step like pattern was observed as well as the elongated flat inclusions, as shown in Fig. 9 (d) (see an arrow in the figure). This pattern may indicate that the steps formed during the changing of the crack growth path through the linking with the inclusions located on another plane from the premature cracking plane. In the case of the T-S specimen, a straight line pattern perpendicularly locating to the direction of the crack growth was frequently observed as shown in Fig. 9 (e) + (f) (see an arrow in the figure). Along this pattern the inclusions were often observed.

PLATE II

Macroscopic crack growth rates

In the case of plate II geometry was less complicated as the MnS-inclusions were needle-shaped. The crack growth of the most interesting orientations, L-T and T-L, is shown in Fig. 13. In accordance with the results of plate I there is no detectable difference in fatigue crack growth for the L-T and T-L specimens in the case of the low-cyclic load range of $\Delta P = 17\text{kN}$. For $\Delta P = 30\text{kN}$ anisotropy becomes efficient and produces a faster crack growth for the T-L specimen where the main crack runs parallel to the inclusions.

Looking at the $da/dN - \Delta K$ relation in Fig. 14 it is clear that very little difference in crack growth exists at low ΔK values. With increasing ΔK anisotropy becomes efficient leading to an acceleration factor in crack growth rate of about 2 : 1 for $\Delta K = 1500 \text{ N/mm}^{3/2}$.

Metallographic examination

Figures 15 (a) - (d) show typical examples of the crack path on the specimen surfaces. It is apparent that both the L-T and T-L specimens showed rather straight forward crack growth (Figs. 15 (b) and (d)). At larger magnifications

the L-T specimen reveals a fine zigzag-like growth (inclusions perpendicular to the crack growth direction), whereas the T-L specimen has larger parts of straight crack growth with sudden changes, Fig. 15 (a), where the crack moves to a different, parallel plane.

Macro and microfractographies

For $\Delta P = 30$ kN the macro- and microfractographies are shown in Figs. 16 and 17, respectively. In the case of the L-T specimen, the inclusions have to be cut by the main crack leading to a comparatively smooth surface. The scanning electron micrographs clearly show subcracks running parallel to the inclusions at $\Delta K = 1500 \text{ N/mm}^{3/2}$ (Figs. 17 (a) and (b)). These subcracks are much less pronounced for $\Delta K = 700 \text{ N/mm}^{3/2}$ which are illustrated in Fig. 17 (c) and (d). The formation of these subcracks might be a mechanism to reduce the crack growth rate. It becomes efficient for large ΔK values, where the plastic zone is large enough to lead to an interaction between main crack and inclusions.

In the T-L specimen the main crack is led by the inclusions thus producing a rough fracture surface. The way in which the main crack follows the path of the inclusions is illustrated in Fig. 17 (e).

DISCUSSION

As described in the foregoing, the forged steel plates used showed relatively strong anisotropy in ductility values measured in the static tensile and Charpy impact tests. It is, however, found in the fatigue tests that, although the strongly deformed MnS inclusions produced different kinds of the microscopic crack growth behaviour, depending on specimen orientation, they resulted only in a minor directionality effect on the fatigue crack growth rate.

Concerning anisotropy in fatigue crack growth rate of rolled and forged steel and aluminum plates, much work has been done by several investigators (2) - (6). It seems that most of the previous studies were conducted using rather clean materials. A general trend obtained so far is that the deformed inclusion-induced directionality effect on the fatigue crack growth rate exists, but it is usually much less than compared with that found in the unnotched specimen (5). Regarding this, Harada and Ohji (5) have clarified that the inclusions play a different role in notched and unnotched fatigue process.

According to the results of the previous studies (2) - (4), anisotropy in the crack growth rate increases with an augmentation of the ΔK -value. In this respect the results obtained in the present study are well in agreement with the previous results. This trend of anisotropy has been interpreted by considering the relation in the plastic zone size formed at the crack tip and inclusion size at the small ΔK -value (corresponding to the initial stage of crack growth).

Due to the difference of stress state at the surface and inside of a specimen, some differences in crack growth mechanism should naturally exist between the surface and inside of the specimen (9). In this study it was found that the strongly elongated MnS inclusions induced different kinds of the crack growth mechanism observed through the metallographic and fractographic examinations. It is, however, recognized that the basic features observed in those crack growth mechanisms indicated a fairly good correspondence between the surface and fractographic observations.

CONCLUDING REMARKS

The directionality effect, mainly related to the elongated MnS inclusions of two forged structural steel plates with a comparatively high content of sulphur (0.011 %) on the fatigue crack growth rate was examined at room temperature from the macroscopic and microscopic points of view. From the obtained results it can be concluded as follows:

- (1) The materials used showed significant anisotropy on ductility measured by tensile and Charpy impact tests. The strength properties showed less difference. The anisotropy was induced by the severely deformed elongated MnS inclusions.
- (2) In the fatigue crack growth tests at the low and the high cyclic load ranges, however, the materials showed no anisotropy in the crack growth rate at low ΔK values. With increasing ΔK anisotropy became more and more efficient.
- (3) The elongated inclusions induced different kinds of microscopic crack growth mechanisms, depending on specimen orientation. The observed results of the microscopic crack growth on the specimen surfaces were comparatively well in agreement with those on the fracture surfaces.

ACKNOWLEDGEMENT

The authors wish to acknowledge the Alexander von Humboldt Foundation that this work was done while the main author, S. Harada, stayed at MPA Stuttgart, University of Stuttgart, as a research fellow of the AvH Foundation.

REFERENCES:

- /1/ Watanabe, J., and Kumada, Y., Proc. 1st. Int. Conf. Frac. Sendai, (1965), 1087.
- /2/ Zinkahm, R.E., Trans. Metallurg. Soc. AIME, Vol. 245, (1969), 1519.
- /3/ Heiser, F.A., and Hertzberg, R.W., Trans. ASME, Ser. D. Vol. 93, No. 2, (1971 - 6), 211.
- /4/ Kage, S., and Nisitani, H., Trans. Japan. Soc. Mech. Engrs., (in Japanese), Vol. 41, No. 344, (1975), 1080.
- /5/ Harada, S., and Ohji, K., Proc. Int. Conf. Frac. Mech. Technol. Hong Kong, Vol. 2, (1977), 54.
- /6/ Ohji, K., et al., Bull. Japan. Soc. Mech. Engrs., Vol. 21, No. 156, (1978), 939.
- /7/ Cullen, W.H., Loss, F.J., Watson, H.E., Bamford, W.H., and Ceshini, L.J.; 8th Water React. Safety Inf. Meeting, Gaithersburg, Oct. 1980
- /8/ ASTM Standard, 1973 Annual Book, Part 31 (1973), 960 E 399-72.
- /9/ Koterazawa, R., Proc. 1st. Int. Conf. Mech. Behavior Mater., Kyoto, Vol. 2, (1972), P. 223.

Table 1: Chemical composition of the material tested (plate I + II)

C	Si	Mn	P	S	Cr	Mo	Ni	Al	Cu	V	Sn	Co	As	Sb	N
.22	.33	1.41	.011	.011	.20	.68	.54	.010	.15	.02	.007	.010	.012	.005	.011

Table 2: Mechanical properties at room temperature - plate I

Orientation	$R_{p0,2}$ [N/mm ²]	R_m [N/mm ²]	A_5 [%]	Z [%]
S	584	720	9	17
T	597	752	16	49
L	627	792	19	61

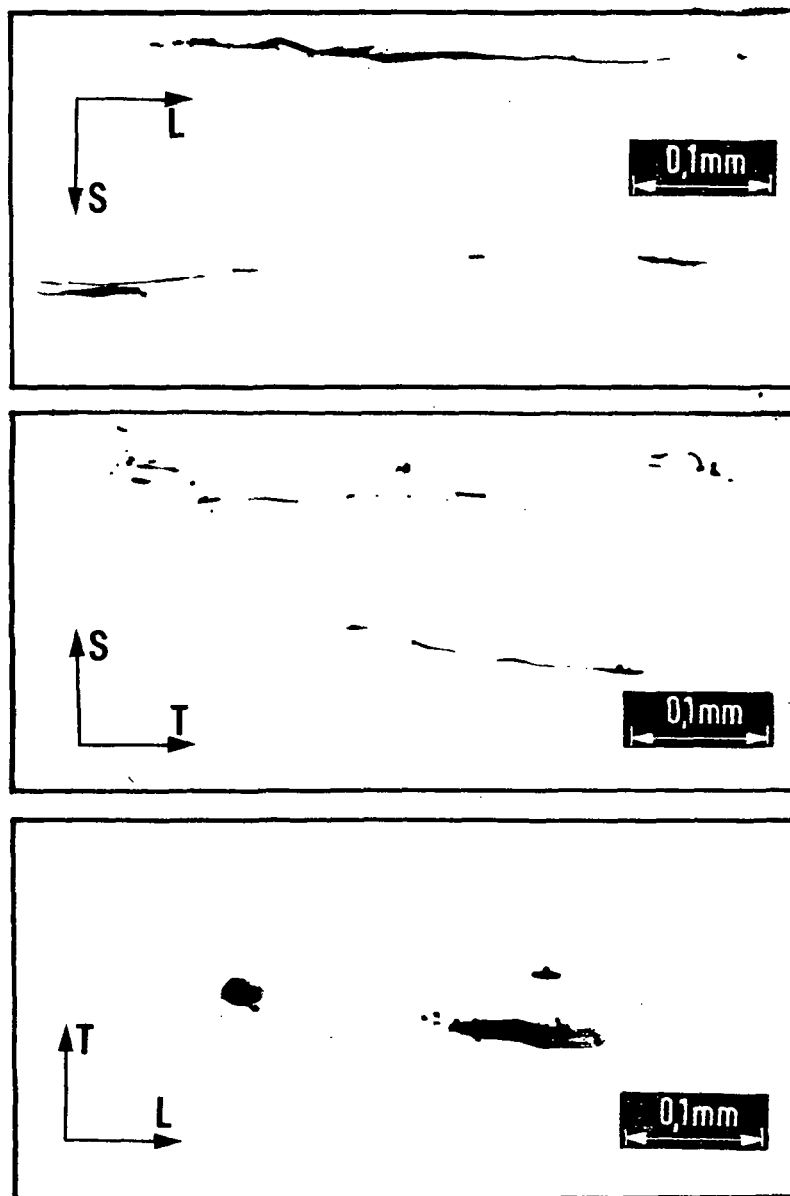


Fig. 1: Board-shaped MnS inclusions in the three reference planes of plate I

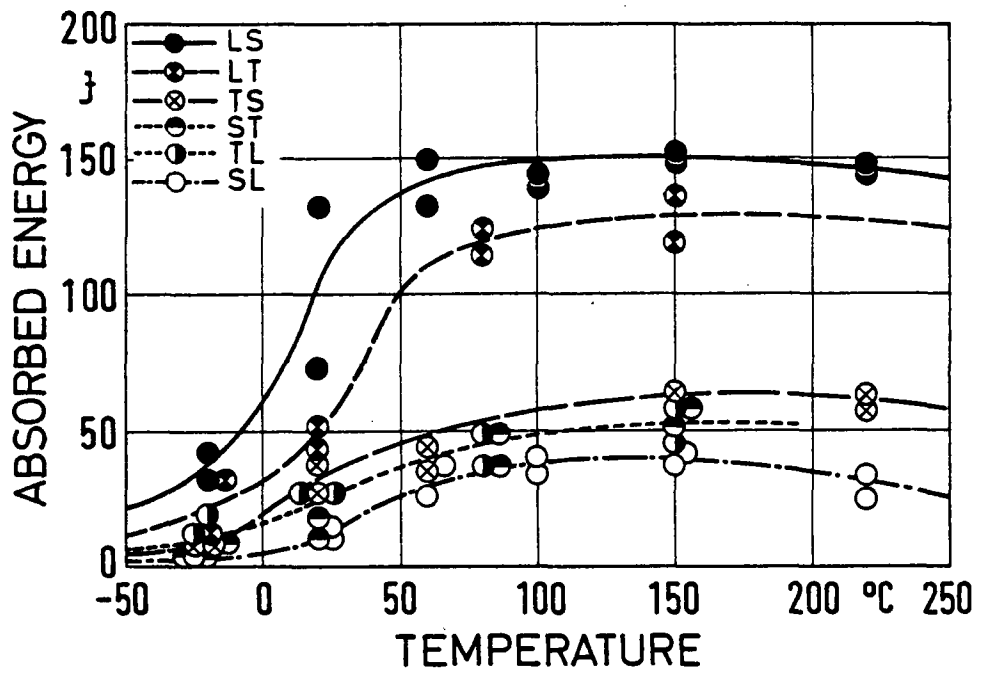


Fig. 2: Charpy impact test - plate I

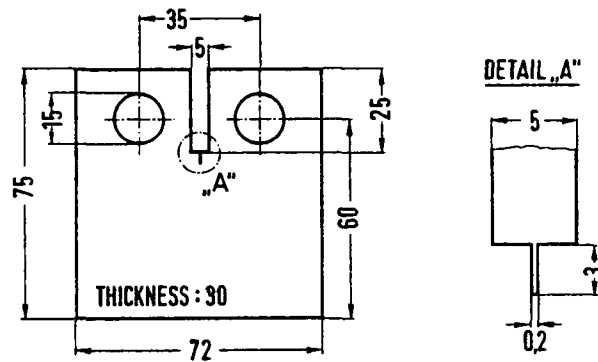


Fig. 3: Dimensions of the CT-specimens

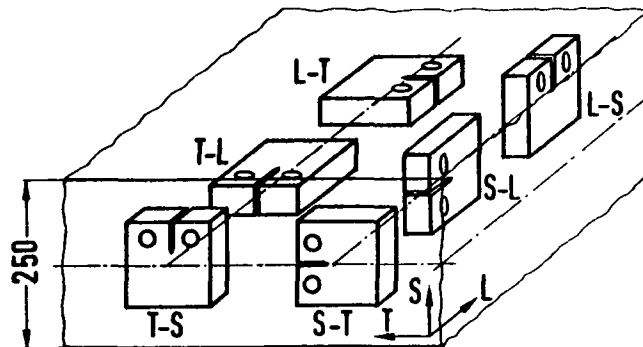
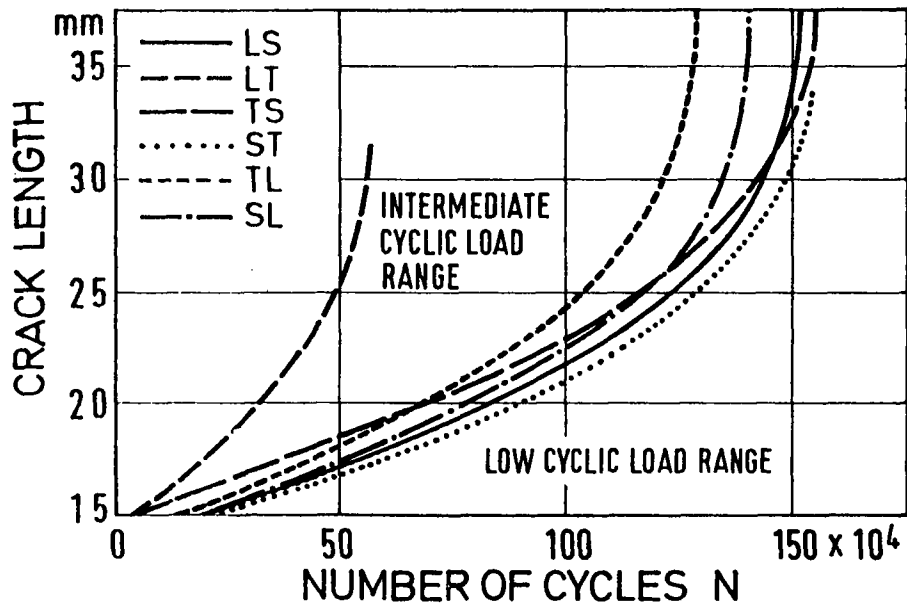
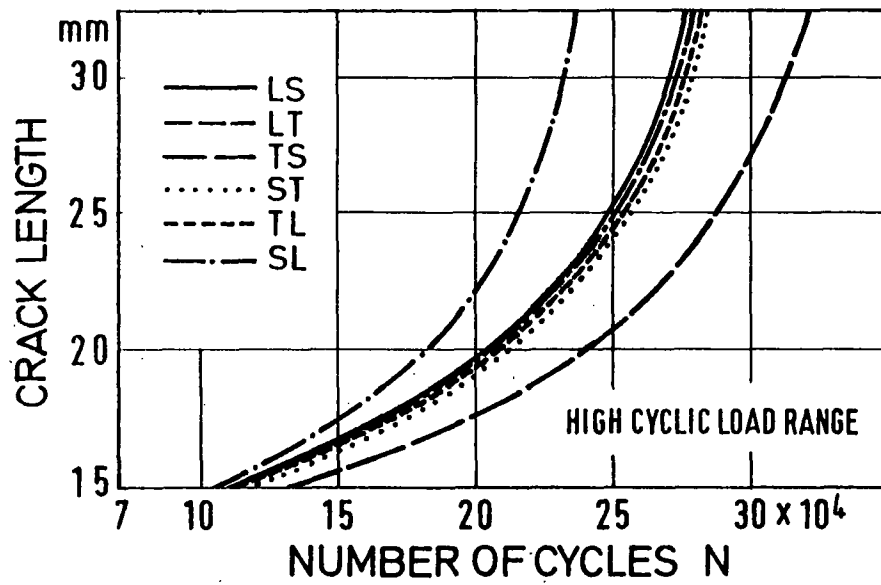


Fig. 4: Specimen orientations - plate I



a)



b)

Fig. 5: Crack growth curves of plate I

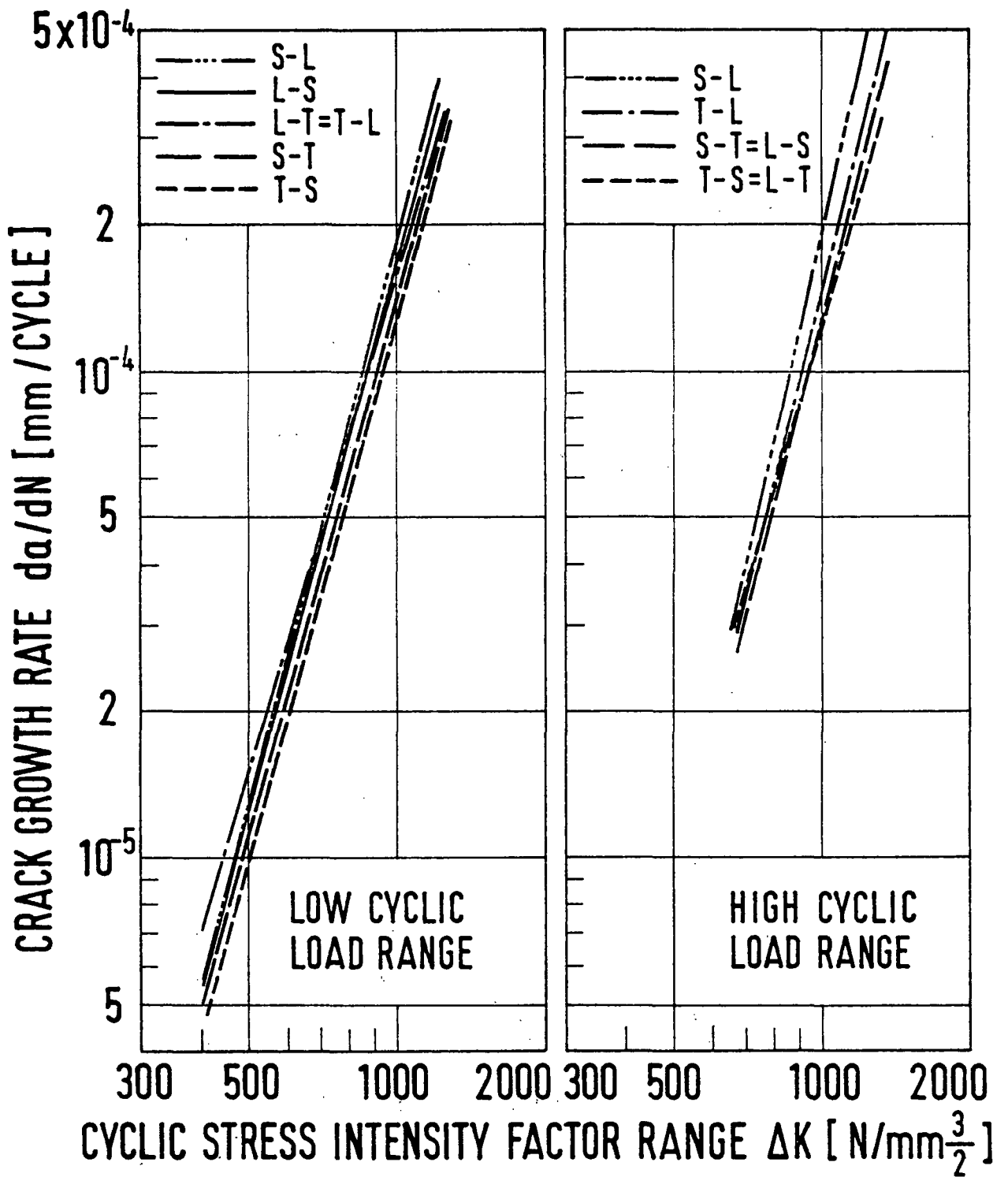


Fig. 6: da/dN - ΔK relations for each specimen of plate I

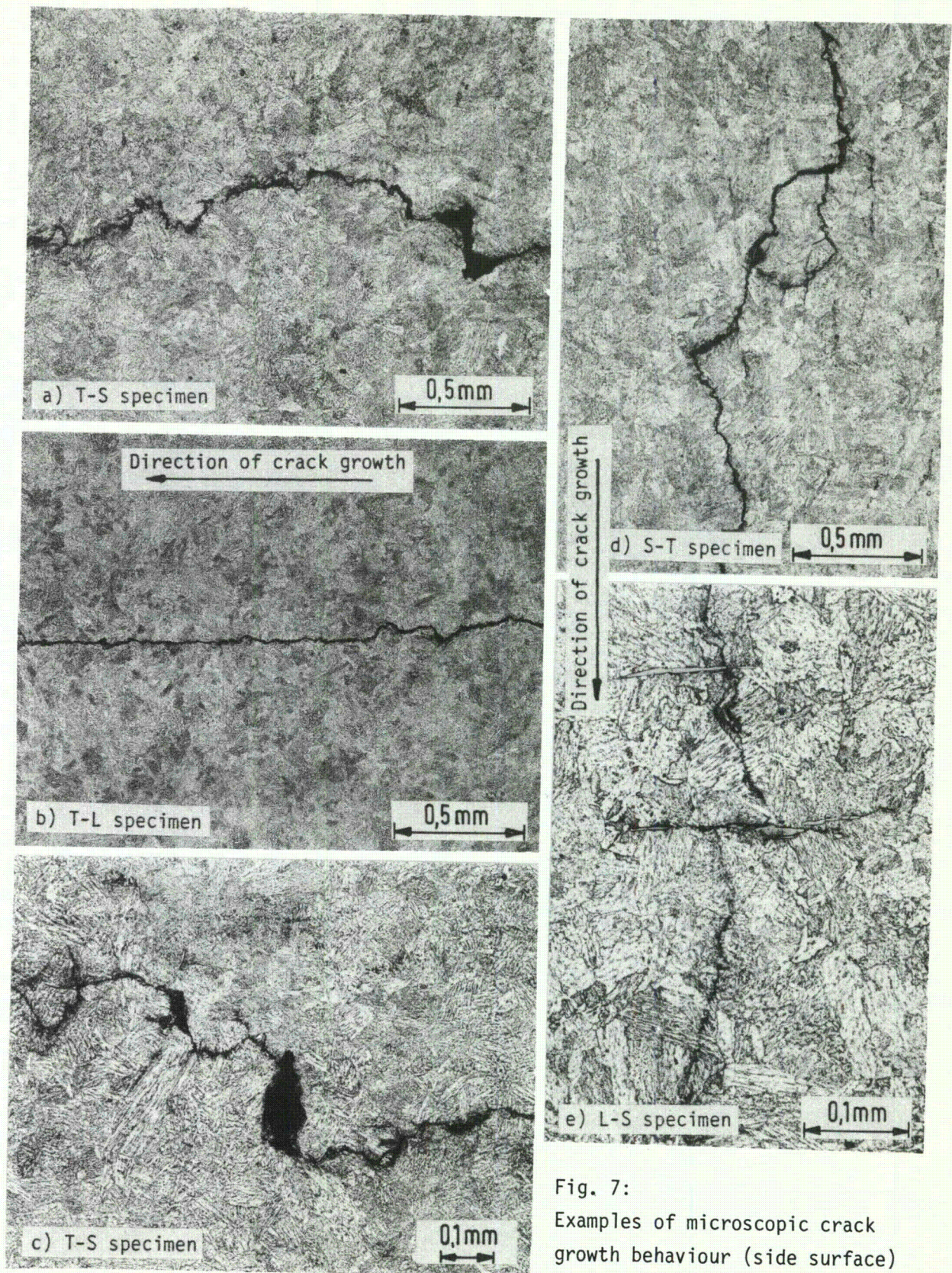


Fig. 7:
 Examples of microscopic crack
 growth behaviour (side surface)
 - plate I

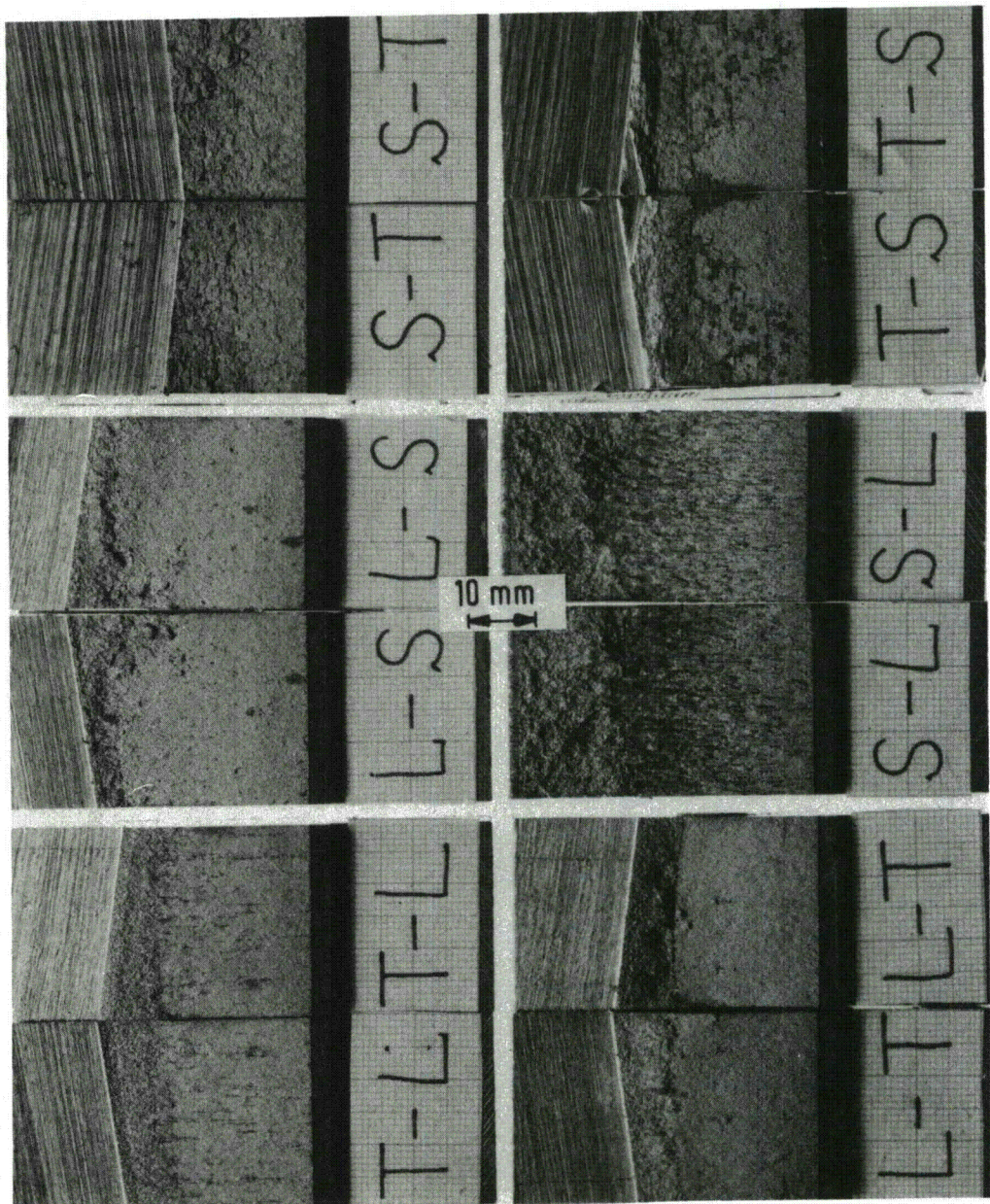


Fig. 8: Macroscopic appearances of the fracture faces of plate I

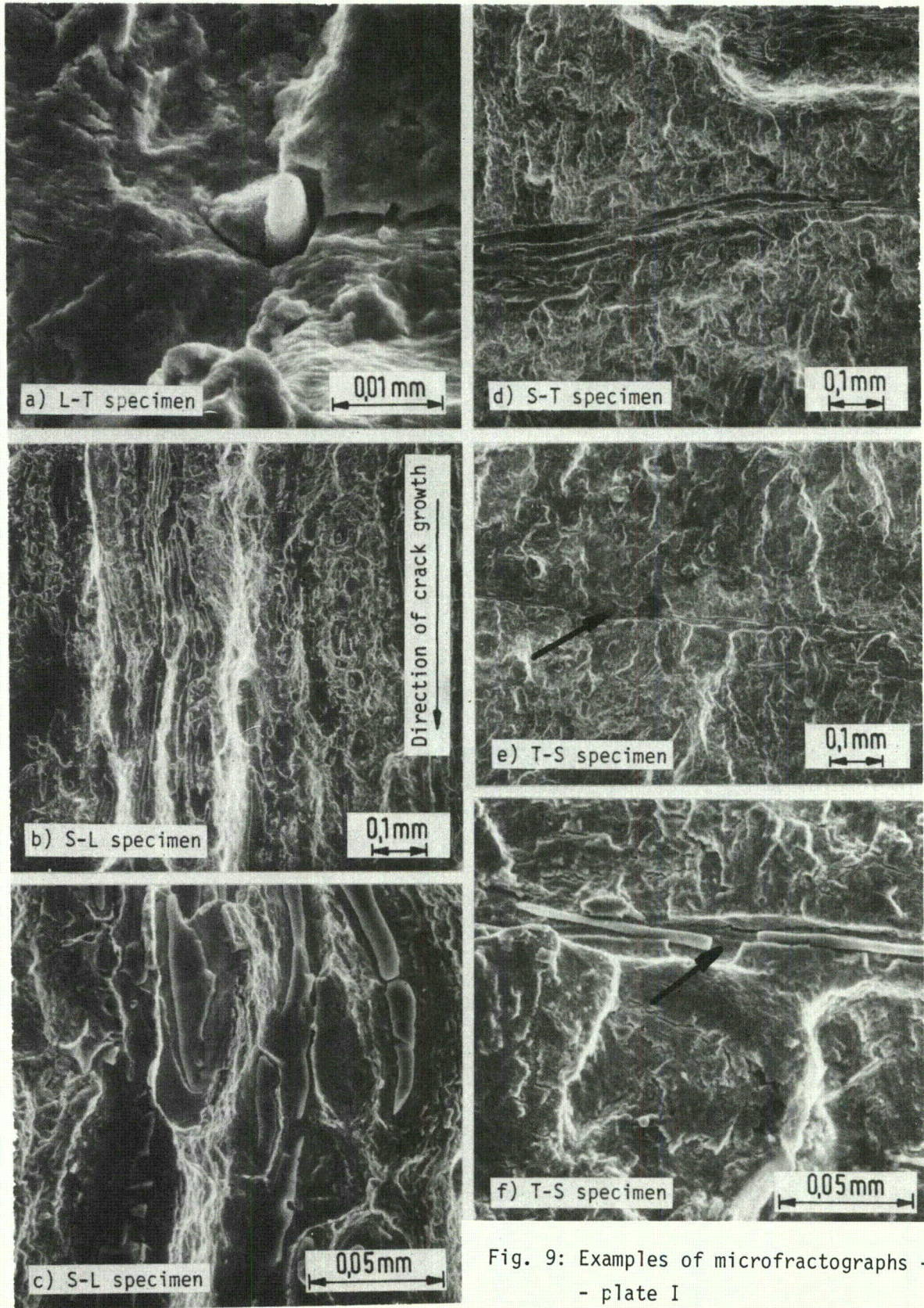


Fig. 9: Examples of microfractographs -
- plate I

Table 3: Mechanical properties at room temperature - plate II

Orientation	$R_{p0,2}$ [N/mm ²]	R_m [N/mm ²]	A_5 [%]	Z [%]
T	546	700	18	52
T	558	712	18	46
L	548	703	23	70
L	548	705	22	70

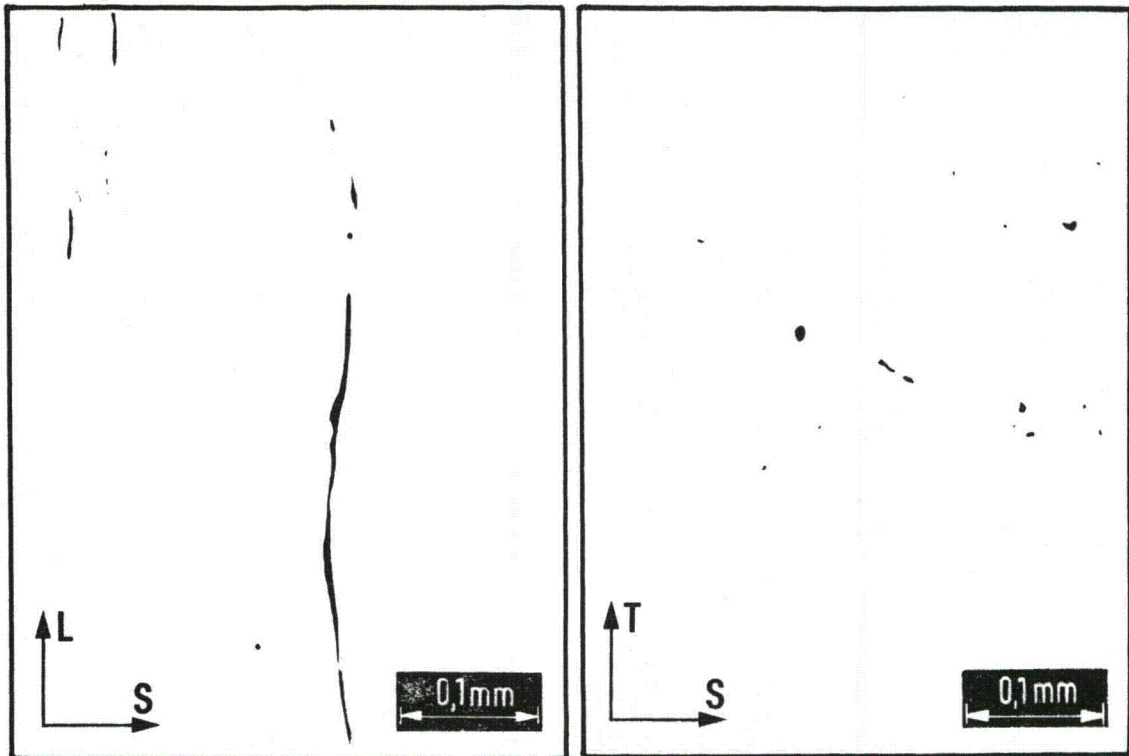


Fig. 10: Needle-like MnS inclusions in two reference planes of plate II

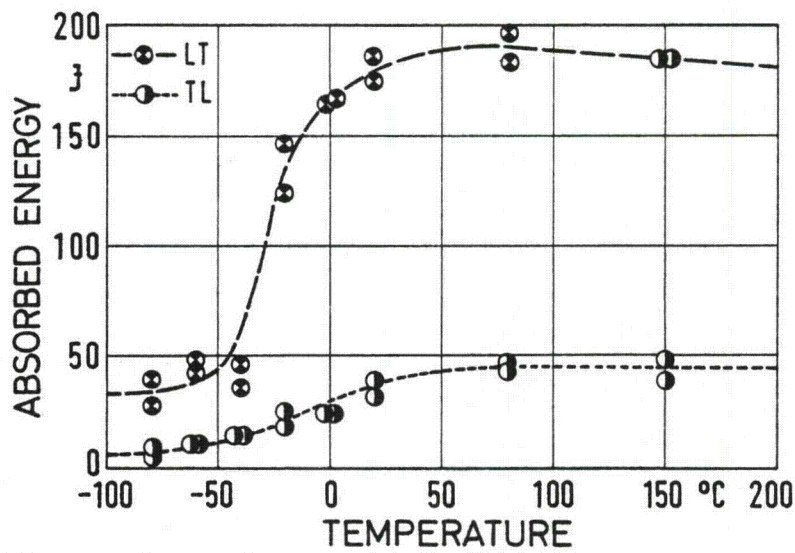


Fig. 11: Charpy impact tests - plate II

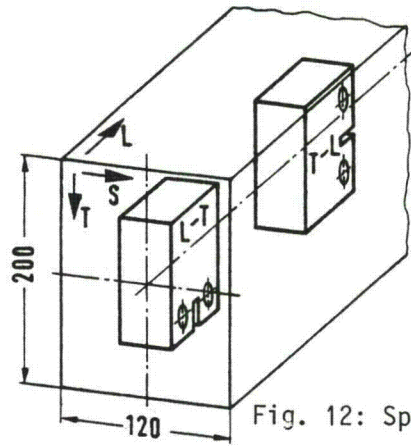


Fig. 12: Specimen orientations - plate II

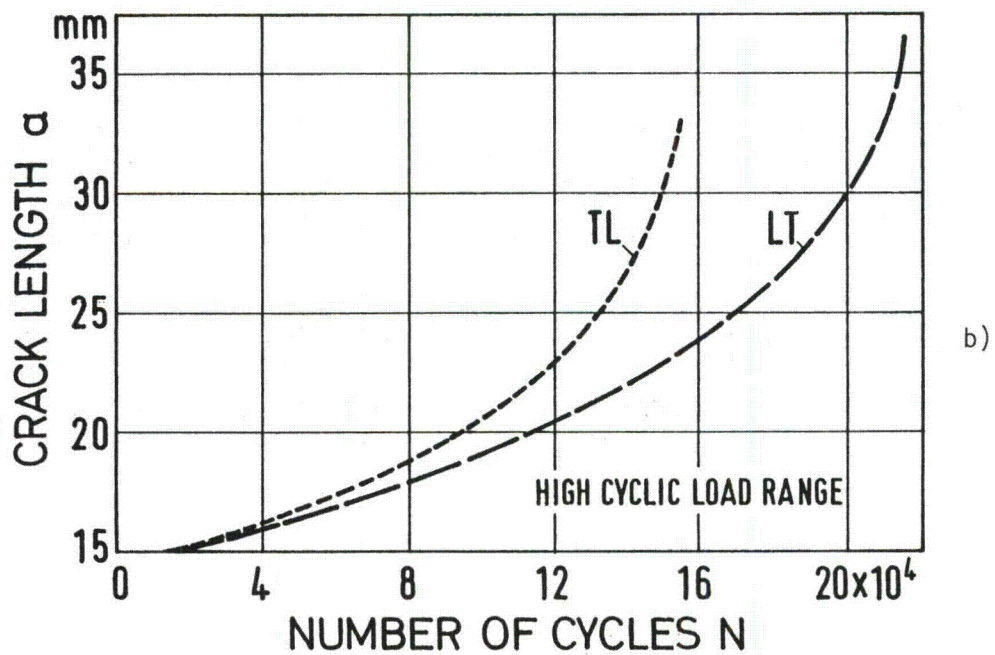
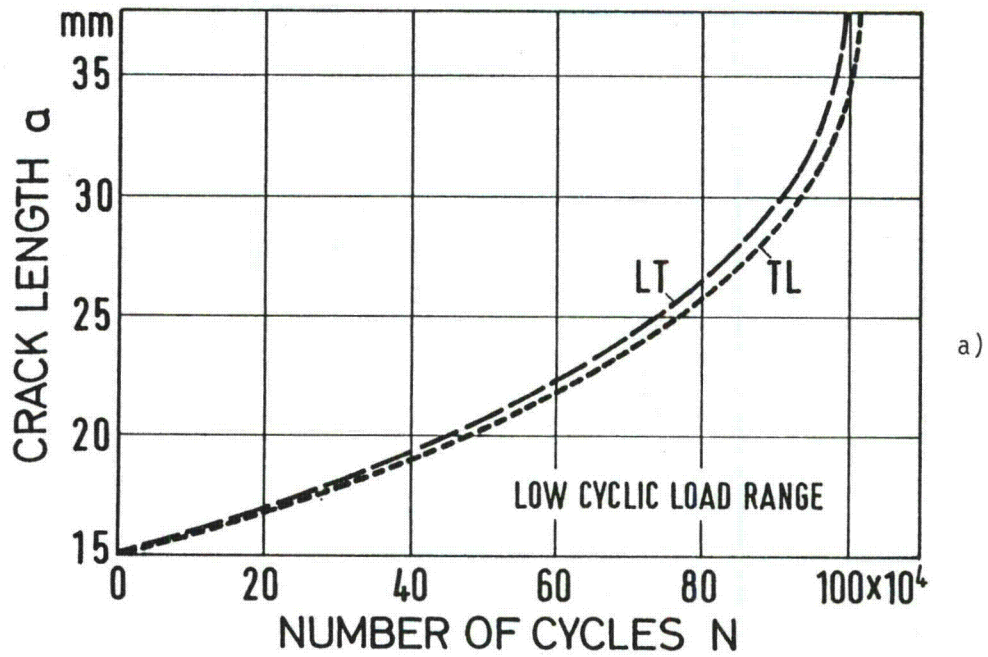


Fig. 13: Crack growth curves of plate II

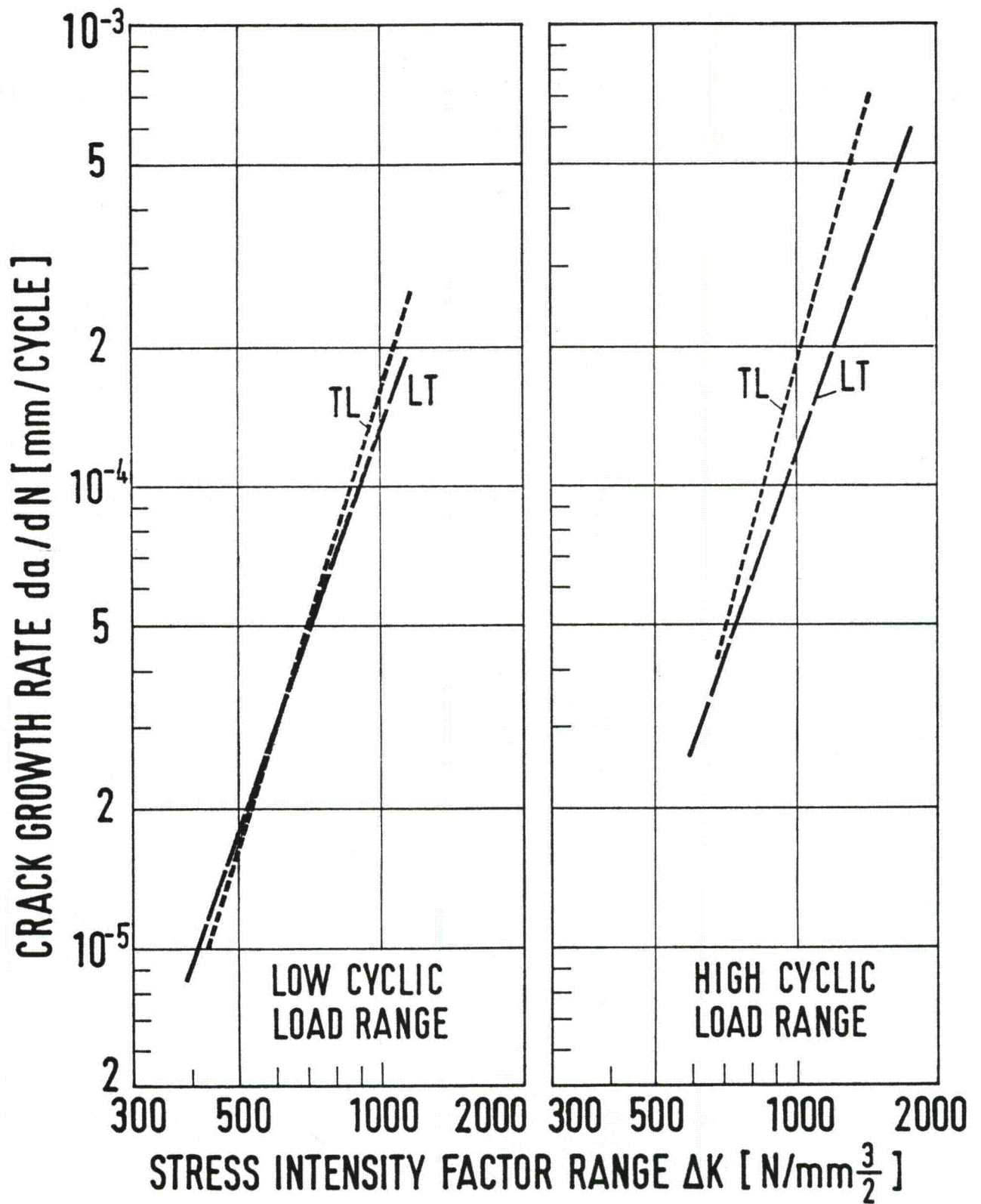


Fig. 14: da/dN- ΔK relations for each specimen of plate II

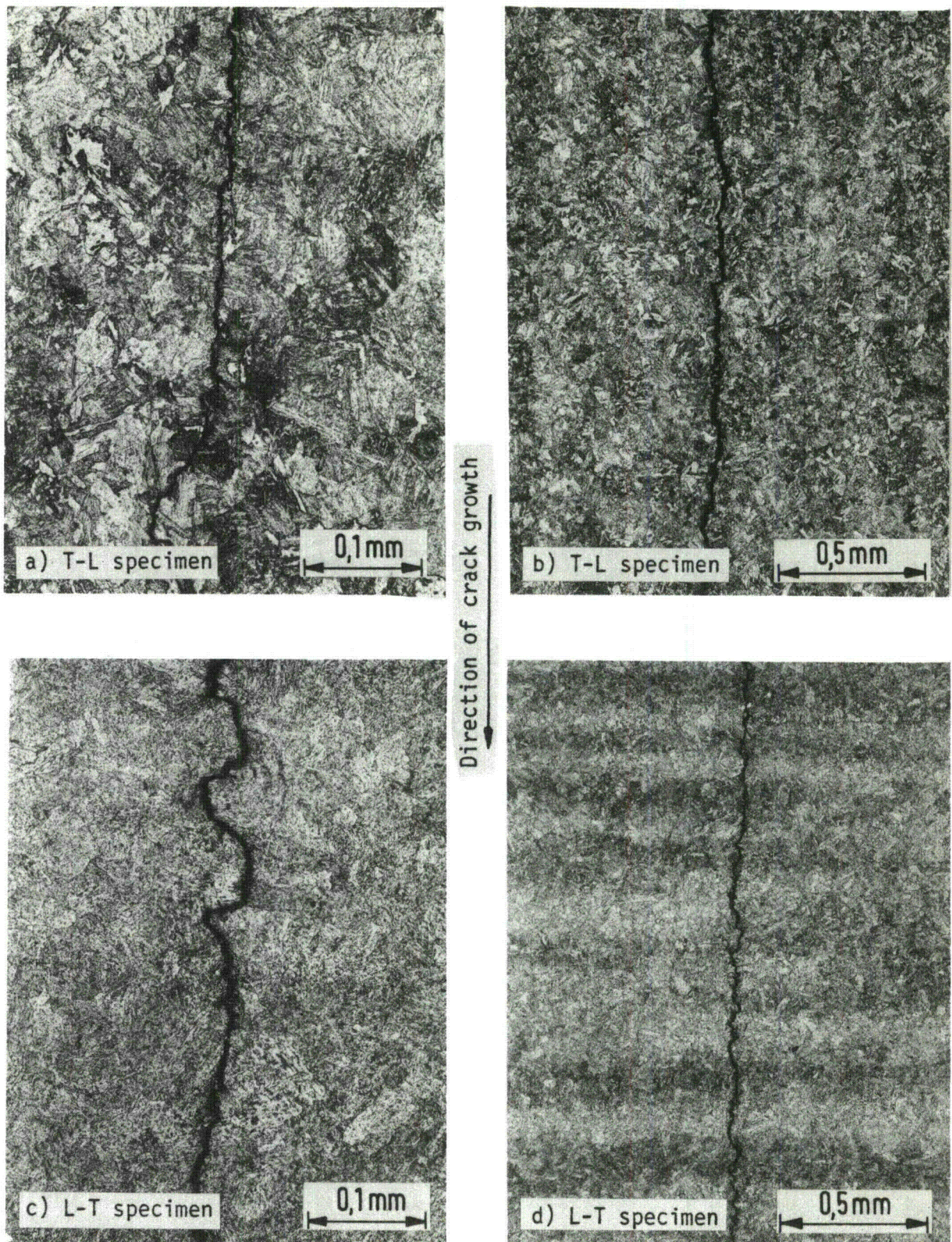


Fig. 15: Examples of microscopic crack growth behaviour (side surface) - plate II

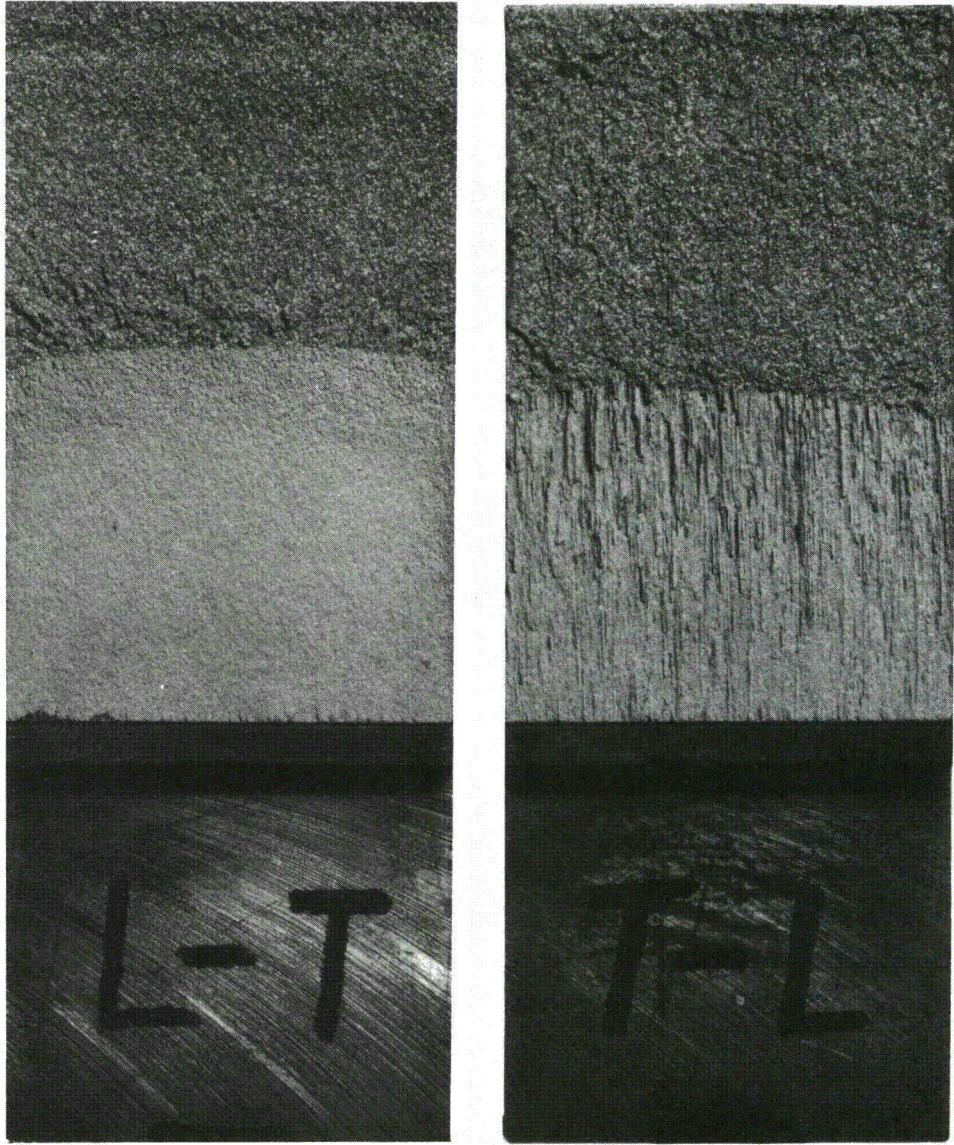
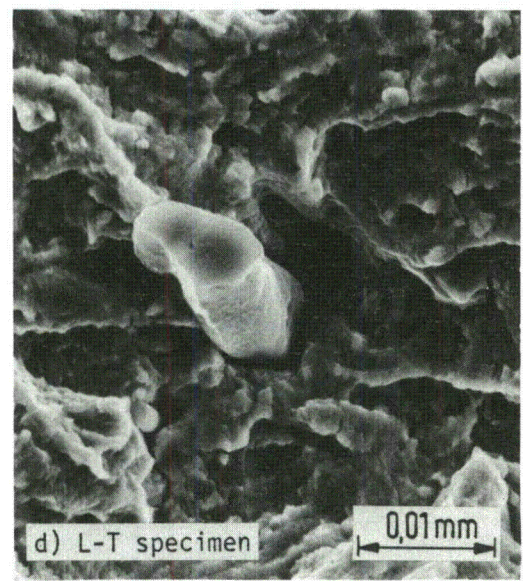
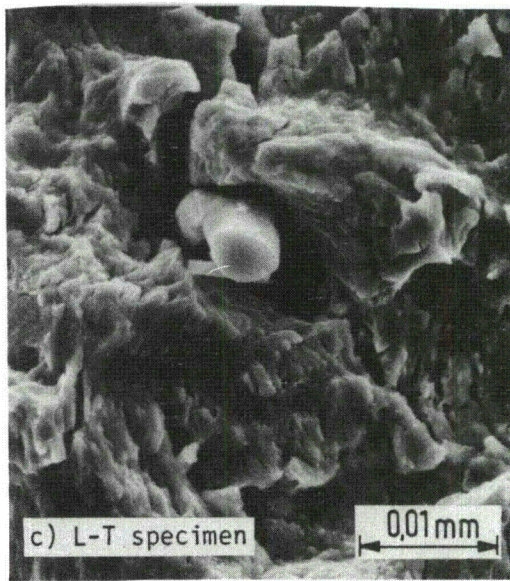
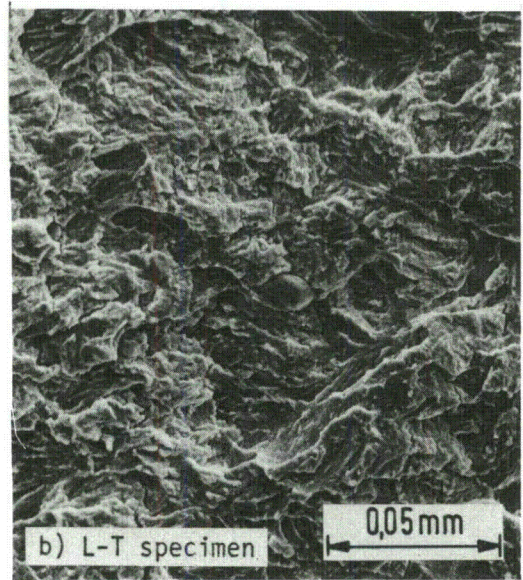
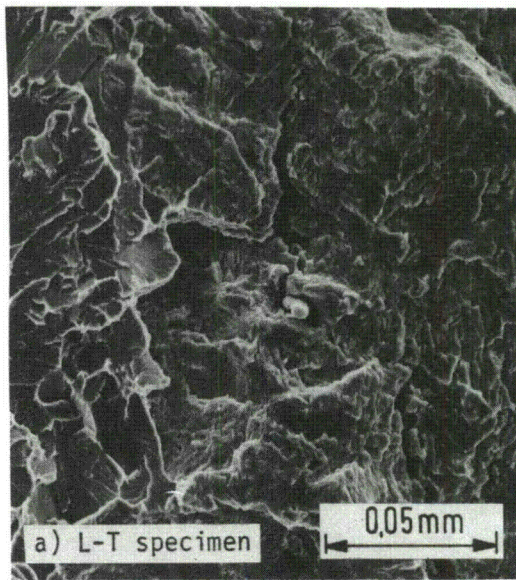


Fig. 16: Macroscopic appearances of the fracture faces of plate II

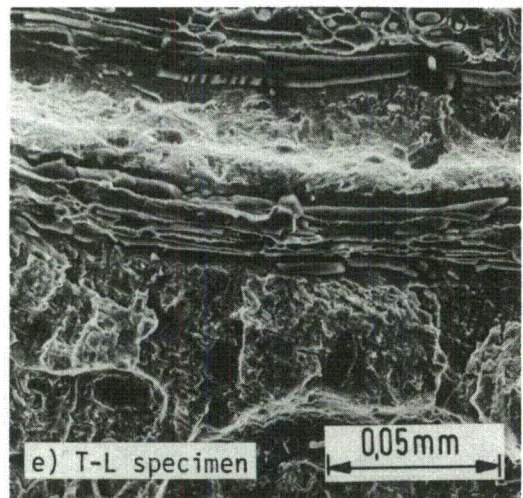


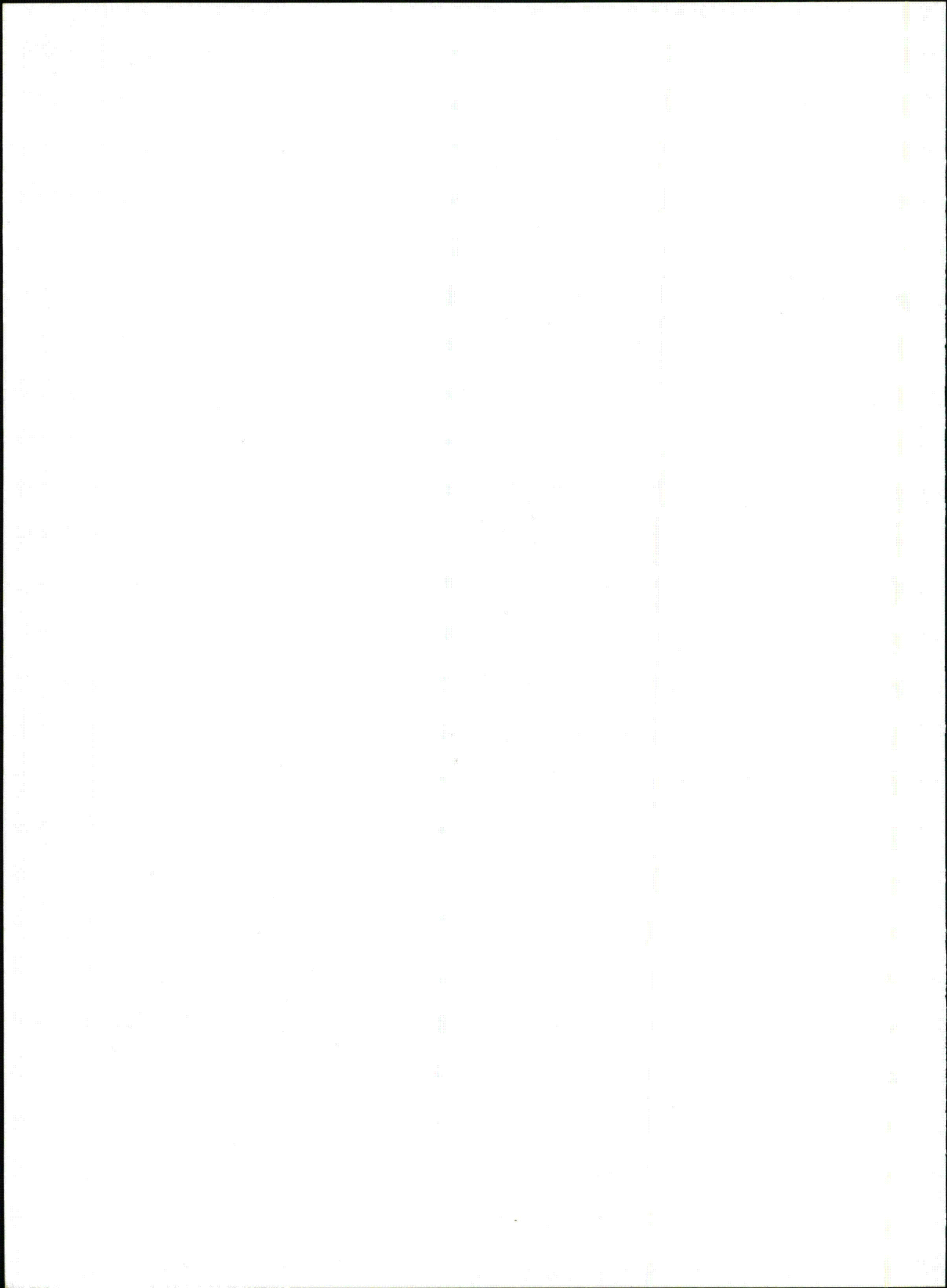
Direction of crack growth
 ←

Fig. 17:

Examples of microfractographs
 - plate II

- a) + b): $\Delta K = 1500 \frac{N}{mm^{3/2}}$ } L-T
 c) + d): $\Delta K = 700 \frac{N}{mm^{3/2}}$ }
 e): $\Delta K = 900 \frac{N}{mm^{3/2}}$ T-L





SOME THOUGHTS ON ESTABLISHING DESIGN
AND INSPECTION CODES FOR CORROSION
FATIGUE

P M Scott and B Tomkins

ABSTRACT

Incorporating any time dependent failure process into codes for practising engineers is a much more difficult process than for those failure processes where time is unimportant. Ideally, a mechanistic understanding is required so that any extrapolation to plant conditions beyond those tested in the laboratory can be justified with some confidence.

Corrosion fatigue crack initiation and crack propagation is one such potential failure mechanism for pressure vessel steels exposed to typical LWR aqueous environments. There are, apparently, a multitude of influencing variables, and only a limited understanding exists of the mechanism and of any limits to the rates of corrosion fatigue crack nucleation and growth.

In this paper, we consider how existing ASME codes, which explicitly or implicitly include quantitative procedures for estimating corrosion fatigue lives, may be improved on the basis of our current understanding of mechanisms. The requirements for safe and relatively simple calculation methods are discussed and the demarcation between scientific certainty and engineering judgement highlighted.

SOME THOUGHTS ON ESTABLISHING DESIGN AND INSPECTION CODES
FOR CORROSION FATIGUE

B Tomkins	and	P M Scott
UKAEA		UKAEA
SNL		AERE
Springfields		Harwell

CURRENT CODES FOR FATIGUE

Design rules for fatigue in engineering components and structures (e.g. pressure vessels - BS 5500, ASME III; bridges - BS 5400) are based on stress/strain-failure (S-N, ϵ -N) curves linked to stress analysis which defines a local 'field' stress for failure. The S-N curves can be related to basic material behaviour or some generic component feature (e.g. a weldment) but they are derived by testing at relatively high frequencies in order to generate the whole fatigue relationship on a reasonable timescale. The more recent development of in-service inspection schedules (e.g. ASME XI App A) linked to a fracture mechanics analysis is forming the basis of defect tolerant assessment procedures. This could eventually be incorporated into the design phase and lead to rules based on fatigue crack development. The key materials input, equivalent to the S-N curve, is then the relationship between crack growth rate, da/dN and some crack characterising parameter (e.g. ΔK). Again this relationship is generated by high frequency testing. but on pre-cracked rather than smooth specimens.

Judgment must be used to determine a factor on the baseline fatigue data to provide a safe design curve. In ASME III a factor of 2 on mean strain range or 20 on mean fatigue life (failure) is applied and BS 5500 uses a factor of similar magnitude. Both use plain specimen tests to provide the baseline data. The ASME III curve is shown in Fig. 1. The design factor is intended to cover effects of size, data scatter and environment. Pressure cycling tests at moderately high frequency on model pressure vessels were also performed to provide confidence in the factors chosen. In the UK, the new Bridge code (BS 5400) use fatigue tests on a range of welded joints to provide baseline fatigue data and recommended design curves are based on a lower limit -2σ fit to the baseline data. This covers data scatter statistically and further design factors can be used as deemed appropriate taking account of structural redundancy. In ASME XI App A, the crack growth curve recommended for use in assessment is shown in Fig. 2. This is a simple upper bound to dry crack growth data. A factor on allowable crack size related to fracture toughness is assumed to cover any further uncertainty in fatigue crack growth rate behaviour.

Although environment is mentioned as an uncertainty covered in the ASME III design factor, it is now recognised that in some circumstances the factor could be inadequate in this regard. When the rules were first defined, no endurance data existed for the ferritic steels concerned tested in reactor water at frequencies and strain rates relevant to plant operation. Some

recent limited GE endurance data on A-516 carbon steel in a BWR environment is shown in Fig 1, but it is in the crack growth area that strong reactor water environment effects have been observed (Fig 2). The problem now recognised is that, because it is impossible to perform endurance tests in real time at plant strain/stress range levels, a relevant data base cannot be obtained if significant deterioration of fatigue properties occurs over a timescale of the order of plant operating life. A similar problem has arisen in the extension of the ASME III code to elevated temperature operation (Code Case N-47) where creep effects can seriously erode fatigue endurance. Fig 3 shows data on Type 316 stainless steel typical of that used to define the data base for design curves for high temperature fatigue in the range 540-650°C. The design curve uses the 2 and 20 factors on an effective lower bound fit to the data. However, the data has of necessity been derived from short term tests (over a few thousand hours) at high strain levels. The extrapolation procedures used to enable a curve to be estimated at plant strain levels are very uncertain. The influence of an interaction between fatigue and some other time dependent failure process such as corrosion or creep is to broaden considerably the data base (Figs 2,3) to such an extent that doubt is thrown on current design factors to contain it. This does not necessarily mean that the factors are inadequate at operating strain levels, but it is not possible to generate endurance data at such levels and judgment on factors must be made. It is clear that mechanistic understanding of the failure processes and their interaction must form a basis for confidence in factors chosen.

Crack growth studies are a means of experimentally exploring a portion of life in real time at relevant levels of strain/stress provided the basic failure process is by crack growth. Although they are limited by testing techniques available, along with mechanistic studies they offer a route to increased confidence in design factors. Tests alone can provide data relevant to only the specific test conditions and clearly it is impossible to cover the whole range of service conditions. What are the bounds to corrosion fatigue data such as that shown in Fig 2 and how should it be used in the assessment of plant? Such questions have taxed the international research community in this area for several years. Two approaches have been used to date. The first is to take a simple upper bound to data available following the 'dry' curve approach. The second is to treat the data statistically because the interaction of corrosion and fatigue produces a broadening of data for testing under nominally the same conditions on the same material. This latter approach has been advocated in the new ASME XI Appendix A 'wet' crack growth curves. However, both approaches evade the central problem of the adequacy of the data base for plant assessment. The lowest test frequency of data used (1 cpm) is at the upper limit of strain rates experienced by plant transients and the highest R ratios tested (0.7) do not cover many plant circumstances. Statistics can only be applied to a clearly defined and relevant database, whilst bounding curves are of value only if they truly bound data relevant to all conditions under assessment. The authors have sympathy with the intention of the new ASME XI statistical approach but feel that limitations in the database inhibit its value at present. Mechanistic studies are, however, providing us with an insight into the controlling limits and rates of corrosion fatigue processes relevant to ferritic steels in LWR environments and current indications are that despite lack of data, judgments can be made on likely performance under plant operating conditions.

MECHANISTIC CONSIDERATIONS

The mechanisms of fatigue failure are now well understood following decades of intensive research. In metals, cracks initiate at free surfaces following the cyclic irreversible movement of dislocations. The fatigue limit and high cycle fatigue behaviour is dominated by crack initiation, the limit being often an effective cyclic yield point. The limited life region of the S-N or ϵ -N curve is dominated by crack propagation so that the well known empirical Coffin-Manson and Basquin laws are often simply integrated crack growth laws. Stresses in the high cycle region and below the fatigue limit are essentially elastic and crack growth under such stress cycles can be described in terms of the cyclic LEFM stress intensity factor (ΔK). Fig 4 shows a schematic plot of da/dN vs ΔK for stresses in this region. At all stress/strain levels, crack advance is accomplished by the same mechanism of local crack tip plasticity, which achieves a finite crack opening when a crack is loaded. Although overall boundary conditions may vary considerably, the crack tip opening (CTOD) provides an upper limit to crack growth rate in fatigue (cyclic CTOD in the case of positive R loading). In practice da/dN falls below this value in the power law portion of Fig 4. Apart from the high ΔK region where fast fracture is approached, the crack growth relationship shows a distinct level of ΔK (ΔK_{th}) below which cracks do not grow. This threshold decreases as R increases but it probably corresponds to a reversible crack opening condition where the cyclic CTOD is achieved by the shear mode II opening and is extremely small (say 0.01 μm). In this region local metallurgical structure strongly influences crack advance. The fact that the da/dN vs ΔK curve is essentially related to material continuum behaviour over most of its range means that there is relatively little scatter on data for a given material; certainly for ductile pressure vessel steels, provided that the environment is benign or only mildly oxidising. Mechanistic considerations would therefore support the use of simple upper bounds or mean curves through the data as a basis for code rules.

In the case of S-N curves, uncertainties on crack initiation make design factors always suspect in the high cycle region. In addition, if significant initial defects or cracks exist in critical regions, the design margins can be dramatically reduced throughout the fatigue range. Fig 5 shows the curves of Fig 1 together with an estimated failure curve based on crack growth studies for material with a 0.5 mm surface crack.

Stress corrosion studies have paralleled fatigue studies although, because of the wide variation in behaviour for different environment/metal systems, mechanistic understanding has been slower to emerge. However, in recent years significant advances have been made both in relation to dissolution controlled failure and hydrogen embrittlement. As with fatigue, stress corrosion has been examined by both failure tests on plain specimens, giving a stress (σ)/time to failure (t_f) relationship, and crack growth tests, giving a relationship between da/dt and K . (Fig 6) The σ - t_f relationship shows a need for plastic deformation in order to initiate cracks but, more importantly, continued deformation with time (i.e. time dependent plasticity or creep). As a result, the threshold stress for failure (σ_{th}) under static loading is of the order of the macroscopic yield stress. The da/dt vs K relationship is shown in Fig 6a and has two important features. Firstly, there is a growth area, which is largely independent of K and is at a relatively high rate in engineering terms (of order 10^6 - 10^{-9} m/s). This indicates a strict corrosion controlled crack advance

with the crack providing only a crack tip plastic strain with continuing strain rate. The maximum crack advance rate is then simply related to electrochemical material dissolution governed by Faraday's law. Such levels of crack extension rate are intolerable in engineering structures. This indicates the importance of the second feature namely the threshold or growth limit (K_{ISCC}) This seems to be associated with a crack tip strain rate limit ($\dot{\epsilon}$) or displacement rate limit ($\dot{\delta}$), below which passivation wins and crack advance by dissolution is impossible. This is a zero crack growth condition.

Corrosion fatigue presents a condition in which both limits and rates from stress corrosion cracking and fatigue can play a part in defining behaviour. The fatigue loading can set up plastic strain rate conditions over a wider range of applied stress than in static load stress corrosion cracking. This leads to a reduction in threshold stress (σ_{th}) and stress intensity factor (K_{ISCC}) for corrosion effects. Similarly corrosion can lead to surface attack (e.g. pitting) which can provide a stress concentrator for fatigue crack initiation in nominally plain specimens. This in turn reduces the fatigue limit dramatically. As far as crack growth is concerned, important parameters in corrosion fatigue are clearly the cyclic frequency which provides a dynamic strain rate and the R ratio. The latter effect is perhaps less obvious but R ratio determines maximum CTOD and hence access to the crack tip for the environment. In particular it appears that the transition from predominantly mode I to mode II crack opening (stage II to stage I in fatigue terms) is important. In stage I, access to the crack tip would be particularly difficult. The overall effect of process interaction is to broaden out the range of K (or ΔK) conditions over which corrosion influences can seriously influence rates of crack growth. In view of the high rates of static stress corrosion cracking which are possible under anodic dissolution control, corrosion fatigue gives cause for concern where such effects dominate. In corrosion fatigue there will also exist a broader cut off in terms of K for the transition from the threshold to this maximum rate condition. In fact, the simple dissolution rate may not be achieved but rather a plateau with a da/dt rate determined by cation solvation and transport at the crack tip. Fig 7 shows corrosion fatigue data where this is occurring. Clearly at very high crack growth rates the CTOD may exceed the plateau rate giving a reversion to fatigue dominated behaviour. Because fatigue naturally involves such small amounts of crack extension per cycle over most of the range, the presence of an aggressive environment can always be expected to influence growth rate over the whole fatigue range where access to the crack tip is achieved. This effect may be contained within the cyclic CTOD on mechanics grounds as this dictates the maximum advance by mechanics alone.

Fig 8 shows corrosion fatigue data from various tests on A533-B steel tested in simulated PWR water. In the figure the apparent plateau crack growth rate is plotted as a function of the estimated crack tip strain rate $\dot{\epsilon}$ (defined as $\dot{\delta} / \delta$). The data is consistent with a dissolution controlled strain rate sensitive process giving an upper limit to da/dt at high $\dot{\epsilon}$ and a threshold $\dot{\epsilon}$ below which no corrosion domination is possible. At intermediate $\dot{\epsilon}$ the plateau rate is an $(\dot{\epsilon})^{1/2}$ relationship consistent with cation transport as a rate determining electrochemical step in the crack tip region.

IMPLICATIONS FOR CODE RULES

If this interpretation of the corrosion fatigue process is correct it has considerable implications for code rules. For crack growth, the impor-

tance of frequency and R ratio in defining rates and thresholds means that data generated, which does not endorse plant operating conditions in this regard, cannot form a completely confident basis for assessment unless it shows an indication of the threshold $\dot{\epsilon}$. For A533-B in PWR water, this threshold seems to vary for tests in various laboratories, but there are indications that the worst data obtained gives an $\dot{\epsilon}$ of $\sim 10^{-2}/s$. If this could be confirmed, then even the high plateau rates obtained to date would not be relevant to most plant transients. Concern would arise if the $\dot{\epsilon}$ threshold dropped below $10^{-4}/s$. The $\dot{\epsilon}$ threshold and K threshold for environmental access can define an envelope within which corrosion fatigue crack growth rates lie in terms of a da/dN vs ΔK plot. This is shown in Fig 9 using the $\dot{\epsilon}$ threshold value of $10^{-2}/s$, and a K threshold of $28 \text{ MPa}\sqrt{\text{m}}$. The latter represents the stage I/stage II fatigue crack growth transition. It can be seen that the envelope lies somewhat outside of the existing data base used in the latest ASME XI rules. This indicates that it should be possible to obtain data outside the data base under combinations of R ratio and frequency other than those used in tests to date. However such combinations would also lie outside nominal and upset plant operating conditions.

Our view of the current ASME XI 'wet' crack growth rules is that they are of limited value in assessing corrosion fatigue crack growth in PWR steels. Effort should be focussed in obtaining clear limits to the process i.e. mechanistically based bounds. This will involve experiments outside the scope of current programmes but it is important to obtain data more relevant to the plant. Current indications are that this will alleviate rather than exacerbate the problem. It is likely that for future development the code should look to expressing information in terms of limits and rates rather than da/dN vs ΔK terms.

As far as design is concerned, we feel that the ASME III code factors should be examined in relation to both time dependent crack initiation and level of initial surface defect tolerance. The latter area is probably covered by current fabrication routes and pre-service inspection schedules which do not allow surface breaking defects. The environmental initiation area is a concern if ferritic material is exposed to the environment above the pitting potential. In general practice this should not be the case. However, an appraisal of the 2 and 20 factors in terms of general defect and stress concentration tolerance is desirable.

8 June 1981

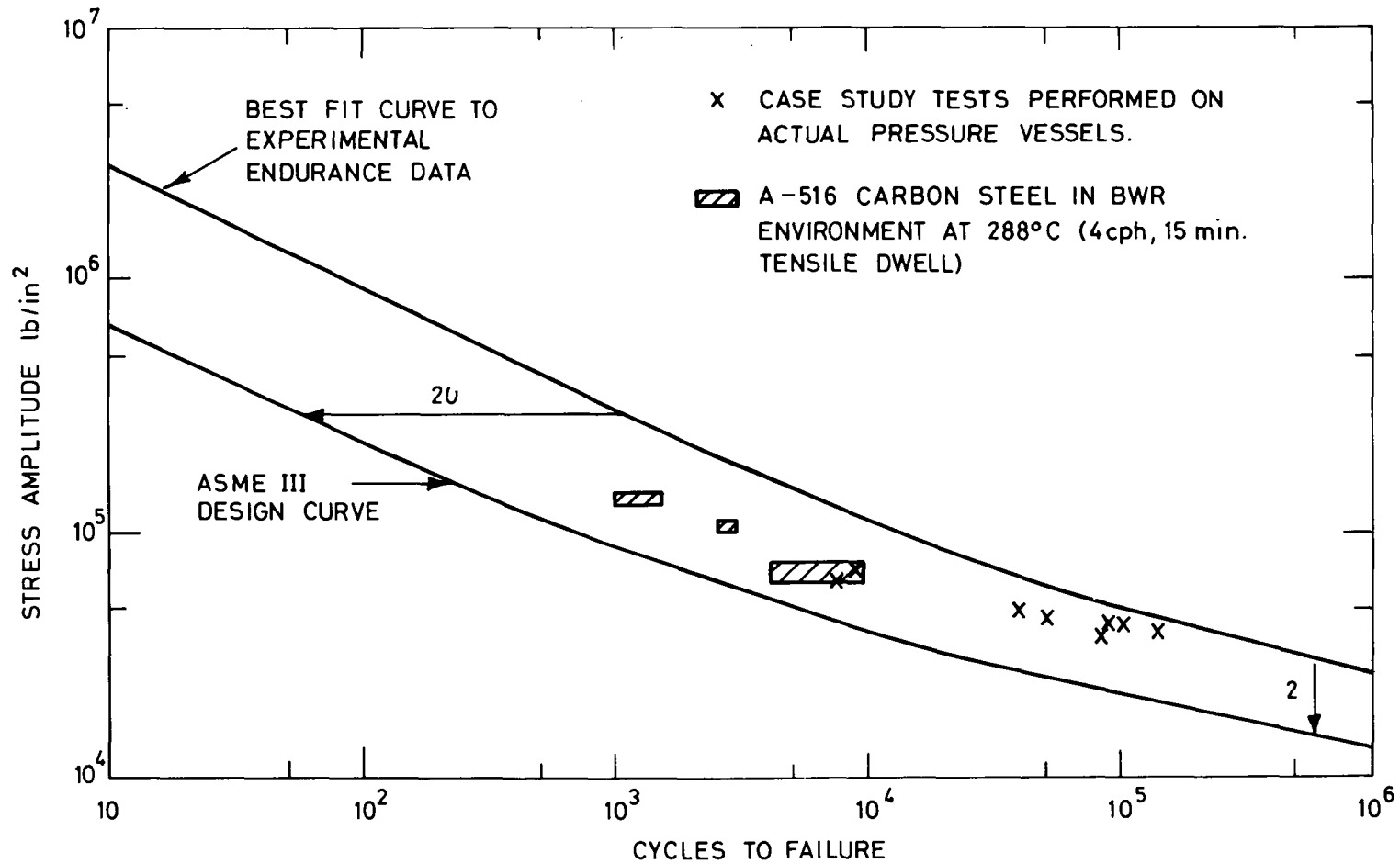


FIG.1. ASME III DESIGN CURVE AND MEAN MATERIALS DATA CURVE FOR PRESSURE VESSELS.

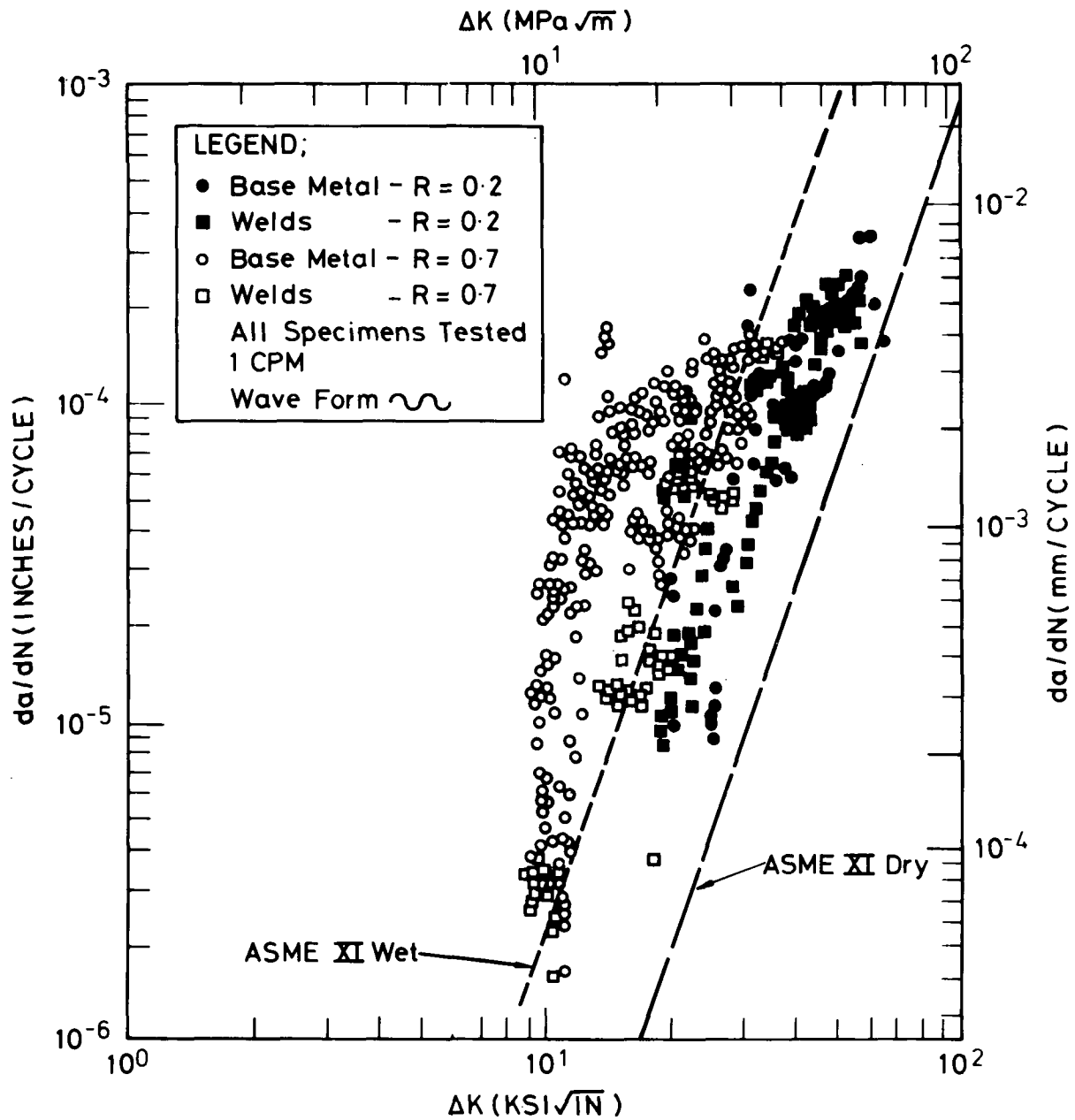


FIG. 2. CORROSION FATIGUE DATA FROM WESTINGHOUSE FOR A533-B-1 AND A508-2 BASE METALS AND WELDMENTS IN PWR PRIMARY WATER WITH ASME XI APPENDIX A LINE FOR FATIGUE CRACK GROWTH IN A DRY ENVIRONMENT.

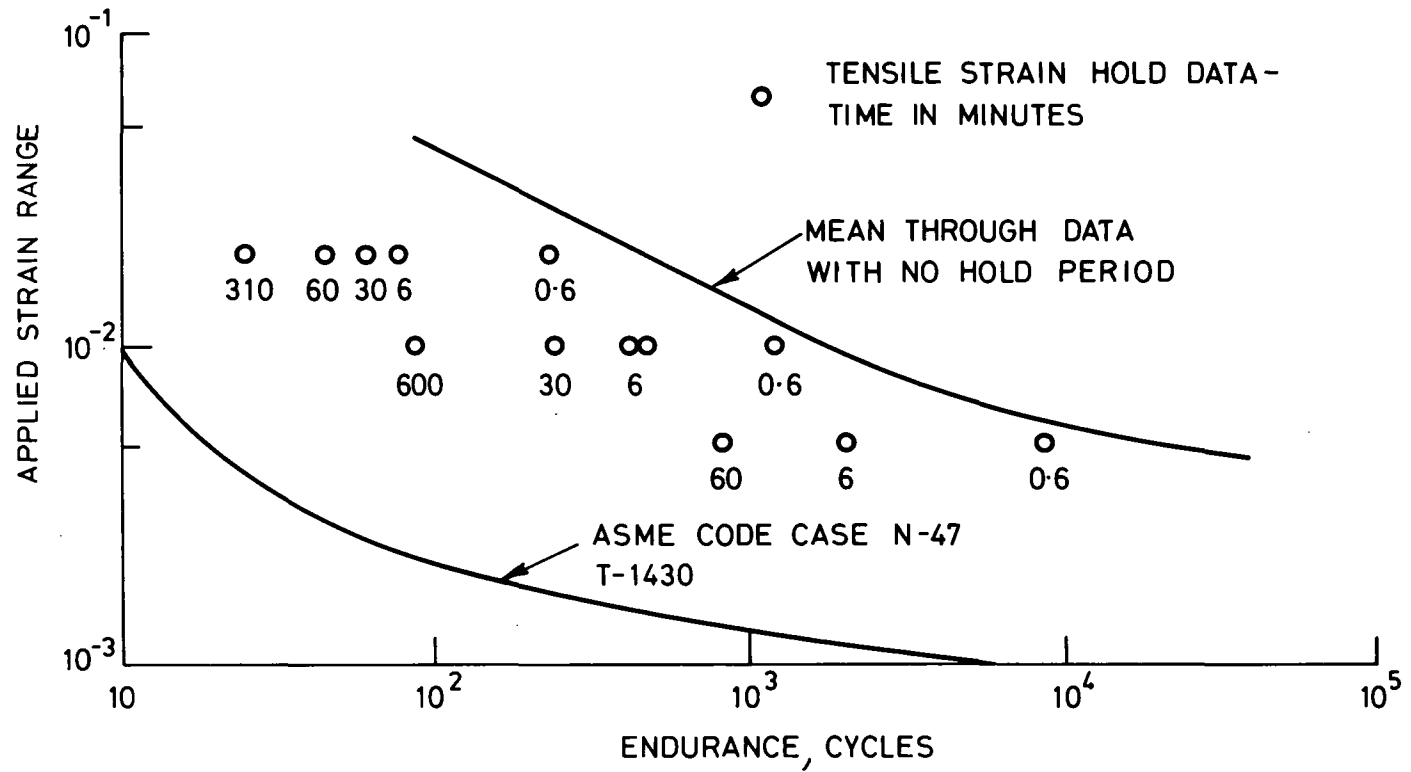


FIG.3. ASME CODE CASE N-47 DESIGN CURVE FOR CREEP-FATIGUE WITH TYPICAL TENSILE HOLD PERIOD STRAIN CYCLING DATA FOR TYPE 316 STAINLESS STEEL AT 593°C

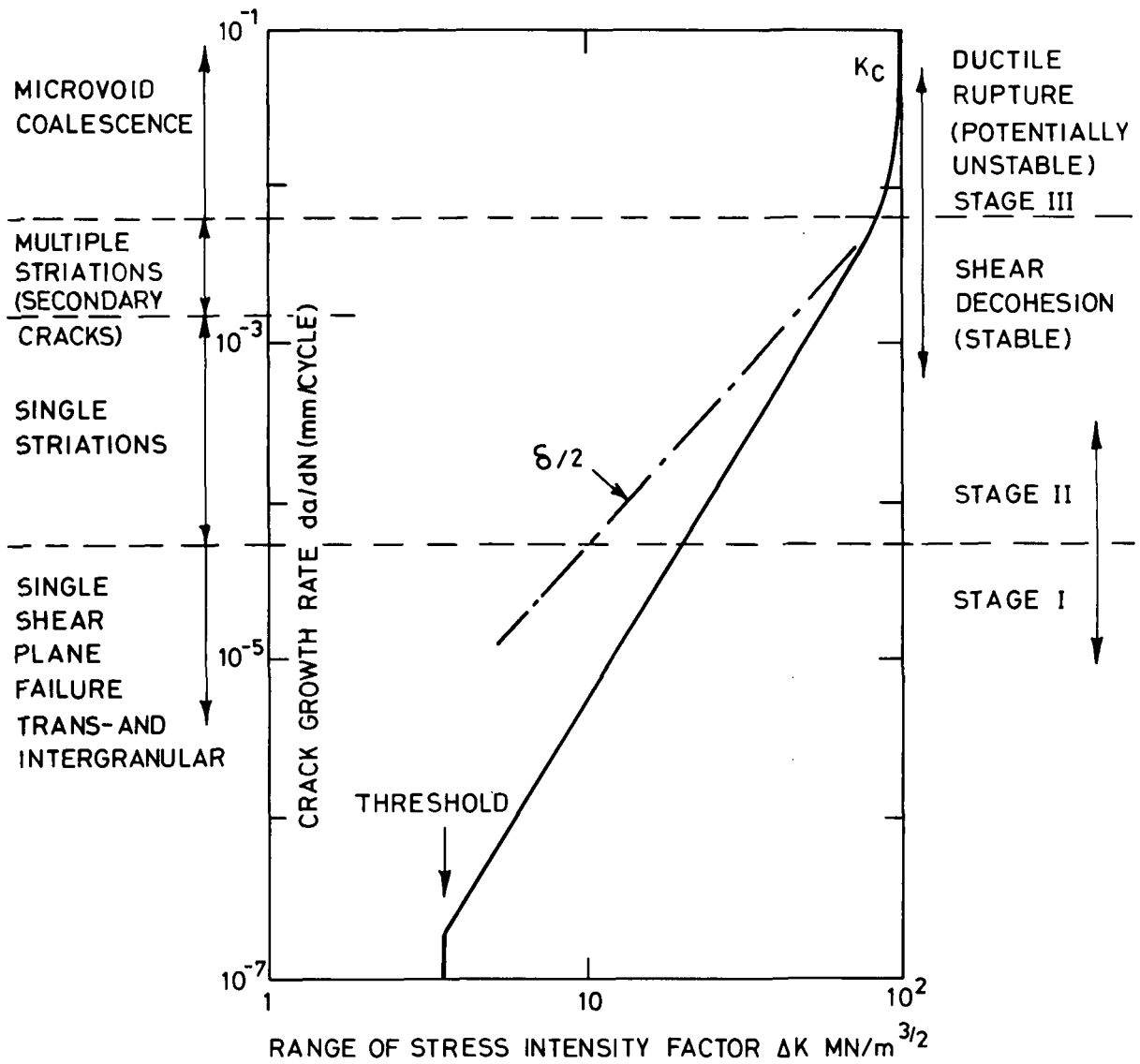


FIG.4. FEATURES OF A FATIGUE CRACK GROWTH CURVE

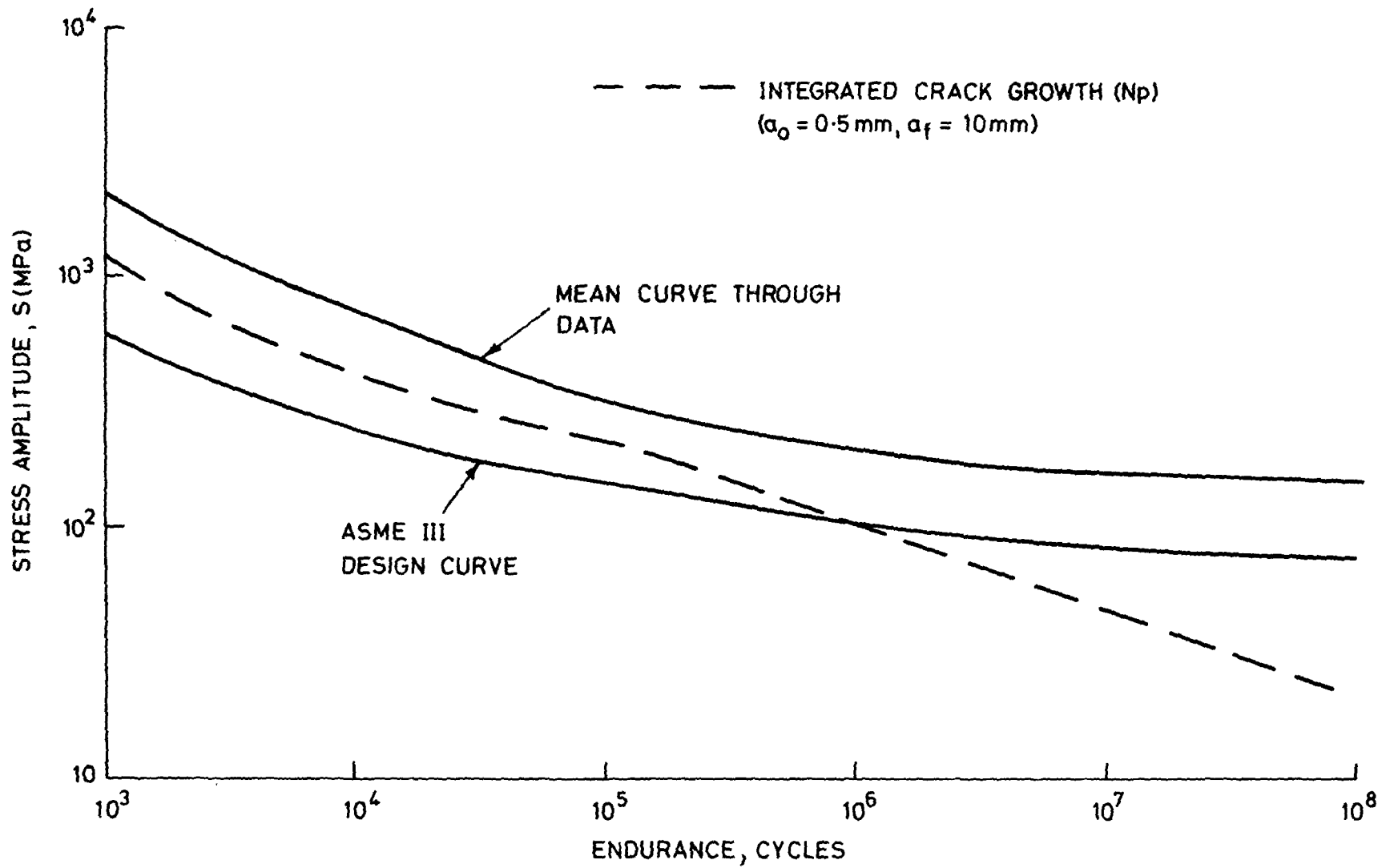


FIG.5. COMPARISON OF INTEGRATED CRACK GROWTH CURVE ($a_0 = 0.5 \text{ mm}$) WITH ASME III DATA AND DESIGN CURVES.

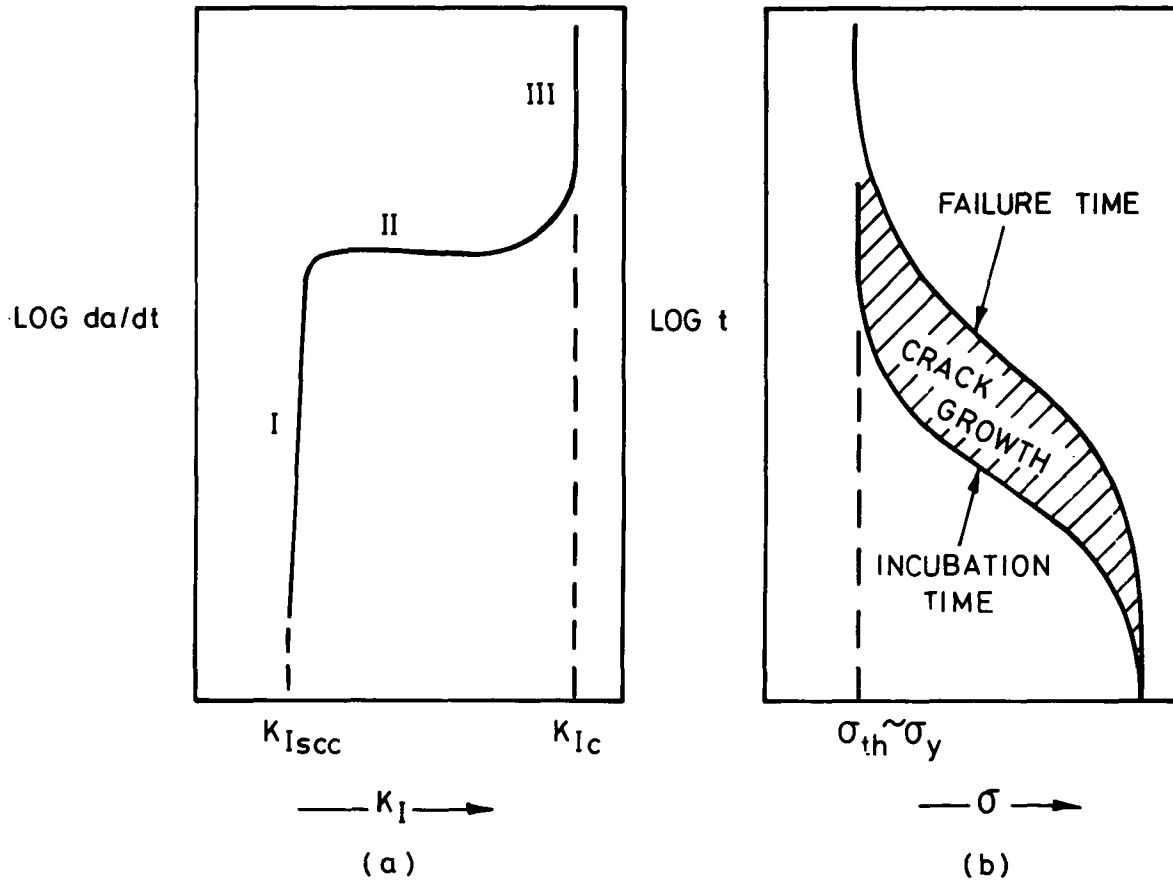


FIG.6. SCHEMATIC REPRESENTATION OF THE CRACK GROWTH KINETICS AND TIME TO FAILURE UNDER SUSTAINED LOADS IN AN AQUEOUS ENVIRONMENT.

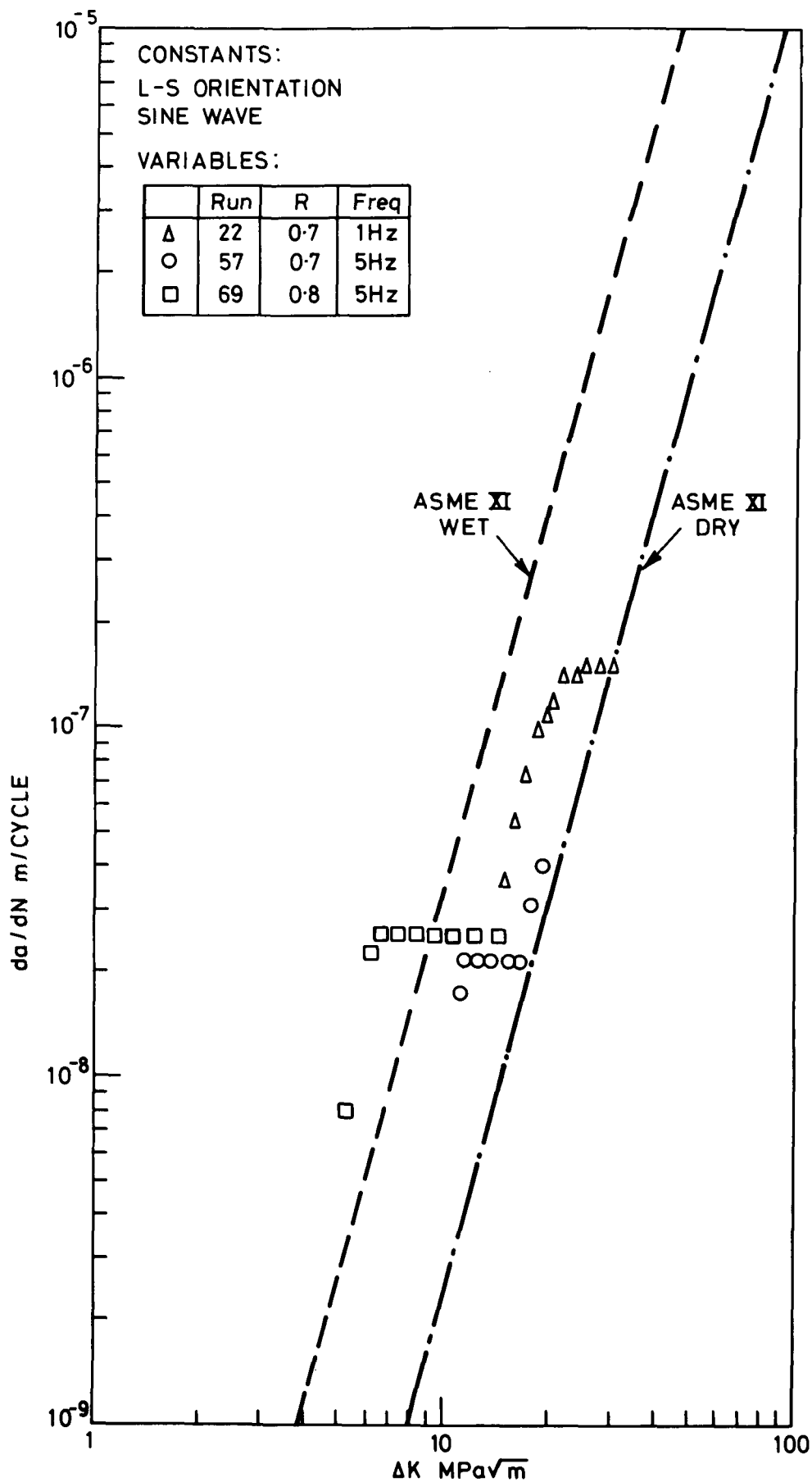


FIG.7. INFLUENCE OF R RATIO & FREQUENCY ON CRACK PROPAGATION RATES IN A533-B STEEL IN PWR WATER AT 288°C.

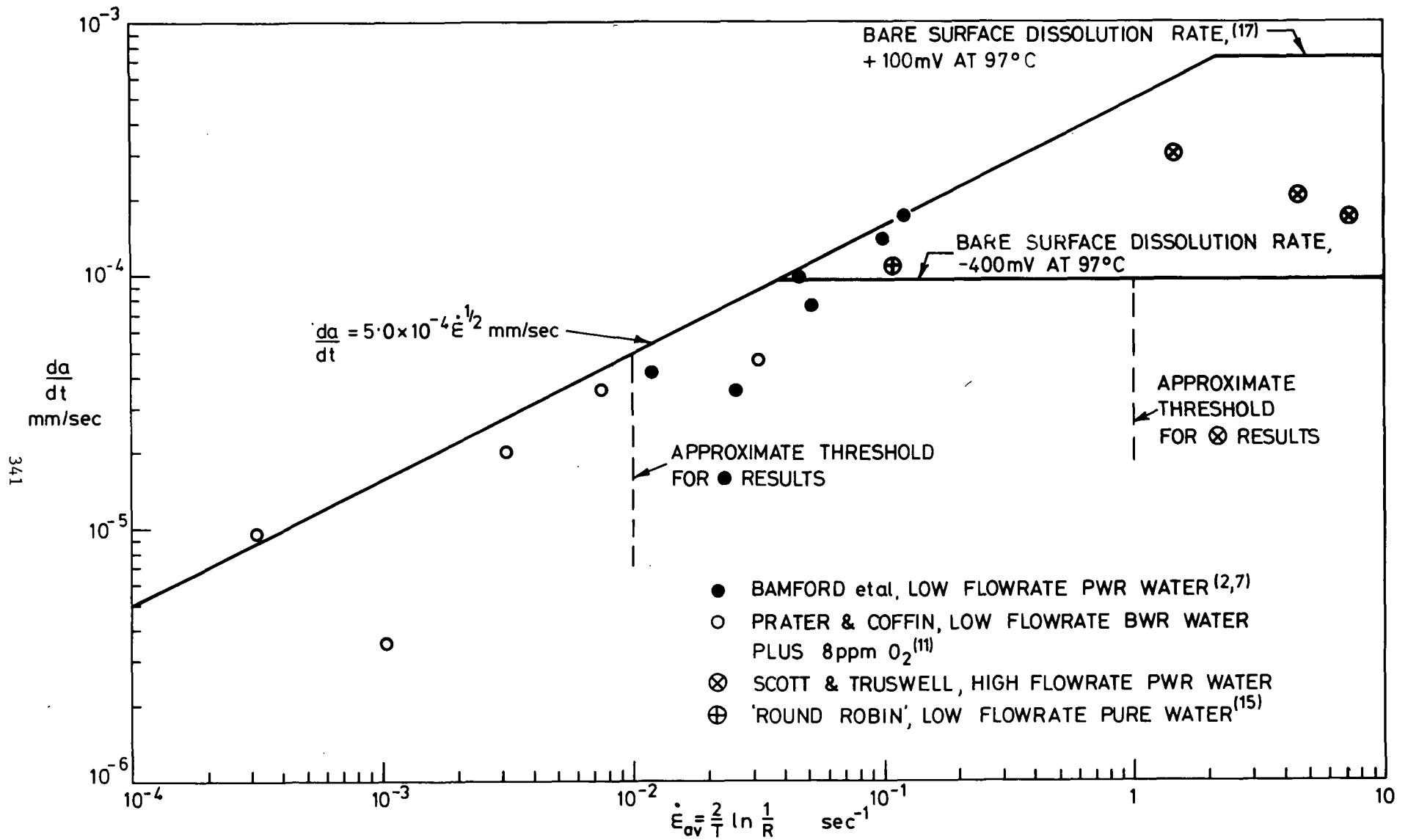


FIG. 8. 'PLATEAU' RATES OF CRACK GROWTH AS A FUNCTION OF CRACK TIP STRAIN RATE

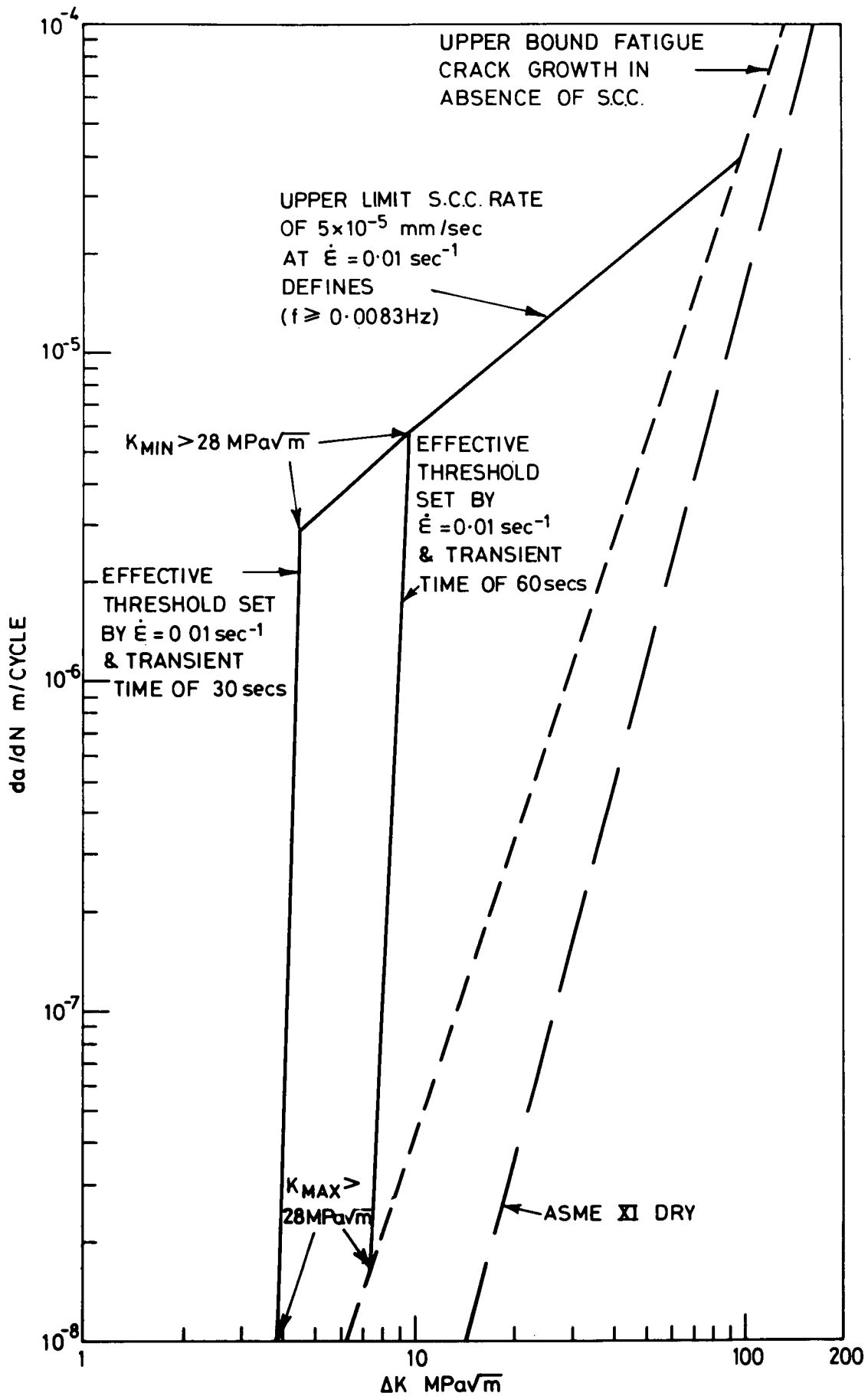


FIG. 9. CALCULATED ENVELOPE FOR CORROSION FATIGUE CRACK GROWTH INCLUDING STRAIN RATE SENSITIVE STRESS CORROSION CRACKING. 342

AUTHOR Prater, TA Coffin, LF	SUBJECT corrosion fatigue, fatigue in notches, fatigue design	NO. 81CRD013
		DATE February 1981
TITLE The Use of Notched Compact Tension Tests for Crack Initiation Design Rules in High-Temperature Water Environments		GE CLASS 1
		NO. PAGES 11
ORIGINATING COMPONENT Metallurgy Laboratory		CORPORATE RESEARCH AND DEVELOPMENT SCHENECTADY, N. Y.
SUMMARY <p>This report describes the techniques used and results obtained for fatigue crack initiation of notched compact tension (CT) tests of SA333 Gr.6 carbon steel in air or in autoclaves mostly at 550 °F, 1500 psi oxygenated water conditions. The fatigue crack initiation life N_i was quantitatively determined from a cycle-by-cycle crack length measurement as the number of cycles to produce 0.003 in. of growth from the notch root. Results for several parameters of the experimental program (including temperature, environment, oxygen content, frequency of cycling, notch radius, R-value, and ΔK) are reported. A majority of the tests were run in 550 °F water at 8 ppm O_2 with 0.002-in. notch radii, and showed a severe degradation in initiation life especially at low frequencies (0.0125 cpm) in comparison to 550 °F air tests. On the other hand, at 1.25 cpm and 8 ppm O_2, decreasing the temperature to 450 °F restored the life to that of air. Reducing the oxygen level to 0.2 ppm in 550 °F water was also beneficial. These latter two findings are preliminary because of limited testing.</p> <p>The test results were interpreted in terms of conventional procedures in which a notch root pseudostress amplitude S_o was calculated for each test and compared to the ASME fatigue data curve for carbon steel. The quantity S_o was obtained from the applied stress intensity range, ΔK, and Neuber notch analysis procedures to account for elastic-plastic notch root conditions. The worst-case notch concept was introduced to account for the observed maximum in the fatigue notch factor k_f with decreasing notch radii and for the environmental notch sensitivity. For the present study, the worst-case notch radius ρ was 0.0065 in.</p> <p>A procedure is described for calculating S_o and N_i from crack growth data. This procedure assumed a crack to be equivalent to the worst-case notch and provided a good prediction of the ASME fatigue data curve from the ASME crack growth curves in air, both for carbon steel. Using this approach and a conservative threshold stress intensity value for fatigue crack growth in 550 °F, 8 ppm water, a value of S_o was determined, below which crack initiation will not occur in this environment, regardless of defect sharpness or frequency of loading. This value of S_o was consistent with the notched CT crack initiation results obtained.</p>		
KEY WORDS corrosion fatigue, fatigue design, CT specimens, fatigue testing		

INFORMATION PREPARED FOR _____

Additional Hard or Microfiche Copies
Available From

Technical Information Exchange
Bldg. 81 Room A133, Schenectady, N.Y., 12345

THE USE OF NOTCHED COMPACT TENSION TESTS FOR CRACK INITIATION DESIGN RULES IN HIGH-TEMPERATURE WATER ENVIRONMENTS

T.A. Prater and L.F. Coffin

INTRODUCTION

While there are two fundamental approaches which form the design basis for fatigue life prediction—crack initiation and crack growth—by far the greatest attention has been given to initiation. However, relatively little attention has been given to that aspect of fatigue crack initiation where environmental conditions can act to degrade the fatigue performance of critical structural materials. Motivation for interest in environmental fatigue crack initiation and for initiating the present investigation stems from observations on the performance of pipe components tested at General Electric's Pipe Test Laboratory at San Jose. As reported earlier,⁽¹⁻⁴⁾ welded 4-in. diameter carbon steel pipes, when subjected to cyclic loads of up to 135% of the materials' yield strength and pressurized at 550 °F and 1500 psi with water containing 8 ppm oxygen, exhibited a reduction in fatigue resistance of some 7 to 32 times greater than in similar tests in air at 550 °F. This decrease in resistance was associated with a pronounced fatigue notch sensitivity in the water environment, the notches arising from the welds and their weld preparation geometry. Although the loading on these components was very severe and not directly related to service conditions, the results were of sufficient concern to warrant an investigation to better understand and predict the fatigue crack initiation process in oxygenated, high-temperature water conditions. The present report is one of two carried out on this topic.⁽⁵⁾

While many methods are available for developing crack initiation information in fatigue, including standardized low-cycle fatigue testing,⁽⁶⁾ the specific features of high pressure and temperature in the present situation require special consideration. Since an investigation under this program was being carried out in our laboratory on fatigue crack growth in compact tension (CT) specimen geometries in autoclaves, we decided to take advantage of this specimen configuration, starting with notches rather than precracks, and measuring the growth of cracks from the notch as a basis for defining the cyclic life for crack initiation. A number of attractive features evolved from this approach including:

- use of well-developed loading and crack growth monitoring techniques
- ability to define quantitatively a crack initiation life in terms of an accurately measured crack depth
- relatively simple means for determining crack initiation at 550 °F and 1500 psi water
- use of geometry representative of notches or other defects found to be controlling in component tests
- use of one specimen geometry to obtain both crack initiation and crack growth test information.

This technique for studying fatigue crack initiation is not new, the procedure having been used by Jack and Price⁽⁷⁾ on mild steel, by Barsom and McNicol⁽⁸⁾ on HY-130 steel in air, and by Clark⁽⁹⁾ to investigate the initiation behavior of Type 403 stainless steel in air and steam environments. Barsom and Rolfe⁽¹⁰⁾ have reviewed the method further, while Wilson⁽¹¹⁾ has performed elastic and elastic-plastic analyses of notched CT geometries.

Whereas most crack initiation studies use uniaxially loaded, strain-controlled tests (the so-called smooth specimen approach) with analytical techniques developed for applying the results to notched bars, the present investigation employs the inverse process. Here, results from notched bar tests are interpreted for smooth specimen, uniaxially loaded applications. Emphasis will be given to the relationship between these two testing methods. The present approach is particularly attractive when difficult environmental conditions are encountered in testing and especially when notch fatigue resistance can be limiting in service applications.

This report describes the technique employed and gives specific crack initiation results for carbon steel in oxygenated pressurized water for several test parameters of interest. Special attention is given to the significance of the findings to design life prediction by crack initiation.

MATERIALS AND TESTING METHODS

All tests were conducted on 1-in. thick, side grooved, standardized CT geometries fabricated

from SA333 Gr. 6 seamless pipe normalized from 1600 to 1700 °F. Specimens were cut from the pipe such that a fatigue crack propagated either parallel to the pipe axis (#CA-) or in the circumferential direction (#CC-).

Notch radii of either 0.002 or 0.02 in were selected for study. Preparation of the surface was critically important. The notch was machined using a shaped milling cutter which was frequently sharpened without removing the cutter from the arbor. No attempt was made to polish the root of the notch; hence, any irregularity in the cutter resulted in scratches parallel to the direction of machining. Microscopic examination of the notch radii revealed some shallow scratches, even though the cutter was resharpened after preparation of each three or four specimens. In all early tests, the contour of the notch was examined on a comparator by measuring the width of the notch at distances of 0.5, 1.0, 2.0, 3.0, and 5.0 mils from the root of the notch. A curve was fitted to these points, and in all instances the radius at the root of the notch was within ± 0.001 in. of the intended radius. Figure 1 shows a portion of the notch root near one edge at some magnification, revealing the initiated crack and the quality of the surface so prepared. Note that the notch root contains some fine machining scratches, a matter of interest later.

Testing was performed in stainless steel autoclaves to provide a water pressure of 1500 psi at 500 °F. A flow rate sufficient to displace the autoclave volume in one hour was maintained during all tests. Autoclave feedwater flowed through a heat exchanger prior to entering the autoclave to reduce temperature gradients in the autoclave. The temperature over the height of the CT specimen was

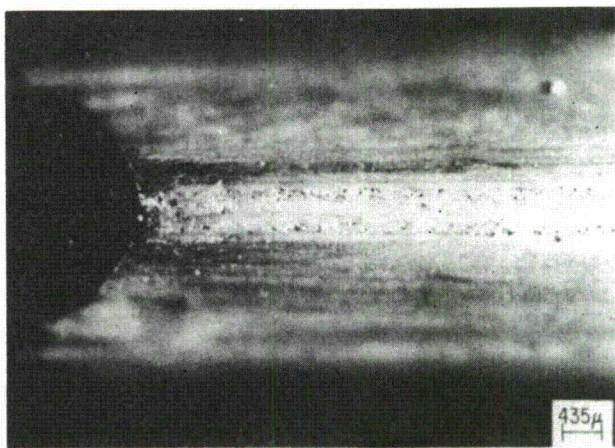


Figure 1. Surface of 0.002 in. notch root showing oxide at initiation sites and surface scratches.

held within ± 2 °F of the temperature at the plane of the crack. Temperature at the plane of the growing crack was maintained within ± 1 °F throughout each test. Two oxygen levels, 8 ppm and 0.2 ppm, were used in the test program. Distilled water was passed through deoxygenating and demineralizing columns before oxygen of the desired level was introduced. To obtain 8 ppm oxygen, the water was saturated with air at atmospheric conditions; to obtain 0.2 ppm oxygen, a mixture of argon plus 0.5 percent oxygen was employed. Resistivity and pH of the water were monitored and controlled. Resistivity always exceeded one $M\Omega$ -cm, and pH was maintained at approximately 5.

Cyclic loading was performed using a closed loop testing machine. The most commonly used wave shape consisted of a linear increase in loading for 90% of the total period, a linear decrease for 5%, and a hold period at minimum load for 5% of the cycle. Cycle periods employed were 0.8 and 80 min. R values (minimum load/maximum load) of 0.2 and 0.5 were employed, with the majority of tests being run at 0.5. Crack growth was monitored from specimen compliance using an *in situ* linear voltage differential transformer attached to the specimen and by ac electrical potential using current leads and potential probes. All tests were controlled through a microprocessor which permits operation in a wide variety of modes, constant P_{max} and P_{min} , constant K_{max} and K_{min} , or modes in which P or K values are changed at programmed intervals of crack length or cycles. The specimen crack length was calculated for each load cycle or as an average for a block of cycles from measured loads and displacements using the microprocessor and standardized compliance formulas.⁽¹²⁾ Block sizes employed varied from one cycle per block in low frequency, high K tests to 100 per block in high frequency, low K tests. Crack length, K_{max} , K_{min} , P_{max} , P_{min} , and ac potential were recorded for each block.

The continuous monitoring and recording of crack length was particularly useful in determining a quantitative definition of fatigue initiation and early growth. In this report, crack initiation is defined as 0.003 in. of growth from the notch root. Figure 2 shows some typical responses of change in crack length vs. cycles of loading. Note that the concept assumes that the notch is in fact a crack, and the crack initiation life is defined as further growth of that crack by 0.003 in. The assumption becomes exact as the notch radius approaches zero, while Wilson⁽¹¹⁾ has shown that the elastic stress concentration factor for a 0.047 in. radius notch in CT geometries differs by only 4% between that for

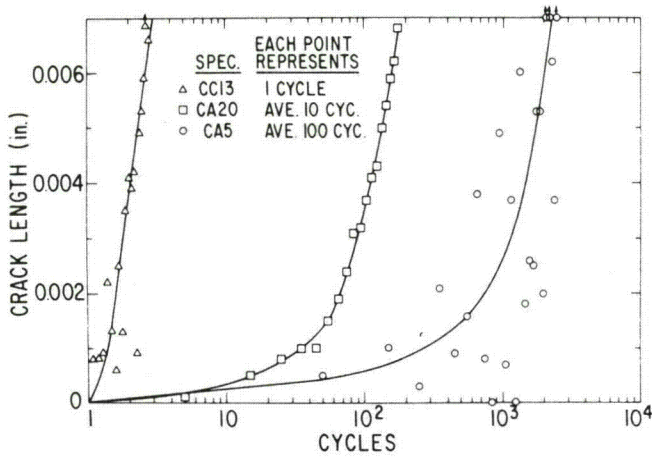


Figure 2. Early crack growth from notch root of CT specimens for three testing conditions. Note improvement in scatter from early test CA5.

the notch and that for a stress intensity calculation based on a sharp crack.

VERIFICATION OF THE METHOD

It was established from crack growth studies that the sensitivity of both compliance and ac potential measurements are within ± 0.001 in. In view of this, the criteria adopted for crack initiation as growth of a crack to 0.003 in. was well in excess of the sensitivity of the measurement techniques being employed. Since this criteria had been established on the basis of growth of a crack already initiated, it was necessary to confirm that this sensitivity could be achieved during initiation. A CT specimen with a machined notch of 0.002 in. radius was cycled for 270 cycles at 1.25 cpm with K_{max} and K_{min} values of 30 ksi $\sqrt{\text{in.}}$ and 15 ksi $\sqrt{\text{in.}}$, respectively. Compliance measurements showed the crack to be 6 mils (Figure 3), and ac potential showed a change of 0.002 mV or about 3.5 mils (Figure 4). Measurements made at 19 equally spaced points along the crack showed the depth to vary from 0.0034 to 0.0123 in., with an average of 0.0070 in. The fracture surface showing this irregularity is shown in Figure 5. Compliance readings appear to provide a better measure of crack initiation than ac potential, probably because of the irregularity of the crack front during initiation and early growth. Consequently, all crack initiation data presented are from compliance measurements.

TEST RESULTS

The method provides a wide variety of test parameters for study. Those considered here include environment (air, high-temperature water at oxygen levels of 0.2 and 8 ppm), temperature (450

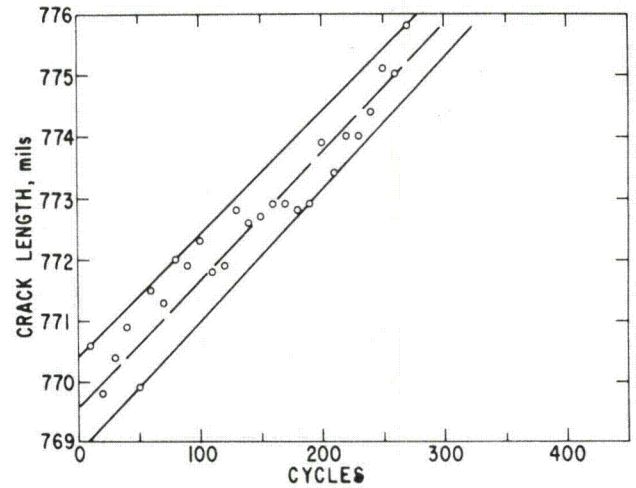


Figure 3. Early crack growth from notch root of CT specimen as measured from specimen compliance - SA333 Gr. 6 steel, 550 °F, 8 ppm O_2 , H_2O , $\rho = 0.002$ in., 1.25 cpm, $\Delta K = 15$ ksi $\sqrt{\text{in.}}$, $R = 0.5$.

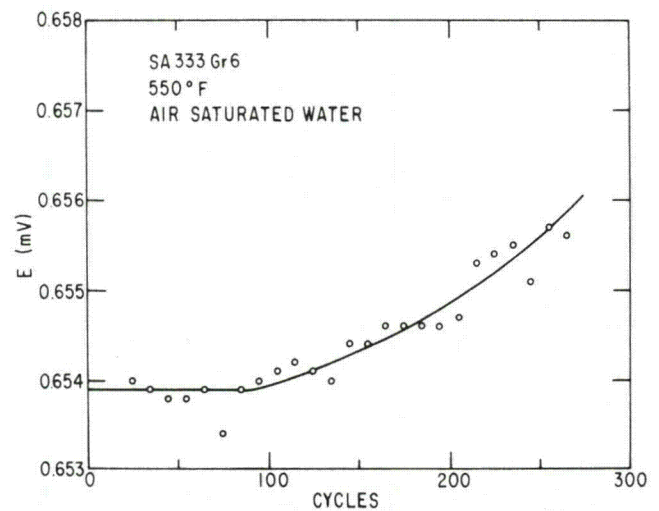


Figure 4. Early crack growth from notch root of CT specimen as indicated by ac electrical potential change - 0.001 mV = 0.00175 in. Same conditions as Figure 3.

and 550 °F), frequency of loading ($\nu = 0.0125$ and 1.25 cpm), notch radius ρ (0.002 and 0.02 in.), stress intensity range ΔK (10 to 25 ksi $\sqrt{\text{in.}}$), and R value ($K_{min}/K_{max} = 0.2$ and 0.5). The use of ΔK and R , while of meaning in crack growth investigations, requires further interpretation for crack initiation applications, as will be discussed later. Other effects such as wave shape can be treated, but the above parameters, if thoroughly explored, require an extensive testing program. Testing to date has yielded an incomplete survey of these variables. Results completed are included in Table 1.

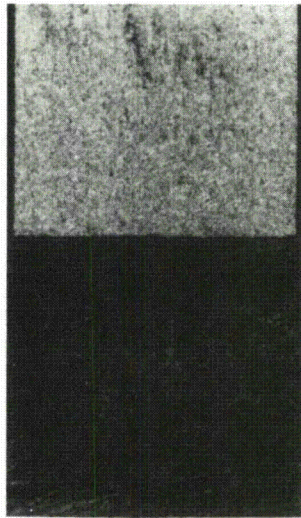


Figure 5. Fractured surface of CT specimen showing irregular, multiply initiated crack front at notch root. Conditions of Figure 3.

A survey of the results shows several interesting cross comparisons of the effect of the several parameters considered. These are summarized in Table 2. Of special interest is the strong effect of environment, particularly 8 ppm O₂ water in degrading the fatigue life. Interestingly, the reduction of the oxygen level in water to 0.2 ppm is strongly effective in restoring the initiation life approaching that of air. Temperature also appears to be a very sensitive parameter. It is found that, based on two comparisons, the air fatigue initiation resistance is restored by reducing the test temperature from 550 to 450 °F. Frequency is likewise a sensitive parameter, reducing the life tenfold with 100-fold decrease in cycles per minute of loading. Surprisingly, the specimen notch radius does not appear to be a critical parameter, and more will be said of this point later. The effect of stress intensity range is interesting. The very large changes when ΔK is doubled indicate a threshold effect on crack

Table 1

SUMMARY OF NOTCHED COMPACT TENSION CRACK INITIATION TEST RESULTS

Spec. No.	Notch Radius (in.)	Temperature (°F)	Environment	ν (cpm)	R $\left(\frac{K_{min}}{K_{max}} \right)$	Stress Intensity Range (ΔK)	Cycles to Initiation (N_i)
CA18	0.002	550	Air	1.25	0.5	25	700
CA 5	0.002	550	Air	1.25	0.5	20	1500
CC11	0.002	550	Air	1.25	0.5	18	1200
CA16	0.002	550	Air	1.25	0.5	22.5	425
CA17	0.002	550	8 ppm O ₂ -H ₂ O	1.25	0.5	25	150
CC 6	0.002	550	8 ppm O ₂ -H ₂ O	1.25	0.5	20	200
CC 9	0.02	550	8 ppm O ₂ -H ₂ O	1.25	0.5	15	500
CC 8	0.02	550	8 ppm O ₂ -H ₂ O	1.25	0.5	20	160
CA 6	0.02	550	8 ppm O ₂ -H ₂ O	1.25	0.5	10	23230
CA 7	0.02	550	8 ppm O ₂ -H ₂ O	1.25	0.5	10	23230
CA12	0.002	550	8 ppm O ₂ -H ₂ O	1.25	0.5	15	150
CC14	0.002	550	8 ppm O ₂ -H ₂ O	1.25	0.5	12.5	300
CC13	0.002	550	8 ppm O ₂ -H ₂ O	0.0125	0.5	20	10
CA14	0.002	550	8 ppm O ₂ -H ₂ O	0.0125	0.5	15	30
CA15	0.002	550	8 ppm O ₂ -H ₂ O	1.25	0.2	32	40
CC17	0.002	450	8 ppm O ₂ -H ₂ O	1.25	0.5	15	9000
CC16	0.002	450	8 ppm O ₂ -H ₂ O	1.25	0.5	20	1800
CA20	0.002	550	8 ppm O ₂ -H ₂ O	1.25	0.5	20	90
CC18	0.002	550	0.2 ppm O ₂ -H ₂ O	1.25	0.5	20	1000

Table 2

SUMMARY OF CROSS COMPARISONS

Parameter	A	B	Equivalence	N_i A	N_i B	Spec. No. A	Spec. No. B
Environment	Air	8 ppm O ₂ -H ₂ O	$\Delta K = 20$	1500	200	CA 5	CC 6
Environment	Air	8 ppm O ₂ -H ₂ O	$\Delta K = 25$	700	150	CA18	CA17
Water Chemistry	0.2 ppm O ₂ -H ₂ O	8 ppm O ₂ -H ₂ O	$\Delta K = 20$	1000	200	CC18	CC 6
Temperature	450 °F	550 °F	$\Delta K = 15$	9000	150	CC17	CA12
Temperature	450 °F	550 °F	$\Delta K = 20$	1800	200	CC16	CC 6
Frequency	$\nu = 0.0125$ cpm	$\nu = 1.25$ cpm	$\Delta K = 20$	10	200	CC13	CC 6
Notch Radius	$\rho = 0.02$ in.	$\rho = 0.002$ in.	$\Delta K = 20$	160	200	CC 8	CC 6
Stress Intensity	$\Delta K = 10$	$\Delta K = 20$	$\rho = 0.02$ in.	23,230	160	CA6,CA7	CC 8
Stress Intensity	$\Delta K = 12.5$	$\Delta K = 25$	$\rho = 0.002$ in.	300	150	CC14	CA17
R-value	$R = 0.2$	$R = 0.5$	$K_{max} = 40$	40	200	CA15	CC 6

initiation above $\Delta K = 10$ ksi $\sqrt{\text{in.}}$ when $\rho = 0.02$ in. When $\rho = 0.002$ in., the differences are smaller, suggesting a threshold less than $\Delta K = 12.5$ ksi $\sqrt{\text{in.}}$. Further discussion of this behavior will be given later. Finally, the R -value comparison was made at equal values of K_{max} , while the ΔK values from Table 1 were 32 and 20 ksi $\sqrt{\text{in.}}$, respectively. The inference here is that ΔK rather than K_{max} is the important quantity in crack initiation in an 8 ppm O₂ water environment. Recent studies on the effect of frequency and R -value in crack growth behavior, on the other hand, show that K_{max} is the controlling parameter.⁽⁴⁾ This would tend to suggest different mechanisms for the two processes of initiation and growth.

The above results are incomplete and represent more of a survey of the effects of the several variables considered rather than a thorough investigation of their effect on environmental crack initiation in SA333 Gr. 6.

INTERPRETATION OF TEST RESULTS

As indicated in the Introduction, an objective of this work is to interpret the findings of the notched CT specimens in terms of the conventional fatigue initiation life prediction approach of uniaxial strain. Of interest in this connection is the CT elastic analysis for notches of various radii performed by Wilson.⁽¹¹⁾ The maximum notch stress range, $\Delta\sigma$, can be derived from a calculation of the stress field distribution at the tip of a crack, from which it can be shown that

$$\Delta\sigma = 2\Delta K/\sqrt{\pi\rho} \quad (1)$$

provided ρ is sufficiently small. Wilson has shown that for radii less than 0.047 in., the error in using Eq. 1 to calculate the stress range is less than 3.8% and decreases with smaller radii. The nominal stress range S_n for the CT geometry, as calculated from direct and bending stress considerations, is

$$S_n = \Delta P \left[\frac{3(W+l)}{(W-l)^2} + \frac{1}{W-l} \right] \quad (2)$$

where ΔP is the load range per inch of thickness and W and l are the total and notch depth of the specimen, measured from the load line. Thus,

$$k_t = \frac{\Delta\sigma}{S_n} \quad (3)$$

For the radii and specimen dimensions used in the present work, $k_t = 6.96$ for a 0.02 in. notch and $k_t = 22.0$ for a 0.002 in. notch. More complete results are shown in Figure 6.

One method of relating the notch conditions to those of uniaxial loading is by use of Eq. 1. Here the elastically calculated stress is considered to be the pseudostress range, assuming the strain distribution to be unchanged by elastic-plastic notch root conditions. Using this procedure, the calculated pseudostress amplitudes are determined. These are listed in Table 3 and are plotted in Figure 7 for the several notched CT tests. It is noted from Figure 7 that the air tests agree reasonably well with the fatigue data curves of pseudostress amplitude S_a vs. life for carbon steel from the ASME Boiler and

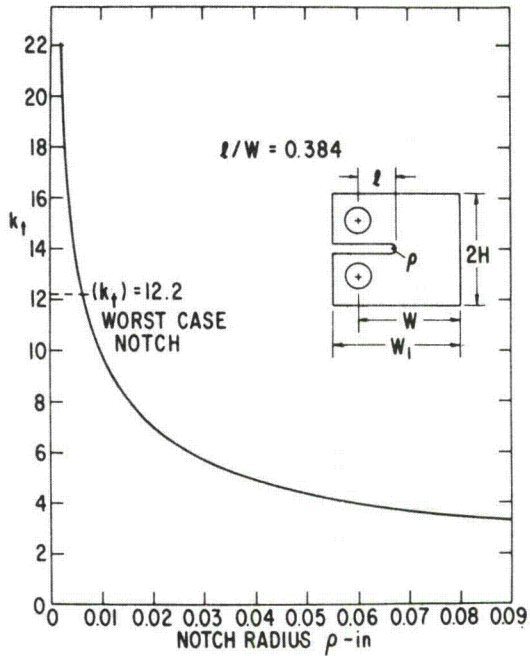


Figure 6. Theoretical stress concentration factor k_t for notched CT specimen vs. notch radius ρ . From Eq. 3.

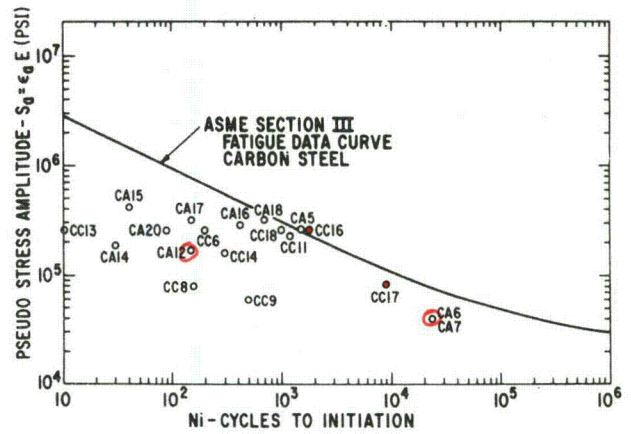


Figure 7. Comparison of notched compact tension data with ASME Section III fatigue data curve for carbon steel. Pseudostress amplitude determined from elastic calculation, Eq. 1, and Table 1. See Table 1 for key.

Table 3

SUMMARY OF LIFE PREDICTION FOR NOTCHED COMPACT TENSION CRACK INITIATION RESULTS

Spec. No.	Cycles to Initiation N_i	(1) Elastic Stress Amplitude $\frac{\Delta K}{\sqrt{\pi \rho}}$ (ksi)	(2) Neuber Notch Stress Amplitude $\frac{(\Delta K)^2}{\pi \rho \sigma_a}$ (ksi)	(3) Elastic Stress Amplitude $\frac{\Delta K}{\sqrt{\pi \rho}}$ (ksi)	(4) Neuber Notch Stress Amplitude $\frac{(\Delta K)^2}{\pi \rho \sigma_a}$ (ksi)
CA18	700	314.8	1386	174.9	412.5
CA 5	1500	252.7	912.2	140	287
CC11	1200	226.8	745.5	126	240
CA16	425	284.4	1139.2	157.5	333
CA17	150	314.8	1386	174.9	412.5
CC 6	200	252.7	912.2	140	287
CC 9	500	59.8	70.1	105	180
CC 8	160	79.7	109.5	140	287
CA 6	23230	39.8	37.7	70	90
CA 7	23230	39.8	37.7	70	90
CA12	150	183.9	508.5	105	180
CC14	300	158	390.1	87.5	130
CC13	10	252.7	912.2	140	287
CA14	30	183.9	508.5	105	180
CA15	40	403.9	2175	224	620
CC17	9000	183.9	508.5	105	180
CC16	1800	252.7	912.2	140	287
CA20	90	252.7	912.2	140	287
CC18	1000	252.7	912.2	140	287

Pressure Vessel Code, Section III, developed from smooth specimen, uniaxial tests in room temperature air. It is disturbing, however, to observe that the tests for $\rho = 0.02$ in. appear to be so much poorer in life when calculated in this manner. Further refinement is required. In order to better determine the notch root behavior for fatigue processes where local plastic strain is developed at the notch root, the Neuber notch analysis method is introduced.⁽¹³⁾ Here the theoretical stress concentration factor is broken down into stress and strain concentration factors such that

$$k_t^2 = k_\sigma k_\epsilon. \quad (4)$$

By assuming that the local stresses at the notch are given by σ and ϵ while the nominal applied stresses on the component or specimen are S_n and e_n , it develops that

$$k_t S_n = 2(\sigma_a \epsilon_a E)^{1/2} \quad (5)$$

Thus, combining with Eq. 1,

$$k_t S_n = 2(\sigma_a \epsilon_a E)^{1/2} = 2(\Delta K / \sqrt{\pi \rho}). \quad (6)$$

To determine the pseudostress amplitude S_a in the notch root for application to the ASME Section III fatigue data curve, we have

$$S_a = \epsilon_a E.$$

Applying Eq. 6

$$S_a = \epsilon_a E = \Delta K^2 / \pi \rho \sigma_a. \quad (7)$$

In the application of Eq. 7, smooth specimen cyclic stress-strain data are used to establish the relationship between ϵ_a and σ_a for the particular temperature and frequency of interest. Thus, Eq. 7 provides the means for determining the notch root pseudostress for direct application to the ASME Section III fatigue data curve. To assist in the specific calculations for Eq. 7, the cyclic stress-strain data as presented in an earlier report⁽⁴⁾ is provided (Figure 8). Thus, assuming a value of S_a , ϵ_a and hence σ_a are determined. The quantity $\Delta K / \sqrt{\pi \rho}$ is then obtained from Eq. 6. The calculation process is simplified with the graphical solution provided in Figure 9. Thus, given ΔK and ρ , S_a can be derived.

When this procedure is applied to the CT test results listed in Table 1, the values indicated in Table 3 (column 2) are obtained. It is immediately seen that the pseudostress quantities so calculated are, in general, significantly greater than the corresponding air fatigue data curve of the ASME Code. This situation is not unusual when dealing

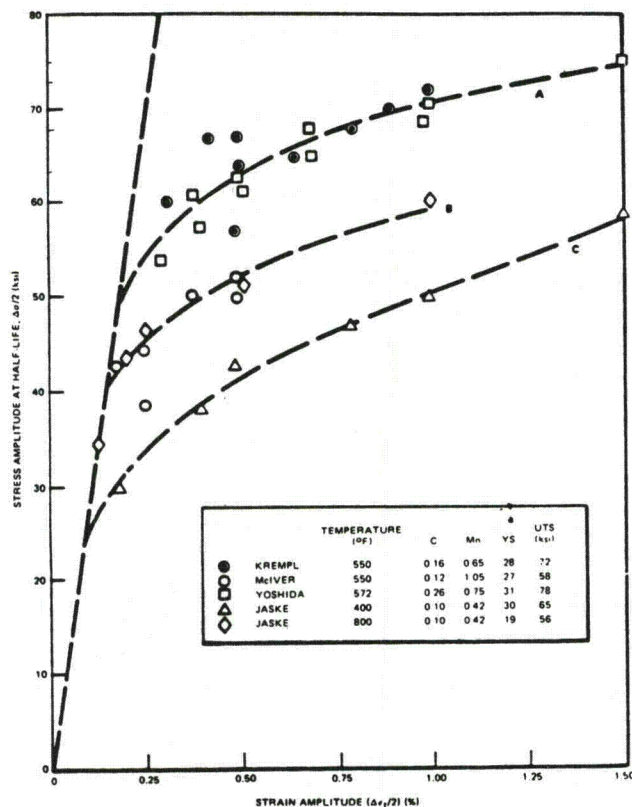


Figure 8. Cyclic stress-strain curves for various carbon steels from several investigators. From Reference 4, Section 5.1.

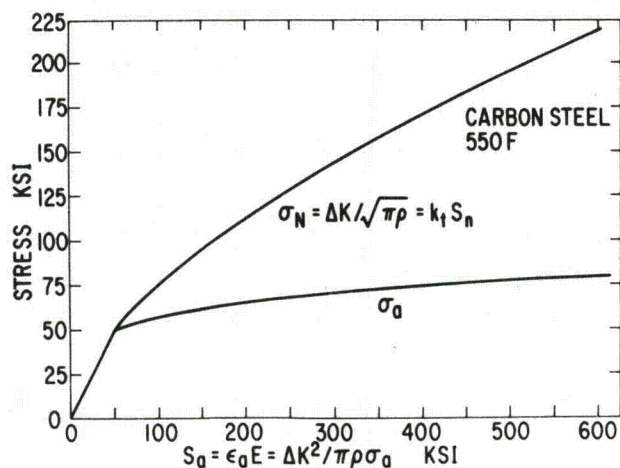


Figure 9. Graphical determination of local stress amplitude σ_a and elastic and Neuber derived notch pseudostress amplitudes for notched CT specimens.

with sharply notched fatigue data as reported by many investigators, and further consideration is required.

It is well known in fatigue investigations that smooth specimen and notch fatigue test data corre-

late very poorly for sharply notched conditions. Some years ago, Peterson,⁽¹⁴⁾ for example, developed the empirical equation:

$$k_f = 1 + \frac{k_t - 1}{1 + \frac{a}{\rho}} \quad (8)$$

to treat this situation, where k_f is called the fatigue notch factor and a is an experimental parameter. A variety of physically related arguments have been offered to explain why sharp notches are more resistant to fatigue crack initiation than can be predicted from analysis, but these will not be considered here. Other investigators have studied this problem. Jack and Price⁽⁷⁾ first proposed the use of Eq. 1 for treating notch fatigue problems, with the restriction that it be applied only for notches above a specific notch radius value. In room temperature air, fatigue lives of uniaxially loaded notch bar tests on mild steel were found to correlate well with ΔK for values of ΔK from 5 to 40 ksi $\sqrt{\text{in.}}$ with a specific notch radius; but for varying notch radii at a specific stress range, there was no influence of the notch radius below 0.010 in. Barsom and McNicol⁽⁸⁾ reported a similar finding for a high-strength steel HY-130, using notched CT specimens. In tests in which the quantity $\Delta K/\sqrt{\rho}$ was maintained equal to 230 ksi, it was found that, for $\rho < 0.008$ in., the fatigue crack initiation life remained constant. Reemsnyder,⁽¹⁵⁾ in reviewing notched fatigue data for mild steel and constructional alloy steels, martensitic stainless steels, and maraging steels described an insensitivity to further degradation in fatigue resistance as the notch root is decreased below 0.010 in. The above analytical procedures follow closely the analysis he used in interpreting his findings.

Of particular importance to the present investigation is the work of Lawrence⁽¹⁶⁾ on the application of the Neuber notch approach to welded components. Since such components contain notches of wide variety and description, he identified in the Peterson relationship (Eq. 8) that a particular notch radius existed which gave a maximum in k_f . This he called the worst-case notch, a situation where, for values of ρ either smaller or larger, the fatigue notch factor was always less. In a structure such as a welded component containing a multiplicity of notches the probability for finding such a notch is very high. If not, use of the worst-case notch would be conservative.

It would appear very attractive to apply this concept to the design of nuclear piping systems using the same logic. It also seems reasonable to extend

the concept somewhat further, that is, to treat all notches and cracks in this aggressive environment as the worst-case notch. The basis for this assumption is that for cracks it is conservative, while for blunt notches there is a strong likelihood that scratches in the notch root can act to make the notch more sensitive to crack initiation in the aggressive environment than would be predicted by the notch geometry. Figure 1 is an example of a notch with scratches.

To that end, the procedures described above for calculating S_a were adjusted using the worst-case notch for the CT geometry. The four air tests were fitted to the ASME fatigue data curve shown in Figure 7, choosing Eq. 7 as the most reasonable life prediction approach. Here, ρ was treated as a disposable parameter. By this procedure, it was found that the worst-case radius was $\bar{\rho} = 0.0065$ in. Columns (3) and (4) were then computed for $\bar{\rho}$ in Table 3. Results for this approach are presented in Figure 10 for comparison with the ASME fatigue data curve for carbon steel. Aside from the fit of the air data to this curve, it is observed that certain tests now fall very close to or above the air curves, indicating, by the assumption of the method, an insensitivity to the environment for some conditions. Included are the two low ΔK tests with a 0.020 in. notch (CA6 and CA7), both tests at 450 °F (CC16 and CC17), and the one test at 0.2 ppm O₂ (CC18). The remainder of the tests in which a notch radius of 0.002 in. was used at 8 ppm O₂ and at two frequencies, fall well below the ASME air fatigue data curve, indicating environmental degradation.

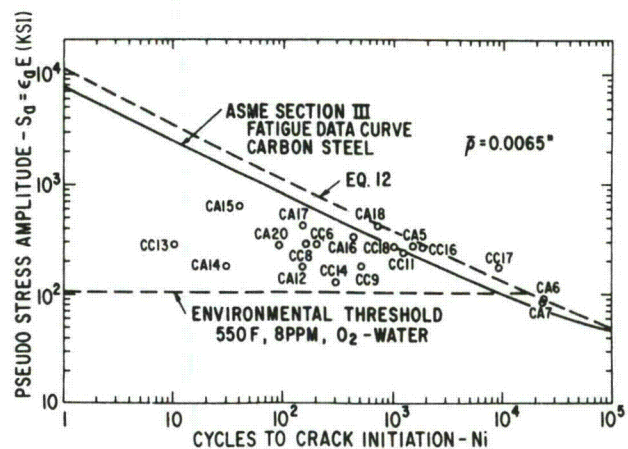


Figure 10. Comparison of notched CT data with ASME Section III fatigue data curve for carbon steel. Pseudostress amplitude determined from Neuber notch analysis, using worst-case notch. Dashed lines from Figure 12. See Table 1 for key.

APPLICATION OF CRACK GROWTH RESULTS TO CRACK INITIATION

Based on the above worst-case interpretation of notch fatigue crack initiation, it would seem possible to utilize crack growth data to predict crack initiation results. The relationship between crack initiation and crack propagation has been considered by many investigators, notably Solomon⁽¹⁷⁾ and Mowbray⁽¹⁸⁾. The present treatment is built around the worst-case notch concept. As is shown in Figure 6, the worst-case notch radius is 0.0065 in., giving k_t a value of 12.2 for the elastic stress concentration factor. An interpretation can be given to Figure 6 that for notch radii of less than $\rho = 0.0065$ in., k_t remains constant. This is the implication of the work of Jack and Price, Barsom, and Reemsnyder. The concept can thus be extended to the sharp crack. Given the crack growth behavior in the form of da/dN vs. ΔK , the initiation life can then be defined as

$$N_i = 0.003/(da/dN). \quad (9)$$

Correspondingly, the value of S_a can be derived from Eq. 7 where

$$S_a = (\Delta K)^2/(\pi \bar{\rho} \sigma_a). \quad (10)$$

The explicit value of S_a can be determined with the help of Figure 9. Alternatively, the ASME air crack growth curve can be represented as

$$da/dN = 1.456 \times 10^{-11} \Delta K^{3.878}. \quad (11)$$

Combining this equation with Eqs. 9 and 10, an expression for S_a results as:

$$S_a = \frac{9.36 \times 10^5 N_i^{-0.515}}{\sigma_a}. \quad (12)$$

The concept can be further extended to relate oxygenated high-temperature water crack growth data to crack initiation in the same environment. As indicated earlier, a parallel program is underway in our laboratory to obtain such data for SA333 Gr. 6 steel. It was determined from that work, for a range of frequencies of 0.0125 to 1.25 cpm and for R values of 0.2 to 0.8, that a limiting environmentally affected crack growth stress intensity factor existed that correlated well with K_{ISCC} , the threshold value of mode I stress intensity for static stress corrosion crack growth. This correlation was based on representing the fatigue crack growth results in terms of da/dN vs. K_{max} , as is shown in Figure 11. For this figure, a conservative estimate for $K_{max} = 22 \text{ ksi} \sqrt{\text{in.}}$ is assumed, below

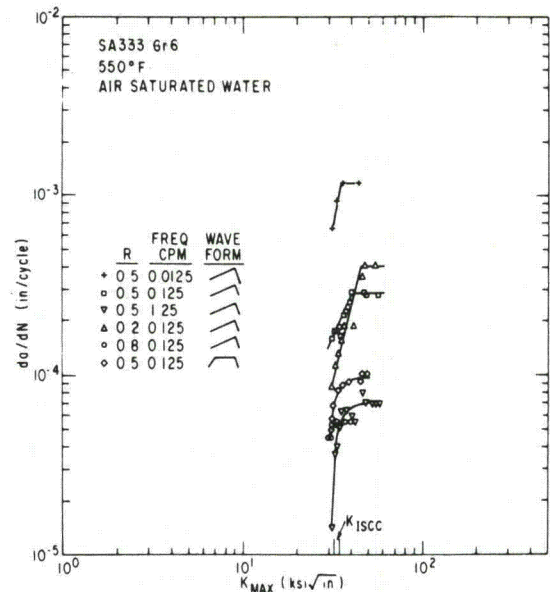


Figure 11. CT cyclic crack growth data summary at 8 ppm O_2 vs. K_{max} , SA333 carbon steel, 550 °F water.

which there will be little environmentally enhanced crack growth. For the present purposes, then

$$\Delta K_{th} = 22 (1-R) \text{ ksi} \sqrt{\text{in.}} \quad (13)$$

such that from Eq. 1 and Figure 9, for $R = 0.5$,

$$(S_a)_{th} = 103 \text{ ksi}. \quad (14)$$

The complete da/dN vs. ΔK environmental crack growth data of Figure 11 can be transformed into plots of S_a vs. N_i by this technique. Figure 12 shows the various representations described above for pseudostress amplitude vs. N_i , including the air results (represented as an upper bound), the environmental crack growth results (represented as a lower bound), and the plateau environmental crack growth results found for the three frequencies employed in the crack growth tests represented in Figure 11. An overlay of Figure 12 onto Figure 10, seen by the dashed lines in Figure 10, provides a basis for comparison of this approach for using crack growth data to predict crack initiation.

APPLICATION TO CRACK INITIATION DESIGN

Figure 10 in a large measure summarizes the work reported in this investigation and interprets the findings in terms of a design approach for fatigue crack initiation for various environmental conditions.

All of the crack initiation results, including those obtained from CT specimen initiation tests or

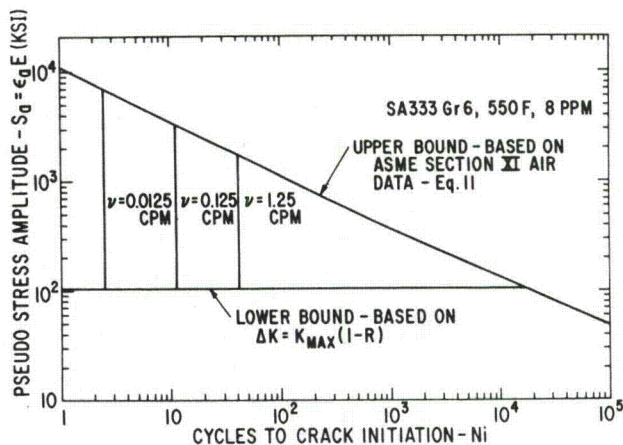


Figure 12. Crack initiation design criteria based on crack growth results. $K_{max_{th}} = 22 \text{ ksi } \sqrt{\text{in.}}$. Worst-case notch.

deduced from crack growth data, are shown in this figure and are represented in terms of a pseudostress amplitude, based on the worst-case notch = 0.0065 in. This pseudostress relationship can be expressed in various forms depending on the analytical approach being considered. For example, if the notch or defect is described in terms of fracture mechanics, then

$$S_a = \frac{(\Delta K)^2}{\pi \bar{\rho} \sigma_a} = 49.0 \frac{(\Delta K)^2}{\sigma_a} \quad (15)$$

and Figure 9 can be used to obtain σ_a . On the other hand, if a nominal stress S_n has been calculated, then from Eq. 6,

$$S_a = \frac{1}{\sigma_a} \left(\frac{k_t S_n}{2} \right)^2 \quad (16)$$

Since k_t , the worst-case theoretical stress concentration factor, is 12.2, then Eq. 16 becomes

$$S_a = \frac{(6.1 S_n)^2}{\sigma_a} \quad (17)$$

Again, Figure 9 is useful in the calculation, since, from Eq. 6

$$k_t S_n = \frac{2 \Delta K}{\sqrt{\pi \bar{\rho}}}$$

When an 8 ppm O_2 water environment is present, then the lower bound of the curve of Figure 10 is applied. Here for lives less than 2×10^4 cycles, $S_a = 103 \text{ ksi}$. Thus, Eq. 15 becomes

$$\Delta K > \left(\frac{103 \times 57.5}{49} \right)^{1/2} = 11 \text{ ksi } \sqrt{\text{in.}} \quad (18)$$

since, from Figure 9, $\sigma_a = 57.5 \text{ ksi}$. Note that the ΔK so computed is the ΔK_{th} determined from crack growth tests.

If the nominal stress is determined in the design, then Eq. 17 becomes

$$S_n > \frac{(103 \times 57.5)^{1/2}}{6.1} = 12.6 \text{ ksi.} \quad (19)$$

Although this nominal stress might appear low, it should be pointed out that spec. CC 14, having an initiation life of some 300 cycles with a pseudostress amplitude of 180 ksi, has a nominal stress of some 17.2 ksi.

Finally, some comments are in order as to when the worst-case concept and the above equations should be applied. The worst-case notch condition is assumed to apply in any structure where the notch conditions cannot be explicitly defined, and particularly in weldments. For those cases where the notch radius is known, as for machined surfaces, and where the environment is air, Eq. 7 or 16 is applied unless $\rho < 0.0065 \text{ in.}$, in which case Eq. 15 or 17 is used. When the environment is 8 ppm O_2 in 550 °F water, Eqs. 15 and 17 apply for all notches, since it is presumed that for all notches, scratches and surface irregularities will exist equivalent to the worst-case notch and the aggressive environment produces a sensitivity to these surface effects not exhibited in air. Further work is needed to define the limits for other temperatures and water conditions.

ACKNOWLEDGEMENT

The authors acknowledge the support of W.A. Catlin and R.E. DeLair during the course of the investigation. Partial support for this work was provided by the Electric Power Research Institute under Contract 1248-1.

REFERENCES

1. BWR Environmental Cracking Margins for Carbon Steel Piping, 1st Semi-Annual Progress Report - NEDC 24625, January 1979.
2. BWR Environmental Cracking Margins for Carbon Steel Piping, 2nd Semi-Annual Progress Report - NEDC 25145, July 1979.
3. BWR Environmental Cracking Margins for Carbon Steel Piping, 3rd Semi-Annual Progress Report - NEDC 25255, January 1980.
4. BWR Environmental Cracking Margins for Carbon Steel Piping, 4th Semi-Annual Progress Report - NEDC 25322, July 1980.

5. *BWR Environmental Cracking Margins for Carbon Steel Piping*, Final Report, in preparation.
6. *ASTM Annual Book of Standards — Part 10, Metals*, Test Method E606-80, Constant Amplitude, Low-Cycle Fatigue Testing, pp. 694-713.
7. A.R. Jack and A.T. Price, *International Journal of Fracture Mechanics*, Vol. 6, No. 4, December 1980, pp. 401-409.
8. J.M. Barsom and R.C. McNicol, "Effect of Stress Concentration on Fatigue Crack Initiation in HY-130 Steel," *ASTM STP 559*, American Society for Testing and Materials, 1974, pp. 183-204.
9. W.G. Clark, Jr., "An Evaluation of the Fatigue Crack Initiation Properties of Type 403 Stainless Steel in Air and Steam Environments," *ASTM STP 559*, American Society for Testing and Materials, pp. 205-224.
10. S.T. Rolfe and J.H. Barsom, *Fracture and Fatigue Control in Structures — Applications of Fracture Mechanics*, Chapter 7, Prentice-Hall, Inc., Englewood Cliffs, N.J., 1977.
11. W.K. Wilson, "Elastic-Plastic Analyses of Blunt Notched CT Specimens and Applications," *Journal of Pressure Vessel Technology, Trans. ASME*, Vol. 96, Series J, 1974, pp. 293-298.
12. S.J. Hudak Jr. and A. Saxena, "Development of Standard Methods of Testing and Analyzing Fatigue Crack Growth Data," AFML Contract F33615-75-C-5064, March 10, 1977.
13. T.H. Topper, R.M. Wetzell, and J.D. Morrow, *Journal of Materials* 4, 1969, p. 200.
14. R.E. Peterson, "Notch Sensitivity," *Metal Fatigue*, (Sines and Waisman, Eds.) Chapter 13, McGraw-Hill, N.Y., 1959.
15. H.S. Reemsnyder, *Society of Automotive Engineers Transactions*, Vol. 88, 1979, pp. 1905-1914.
16. F.W. Lawrence, et al., *Fatigue Testing of Weldments*, *ASTM STP 648*, 1978, pp. 134-158.
17. H.D. Solomon, "Low Cycle Fatigue Crack Propagation in 1018 Steel," *Journal of Materials*, Vol. 7, No. 3, 1972, pp. 299-306.
18. D.F. Mowbray, "Derivation of a Low-Cycle Fatigue Relationship Employing the *J*-Integral Approach to Crack Growth," *Cracks and Fracture*, *ASTM STP 601*, American Society of Testing and Materials, 1976, pp. 33-46.

General Electric Company
Corporate Research and Development
Schenectady, New York

AUTHOR Prater, TA Coffin, LF	SUBJECT corrosion fatigue, fatigue crack growth	NO. 81CRD067
		DATE April 1981
TITLE Crack Growth Studies on a Carbon Steel in Oxygenated High-Pressure Water at Elevated Temperatures		GE CLASS 1
		NO. PAGES 15
ORIGINATING COMPONENT Metallurgy Laboratory		CORPORATE RESEARCH AND DEVELOPMENT SCHENECTADY, N. Y.
SUMMARY Results of an extensive investigation on the stress corrosion and corrosion fatigue crack growth of SA333 Grade 6 carbon steel in 8 ppm oxygen water at 1500 psi and three temperatures are reported. These results provide a background for the crack growth phenomenology of this material/environment interaction as well as serving as a data base for a suggested defect tolerant design approach and for failure analysis. Using a sawtooth waveform and a constant load range, da/dN vs. ΔK crack growth data exhibited plateau regimes ($a \propto N$) for three frequencies (1.25, 0.125, and 0.0125 cpm) at $R = 0.5$ in 550°F water such that a tenfold decrease in frequency produced a fourfold increase in growth rates. The plateau behavior was also observed at R -values of 0.2 and 0.8 and at 450°F but disappeared at 300°F. For load shedding (decreasing load range), on the other hand, the plateau also disappeared. Static crack growth data were obtained at 550°F and were linear on a plot of $\log da/dt$ vs. $\log K$. K_{ISCC} was determined to be 31 ksi in. ^{1/2} . When plotting the above cyclic data in the form da/dN vs. K_{max} , it was shown that the environmental crack growth acceleration mostly took place above K_{ISCC} . Using the Wei-Landes linear superposition model, calculation of the cyclic growth from static crack growth data underestimated the growth except at high K_{max} at the lowest frequency. It was interpreted that the occurrence of the plateau region represented a retardation in crack growth for constant load range tests and was associated with increasing crack depth and reduced environmental sensitivity. Support for this view came from load shedding tests where, for the same ΔK and shorter cracks, the plateau disappeared, and from the peaking and subsequent falling off of the growth rate for constant load range tests when the oxygen concentration was lowered to 0.2 ppm. Similarity between the cyclic crack growth rates in air at 550°F and water at 300°F, together with the similarity of the static crack growth behavior with that of creep crack growth, suggests that time-dependent deformation plays an important role in the stress corrosion and corrosion fatigue processes of carbon steel in air-saturated high-temperature water. A defect-tolerant design approach for situations involving corrosive environments is discussed whereby the fatigue life of the structure is determined by allowing cyclic crack growth from pre-existing defects until the sustained load stress intensity factor approaches, but does not exceed, K_{ISCC} . Thus, cyclic but not sustained load crack growth is permitted in the design. Application of this approach is discussed in light of the test results obtained.		
KEY WORDS <p style="text-align: center;">corrosion fatigue, fatigue testing, CT specimens, crack growth, fatigue design</p>		

INFORMATION PREPARED FOR _____

Additional Hard or Microfiche Copies
Available From

Technical Information Exchange
Bldg. 81 Room A133, Schenectady, N.Y., 12345

CRACK GROWTH STUDIES ON A CARBON STEEL IN OXYGENATED HIGH PRESSURE WATER AT ELEVATED TEMPERATURES

T.A. Prater and L.F. Coffin

INTRODUCTION

Experience in the testing of welded carbon steel pipes in oxygenated high-temperature water at General Electric's Pipe Test Laboratory at San Jose has revealed that cracking can be greatly accelerated relative to comparable air tests. As reported earlier,⁽¹⁻⁴⁾ welded four-inch diameter carbon steel pipes, when subjected to loads up to 135% of the material's yield strength and pressurized to 1500 psi in 550 °F water containing 8 ppm oxygen, exhibited a reduction in fatigue life of some 7- to 32-fold in comparison to similar tests in air at 550 °F. This decrease in resistance was related to the initiation and growth of cracks mostly occurring at notches associated with welds and weld preparation geometry and their propagation around and through the pipe wall. Although the loading on these piping components was very severe and not directly related to service conditions, the wide usage of carbon steel piping in LWR systems warranted further investigation of the problem to better understand and predict the fatigue behavior of carbon steel in oxygenated high-temperature water conditions.

In general, a failure process usually involves crack initiation followed by crack propagation, whether the cause of the failure arises from fatigue or stress corrosion or some combination thereof. One of the concerns associated with these environmentally enhanced pipe failures was the relative importance of crack initiation or crack propagation. In a companion study, the crack initiation behavior was investigated, wherein notched compact tension test specimens were subjected to high-temperature oxygenated water and the effect of a variety of testing parameters explored.⁽⁵⁾ The present report considers static and cyclic crack growth behavior of carbon steel under similar testing conditions.

Various uses can be made of crack growth information obtained for the material of interest in an environment thought to be representative of service. One of these is the development of a quantitative description of the response of carbon steel to various environmentally sensitive parameters. These include the effect of frequency of cycling, the slope of the applied load vs. time (waveshape), the *R*-value (ratio of minimum to maximum load

or stress intensity factor), temperature, and oxygen level. From this testing experience, a qualitative and possibly quantitative model can be constructed which may be useful both in explaining the observed phenomenon and in sorting out the critical variables controlling the behavior.

A second need for the generation of crack growth data in the environment of interest is for failure analysis. Here one is interested in predicting the consequences of cracking in structures found, after some service, to contain growing cracks. From appropriate crack growth information, an assessment of the significance of the appropriate actions can be made: for example, to replace the part, to reduce the severity of the loading, to modify the environment, etc. This is essentially the function of the ASME Boiler and Pressure Vessel Code, Section XI. One of the purposes here is to compare the behavior of carbon steel in exaggerated high-temperature water conditions to the data base of the code.

A third use for crack growth information pertains to the development of a design life prediction approach based on the assumption that the structure contains cracks to begin with. This is in contrast to the present design procedures for nuclear components based on crack initiation. For that case the component is assumed to be free of defects. While the ASME Code acknowledges and allows for the presence of acceptable manufacturing defects, compliance with the code fatigue design procedures assumes that crack initiation will not occur during the component's expected design life. However, preexisting or service-occurring defects can be present as a result of a variety of special conditions (including water chemistry, material fabrication, heat treatment and loading), whose presence may be undetected and whose effect may not be properly accounted for when using a "defect-free" design concept. Examples might include:

1. Pitting due to exposure to off-nominal or out-of-specification water chemistry.
2. Surface cracks due to grinding or improper machining.
3. Undetected weld cracks.

4. Service-induced cracks initiated from unanticipated high-frequency mechanical or thermal stresses.
5. Cracking at crevices under highly aggressive local chemical conditions.

If a design approach is considered which assumes the presence of cracks in a given component, a knowledge of the specific crack growth behavior associated with the design is essential in determining if or how far cracks might grow during service to compromise the performance of the component.

The present report summarizes the findings to date from our Laboratory for the crack growth behavior of carbon steel SA333 Grade B in 8 ppm O₂ water at temperatures up to 550 °F for a variety of testing parameters. A similar investigation has been carried out at General Electric's Nuclear Energy Engineering Division at San Jose in 0.2 ppm O₂ and will be reported separately.⁽⁶⁾ Emphasis in the present report will be given to the significance of these results as they relate to a preexisting flaw design procedure and to the interactive effects between cyclic dependent and time-dependent crack growth.

TEST PROCEDURES

All tests were conducted on one-inch thick, side grooved, compact tension (CT) specimens fabricated from seamless pipe previously normalized from 1600 to 1700 °F. Some specimens were machined with the notch parallel to the pipe axis and some with the notch in the circumferential direction; however, tests showed that crack growth rate was insensitive to orientation. The notch was machined with a shaped cutter which was frequently sharpened to maintain the desired notch radius. Tests were conducted in stainless steel autoclaves to provide a water pressure of 1500 psi at 550 °F. A flow rate sufficient to displace the autoclave volume in one hour was maintained during all tests. Autoclave feedwater flowed through a heat exchanger prior to entering the autoclave to reduce temperature gradients in the autoclave. The temperature from top to bottom of the CT specimen was held within ± 2 °F of the temperature at the plane of the crack. Temperature at the plane of the growing crack was maintained within ± 1 °F throughout each test. Two oxygen levels, 8 ppm and 0.2 ppm, were used in the test program. To obtain 0.2 ppm oxygen, distilled water was passed through deoxygenating and demineralizing columns after which a mixture of argon plus 0.5% oxygen was bubbled through the water. Eight ppm oxygen water was obtained by bubbling air through demineralized distilled water. Resistivity was continu-

ously monitored and always exceeded 1 M Ω -cm. The pH of the 8 ppm oxygen water was approximately 5 and that of the 0.2 ppm oxygen water approximately 6.5.

Cyclic loading was performed using a closed loop testing machine. The experimental setup employed, including ancillary equipment used to control tests and record data, is shown in Figure 1. The most commonly used waveshape consisted of a linear increase in loading for 90 percent of the total period, a linear decrease for 5 percent, and a hold period at minimum load for 5 percent of the cycle. Variations of this waveform were used in some tests to differentiate between the effects of loading time and total period. Cycle periods employed were 0.8, 8, and 80 minutes. *R*-values (minimum load/maximum load) of 0.2, 0.5, and 0.8 were employed, with the majority of tests being run at 0.5. Crack growth was monitored from specimen compliance using an in situ linear voltage differential transformer attached to the specimen and by ac electrical potential using current leads and potential probes. Schematic drawings of these two systems are shown in Figures 2 and 3. All tests were controlled through a microprocessor which permits operation in a wide variety of modes, constant P_{\max} and P_{\min} , constant K_{\max} and K_{\min} , or modes in which P or K values are changed at programmed intervals of crack length or cycles. The specimen crack length was calculated for each load cycle or as an average for a block of cycles from measured loads and displacements using the microprocessor and standardized compliance formulas.⁽⁷⁾ Block sizes employed varied from one cycle per block in low frequency, high K tests to one hundred per block in high frequency, low K tests.

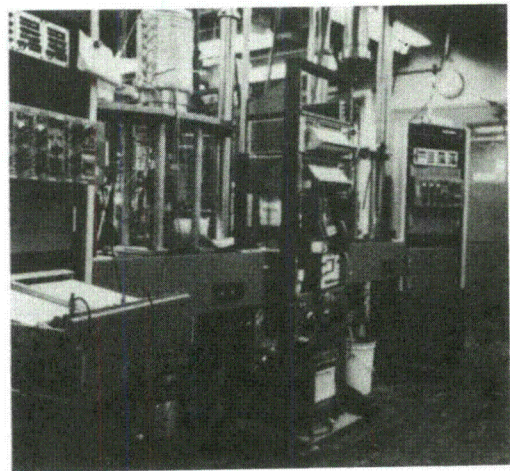


Figure 1. Experimental equipment employed in monitoring crack growth of CT specimens tested under cyclic loading in an autoclave.

Crack length, K_{max} , K_{min} , P_{max} , P_{min} , and ac potential at maximum load were recorded for each block, indicated in the appropriate columns of Figure 4, together with the cycle count. (Column captions read downward.)

A curve relating crack length to cycle count as depicted in Figure 5 was constructed for each test. Since the stress intensity range is known at each point along this curve from the printout shown in Figure 4, a da/dN vs. ΔK plot could be prepared by plotting the slope of the a vs. N curve against the

stress intensity at small increments of change in the stress intensity. Hence, many data points are used in determining each point plotted in the several figures showing the relationship between da/dN and ΔK .

Constant load tests were conducted in an autoclave identical to that employed for cyclic tests with the load being applied through a lever system. At infrequent intervals, a small fraction of the load was removed to facilitate crack growth measurements by compliance; hence, the tests are not truly at constant load. However, the amount of load removed was small (about 15 percent) and the intervals between load removal were sufficiently long (12 hours) so that the crack growth measured is believed to be nearly the same as would be attained under constant load. Crack growth in these tests was also monitored by ac potential drop.

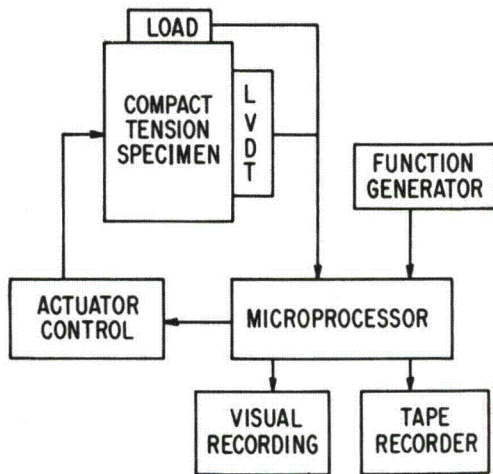


Figure 2. Measurement system employed to monitor crack growth by specimen compliance.

TEST RESULTS

Frequency Effects

The effect of frequency can be noted by comparing the results of three tests conducted in 8 ppm oxygen water at 550 °F and frequencies of 0.0125, 0.125, and 1.25 cycles per minute using the ramp shape waveform described earlier. In each test the precracked specimen was initially cycled between $K_{max} = 30 \text{ ksi in.}^{1/2}$ and $K_{min} = 15 \text{ ksi in.}^{1/2}$

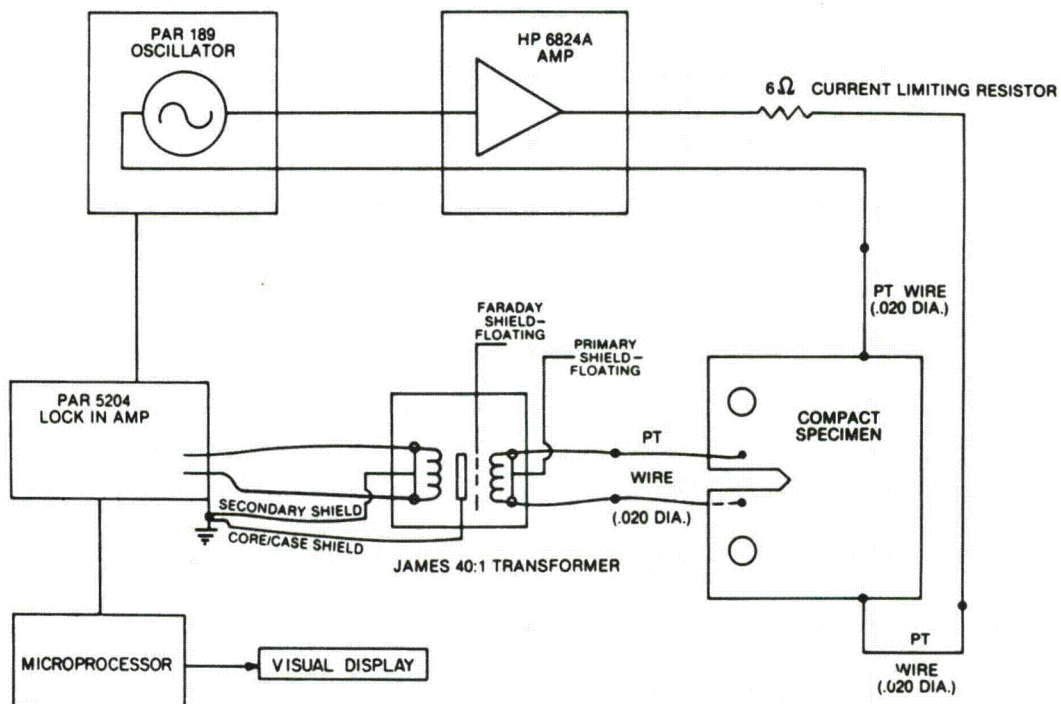


Figure 3. Measurement system employed to monitor crack growth by ac electrical potential.

*** 'K' CONTROL PROGRAM ***

MACHINE

LOAD RANGE [#]? 10000
DISPLACEMENT RANGE [IN]? .05
TARE LOAD [#]? 645

SAMPLE

FULL THICKNESS(B) [IN]? 1
ROOT NOTCH THK(B') [IN]? .9
DEPTH(W) [IN]? 2
ELASTIC MODULUS [PSI]? 27E6
INITIAL 'A/W' VALUE [IN/IN]? .384

TEST

SLOPE DATA MIN AMP% [50 OR 10]? 10
CYCLE NUMBER AT START [N]? 590
CYCLES FOR INITIALIZATION [N]? 0
NUMBER OF CYCLES PER BLOCK [N]? 10
NUMBER OF BLOCKS PER PRINT-OUT [N]? 1

PROGRAM

CONSTANT 'K' TEST [YES OR NO]? YES
K(MAX) [KSI]? 25
K(MIN) [KSI]? 12.5
'A/W' VALUE AT TERMINATION? .41

CC	LM	LM	'M	'M	'V	'M	'ML	AML	'IA	'IA
YN	DA	DI	KA	KI	AA	PA	VAD	CAD	POM	VOM
CT	X	N	'X	'N	'L	'X	'X	X	'ZP	'ZP
E+0	E+1	E+1	E+2	E+2	E-4	E+1	E-5	E-7	E+1	E-5

START FUNCTION GENERATOR

590	456	228	250	125	7600	0	0	0	0	0
591	456	228	250	125	7598	464	653	8030	250	319
592	456	228	250	125	7611	464	652	8042	245	311
593	456	228	250	125	7602	464	652	8037	245	312
594	456	228	250	125	7598	464	652	8035	246	313
600	456	228	250	125	7604	464	653	8034	247	315
610	456	228	250	125	7601	464	653	8030	248	316
620	456	228	250	125	7599	464	654	8028	248	317
630	456	228	250	125	7599	464	653	8032	248	316
640	456	228	250	125	7599	464	653	8029	248	317
650	456	228	250	125	7599	464	653	8029	247	315
660	456	228	250	125	7598	464	653	8025	248	317
670	456	228	250	125	7597	464	654	8026	248	318
680	456	228	250	125	7600	464	654	8028	247	317
690	456	228	250	125	7602	464	654	8033	248	317
700	456	228	250	125	7599	464	653	8029	247	316
710	456	228	250	125	7601	464	653	8028	247	316
720	456	228	250	125	7597	464	654	8025	248	317
730	456	228	250	125	7602	464	655	8030	247	317
740	456	228	250	125	7600	464	655	8031	247	318
750	456	228	250	125	7596	464	655	8034	247	317
760	456	228	250	125	7599	464	655	8031	247	317
770	456	228	250	125	7596	464	655	8029	248	319
780	456	228	250	125	7599	464	656	8028	248	318

Figure 4. Printout of microprocessor input and test data for crack growth test in autoclave.

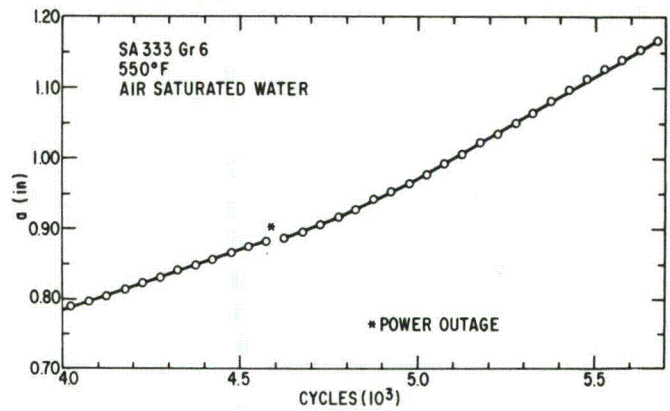


Figure 5. Crack growth of a CT specimen cycled at 0.125 cycle per minute, with $R = 0.5$, in 550 °F, air-saturated water.

($R = 0.5$). Both maximum and minimum loads were maintained constant throughout the test, hence K_{max} and K_{min} increased steadily as the crack grew. A feature of this mode of testing is that the crack depth at any given values of K_{max} and K_{min} was the same in all tests. Since crack depth will be shown later to influence crack growth rate, this is an important feature of the test procedure. The increase in crack length a with cycles N is shown in Figure 5 for the specimen cycled at 550 °F and 0.125 cycles per minute. Note the linear relationship between a and N over a broad range of crack growth. This indicates that the crack growth process for this material, environment, loading condition and frequency is one of constant da/dN for a broad range of ΔK values. Two similar tests were conducted at 450 °F at frequencies of 0.125 cpm and 1.25 cpm. In each of these tests, except for a brief initial period, the increase in crack length also is approximately linear with loading cycles. The results of these tests are plotted in Figures 6 and 7. Each curve exhibits a plateau value of da/dN above which further increases in stress intensity range cause no further increase in crack growth rate. ASME Boiler and Pressure Vessel Code, Section XI crack growth rate curves for tests in air and water are shown for comparative purposes in Figures 6 and 7.

Figure 8 shows the variation of the plateau crack growth rate with test period τ . For the range of test conditions investigated, this relationship is seen to be linear on a logarithmic scale; the 550 °F data can be represented by the equation:

$$(da/dN)_{plat} = 7.19 \times 10^{-6} \tau^{0.597} \text{ in./cycle} \quad (1)$$

where τ is expressed in seconds. For crack velocity,

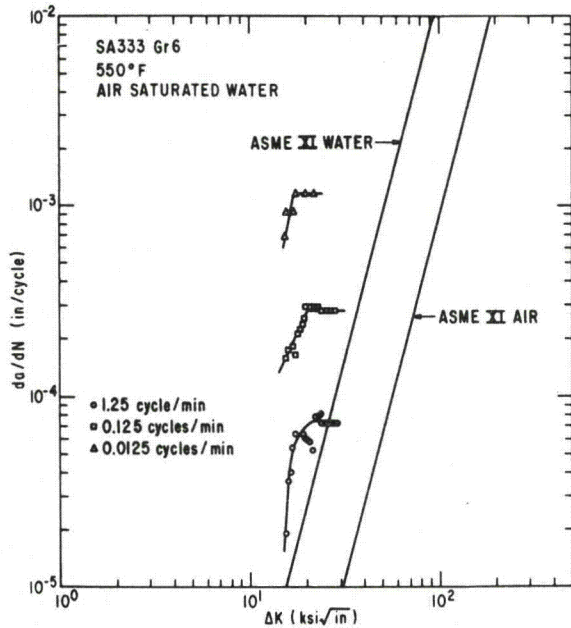


Figure 6. Crack growth rates for 550 °F cyclic tests of three frequencies.

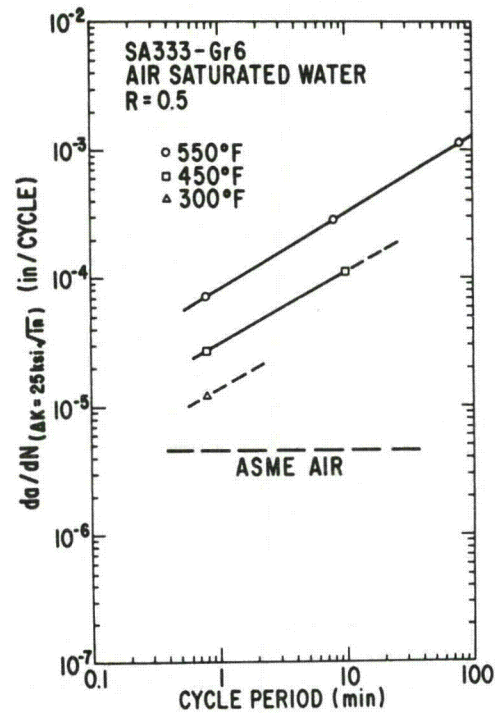


Figure 8. Effect of frequency on cyclic crack growth rates at 450 and 550 °F.

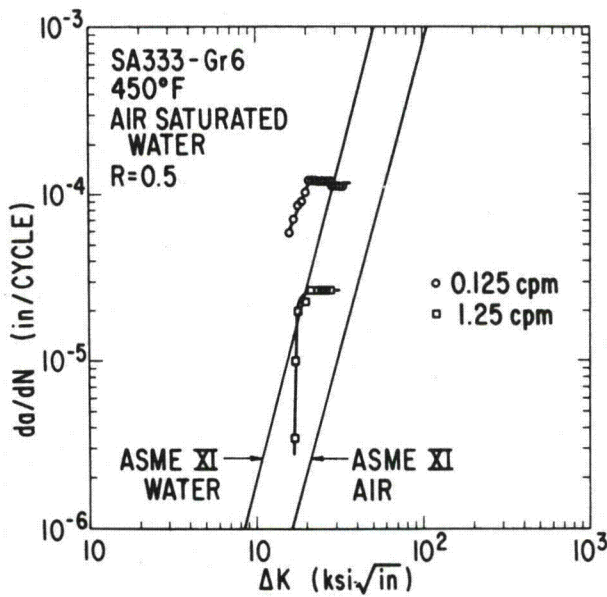


Figure 7. Crack growth rates for 450 °F cyclic tests of two frequencies.

$$(da/dt)_{\text{plat}} = 7.19 \times 10^{-6} \tau^{-0.403} \text{ in./sec.} \quad (2)$$

The limited test data at 450 °F exhibit a very similar relationship. The only test run at 300 °F, which will be described later, did not exhibit a plateau, but the crack growth rate at $\Delta K = 25 \text{ ksi in.}^{1/2}$ is included in Figure 8 for comparison.

Each of these tests was continued until invalid crack extension conditions were reached as defined in ASTM specification E399;⁽⁸⁾ however, in all cases plane-strain conditions appear to exist throughout the entire test. To be assured that plateauing is not related to entering the invalid regime, a test was run in air, but otherwise under conditions identical to the specimen tested at the intermediate frequency (0.125 cpm) at 550 °F. The crack growth rate in this test showed no tendency to plateau (Figure 9). Similarly, in a test conducted in 300 °F water at a frequency of 1.25 cpm, the crack growth rate increased continuously with increasing ΔK (Figure 10). In both cases, the crack growth rates at a given ΔK were considerably lower than reported in Figures 6 and 7.

To gain further insight into the plateauing phenomena, tests were run in a "load shedding" mode at the two highest of the three frequencies used to obtain the data plotted in Figure 6. Again, complete da/dN vs. ΔK curves were constructed from data of a single specimen, but in these tests the crack growth at small values of a was accomplished at high K_{max} and ΔK values, while growth after a had become large was done with low values of K_{max} and ΔK . Data from these tests are plotted in Figure 11. No plateau is exhibited in the plot of these data. Since, in the previous tests, the high ΔK and K_{max} values were not reached until the

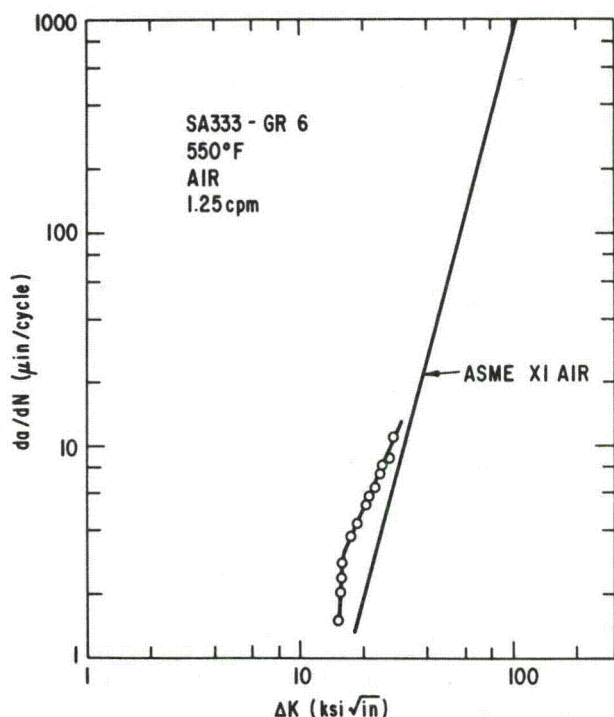


Figure 9. Rate of crack growth in a CT specimen cycled in air at 550 °F.

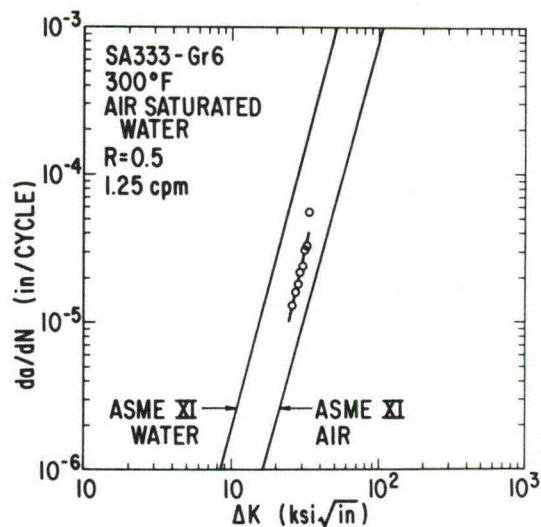


Figure 10. Rate of crack growth in a CT specimen cycled at 300 °F in air-saturated water.

crack was quite deep, the tendency to form a plateau is apparently caused by some interaction of the loading, deep cracks, and the environment.

Waveform

Tests performed to establish the effect of frequency give no indication of the portion of the cycle which contributes most to crack growth nor

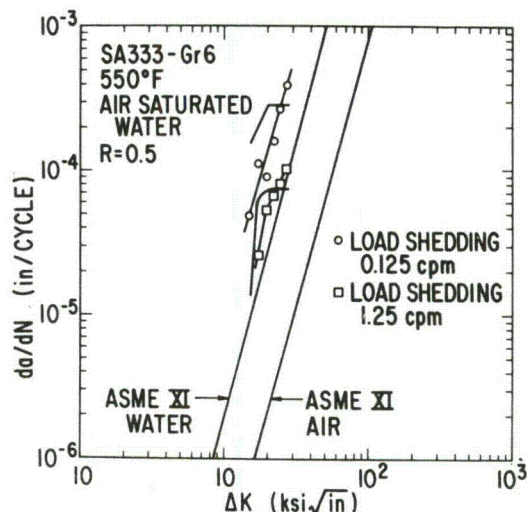


Figure 11. Crack growth rates in "load shedding" compared to those obtained in tests with steadily increasing K .

the relative importance of the loading time as distinct from the cycle time. A constant P_{max} and P_{min} ($R = 0.5$) test was run at a cycle frequency of 0.125 cycles per minute, but with the loading rate that had previously been employed in the test run at 1.25 cycles per minute (i.e., a loading time of 43 seconds). The maximum load was held for 6 minutes 53 seconds, while the unloading time was the same as had earlier been used for the 0.125 cpm frequency test. This cycle has the same total period as the 0.125 cpm test and the same loading time as the 1.25 cpm test run earlier. The results of this test, plotted in Figure 12, lie closer to the 1.25 cpm data than to the earlier 0.125 cpm data. This suggests that rate of loading is more important in controlling crack growth rate than is the length of the cycle.

R Value

Three tests identical except for R value were made with $R = 0.2, 0.5,$ and 0.8 by cycling under constant P_{max} and P_{min} throughout the entire test. Cycling was done at 0.125 cpm and was started with P_{max} selected to yield $K_{max} = 30 \text{ ksi in.}^{1/2}$. The results of these tests are displayed in Figure 13. Again, all three curves show a plateau, the plateau value of da/dN increasing with decreasing R value. The rate of crack growth at low values of ΔK is greatest for $R = 0.8$ and least for $R = 0.2$.

K_{max}

K_{ISCC} has been found to be approximately $31 \text{ ksi in.}^{1/2}$ by statically loading CT specimens at 550 °F in 8 ppm oxygen water. No measurable crack growth took place in 500 hours at

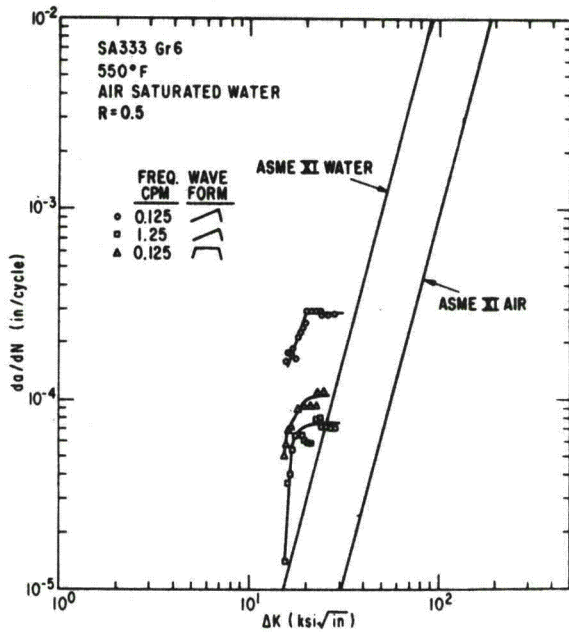


Figure 12. Effect of waveform on rate of crack growth in cyclic tests.

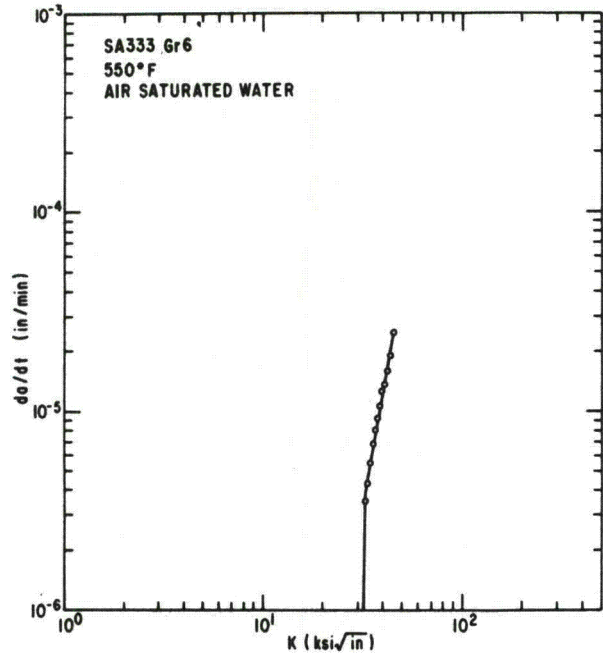


Figure 14. Crack growth rate under static loading conditions.

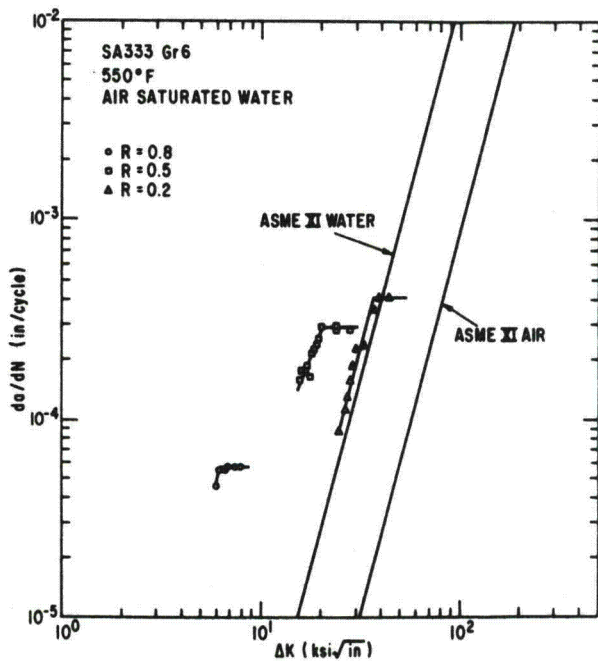


Figure 13. Effect of R value on rate of crack growth in cyclic tests.

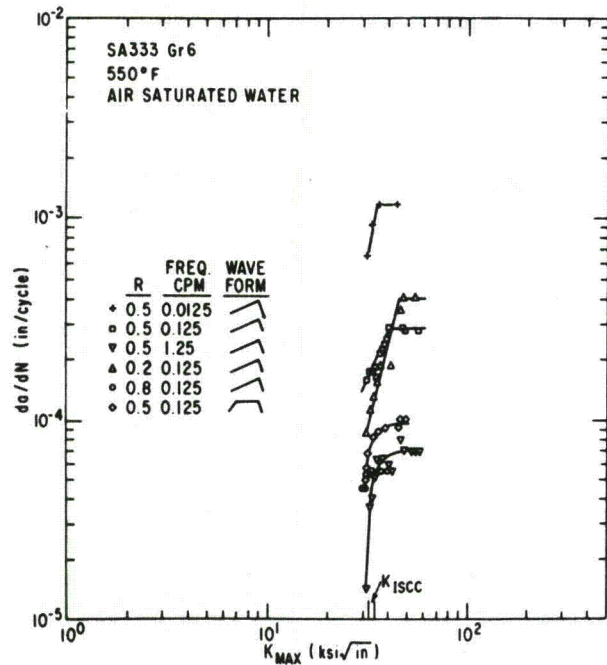


Figure 15. Crack growth rates vs. K_{max} for various frequencies, R values, and waveforms.

30 ksi in.^{1/2}, but significant growth took place at 32 ksi in.^{1/2} and above (Figure 14). When data from Figures 6, 12, and 13 are replotted replacing ΔK with K_{max} (Figure 15), it becomes clear that there is a minimum value of K_{max} below which

environmentally influenced crack growth will not take place, and that this minimum value is unaffected by frequency or R value. This value appears to be close to K_{ISCC} as determined in the constant load tests.

FRACTOGRAPHY

Cyclically Tested Specimens

After completion of a test, the CT specimen was fractured after cooling in liquid nitrogen to allow examination of the crack surface. The crack depth was measured to confirm the last depth calculated by the microprocessor. The agreement was generally within five percent, with the actual depth tending to be slightly greater than the last calculated value. The crack front of all specimens tested in 8 ppm oxygen water was straight or showed slightly more growth along the centerline than at the specimen edge. Figures 16 and 17 show typical crack profiles. The fracture appearance is independent of specimen orientation, as is the crack growth rate. Figure 16 depicts the fracture of a specimen with its notch cut in the circumferential direction, while Figure 17 depicts one with an axial notch. In each of these specimens, there is a crystalline deposit on a portion of the fracture developed during the early stages of precracking. This has been identified as iron oxide. It has also been noted on some other fractures, but its presence has not been related to any particular environmental or test conditions. The only instance in which growth along the centerline was less than that at the edge was the one test performed in 0.2 ppm oxygen water. This specimen is shown in Figure 18. The specimen tested in air at 550 °F exhibited a straight crack front (Figure 19). Specimens cycled at 550 °F are characterized by smooth fracture surfaces, while those tested at 450 °F exhibit considerably greater roughness (Figure 20), and the one test conducted at 300 °F shows marked "ridging" parallel to the direction of crack propagation (Figure 21). This

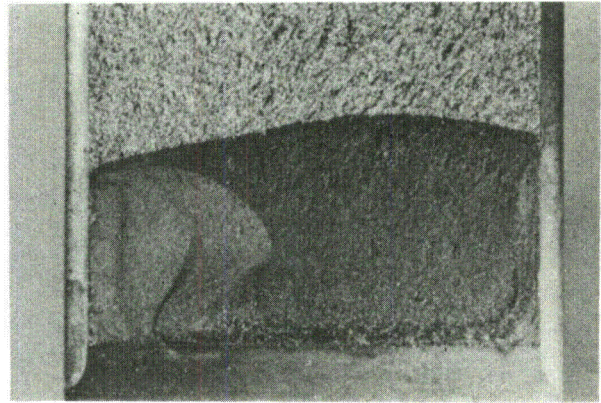


Figure 17. Fracture surface of specimen with axially oriented crack cycled at 550 °F in 8 ppm oxygen water, exhibiting faster growth along centerline than at edges.

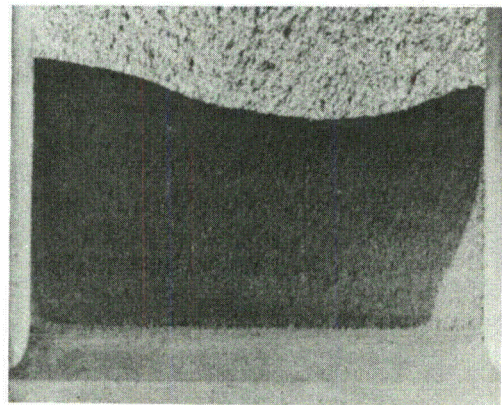


Figure 18. Fracture surface of specimen with circumferentially oriented crack cycled in 0.2 ppm oxygen water showing slower growth along centerline than at edges.

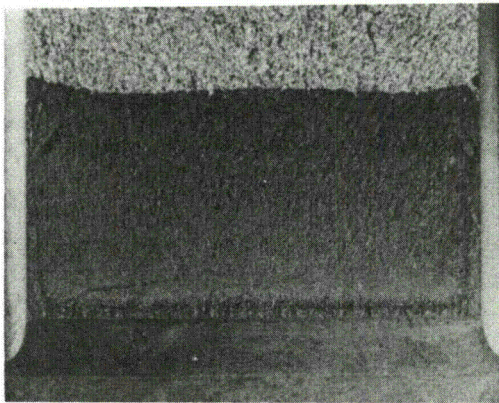


Figure 16. Fracture surface of specimen with circumferentially oriented crack cycled at 550 °F in 8 ppm oxygen water; typical crack front.

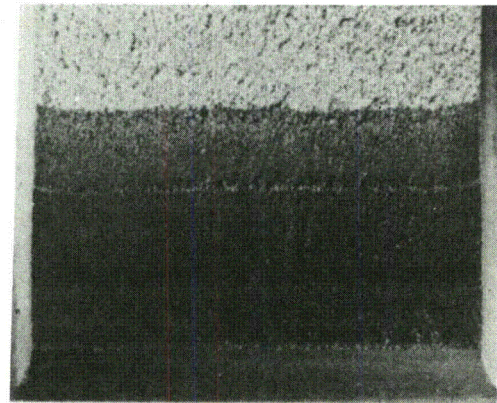


Figure 19. Fracture surface of specimen with circumferentially oriented crack cycled in air at 550 °F.

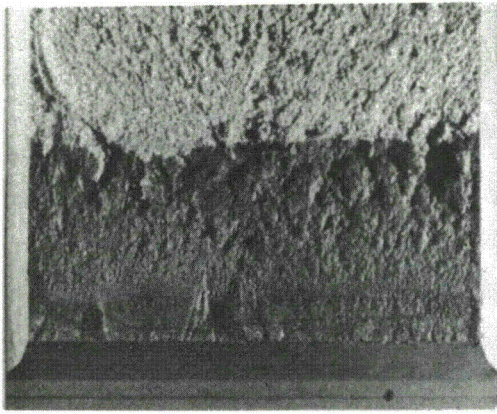


Figure 20. Fracture surface of specimen with circumferentially oriented crack cycled in 8 ppm oxygen water at 450 °F. Note roughness of surface.

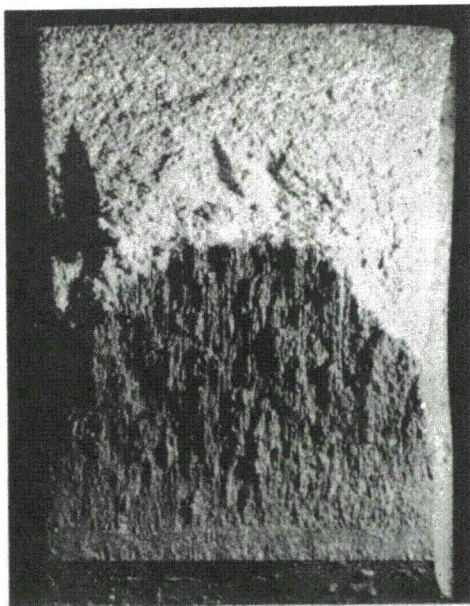


Figure 21. Fracture surface of specimen with axially oriented crack cycled in 8 ppm oxygen water at 300 °F exhibiting extensive ridging.

ridging is believed to be related to the temperature and environment. The two other distinguishing features of this fracture (namely, the accelerated growth rate along the centerline and the plastic deformation of the specimen depicted by the curved surfaces) are believed to result from growing the crack to a "nonvalid" depth. It will be noted that this crack depth is greater than any of the others pictured. Similar plastic deformation was noted in other specimens when a values exceeding 1.2 in. were attained. It appears probable that the crack

front during this test developed its marked curvature during the later stages of crack growth when restraint at the specimen surface was reduced through plastic deformation.

Constant Load Tests

Crack front profiles in specimens tested under constant load are similar in shape to those tested under cyclic conditions, but the fractured surface has distinctly different appearance. In each instance, deep fissures parallel to the direction of crack growth were noted on the fractured surface and extending well beyond the crack front (Figure 22).

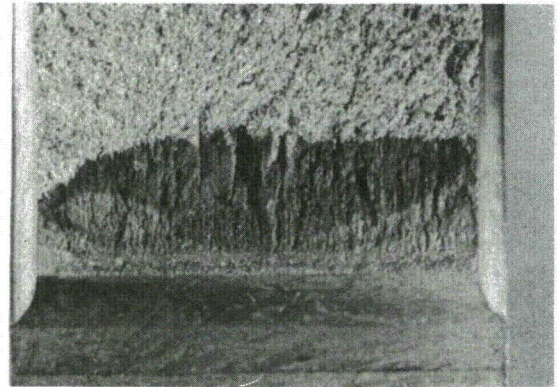


Figure 22. Fracture surface of specimen with axially oriented crack grown under constant load exhibiting fissures parallel to direction of crack growth.

DISCUSSION

Elements of a Defect-Tolerant Design Approach

Prior to a detailed discussion of the physical aspects of the above findings, it would seem desirable to develop further the concept of a defect-tolerant design approach. As indicated in the Introduction, this concept is built around the recognition that complex fabricated components will possess preexisting flaws or may develop flaws in the course of their service. Since it has been shown⁽¹⁻⁵⁾ that notches are especially important as sources for crack initiation in oxygenated high-temperature water and that sharp notches cannot be avoided in welded components, one approach to a design of piping components is to accept the fact that crack growth is possible during service and base the design on limiting the growth to some acceptable size.

A detailed discussion of the background for a defect-tolerant design approach was presented ear-

lier.⁽¹⁾ It will briefly be reviewed here in order to show its connection to the present investigation. The basic concept for this approach assumes the existence of a threshold stress intensity for environmental crack growth under static loading conditions, defined as K_{ISCC} , determined from the applied stress and the dimensions of the assumed defect. When the structure is under sustained loading, if K_{max} exceeds K_{ISCC} , static crack growth will occur. Referring to Figure 23, an initial flaw size a_0 is assumed to exist in the component. For the sustained load portion of the load-time history of the component, the K for this flaw is initially well below that for a_{crit} , where a_{crit} is the crack length obtained from a limiting curve representing the design conditions for sustained load crack growth. An appropriate factor of safety could be included in this limiting curve. The process, whereby the crack length a grows from a_0 to a_{crit} by the cyclic portion of the load-time history, is referred to as the cyclic growth margin. Thus, cyclic crack growth from the defect is allowed during the component's life until it reaches a size where the environmentally caused, sustained-load, crack growth limit is exceeded. The assumption is that most of the life of the component is under sustained load, and crack growth under such conditions is undesirable.

Of particular interest with respect to this concept, is the cyclic crack growth margin and its prediction in the presence of environments which can influence crack growth processes. Two situations can be envisaged, as shown schematically in Figure 24. Here, the action of the nominal applied stress is shown for a given cycle of loading of the component, the current crack size now being $a_0 < a < a_{crit}$. Two material-environment conditions are represented — one by the solid curve, the other dashed. The solid curve is for a material highly resistant to the environment and possessing, for a given flaw size, a high K_{ISCC} -determined limit. In this case, K_{max} associated with the flaw size and nominal stress is well below, or at the most, approaches this limiting curve. For the dashed material-environment combination, however, K_{max} exceeds the K_{ISCC} -determined limit during the cycle, although the sustained load stress remains below it. In the present work, it is assumed that the factor of safety used in each of these limit curves is unity. Thus, for the solid line condition, $K_{max} < K_{ISCC}$, while for the dashed line situation, $K_{max} > K_{ISCC}$.

The behavior described in Figure 24 can at the same time be related to the specific cyclic crack growth response of the material in the environment

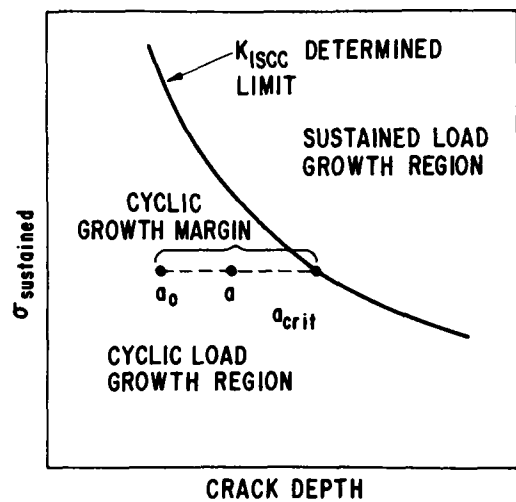


Figure 23. Model for cyclic crack growth margin for designing with defects and environment.

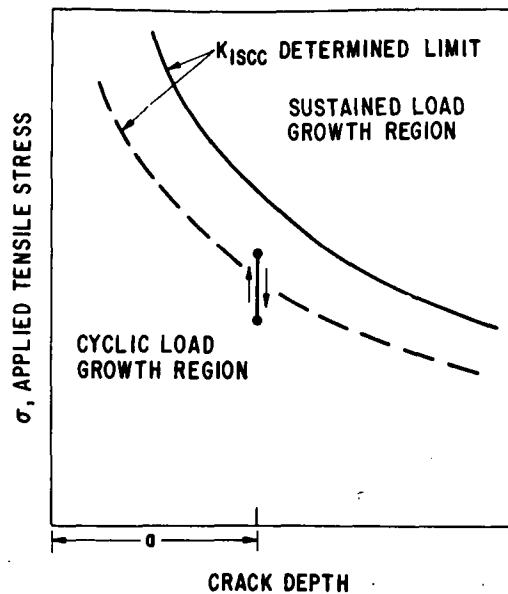


Figure 24. Model for cyclic stressing at a specific crack depth for two materials with differing K_{ISCC} determined limits.

of interest. A schematic representation of the response for the present case based on the results shown in Figures 6 and 15 is shown in Figure 25. Thus, when the cyclic load conditions are below the K_{ISCC} determined limit (the solid curve) in Figure 24, the crack growth regime described in Figure 25 is entirely that for inert (time-independent) conditions. On the other hand, if the cyclic load growth condition of Figure 24 exceeds the K_{ISCC} determined limit (the dashed line), the correspond-

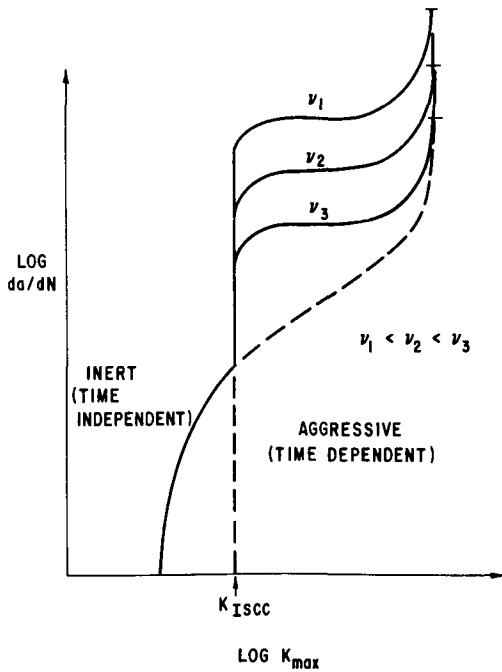


Figure 25. Cyclic crack growth for carbon steel in oxygenated high-temperature water.

ing crack growth response of Figure 25 crosses into the aggressive (time-dependent) regime for a portion of the cycle. Prediction of crack growth under these conditions is necessary, and an appropriate methodology for this prediction is required.

Applicability of Experimental Crack Growth Results to Design Criterion

Implementation of the above concept to the material, geometry, and environment of the present problem is dependent on many considerations. Exclusive of analytical aspects, from a stress corrosion and fatigue viewpoint, a knowledge of K_{ISCC} is critically important. From the present work (Figure 14), the static crack growth behavior of SA333 Grade 6 steel in 8 ppm O_2 , 550 °F water can be compared to that found generally for metals in aqueous environments. A typical K - da/dt (called K -velocity) plot is shown in Figure 26, after Speidel et al.⁽⁹⁾. In the present work, it would appear that only Region I exists, at least for the limits of the present testing procedures, where $K_{ISCC} < 31 \text{ ksi in.}^{1/2}$ for the conditions indicated. Above this value it is found that, for Region I

$$\frac{da}{dt} = AK^n = 8.9 \times 10^{-14} K^{5.1} \text{ in./min} \quad (3)$$

for $K < 45.5 \text{ ksi in.}^{1/2}$ Tests performed above 45.5 ksi in.^{1/2} are invalid for our specimen size, but indications suggest an enhanced crack growth rather

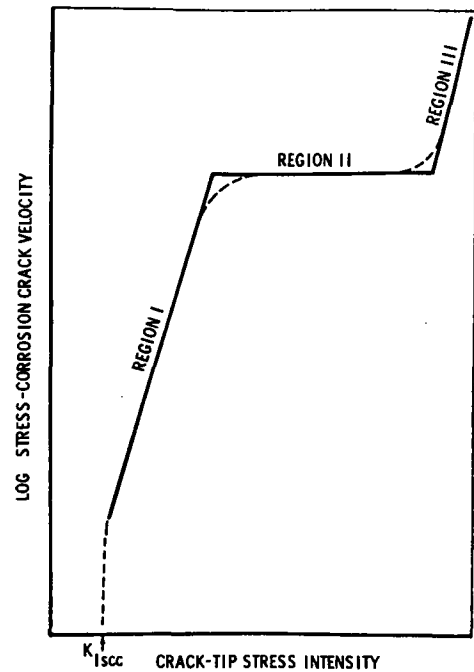


Figure 26. Influence of stress intensity on stress corrosion crack velocity (after Speidel et al.⁽⁹⁾).

than the more beneficial plateau growth pictured schematically in Figure 26. The absence of Region II in the present work suggests that stress corrosion is controlled by physical processes other than those commonly found in aqueous stress corrosion. It is to be noted that the behavior found in Figure 14 is much like creep crack growth,⁽¹⁰⁾ and what may be involved here is an interplay between the oxidizing environment and continued film rupture brought on by localized time-dependent deformation.

Quantitative cyclic crack growth is also important for the implementation of a defect-tolerant design. According to Figure 24, quantitative growth information is needed for values of ΔK when K_{max} is both less than and greater than K_{ISCC} . While useful results have been obtained (specifically Figure 15) showing good correlation of cyclic crack growth resistance with K_{max} for various frequencies and R -values where

$$K_{max} = \Delta K / (1 - R), \quad (4)$$

nevertheless, generalized quantification of da/dN vs. ΔK or K_{max} for various frequencies, waveshapes, and R values remains incomplete. Some information has evolved from this work relative to the effect of frequency. This is shown in Figure 8. Here, a pattern appears to be emerging regarding the effect of frequency on the plateau crack growth rate for various temperatures. Clearly, very low

frequencies seem to be a crack growth accelerant, and results shown in Figure 8 indicate that saturation in plateau crack growth rate has not occurred for the lowest frequency tested to date.

It might appear that at very low frequencies high growth rates occur with increasing values of K_{max} when $K_{max} > K_{ISCC}$, from the view that the behavior is largely due to static growth. However, because of the plateau phenomenon shown in Figure 6, the situation is not quite as simple as this. Factors such as the plateau behavior at 450 and 550 °F for deep cracks in increasing ΔK tests and the absence of a plateau for shorter cracks during decreasing ΔK are complications to this simple model. Further discussion regarding these complications is given below.

Application of Linear Superposition Model to Predict Crack Growth

A reasonably accurate method for determining the interactive effects between cyclic-dependent and time-dependent crack growth would appear to be critical in the application of crack growth data both to damage assessment and to a defect-tolerant design. This interaction would be operative over a broad range of waveshapes, and would even include a simple triangular wave form of equal ramp rates, particularly when considering the effect of cyclic frequency. Thus, a base set of experiments is needed to describe pure cyclic-dependent effects and would have to be obtained in the absence of the environment at very high frequencies. The present set of experiments (Figure 6) involving a waveform consisting of a slow loading rate and a rapid unloading rate at three different frequencies clearly has a time-dependent contribution, and requires consideration from this viewpoint.

To this end, certain aspects of the Wei-Landes linear superposition approach⁽¹¹⁾ were applied to these data to determine whether this model is useful in explaining the plateau cyclic crack growth. Specifically, the static crack growth information of Figure 14 was introduced into an analysis for the waveform used to generate Figure 6. Referring to Figure 14, the K - da/dt relationship found to represent the experimental behavior was broken down into three zones:

Zone I

$$\left. \begin{aligned} 0 < K < 33 \text{ ksi in.}^{1/2} * \\ da/dt = 0 \end{aligned} \right\} \quad (5)$$

* While the measured K_{ISCC} was 31 ksi in.^{1/2}, a value of 33 was the first value of K where crack growth rate could be measured.

Zone II

$$\left. \begin{aligned} 33 < K < 45.5 \text{ ksi in.}^{1/2} \\ da/dt = AK^n = 8.9 \times 10^{-14} K^{5.1} \end{aligned} \right\} \quad (6)$$

Zone III

$$\left. \begin{aligned} 45.5 < K \\ da/dt \text{ unbounded} \end{aligned} \right\} \quad (7)$$

The applied K vs. time behavior is shown in Figure 27 where the constant value of K_{ISCC} is replaced by that expressed in Eq. 6. Beyond a K value of 45.5 ksi in.^{1/2}, the assumed static crack growth is infinitely fast, and the analysis has no meaning. Using the waveform of Figure 27 with $R = 0.5$, it can be shown that for the rising portion of the loading

$$K = (K_{max}/2)(1 + t/\tau) \quad (8)$$

where t is measured from K_{min} , and where τ is the period of the cycle. The unloading portion of the cycle is neglected in this analysis. For Zone II, it can also be shown that

$$da/dN = \int_{\tau-\tau'}^{\tau} AK^n dt \quad (9)$$

where τ' is the time spent when $33 < K < 45.5$ ksi in.^{1/2}. Substitution of Eq. 8 into Eq. 9 and integration results in the expression:

$$da/dN = (\tau A/n+1)(K_{max}/2)^n \left[2^{n+1} - \left(2 - \frac{\tau'}{\tau} \right)^{n+1} \right] \quad (10)$$

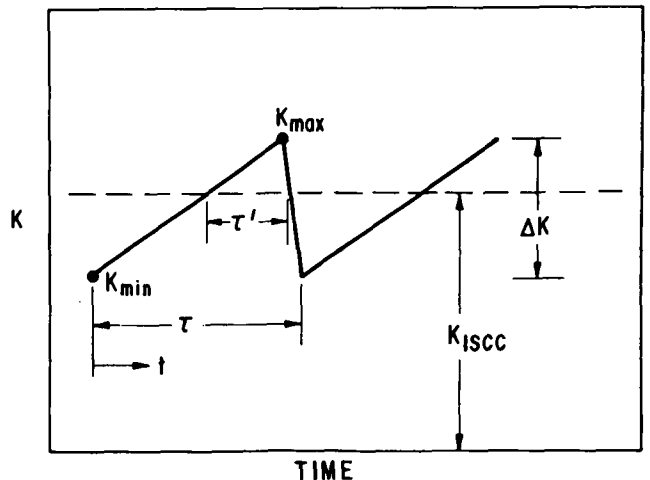


Figure 27. Applied K vs. time behavior for prediction model for cyclic behavior from static crack growth at K_{ISCC} .

Selecting the experimental conditions used to generate the data shown in Figure 14, a comparison of those data with the analytical prediction given in Eq. 10 is shown in Figure 28. This figure shows an interesting comparison in the use of the static crack growth data to predict the shape of the cyclic crack growth response of SA333 Grade 6 carbon steel in oxygenated water. Similar comparisons have been made using the data of Figure 13 for various R values.

Factors Influencing Cyclic Crack Growth of Carbon Steel in Oxygenated High-Temperature Water

Use of static crack growth data to predict cyclic behavior as seen in Figure 28 shows, for the three frequencies considered, an underprediction of the actual growth rate. However, at the lowest frequency and the highest value of K_{max} , the prediction and the experimental results converge. Presumably the cyclic effects (not accounted for by the above analysis) act to accelerate the growth rate. Various explanations can be offered for this

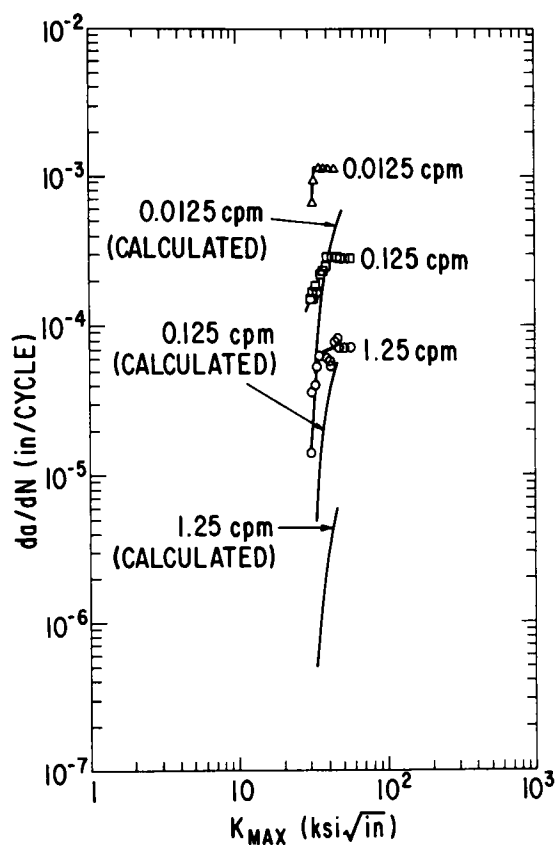


Figure 28. Comparison of cyclic crack growth rates calculated from static crack growth data with experimentally determined cyclic crack growth rates.

behavior. For example, the added contribution of cyclic loading to film rupture could accelerate the corrosive action at the crack tip. Another possibility is the enhanced flushing action associated with the cyclic loading, introducing fresh fluid and renewing the depleted oxygen supply at the crack tip, and thus increasing the corrosion rate.

The plateau effect can be looked upon as being a retardant to crack growth. It is possible that the behavior arises from the geometry such that, independent of K , the crack growth rate depends on the depth of the crack. Comparative results shown in Figure 11 suggest this possibility. Here it could be argued that, as the crack deepens, the crack-tip chemistry becomes less aggressive, possibly because of oxygen depletion, and crack growth is retarded. It will be recalled that the crack depths achieved in producing the high ΔK portion of the load shedding results of Figure 11 were considerably less than those used in developing Figure 6. This is shown in Figure 29, where the crack depth is correlated with K_{max} for cyclic tests implying increasing or decreasing K values during growth, other conditions being the same. If one assumes that the aggressiveness of the environment decreases with increasing crack depth, such that crack growth rate

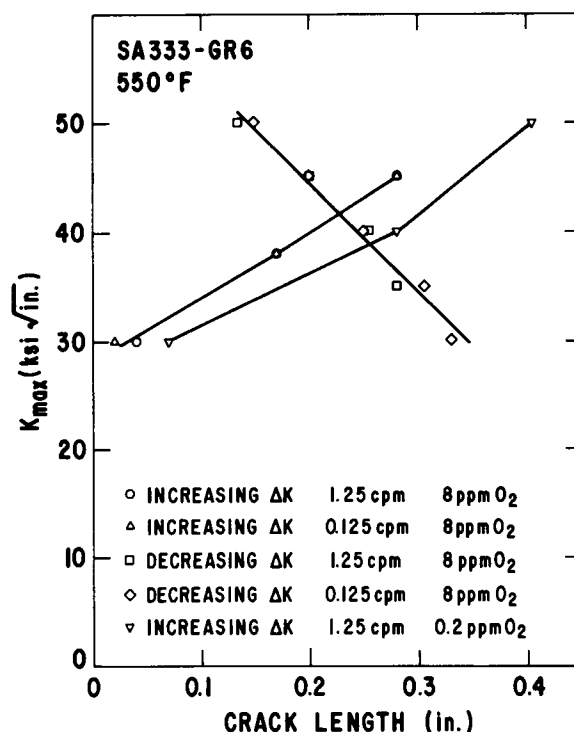


Figure 29. Correlation of crack depth and K_{max} for cyclic tests employing increasing and decreasing K values during crack growth.

da/dN will vary with crack depth, all other factors being equal (including ΔK , τ , R , etc.), then qualitative agreement between the behavior shown in Figure 29 and the results in Figure 11 exists. Further work is required to confirm these results.

There is other evidence to suggest a crack depth dependence on the corrosion fatigue processes for this system. Investigations performed at San Jose⁽⁶⁾ reveal a dropoff in fatigue crack growth rates after reaching a peak rather than the plateau behavior with increasing ΔK when the oxygen level is maintained at 0.2 ppm. These oxygen conditions were duplicated in the present testing configuration, and the results, for a single test at 550 °F and 1.25 cpm, are supportive of the San Jose findings (Figure 30). The argument that further reduction in the aggressiveness of the crack-tip environment with a lower oxygen level and increasing crack depth over the 8 ppm O₂ results can be offered as a possible explanation of this behavior. The concave crack front (i.e., one which exhibited slower growth along the specimen centerline than at the edges) developed in this test (Figure 18) but never observed in specimens tested in 8 ppm oxygen water, may be associated with the reduced aggressiveness of the environment. Further work is required to confirm these results.

Another factor of some importance in characterizing the crack growth behavior of carbon steel in

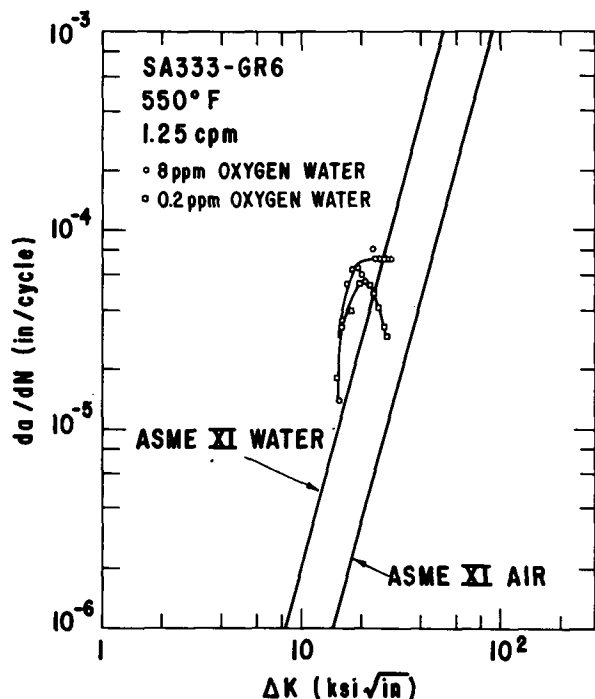


Figure 30. Crack growth rates for 550 °F, 1.25 cpm cyclic tests in 0.2 ppm and 8 ppm oxygen water.

oxygenated water environments is the effect of waveshape. With reference to Figure 12, it is seen that a nearly square wave consisting of a rapid loading, a hold period, and rapid unloading repeated at a frequency of 0.125 cpm has a much lower growth rate at the same frequency than the ramp loading waveform used in this investigation. According to the linear superposition analysis presented earlier, a sustained holding of the peak load would produce a larger growth rate than a ramp loading to that peak value for the same frequency of cycling. This is not found to be the case, as seen in Figure 12, supporting the notion first reported by Barsom⁽¹²⁾ that waveform is important. The present results indicate that a rising ramp rate waveform is more damaging than a square waveform. Mechanistically, it would appear that the lower the crack-tip strain rate, the more environmental influence on the crack growth rate, assuming constant environmental conditions. While Barsom has found no environmental enhancement in crack growth in an aqueous environment over air for a square wave loading at room temperature, in the present case the crack growth obtained for square wave loading in 550 °F oxygenated water is greater than that in air presumably because a crack-tip strain rate develops from time-dependent deformation (creep) to interact with the more aggressive environment.

A final factor considered in the present experimental program is test temperature. At 450 °F, in air-saturated water, the same plateau behavior is obtained with increasing ΔK as is found at 550 °F, although the plateau crack growth rate is reduced (Figure 7). Reducing the temperature to 300 °F further reduces the growth rate and eliminates the plateau behavior altogether. In fact, the water crack growth rate at 300 °F is quite similar to that of air at 550 °F, at least at 1.25 cpm. Thus, it would appear that the environmental acceleration in crack growth of carbon steel in oxygenated water is largely a high-temperature problem. An important consideration in this view is the role of creep in contributing to crack-tip strain. The existence of a time-dependent deformation rate at the crack tip, the resulting film rupture, and subsequent local oxidation provides an attractive model for explaining the role of temperature on static crack growth, and of frequency. More work is required to develop this viewpoint.

ACKNOWLEDGEMENT

The authors acknowledge the support of W.A. Catlin, R.E. DeLair, and D.C. Lord during the course of this investigation. Partial support for this work was provided by the Electric Power Research Institute under Contract 1248-1.

REFERENCES

1. *BWR Environmental Cracking Margins for Carbon Steel Piping*, 1st Semi-Annual Progress Report - NEDC 24645, January 1979.
2. *BWR Environmental Cracking Margins for Carbon Steel Piping*, 2nd Semi-Annual Progress Report - NEDC 25145, July 1979.
3. *BWR Environmental Cracking Margins for Carbon Steel Piping*, 3rd Semi-Annual Progress Report - NEDC 25255, January 1980.
4. *BWR Environmental Cracking Margins for Carbon Steel Piping*, 4th Semi-Annual Progress Report - NEDC 25322, July 1980.
5. T.A. Prater and L.F. Coffin, "The Use of Notched Compact Tension Tests for Crack Initiation Design Rules in High-Temperature Water Environments," General Electric TIS Report 81CRD013, February 1981.
6. T. Hale, "Crack Growth Behavior of a Carbon Steel" (to be published).
7. A. Saxena and S.J. Hudak, Jr., "Review and Extension of Compliance Information for Common Crack Growth Specimens," in *Development of Standard Methods of Testing and Analyzing Fatigue Crack Growth Data*, by S.J. Hudak, Jr., A. Saxena, R.J. Bucci, and R.C. Malcolm, AFML Contract F33615-C5046, Westinghouse Research Laboratories, Pittsburgh, PA 15235.
8. "Standard Test Method for Plane-Strain Fracture Toughness of Metallic Materials," 1979 *Annual Book of ASTM Standards*, Part 10, p. 540.
9. M.O. Speidel, M.J. Blackburn, T.R. Beck and J.A. Feeney, *Corrosion Fatigue: Chemistry, Mechanics and Microstructure*, National Association of Corrosion Engineers, NACE-2, 1972, pp. 324-345.
10. S. Floreen and R.H. Kane, *Fatigue of Engineering Materials and Structures*, Vol. 2, 1980, pp. 401-412.
11. R.P. Wei and J.D. Landes, *Materials Research and Standards*, Vol. 9, July 1969, p. 25.
12. T.A. Prater, F.P. Ford, and L.F. Coffin, *Metal Science*, Aug.-Sept. 1980, p. 424.
13. J.M. Barsom, *Corrosion Fatigue: Chemistry, Mechanics and Microstructure*, National Association of Corrosion Engineers, NACE-2, 1972, pp. 424-426.

Subcritical fatigue crack growth under combined primary and secondary loads

by H. Fuhlrott and H.-D. Schulze

RWTÜV, Essen, Federal Republic of Germany

presented at the IAEA Specialists' Meeting on Subcritical crack Growth, Freiburg, 13. - 15.05.1981

Introduction

It is possible to characterize the fatigue crack growth by the Paris law

$$da/dN = C \cdot (\Delta K)^n = C \cdot (\Delta \sigma \cdot \sqrt{\pi a} \cdot F(a/w))^n \quad (1)$$

taking account of test conditions such as environment, temperature and frequency.

Using specimens the parameters C and n can be determined experimentally, specifically for material and test conditions.

There are problems in predicting the amount of fatigue crack growth for a component, if the initial crack geometry is imprecisely known if the geometry factor $F(a/w)$ for the component can only be estimated and if the stresses have primary and secondary portions which can be assessed in several ways.

Therefore to cover some uncertainties an analysis is conducted on the basis of conservative assumptions. If the assumptions are too conservative this leads to a needless rejection of the component.

An example will be used to illustrate how the fatigue crack growth can be realistically estimated.

The problem

A pipe had long axial flaws, which originated in the manufacturing process. The load in operation is primarily swelling internal pressure and secondarily an alternating strain-controlled deformation

...

caused by thermal expansion. The data are listed in Table 1 and a sketch is given in figure 1.

Table 1:

outside diameter:	38 mm
wall thickness:	5.6 mm
material:	ferritic, low-alloy steel
internal pressure (primary):	0 up to approximately 200 bar, swelling
deformations (secondary):	compression $\delta_{\min} = \sim - 0,05$ mm tension $\delta_{\max} = \sim + 0,05$ mm
initial flaw:	~ 1 mm depth, longitudinal
phase displacement:	$0 : p = 0, \delta = 0$ $\pi/2 : p_{\max}, \delta = \delta_{\min}$ $\pi : p_{\max}, \delta = 0$ $\frac{3\pi}{2} : p = 0, \delta = \delta_{\max}$ $2\pi : p = 0, \delta = 0$

The stresses for the defect-free component were determined by the finite element method. The changes in temperature cause external compression with tensile stresses at the inner pipe surface and external tension with compressive stresses at the inner pipe surface. The programme could not be used to calculate the shift of stresses for the existing flaws.

A conservative calculation of the fatigue crack growth according to the ASME-Code showed that fatigue crack growth was not negligible and for that reason the possibility of failure could not be excluded.

Therefore detailed studies were required to determine the realistic number of cycles which could be tolerated by the component under the given pre crack and load conditions.

The following questions had to be resolved:

- 1) Which effects do the stresses have for crack growth behaviour?
- 2) Is it possible to predict the fatigue crack growth realistically?
- 3) How much fatigue crack growth can be expected depending upon other loads, precracks and numbers of cycles?

Methods

a) Characteristic values of the material

For a rough characterisation of the crack growth behaviour under various conditions based on service conditions (temperature) the crack growth rate was determined experimentally using SEN-Specimens.

The reduced data lie in a common scatter band. More detailed measurements were not taken since the various conditions selected had no significant effect on crack growth within the scatterband (figure 2).

b) Component tests

The conditions given in table 1 were simulated as far as possible in component tests:

Pipe sections approximately 500 mm in length were welded between two bulky steel blocks. The planes perpendicular to the crack plane and parallel to the pipe axis were parallel face ground. By means of these blocks the tensions and compression were produced in the test specimens by a servo-hydraulic closed loop test machine.

The internal pressure was also produced using a closed loop servo hydraulic system. The pressure medium was hydraulic oil (figure 3).

The set points were produced by a digital microcomputer. The actual values were recorded using a multichannel y-t-recorder. These were internal pressure, deformations at three points and force.

In each test up to 20 000 cycles were applied. The frequency was .25 cps.

After each test metallographic sections were taken at three or more points in order to measure crack growth.

The remaining sections were all broken at low temperature in order to establish the depth of the initial flaws and the extent of crack growth over the whole test length. Examples of the results obtained are shown in figures 4, 5 and 6.

c) Fracture mechanics analysis of test results

There are a number of possibilities for the formulation of stresses:

- 1) $\sigma_t = \sigma_t(\rho_i)$, assuming that the secondary stresses with growing crack are shifted and can be integrated to zero at the crack tip.
- 2) $\sigma_t = \sigma_t(\rho_i, \delta)$, assuming that the secondary stresses have the effect of primary stresses and are to be added in toto to the primary ones.
- 3) $\sigma_t = \sigma_t(\rho_i, \alpha\delta)$, assuming that the secondary stresses only partially have the effect of primary stresses.

Bowie's solution /1/, /2/ was taken as the geometry factor F (a/w). For a numerical integration the Function F(a/w), given in graphic form, was linearized with an accuracy of $\pm 3\%$ (figure 7). Other solutions give similar results (e.g. /3/).

The integration was performed numerically and stepwise (e.g. as in /4/).

With the procedure employed here the difference between the initial crack depth a_i and the final crack depth a_{end} ($\Delta a = a_{end} - a_i$) was divided into constant intervals of the length .04 to .004 mm and K_I was calculated for the centre of the interval.

A comparison of the calculated results with the measured results obtained in the component tests shows that only the formulation $\sigma_t = \sigma_t(\rho_i, \delta)$ leads to satisfactory agreement (figure 8).

Equal agreements between experiments and calculations were obtained

for all component tests carried out. For the calculation the scatterband in fig. 2 was used. There was no further adjustment of parameters. This verifies the applied fracture mechanics method for calculating crack growth experimentally.

For the user however not only a correct description of the experiments is interesting but also a transfer to a wide range of parameters for initial crack lengths and load amplitudes.

With the method developed here transfer to this range of parameters is possible.

Two diagrams illustrate this. Figure 9 shows the calculated number of cycles up to failure related to initial flaw depth a_i for various stresses $\Delta\sigma_t$.

Figure 10 shows the tolerable number of cycles related to hoop stress $\Delta\sigma_t$ for various initial flaw depths. For these calculations the upper bound of the da/dN versus ΔK curve was used.

Summary

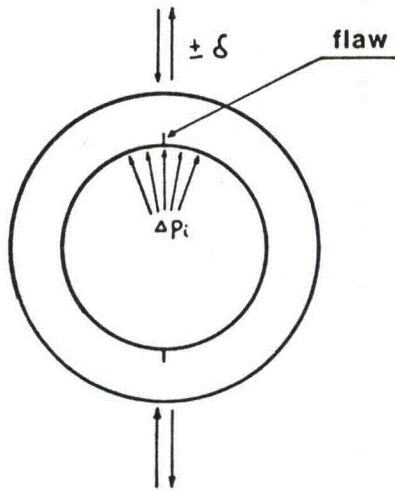
For pipes with flaws which were subjected to load both through primary stresses and secondary stresses it was intended to determine flaw growth over the operating time. Since the effect of the combined primary and secondary stresses on the fatigue crack growth could not be determined on the basis of present knowledge component tests were carried out. The experimental results were then subjected to fracture mechanics analysis.

It was found that in a first approximation the secondary stresses should be evaluated in the same way as additional primary stresses in the analysis of fatigue crack growth.

Because of the agreement between experimental and analytic results a transfer to other parameters is possible.

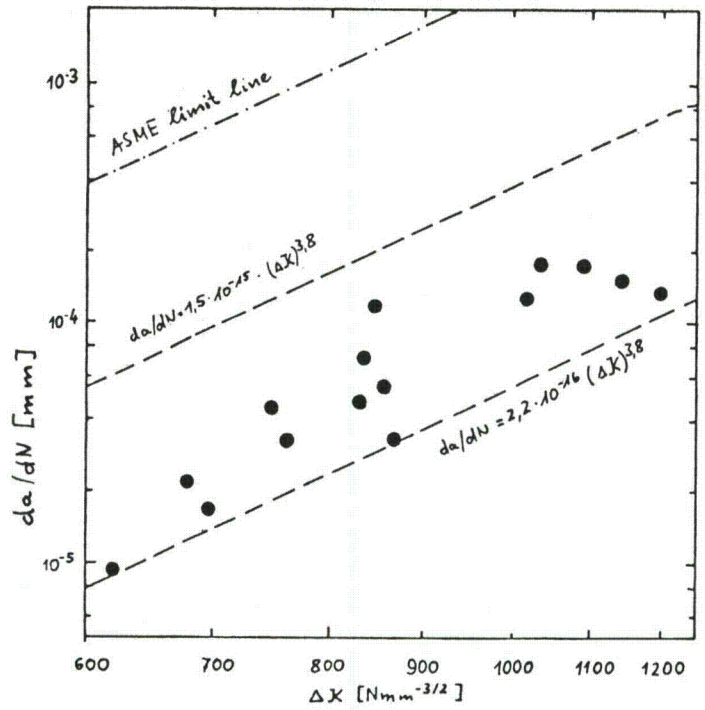
References:

- /1/ Labbens, R., Pellissier-Tanon, A., and Heliot, J., "Practical Method for Calculating Stress-Intensity Factors Through Weight Functions", ASTM STP 590 (1976) pp. 368 - 384.
- /2/ Bowie, O.L., and Freese C.E., "Elastic analysis for radial crack in a circular ring", Engineering Fracture Mechanics, 4 (1972) pp. 315 - 322.
- /3/ Francesco Cesari and Hellen, T.K., "Evaluation of Stress Intensity Factors for Internally Pressurised Cylinders with Surface Flaws", Int. J. Pres. Ves. & Piping, 7 (1979), pp. 199 - 227.
- /4/ Hudson, C.M. and Lewis, P.E., "NASA-Langley Research Center's Participation in a Round-Robin Comparison Between Some Current Crack-Propagation Prediction Methods", ASTM STP 687 (1979) pp. 113 - 128.



Outline of the specimens and loads

Figure 1



Fatigue crack growth rate, da/dN , versus cyclic stress intensity factor range, ΔK , for various test conditions.

Figure 2

Experimental setup

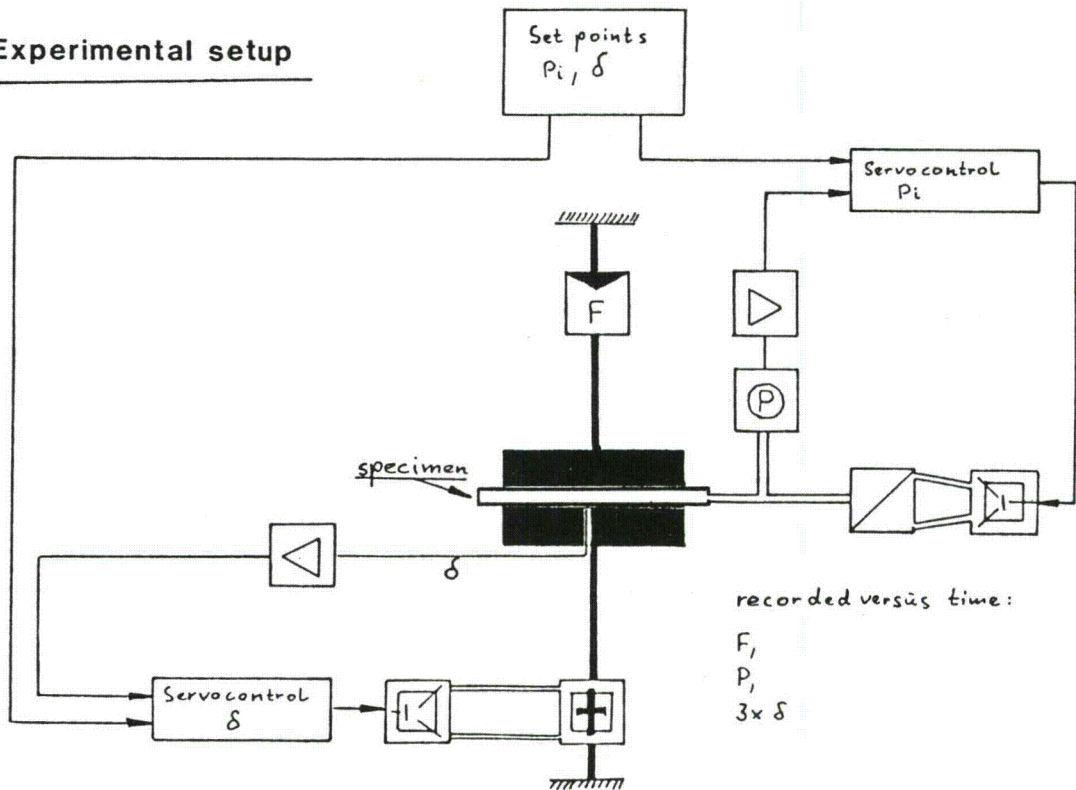


Figure 3

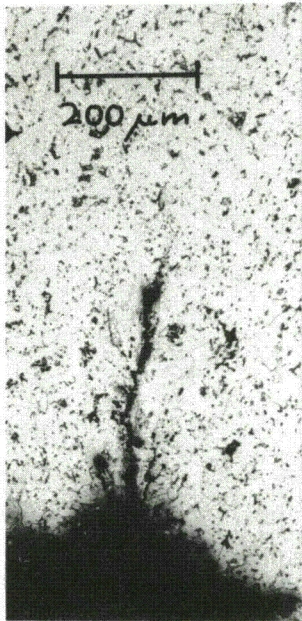


Figure 4

INITIAL FLAW

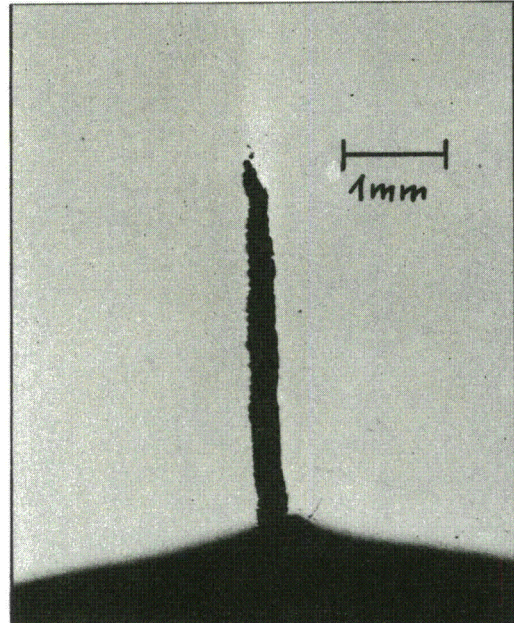
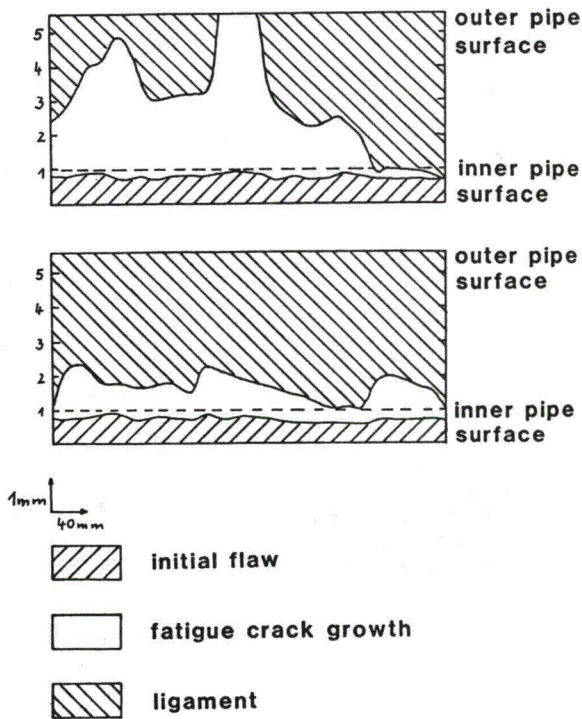


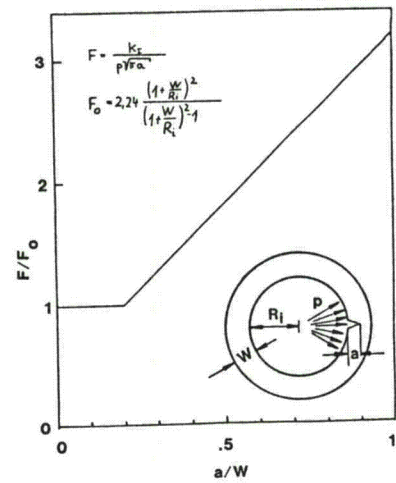
Figure 5

GROWN FLAW



Fatigue crack growth in a component test

Figure 6



Axially cracked long cylinder under internal pressure $R_i/W = 2$, approximation to Bowle's solution

Figure 7

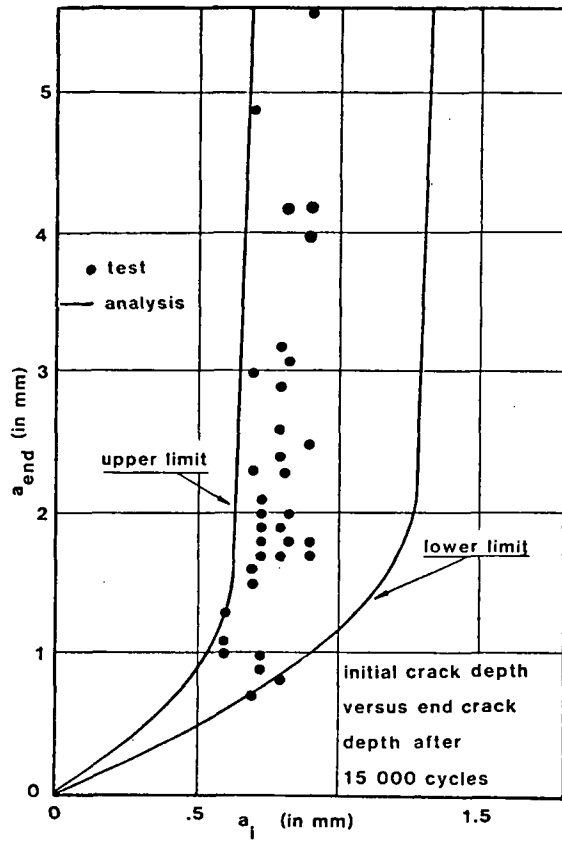


Figure 8

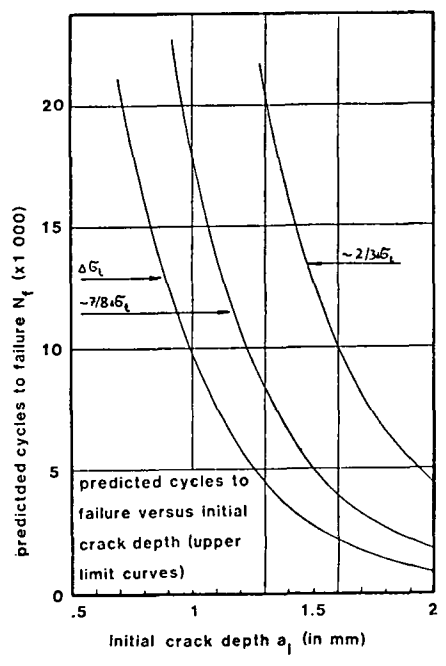


Figure 9

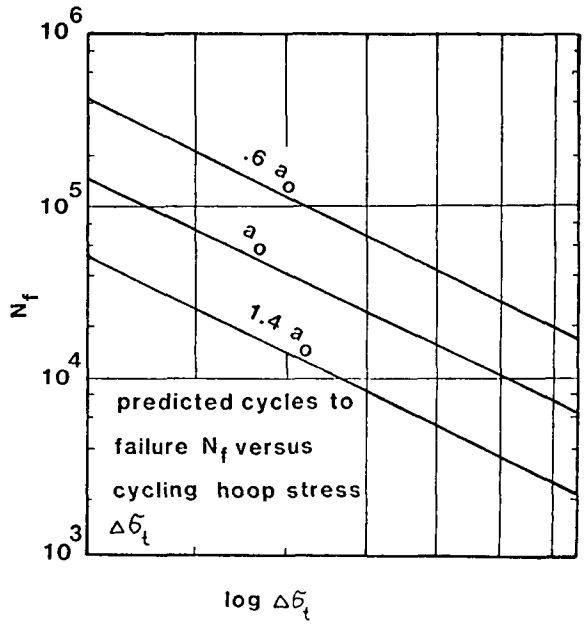


Figure 10

CRACK INITIATION AND CRACK GROWTH AT THE INNER NOZZLE
CORNER SURFACE UNDER THERMAL SHOCK LOADING

Jansky, J., Sauter, A. and Beisswänger, F.¹⁾

1. Objective

The investigations conducted within the scope of the HDR-Safety Programme are concerned with research into operating and emergency and its effects on Reactor Pressure Vessels (RPVs) and Piping. Within these investigations, the effect of the thermal shock on the RPV-structure and piping system under operating conditions has been examined. This programme is sponsored by the Ministry of Research and Technology (BMFT).

2. Basic Statements

The progression of a vessel damage, not only under thermal shock, can be divided into three phases:

- crack initiation
- crack propagation
- failure (leak or rupture)

The time history and crack properties during the three damage phases in structure depend on the kind and degree of loading as well as on the material properties (local, global) and on the flaw conditions due to manufacturing and operating process.

Thermal shock loading on a RPV primary system is usually associated with emergency cooling nowadays. In the last time, the examination of the crack failures in the nuclear plants shows that during certain operating conditions, parts of the primary or secondary reactor system are subjected to thermal cycles /1, 2/ which necessitate research into the propagation rates to estimate the safety margin with respect to component failure.

This consideration leads to the experimental matrix shown in Fig. 1. The first phase consists of thermal fatigue tests on plates (ferritic with and without stainless steel cladding) to investigate cycles to crack initiation, and the possibilities to detect a crack by nondestructive testing. In addition, the plate experiments should give some hints concerning crack shape and crack propagation rates in the plate under thermal shock loading.

¹⁾ Staatliche Materialprüfungsanstalt (MPA)
University of Stuttgart, FRG

The second phase of the thermal shock tests was identical with the second part of the structural damage with crack propagation and crack formation tests under constant internal pressure. The number of cycles to crack initiation was to be checked to compare the results of the plate tests with the possible influence of ratcheting deformation on the initiation and propagation of the crack.

The last phase of the thermal shock tests is conducted on a clad RPV-nozzle corner and deals with crack initiation, propagation and possible ratcheting deformation.

During the three phases of this programme, the finite element calculations were performed with values representing thermal shock experimental conditions.

3. Theoretical Conclusions

The theoretical abstraction of the thermal shock loading, Fig. 2, shows the variables which are derived from plant operation conditions, and which shall occur in conservative amounts in the tests. This Figure shows variables which have all been verified for constant temperature difference ΔT during cooling:

- The slope of the stress intensity function ΔK versus hypothetical crack depth becomes steeper with increasing heat transfer coefficient at the cooled wall
- the crack initiation depth, defined here as the starting line of crack propagation in the form of striations, reduces with increasing heat transfer values
- the stress intensity values increase and penetrate deeper into the wall with prolonged cooling time. The maximum, hereby, is asymptotically attained by higher cooling times (for 250 mm RPV wall thickness, 30 min; this has been investigated by Cheverton et al /3, 4, 5, 6/ within the scope of NRC testing series)
- the maximum stress intensity ΔK becomes greater with increasing thermal expansion coefficient
- the cooling penetrates faster into the wall with increasing thermal conductivity of material. Therefore, the same time of thermal shock penetrates deeper into the ferritic than into the stainless steel because the stainless steel has an insulation effect
- the thermally produced stress intensity versus wall thickness has a maximum and diminishes afterwards, when a threshold value is reached the crack is arrested.

The test parameters were conservatively chosen with respect to operation conditions in RPV and primary systems:

- maximum temperature difference $\Delta T = 300 \text{ K}$
(operation temperature: $320 \text{ }^\circ\text{C}$, feedwater = cooling water: $20 \text{ }^\circ\text{C}$)
- maximum heat transfer between cooling medium and cooled wall realized by water jet cooling vertically against the wall
- tap water having an O_2 content of 700 pp overestimates operational feedwater chemical compositions (corrosion influence)
- high strength material with relatively low toughness (Charpy-V-values of approx. 55 J (0 ft-lbs) at room temperature)
- with respect to vessels, the thermal shock stresses are superimposed at a nozzle corner on the highest pressure induced stresses.

4. Test Devices and Material

The devices which have been developed for pressurized thermal shock test on a model vessel are shown in Fig. 3. The plates and the model vessel were heated by electrical surface heating. The cooling modes were:

- at a point (in the plates) with one jet
- at a circumferential line (in the model vessel) with 160 jets in the radial direction

Utilization of water jetting produced very high heat transfer values in the range of $100\,000 \text{ W/m}^2$. The pressure relief valve in the outlet line maintained a constant internal pressure.

The plates were made of StE 36, the cladding was austenitic (18 % Cr, 9 % Ni, Nb) and the model vessel was made of 0.6 % Cr, 0.5 % Mo steel.

The toughnesses were specified with $a_{\sqrt{20} \text{ }^\circ\text{C}} = 55 \text{ J}$.

5. Crack Shapes

The ferritic plate was thermally shocked 22 000 times; for the clad plate, three different areas were thermally shocked with 8 000 cycles each. The cracks on the cooled ferritic plate surface are shown in Fig. 4. Their direction depends on the direction of the principle stresses at cooled area.

The model vessel nozzle area has been cooled with $N = 4\,300$ cooling cycles. The cracks are concentrated in the axial section of the nozzle and are parallel to the nozzle length axis; the rectangular section of the nozzle had no significant cracks.

6. Ratcheting Deformation

If a component is simultaneously subjected to constant membrane stresses and cyclic thermal strains greater $\frac{R_p}{E} 0.2$ it will eventually undergo a rearrangement in membrane stress to behave more elastically in a sense, as shown in Fig. 6, the membrane stress component becomes smaller. The remaining constant membrane stress will on behalf of the plastic strain cycles monotonically increase structure deformation (ratcheting).

The plastic drift of the circumferential strains results in ovalisation of the nozzle cross-section, Fig. 6; the inside circumferential stress is superimposed by a positive component in the axial section, and a negative one in the rectangular section.

This ratcheting deformation nearly stopped in the model vessel in axial direction after 2 000 cycles, as the first cracks occurred ($2\varepsilon_c < \frac{R_p}{E} 0.2$). and by 3 000 cycles in the rectangular section as the fully elastic^E properties were obtained.

7. Crack Initiation

The biaxial thermal shock strains induced in the plates and the model vessel (calculated by the FE-Method, Fig. 7) were transformed into equivalent strains (Mises) and plotted against crack initiation cycle number. Figures 8 and 9 show the crack initiation curves for thermal shock compared with the ASME-design-curves. The comparison showed that by less than 0.3 % strain rate, the ASME-diagram (ferritic material) seems to be not conservative in a sense of crack initiation.

8. Crack Shape and Crack Propagation

The thermal shock cracks were semi-elliptical with a relation $a/2c = 1/4$ to 1.6. The long cracks are composed of several small linear crack which have been connected by sharing. The composed cracks again grow to a crack depth in the same relation $a/2c$ as mentioned above, Fig. 10.

The first striations resulting from cyclic crack propagation were found in depths of 0.22 mm (ferritic plate) and 0.35 mm (model vessel). Due to the inverse relation between heat transfer and crack initiation depth, it can be assumed that the heat transfer on the surface of the model vessel was lower than the heat transfer on the surface of the plate.

The documentation of striation within the fracture surface can be seen for the ferritic plate in Fig. 11 and for the nozzle corner crack in Fig. 12.

Recalculation of stress intensity factors according to ASME-XI reference crack growth curves for air and water shows in comparison with theoretically

predicted ΔK -values through the wall thickness that the ASME-curve for water describes nearly the actually occurred crack growth under then selected boundary conditions for thermal loading, Fig. 13. The highest crack growth reached in a ferritic plate was $1 \cdot 10^{-3}$ mm/cycle (cooling time: 0.3 s) in the 0.5 mm depth under the cooled surface. The max. crack growth rate could be measured with $2.26 \cdot 10^{-3}$ in the depth of 3.1 mm of the model vessel nozzle crack, Fig. 14. The crack growth rate in the ferritic plate after having reached a maximum, shows a decreasing tendency to striations with $da/dN = 3 \cdot 10^{-4}$ by the stress intensity of $\Delta K = 14.1 \text{ MN} \cdot \text{m}^{-3/2}$. For the cooling time of $t = 0.3$ s and number of loading cycles $N = 22\ 000$, the maximum possible crack depth was reached because the stress intensity value was in equilibrium with the material threshold value. The crack growth rates of the model vessel are progressing within the examined fracture, because of longer cooling time. The theoretical maximum of the crack growth rate could be expected by a selected cooling time of 10 s, in a depth of 4 mm under the cooled nozzle surface.

Because of striation spacing scatter band in the the cyclically produced fatigue fracture, Fig. 15 according to /7/, more experimental work especially with deeper cracks must be carried out. One of such a step in this direction will be the HDR-thermal shock experiment on reactor pressure vessel under operating conditions (summer time 1981).

Summary

Within the scope of the HDR-safety programme sponsored by the BMFT, the thermal shock loading with

$$\Delta T = 300 \text{ K}$$

under operating condition

$$p = 140 \text{ bar}$$

$$T = 320 \text{ }^\circ\text{C}$$

on the decommissioned superheated steam reactor pressure vessel is being prepared (summer time 1981).

This paper reported about preliminary experimental work for estimating crack initiation loading cycles on ferritic and austenitic materials and crack growth rates. The maximum crack growth rates under operating conditions and with a high content of oxygen in the pressurized water (700 ppm) is comparable with the ASME-curve water within a ΔK range to $40 \text{ MN} \cdot \text{m}^{-3/2}$.

- /1/ Investigation and Evaluation of Cracking Incidents in Piping in Pressurized Water Reactors
NUREG-0691, September 1980
- /2/ Kussmaul, K., Blind, D. and Jansky, J.: Cracking in Ferritic Feedwater Piping Systems of Boiling Water Reactors to be presented at SMiRT, Paris, 1981
- /3/ Cheverton, R.D.: Pressure Vessel Fracture Studies Pertaining to a PWR LOCA-ECC Thermal Shock: Experiments TSE-1 and TSE-2, ORNL/NUREG/TM-31; September 1976
- /4/ Cheverton, R.D.; Bolt, S.E.: Pressure Vessel Fracture Studies Pertaining to a PWR LOCA-ECC Thermal Shock: Experiments TSE-3 and TSE-4 and Update of TSE-1 and TSE-2 Analysis; ORNL/NUREG-22
- /5/ Cheverton, R.D.: Quick-Look Report for TSE-5A; October 9, 1980
- /6/ Cheverton, R.D.: Thermal Shock Experiments TSE-5, 5A and 6 - Presentation to the Vessel Integrity Review Group; July 23, 1980
- /7/ Blind, D., Sturm, D. and Trunk, H.: Electron micrographical investigations of a corrosive fatigue fracture surface developed under pressure water reactor conditions
IAEA-Specialists Meeting on Cyclic Crack Growth, Freiburg 13 to 15 May 1981

- Fig. 1: Experimental matrix
- Fig. 2: Thermal loading of vessel wall
- Fig. 3: Test rig for model vessel
- Fig. 4: Crack formation on the ferritic plate
- Fig. 5: Description of ratcheting mechanism, by thermal shock and internal pressure
- Fig. 6: Ratcheting deformation of nozzle cross-section
- Fig. 7: Theoretical stress analysis for model vessel
- Fig. 8: Crack initiation curve for ferritic material by thermal loading
- Fig. 9: Crack initiation curve for stainless steel material by thermal loading
- Fig. 10: Formation of striations at the nozzle corner crack
- Fig. 11: Striations on the crack surface (ferritic plate)
- Fig. 12: Striations on the crack surface (nozzle corner)
- Fig. 13: Stress intensity versus wall thickness in a ferritic plate at $t = 0.3$ s; $\Delta T = 300$ K
- Fig. 14: Stress intensity versus wall thickness in a model vessel at $t = 10$ s and $T = 300$ K
- Fig. 15: Fatigue crack growth rate versus crack depth

Versuchsetappe

Versuchsziel

Platten

- a) ferritisch
- b) plattiert

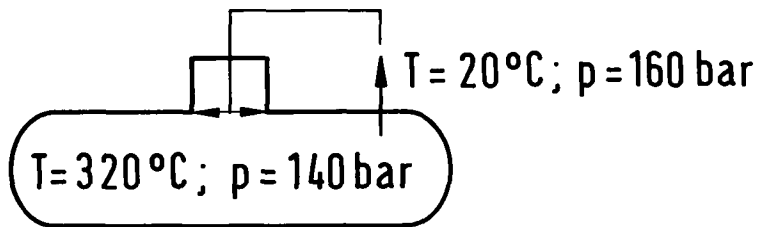
$T = 320\text{ }^{\circ}\text{C}$



Wasser $T = 20\text{ }^{\circ}\text{C}$

$N_A = ?$

Modellbehälter (ferritisch)

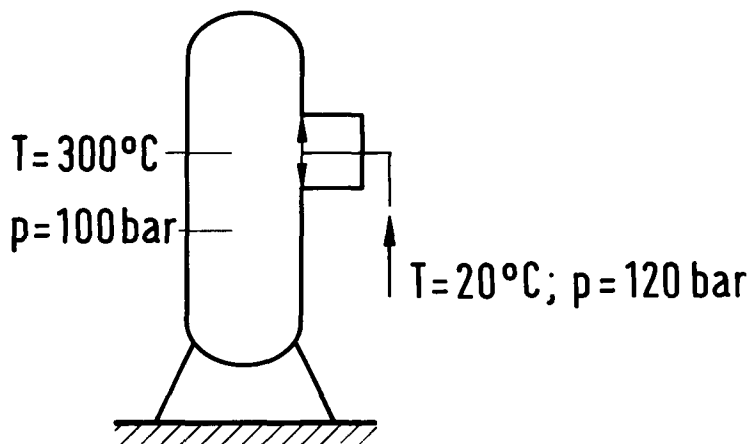


$N_A = ?$

$\frac{da}{dN} = ?$

$a_{kr} = ?$

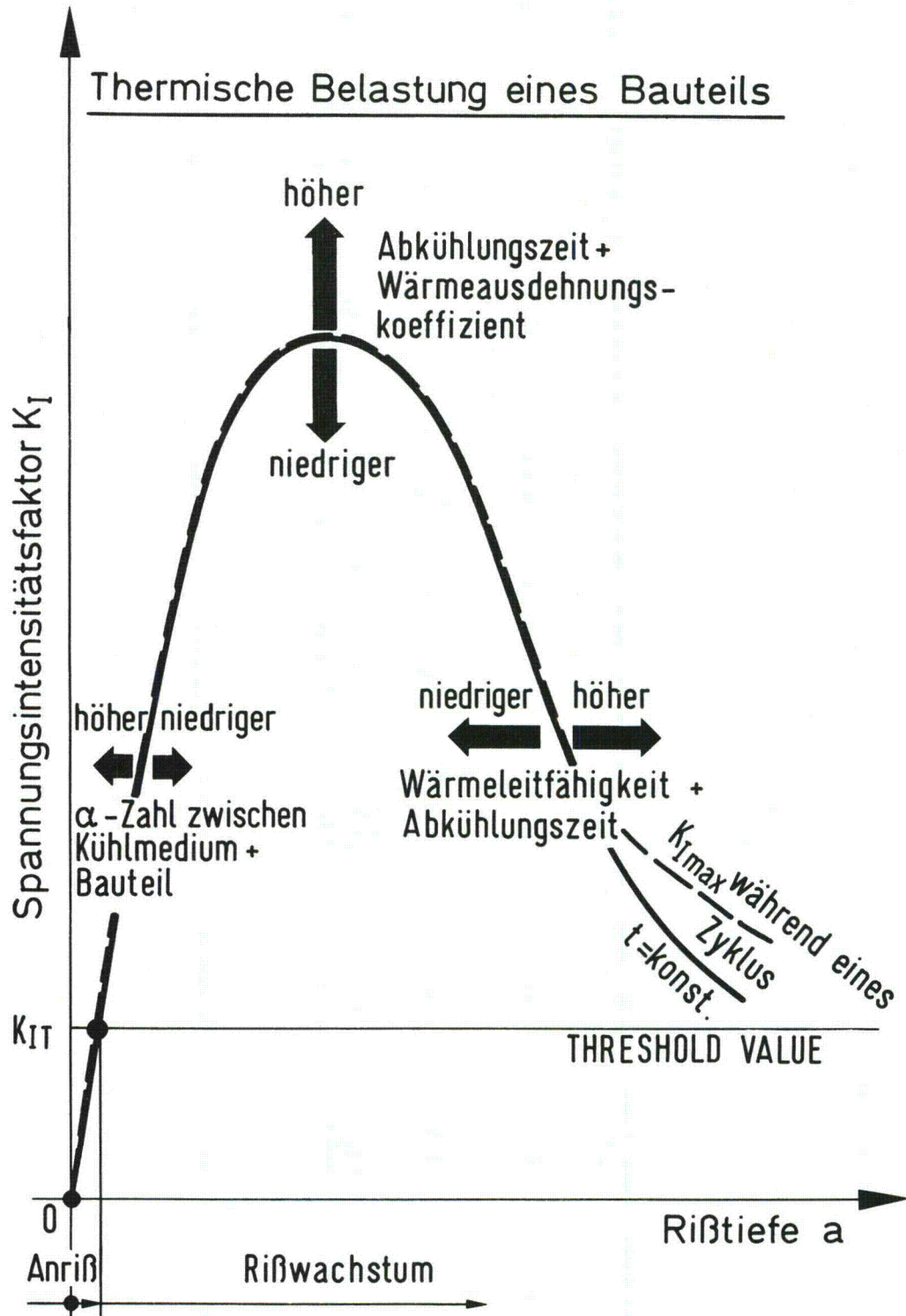
HDR - RDB (plattiert)

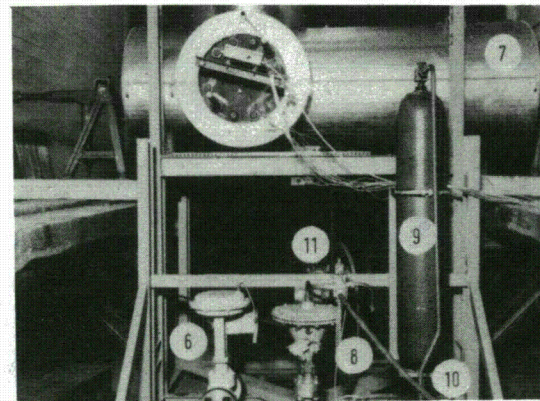
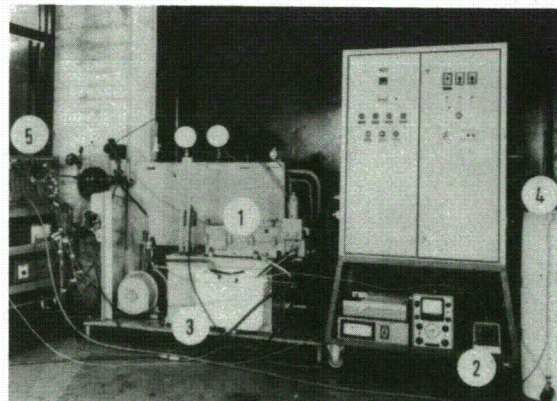
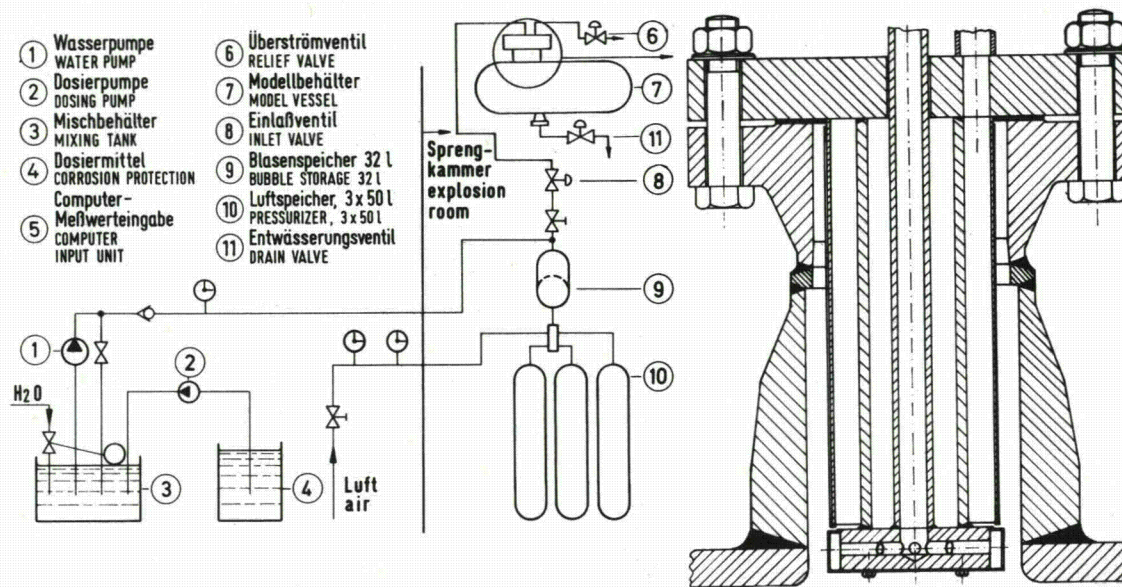


$N_A = ?$

$\frac{da}{dN} = ?$

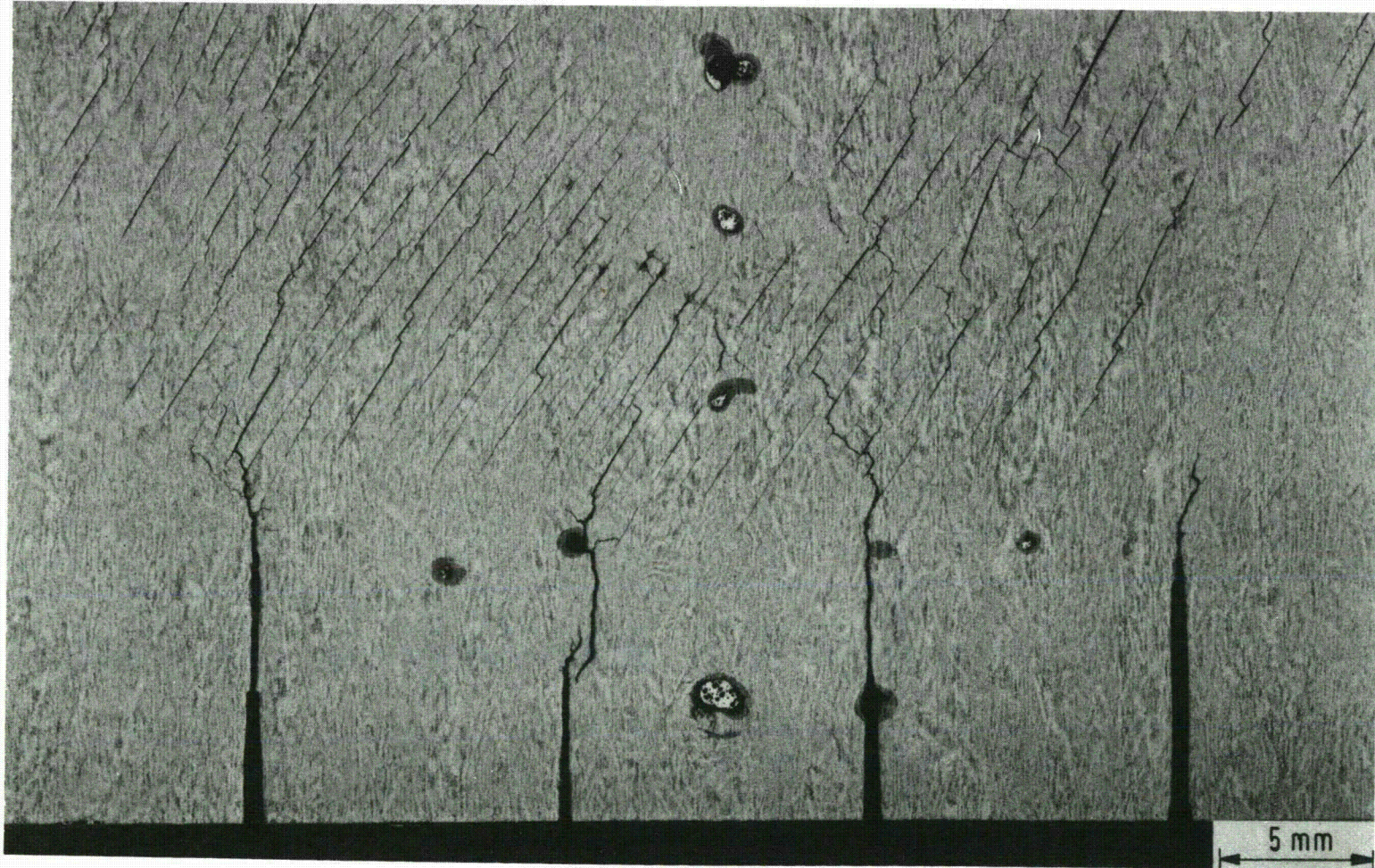
$a = 12\text{ mm}$





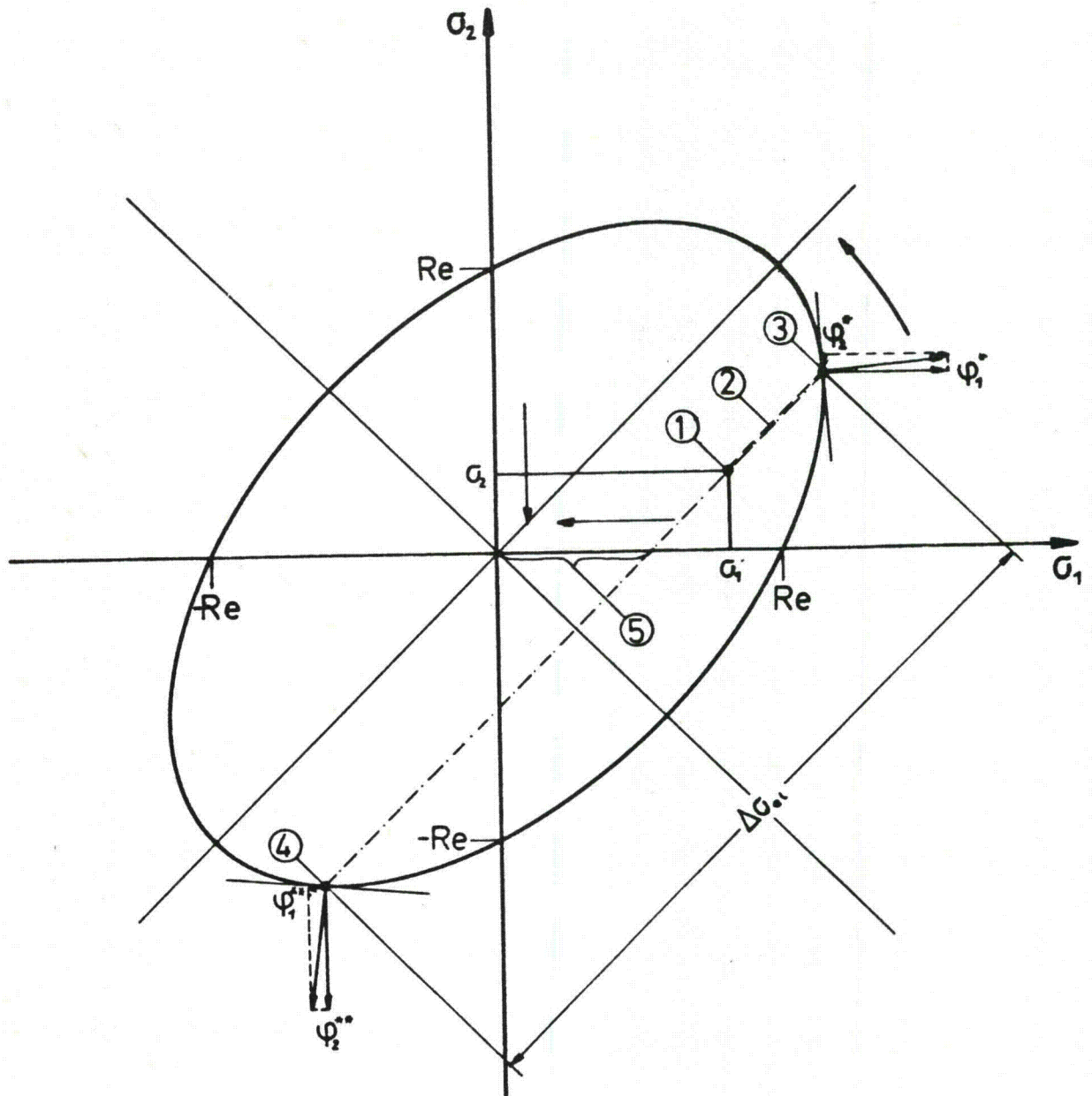
MPA - Thermoschockanlage mit Modellbehälter
MPA - THERMAL SHOCK FACILITY WITH MODEL VESSEL

MPA 5152



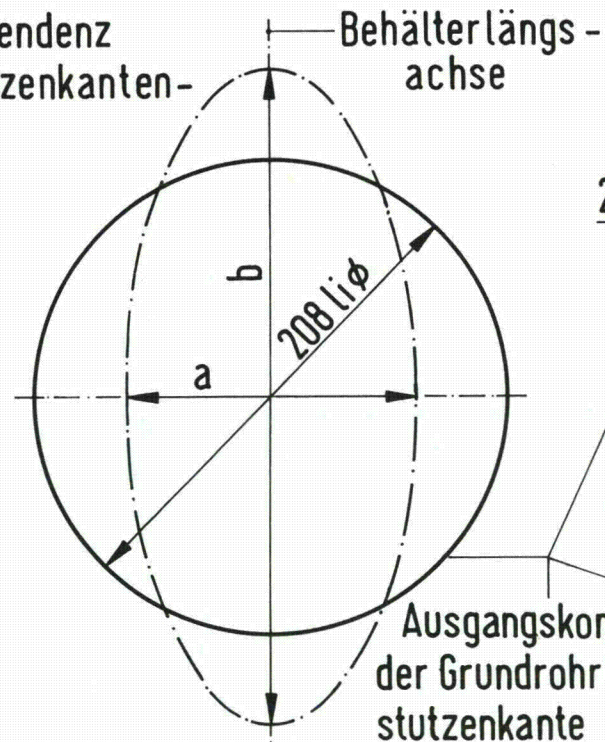
Oberflächenschliff (N = 22 000, $\Delta T = 300$ K)

MPA 5609
STUTTGART



Ratcheting-Verformung in einem
0°-Stutzenanschnitt eines mit Innendruck und
Wärmespannungen belasteten Behälters

Verformungstendenz
Grundrohrstutzenkanten-
kontur



0°-, 180° Schnitt

208 li φ

~2

Wasserstrahltreffpunkt

90°-, 270°- Schnitt

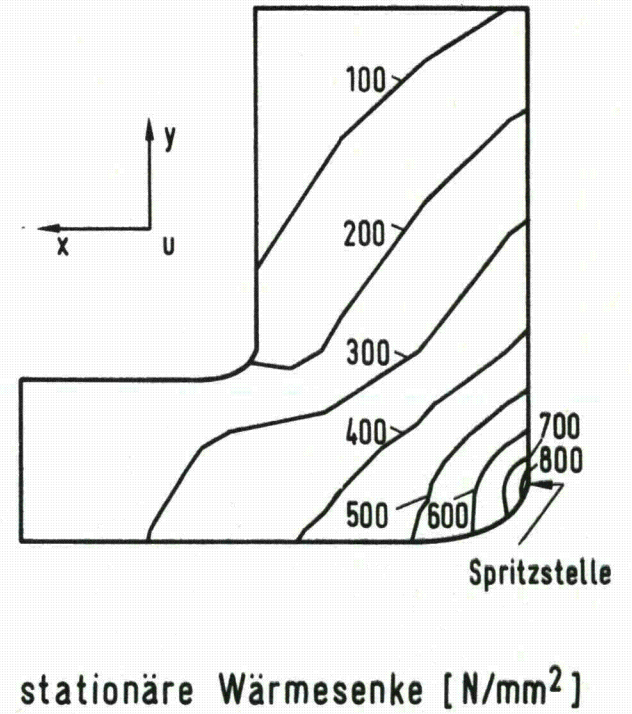
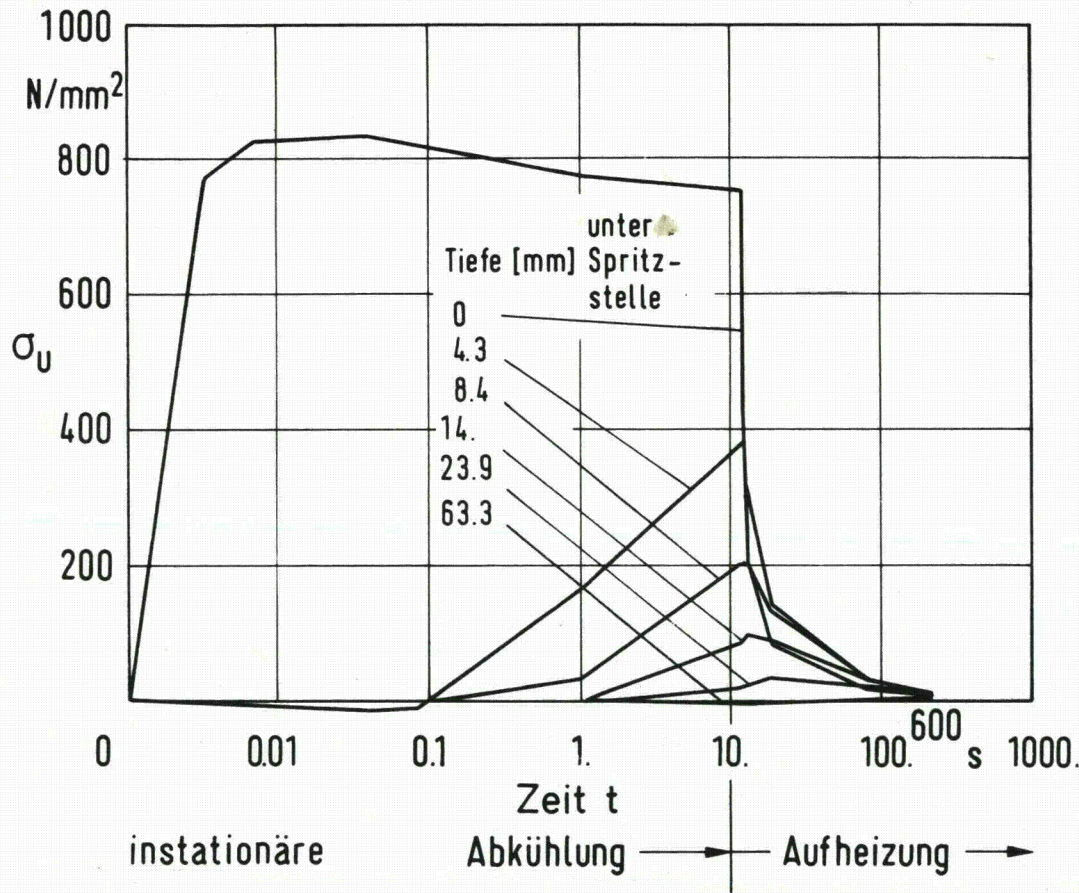
208 li φ

~20

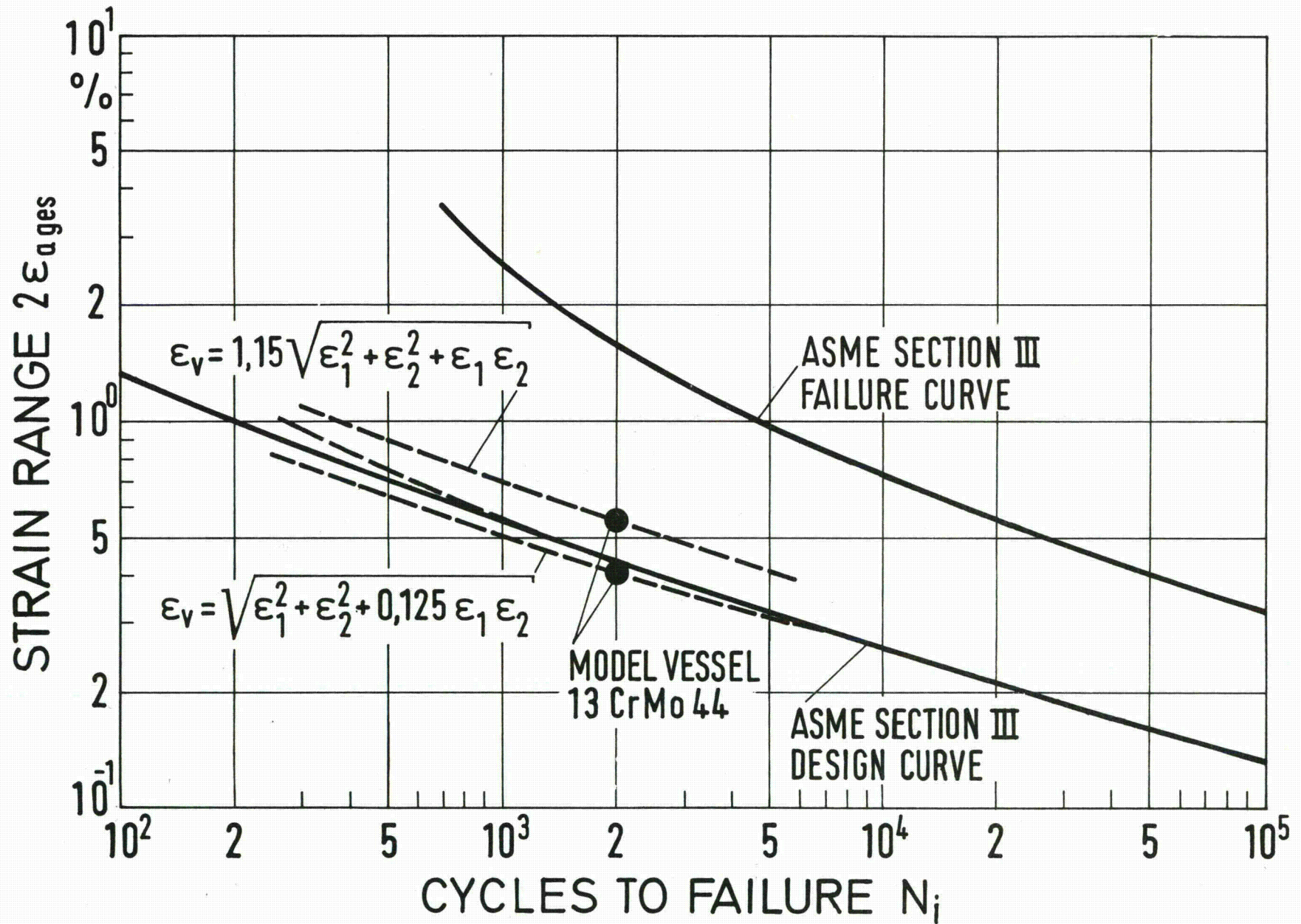
~3,5

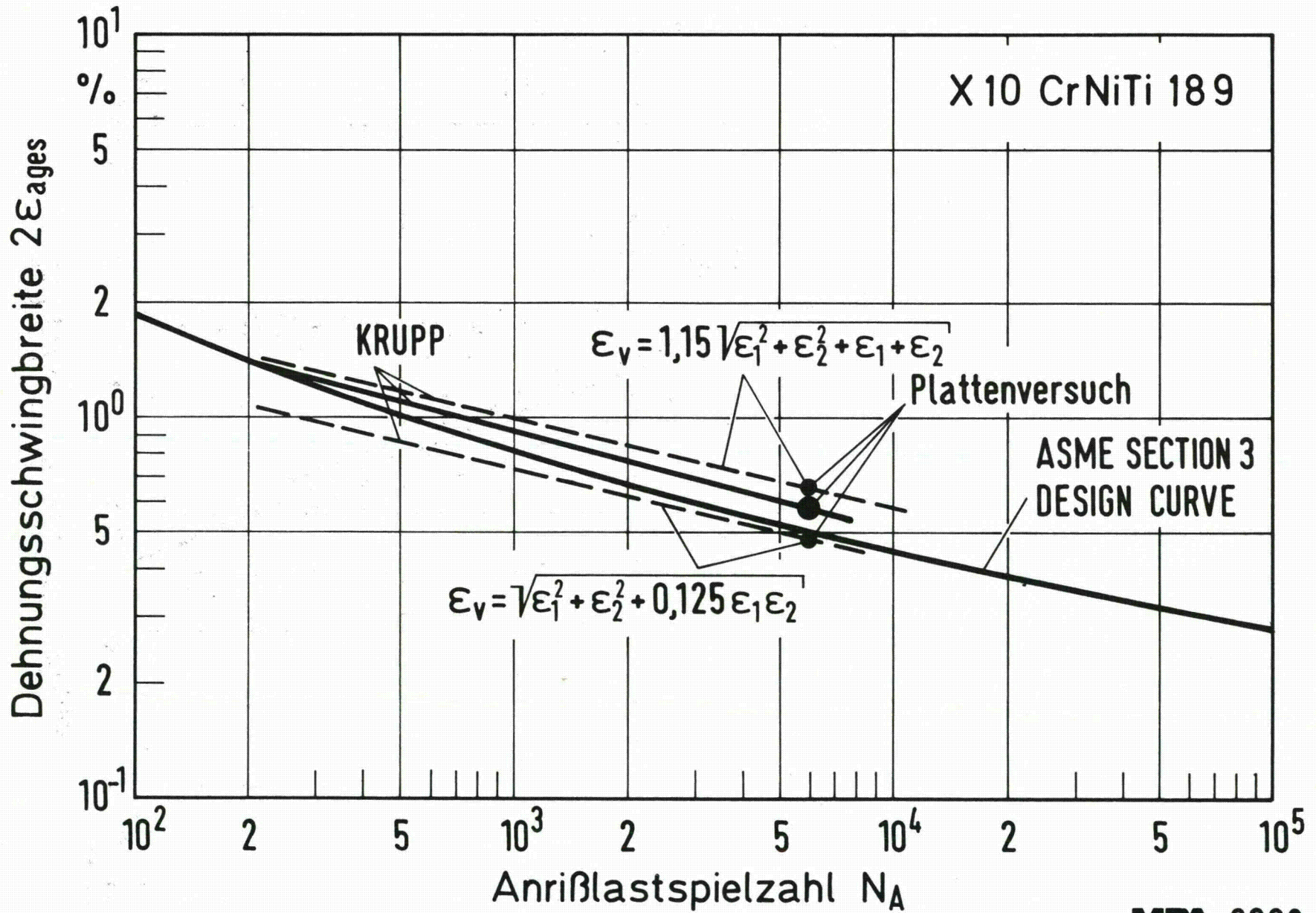
Zahl der Lastwechsel	a [mm]	b [mm]		
0	208	208		
2030	203,3	212,0		
2360	201,5	2966	200,8	211,8
2966	200,8	211,8		

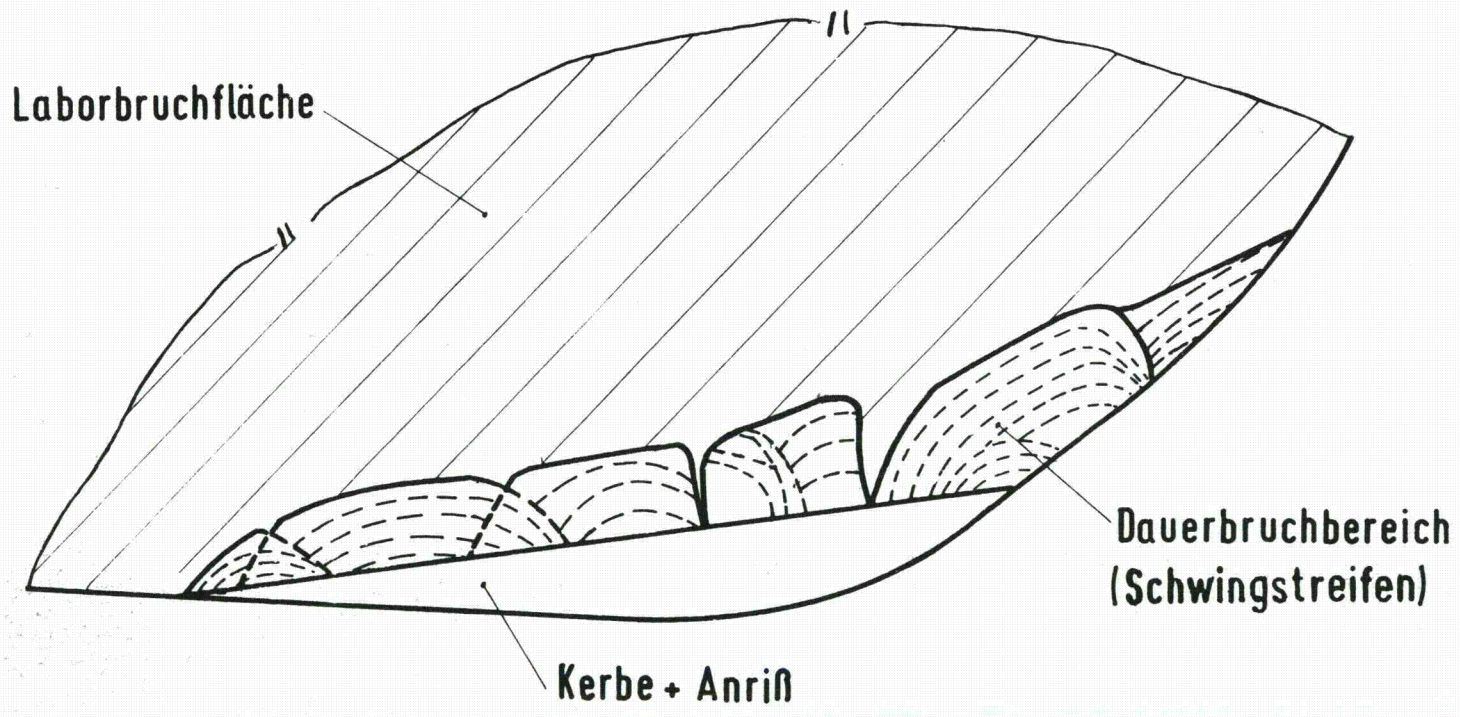
Ratcheting-Verformung des Modellbehälters



Modellbehälter 2-d Umfangsspannungen

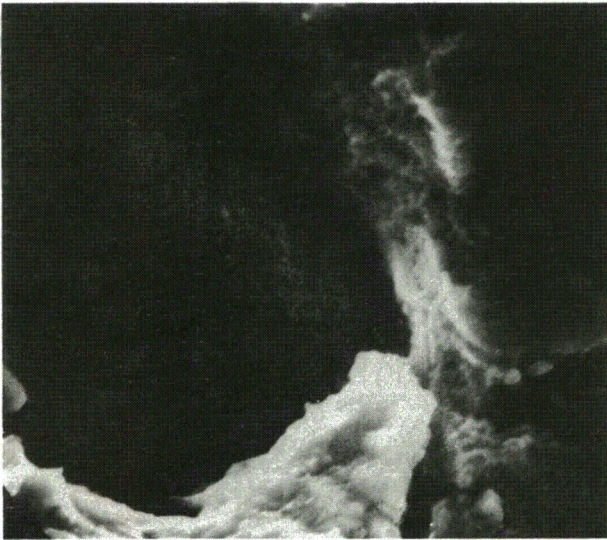






397

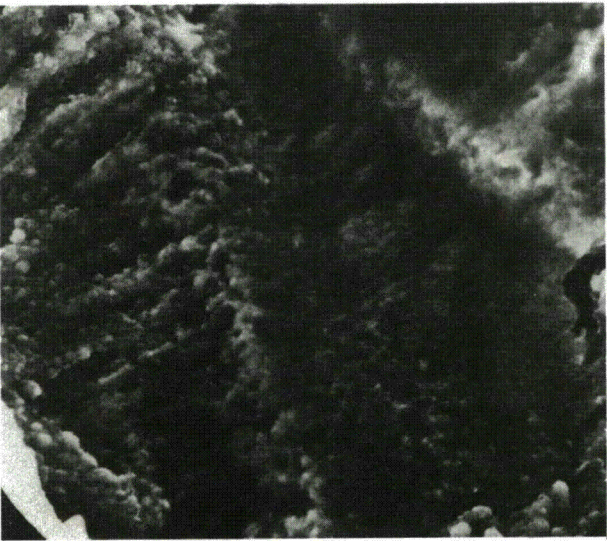
Schwingstreifenorientierung im Bereich des Dauerbruches



Übergang
Anriß → Rißfortschritt
0,352 mm unter Oberfläche

$$\frac{da}{dN} = 4 \cdot 10^{-4}$$

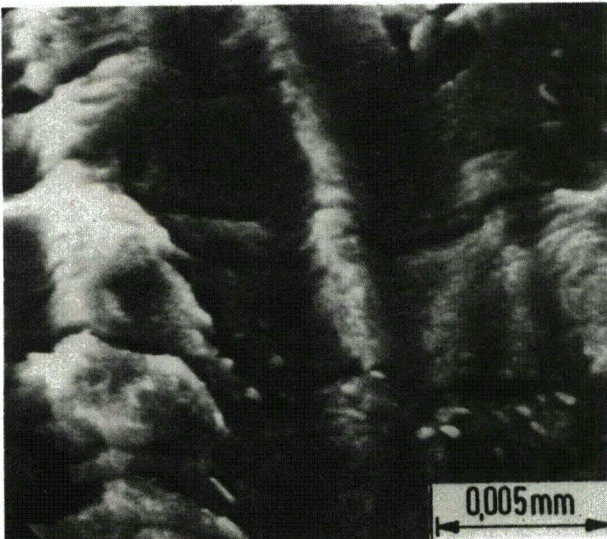
$$\Delta K = 18 \text{ MNm}^{-\frac{3}{2}}$$



0,5 mm unter Oberfläche

$$\frac{da}{dN} = 10 \cdot 10^{-4}$$

$$\Delta K = 22 \text{ MNm}^{-\frac{3}{2}}$$



Übergang

Rißeiterweiterung → Restbruch
0,948 mm unter Oberfläche

$$\frac{da}{dN} = 3 \cdot 10^{-4}$$

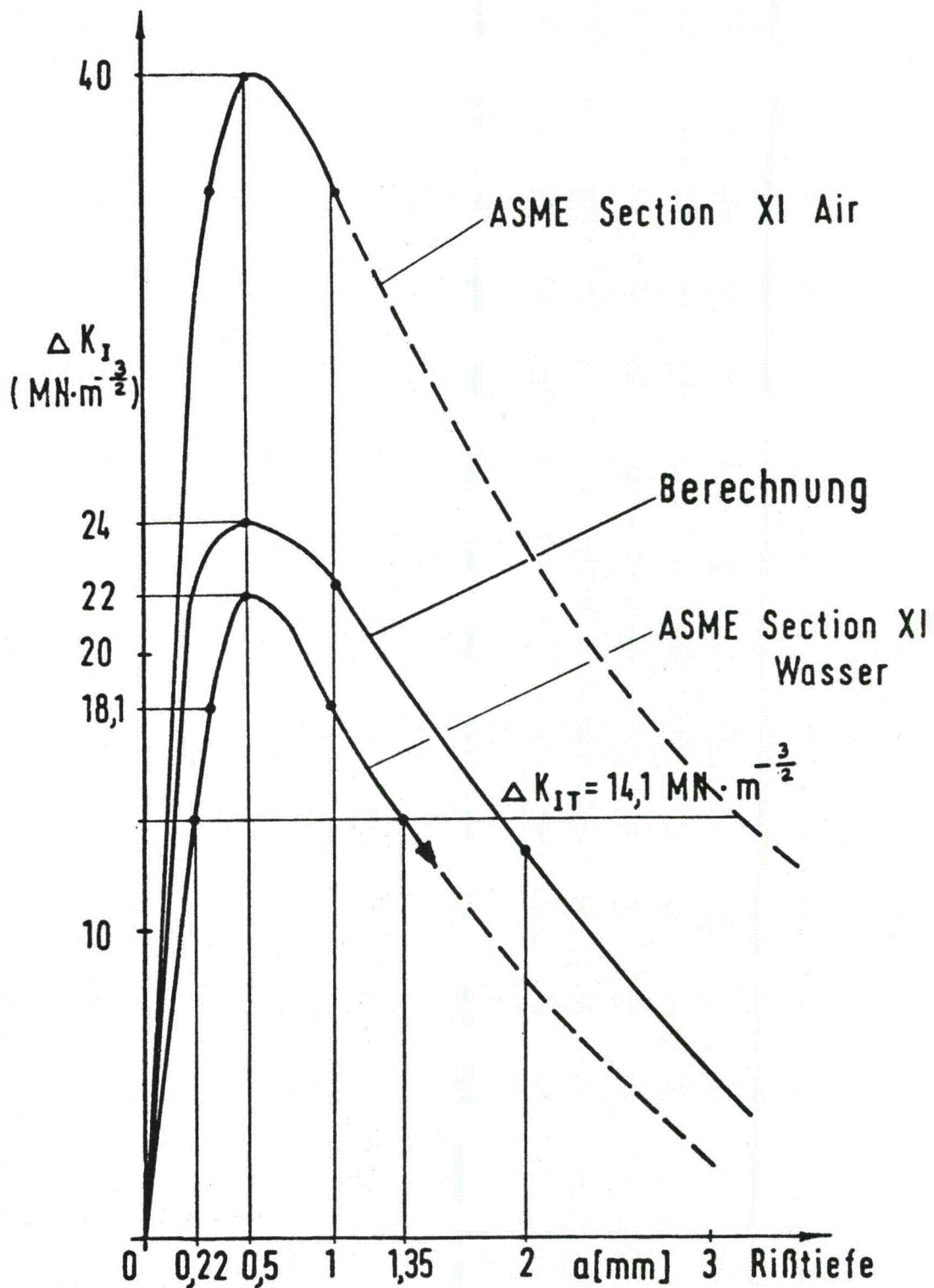
$$\Delta K = 18 \text{ MNm}^{-\frac{3}{2}}$$



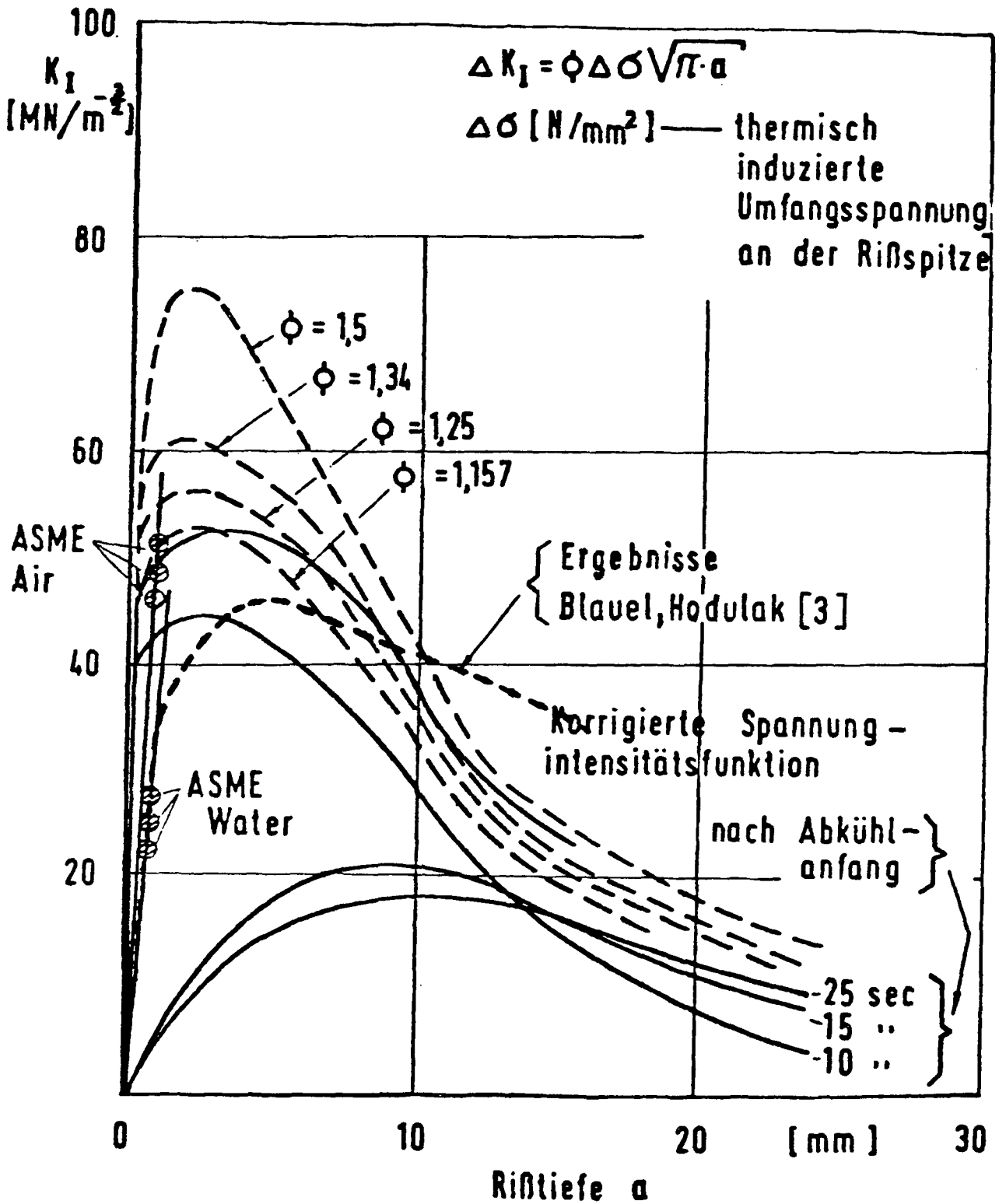
$$\frac{da}{dN} = 1,11 \cdot 10^{-3}$$

$$\frac{da}{dN} = 7,3 \cdot 10^{-4}$$

**Schwingstreifen
auf der
Schiffchenbruchfläche**



Spannungsintensitätsverteilung bei Abkühlung einer ferritischen Platte. (Vergleich zwischen errechneten und experimentell ermittelten Werten)



Spannungsintensitätsfaktor über die Modellbehälter-
 Wanddicke

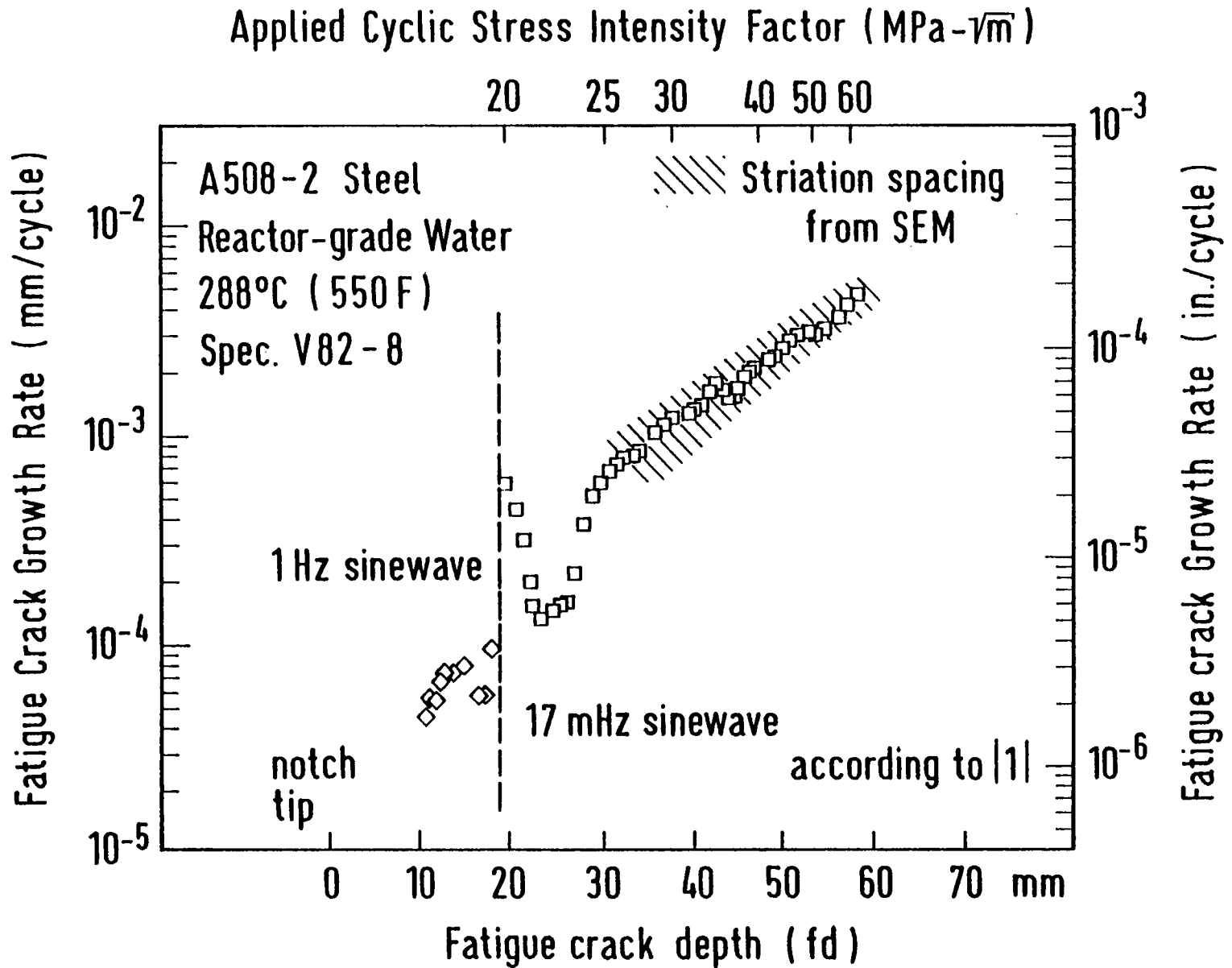


Figure 5: Fatigue crack growth rate versus crack depth

THERMAL FATIGUE CRACK GROWTH ANALYSIS IN A NOZZLE CORNER

J.G. Blauel and L. Hodulak

Fraunhofer-Institut für Werkstoffmechanik, 7800 Freiburg/FRG, Rosastr. 9

Parallel to experimental investigations described in the accompanying paper by Jansky and Beißwänger [1], calculations of the crack growth under local thermal shock fatigue are performed. Estimates of crack growth are based on stress distributions obtained by a finite element analysis for thermal transients in the structure without crack. Stress intensity factors are calculated using interpolation formulae derived from known "basic solutions" for part-through cracks under constant and linearly varying load. The crack propagation at selected parts of the crack front is calculated stepwise by integration of the Paris law with material constants C and n interpolated from test results on compact specimens at constant temperatures. Experimental results for the model vessel test MB1 at an internal pressure of 14 N/mm^2 and a temperature of 320°C exposed to a repeated local spraying with cold water are presented and compared to predictions.

presented at IAEA CSNI Specialists' Meeting on Subcritical Crack Growth,
Freiburg FRG, May 1981

1. Introduction

To simulate a situation of highest criticality for the integrity of a reactor pressure vessel, thermal shock tests are conducted in the framework of the HDR (superheated steam reactor) safety research program sponsored by the German Ministry of Research and Technology. In particular, it is intended to initiate and grow cracks in the nozzle corner region of the HDR pressure vessel by repeated local cooling shocks under PWR service conditions. To develop the experimental methods and qualify the tools of analysis, experiments together with pre- and posttest calculations on plates and model vessels have been conducted and are still in progress (see the accompanying paper by Jansky et al. [1]). This paper discusses an approximate calculation of the crack growth for complex geometrical and loading conditions in the nozzle corner of a pressure vessel under thermal shock fatigue. Specific results are prepared for comparison with experimental findings from first tests on model vessel MB 1.

2. Problem and method of solution

Fig. 1 shows the geometry and the loading as well as the material conditions of the model vessel MB 1 with a thick walled nozzle. The MB 1 operated at an internal pressure of 14 N/mm^2 and a temperature of 320°C and experienced cyclic thermal shocks by rotationally symmetric line spraying with cold water. The spraying time was typically 10 s. It then took a time of about 600 s to restore the surface temperature to 320°C before starting the next shock. A few thousand cycles were necessary to initiate cracks at the nozzle corner and to make them grow to a depth of approximately 4 mm.

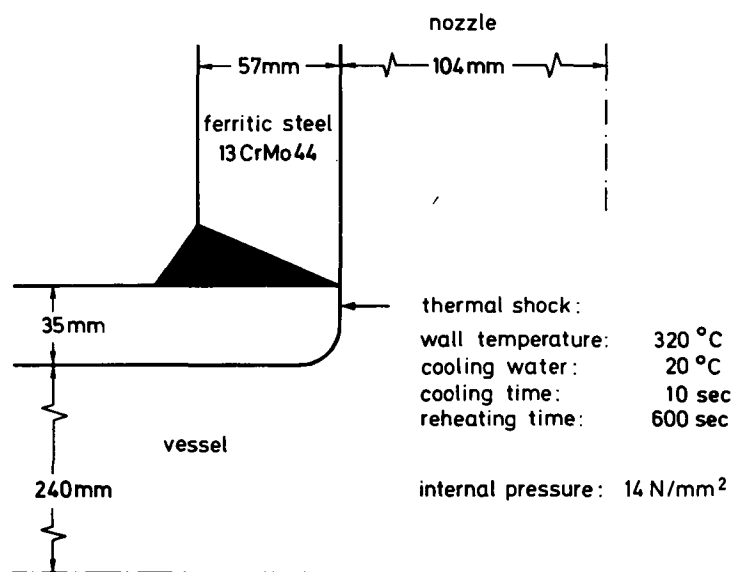


Fig. 1 Nozzle geometry and loading of model vessel MB 1

Estimates of the crack growth are based on stress distributions obtained by a 2D finite element analysis of Jansky and Sauter [2] for thermal transients in the nozzle without a crack. In the upper part of Fig. 2 lines of constant circumferential stress σ_z and a possible development of a crack at a 12 o'clock position in the nozzle initiated at the locus of spraying are shown schematically. Within the framework of LEFM the crack propagation at a selected part of the crack front can be calculated stepwise through integration of the Paris growth law, provided the stress intensity factors (SIF) can be found for all crack geometries developed and the relevant material data are known. Simplifying assumptions are made for the crack shapes and the stress distributions to avoid extensive FE calculation and to allow the use of known SIF relations. The material crack growth data characterizing thermal fatigue are tentatively interpolated from small specimen fatigue tests for MB 1 material under pure sinusoidal loading at constant temperatures.

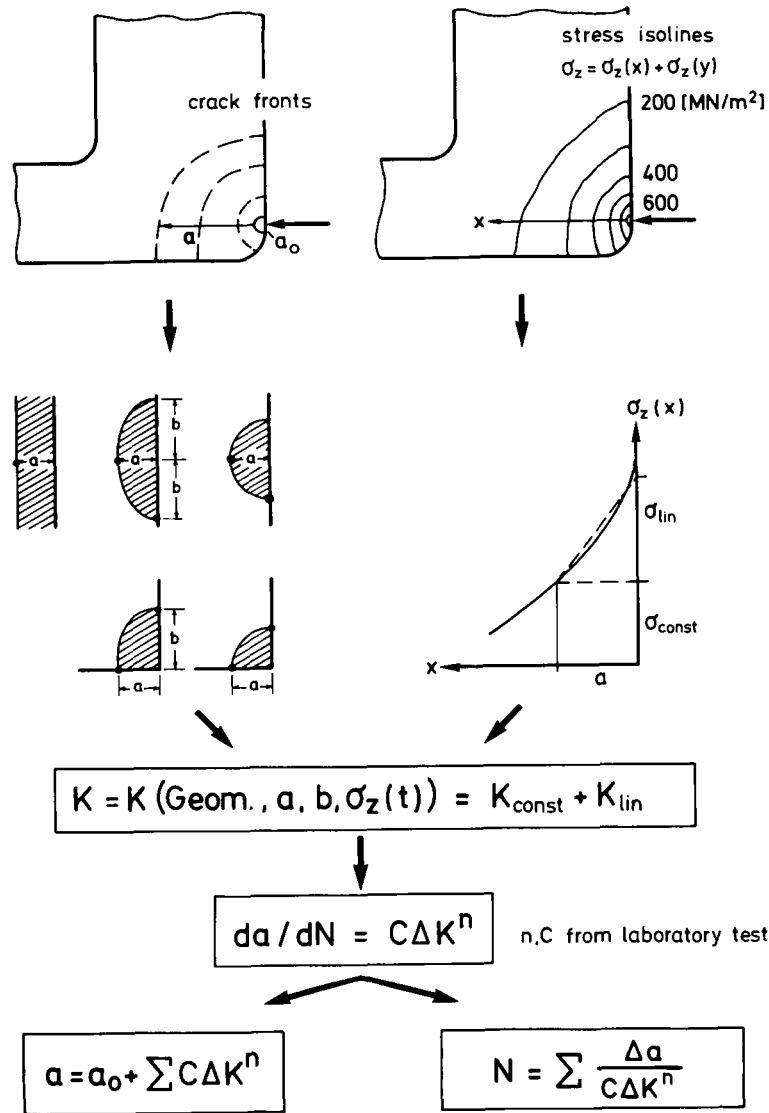


Fig. 2: Estimation scheme for stress intensity factor and crack growth

Because only limited experimental results are presently available for comparison, the crack growth calculations are made for hypothetical cracks. These calculations are mainly used to show the sensitivity of the results to the choice of the input data and the various assumptions and simplifications made.

3. Estimation of the SIF

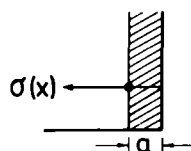
All cracks are assumed small compared to the dimensions of the nozzle and two simplified crack growth models are studied:

1. crack growth is calculated in only one direction (the depth, a , that is the vessel axis) under the assumption of a self-similar crack shape development
2. crack growth is calculated in two directions (the depth, a , that is the vessel axis and the length, b , that is the nozzle axis) and the crack shape (elliptical) is adjusted in each calculation step.

The SIF's are then estimated using interpolation formulae derived from known "basic solutions" for the given geometry and loading conditions (see also [3] and [4]). The "basic solutions" are solutions for the straight, the circular, and the elliptical crack in a semi- (quarter-)infinite space under constant or linearly varying stress distributions. A general formulation for mode I loading can be written as,

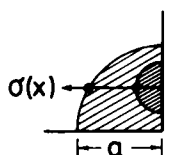
$$K = F (M_{\text{const}} \sigma_{\text{const}} + M_{\text{lin}} \sigma_{\text{lin}}) \sqrt{\pi a} \quad (1)$$

Here σ_{const} and σ_{lin} are a constant and a linearly varying component approximating the actual nonlinear stress profile over the local depth, a , of the crack; if appropriate, a correction is made for the two-dimensional character of the real thermal stress field (see Fig. 2, upper right). M_{const} and M_{lin} take account of the influence of crack and nozzle geometry. The correction function, F , is used to take account of the transition between semi-elliptical and quarter-elliptical crack shapes during growth for the geometry of interest. Specific results are summarized below:



The diagram shows a vertical crack of depth a in a semi-infinite body. A constant stress $\sigma(x)$ is applied across the crack. The crack is represented by a shaded rectangular area of width a and height $\sigma(x)$.

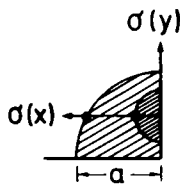
$$K_a = \left\{ 1.122 \cdot \sigma(x)_{\text{const}} + 0.439 \cdot \sigma(x)_{\text{lin}} \right\} \sqrt{\pi a} \quad (2)$$



The diagram shows a vertical crack of depth a in a semi-infinite body. A linearly varying stress $\sigma(x)$ is applied across the crack, represented by a shaded area that tapers from $\sigma(x)$ at the surface to zero at the tip. The crack is represented by a shaded area of width a and height $\sigma(x)$.

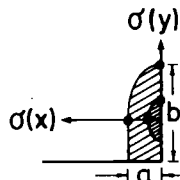
$$K_a = F \left\{ 1.05 \cdot \frac{2}{\pi} \cdot \sigma(x)_{\text{const}} + 0.205 \cdot \sigma(x)_{\text{lin}} \right\} \sqrt{\pi a} \quad (3)$$

with $F = 1 + 0.007a$ for $a = 0 \dots 18 \text{ mm}$



$$K_a = F \left\{ 1.05 \cdot \frac{2}{\pi} \cdot \sigma(x)_{\text{const}} + (0.205 - 0.003a) \sigma(x)_{\text{lin}} \right\} \sqrt{\pi a} \quad (4)$$

with $F = 1 + 0.007a$ for $a = 0 \dots 18 \text{ mm}$



$$K_b = F_b \left\{ \frac{1.05}{\sqrt{Q}} \cdot \sigma(y)_{\text{const}} + (0.439 - (0.234 + 0.003a) \frac{a}{b}) \cdot \sigma(y)_{\text{lin}} \right\} \sqrt{\frac{a}{b}} \sqrt{\pi a}$$

with $F_b = 1.20$

$$K_a = F_a \left\{ \frac{1.05}{\sqrt{Q}} \cdot \sigma(x)_{\text{const}} + (0.439 - (0.234 + 0.003a) \frac{a}{b}) \sigma(x)_{\text{lin}} \right\} \sqrt{\pi a}$$

with $F_a = 1 + 0.007a$ for $a = 0 \dots 18 \text{ mm}$

(5)

For the evaluation of the crack growth only in depth-direction under the assumption of a constant crack shape the stress intensity factors at the apex, K_a , are calculated using eqs (2)-(4). The factor M_{const} and M_{lin} for straight cracks in eq. (2) are taken from Tada, Paris, Irwin [5]. In eq. (3) the corrections M_{const} and M_{lin} are taken from Kobayashi, Enetanya and Shah [6] and Hayashi and Abé [7], respectively. In eq. (4) M_{lin} is modified to include the influence of the stress gradient $\sigma(y)$ in the second direction for the specific geometry and loading of the MB 1. The function F approximately interpolates between the SIF of a small semi-circular crack at its apex (for $a \rightarrow 0$) and the SIF of a quarter-circular crack at the crack front portion somewhat beneath the vessel surface (for $a \rightarrow 18 \text{ mm}$).

The crack growth evaluation in two directions is based on SIF's for the apex, K_a , and the surface, K_b , which are calculated using eq. (5). Depending on the aspect ratio a/b , which is adjusted in each step of the propagation calculation, M_{lin} can be approximated as $M_{\text{lin}} = 0,439 - 0.234 \frac{a}{b}$, while M_{const} is approximated as $1,05/\sqrt{Q}$, where Q is the shape factor according to ASME [8]. For K_b the nozzle geometry correction, $F_b = 1.2$ is chosen to yield $M_{\text{const}} = 1.25/\sqrt{Q}$, which corresponds closely to the SIF of semi-(quarter-) elliptical cracks at the part of the crack front near the specimen surface.

Resulting SIF's as a function of crack depth for the geometry and loading conditions of Fig. 1 are plotted in Fig. 3. From the behavior of the thermal stresses for each crack model the initial increase of the SIF with crack depth is followed by a gradual decrease after a certain crack depth is exceeded. The influence of the crack model on the results shown here is even more apparent in Fig. 4, where the crack growth is plotted. It should be noted that the results obtained with eq. (5) depend strongly on the aspect ratio a_0/b_0 of the starter crack, with in Fig. 4 is assumed $a_0/b_0 = 0.43$.

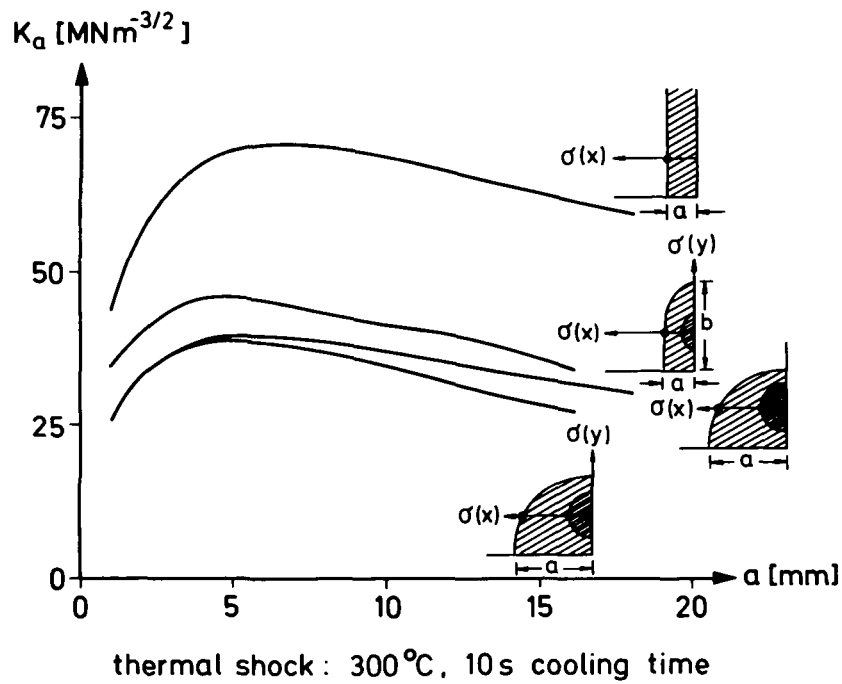


Fig. 3 Stress intensity factor K_a at crack apex as function of crack depth a — influence of crack idealization and stress distribution (geometry and loading: Fig. 1)

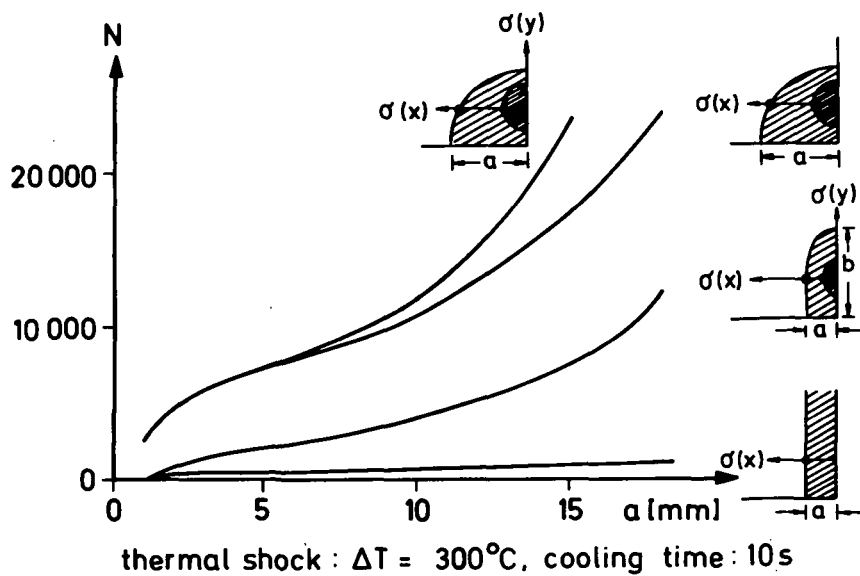


Fig. 4 Number N of cycles necessary to extend crack $a_0/b_0 = 0.43$ to depth a — influence of idealization for K estimation (geometry and loading: Fig. 1; material constants: Fig. 6 "interpolation")

4. Treatment of material constants

For the calculation of the crack growth by integrating the Paris relation

$$da/dN = C \cdot \Delta K^n \quad (6)$$

that is

$$a = a_0 + \Sigma \Delta a = a_0 + \Sigma C \cdot \Delta K_a^n \cdot \Delta N$$

$$N = \Sigma \Delta N = \Sigma (\Delta a / (C \Delta K^n)) \quad (7)$$

$$b = b_0 + \Sigma \Delta b = b_0 + \Sigma (\Delta K_b / \Delta K_a)^n \cdot \Delta a$$

the material parameters C and n must be found experimentally. Since C and n measured under mechanical fatigue depend on temperature, frequency, stress ratio $R = \sigma_{\min}/\sigma_{\max}$ and the surrounding atmosphere, their use for thermal fatigue conditions poses problems: Firstly in thermal fatigue the stress cycling may be accompanied by some temperature cycling at the crack tip which will influence the growth rate; the amplitude and the mean value of the temperature cycle will depend on the crack depth. Secondly the SIF as a function of time during a thermal cycle depends on the crack depth (Fig. 5) and is different from a sinus function usually used in tension-tension fatigue tests in the laboratory.

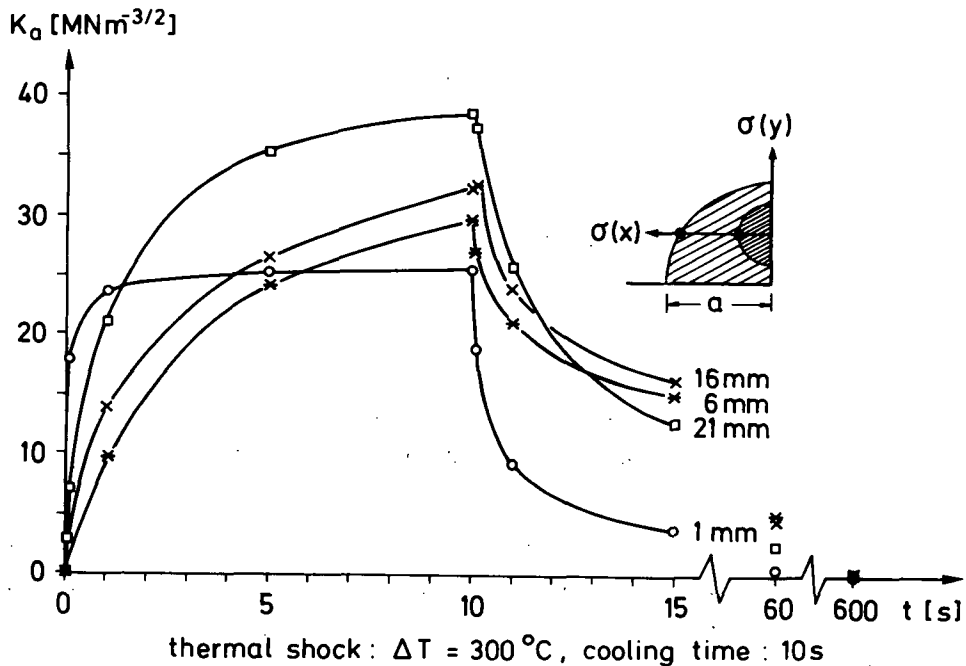


Fig. 5 Stress intensity factor K_a at apex of semi- to quarter-circular crack as a function of time into one thermal shock specified in Fig. 1 for different crack depths a

The strong dependence on temperature and other parameters of the crack growth for the model vessel-material 13 Cr Mo 44 as evaluated by Prümmer, Blauel and Kofler [8] is shown in Fig. 6 together with the ASME B and PV Code Limit curves [9] for a general ferritic material.

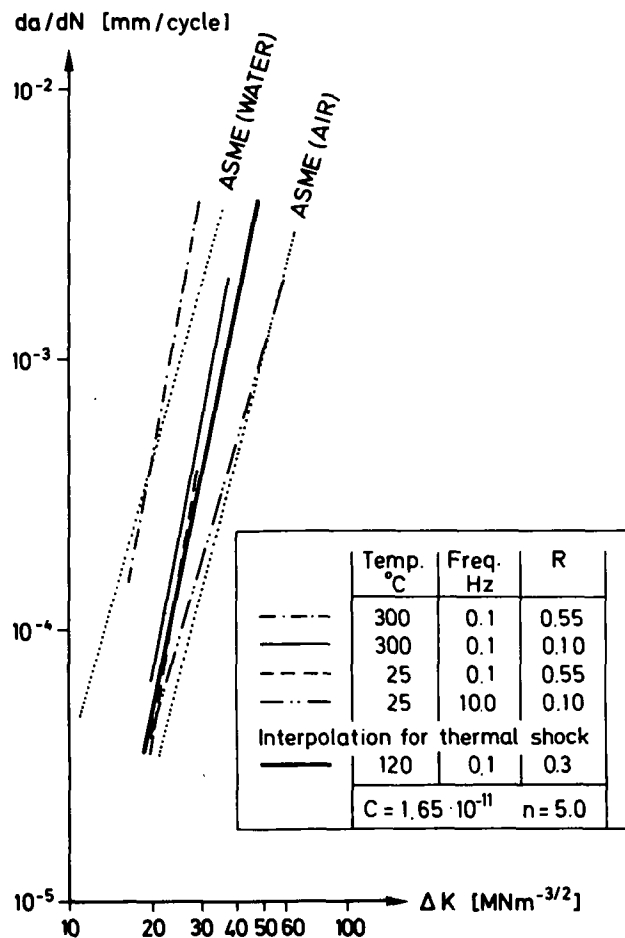


Fig. 6 Fatigue crack growth data of the model vessel material (ferritic steel 13 Cr Mo 44) measured under pure tension loading with 28 mm thick compact specimens [8] - the ASME-Code limit curves [9] are shown for comparison

For the model calculations using eq. (7) C- and n-values are chosen by interpolating the results in Fig. 6 for a mean temperature $T = 120^{\circ}\text{C}$, a mean stress ratio $R = 0.3$, and an approximate frequency of 0.1 Hz as estimated from Fig. 5 for relatively small cracks and an internal pressure of 14 N/mm^2 . An influence of the spraying water has been neglected for this frequency. As a further step of refinement, C- and n-values are interpolated for the temperature at every crack front location, a and b. Then the crack growth calculation is made as follows:

$$a = a_0 + \sum C(a) \cdot \Delta K_a^{n(a)} \cdot \Delta N$$

$$b = b_0 + \sum C(b) \cdot \Delta K_b^{n(b)} \cdot \Delta N$$

$$N = \sum \frac{\Delta a}{C(a) \cdot \Delta K_a^{n(a)}}$$

Fig. 7 demonstrates the influence of the material parameters C and n on crack growth for the semi-/quarter-elliptical crack model under the thermal shock loading of Fig. 1.

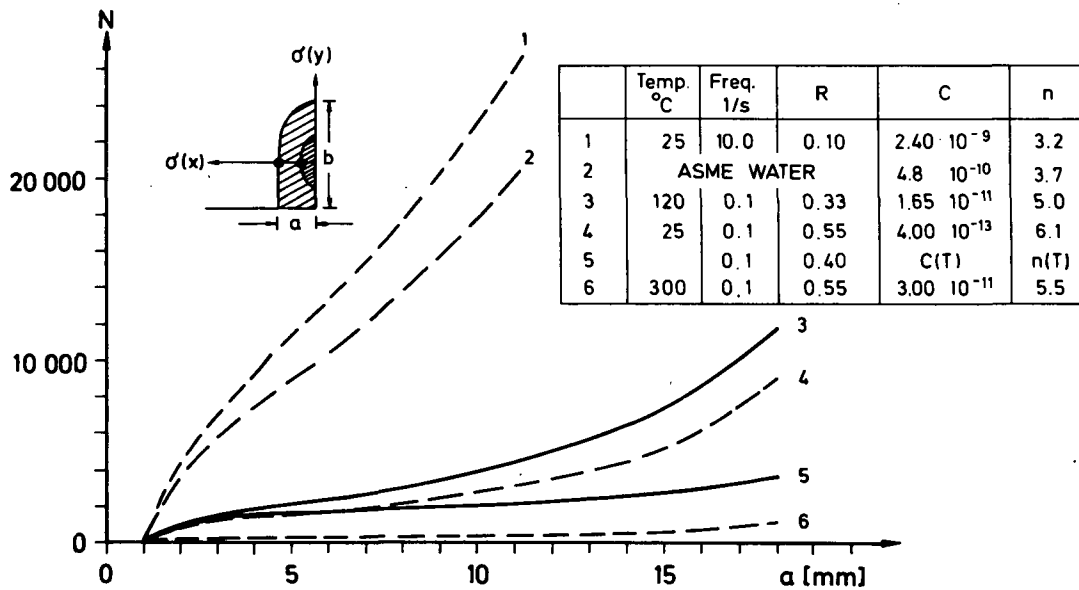


Fig. 7 Number N of cycles necessary for crack extension from $a_0 = 1$ mm to a. Dependence on material constants

5. Application and concluding remarks

The inexpensive approximate calculation method as developed so far for the specific case of nozzle corner cracks in model vessel MB 1 under thermal shock loading has been used by Blaue1 and Hodulak [10] to investigate the influence of crack depth and initial crack shape, of cooling time, and of material parameters C and n on the SIF and crack growth. As an example, the influence of the cooling time on the crack growth is shown in Fig. 8.

In figure 9 the experimental findings according to Jansky [1] are compared to calculations based on the estimation scheme of Fig. 2. Depending on the choice of the material parameters C and n relatively close correspondence or under- and overestimations are found for either the local crack growth rates da/dN as compared to the striation spacing on the fracture surface or the predicted number of cycles and that actually applied during the test. It is obvious that the badly defined starter notch away from the spraying center poses problems in the analysis; other discrepancies may be explained through differences between the thermal boundaries assumed in the stress analysis and those prevailing in the test. The limited number of test results does not yet allow a verification of the fracture mechanics analysis. Further experiments are being prepared.

ACKNOWLEDGMENT

This work was supported by the German Ministry of Research and Technology through KFK contract No. 825/02/480188 RS 0123/B/FhG 674

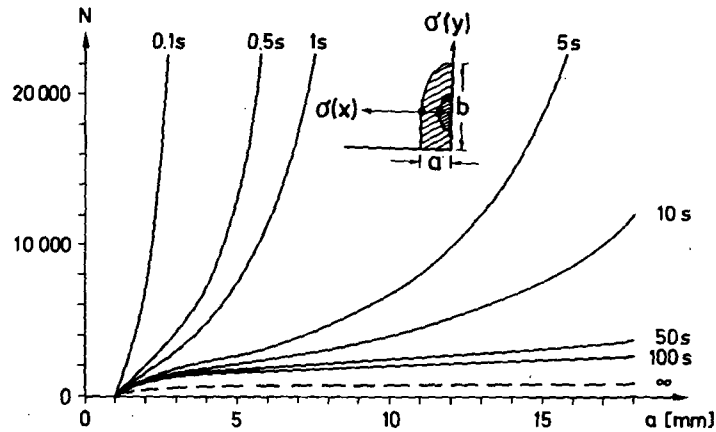
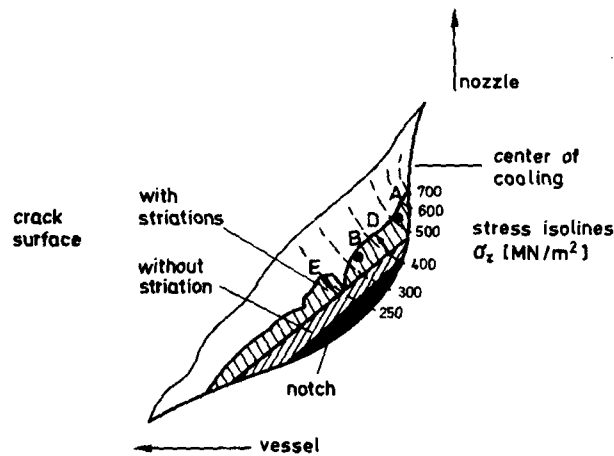


Fig. 8 Number N of cycles necessary for crack extension from $a_0 = 1$ mm to a — dependence on cooling time

Apart from hypothetical cracks, the experimentally observed crack phenomena in MB 1 were also analyzed.



Location	crack growth rate da/dN (mm/cycle)		
	striation spacing	calculated: $C\Delta K^n$ $C = 1.65 \times 10^{-11}$ $n = 5$	ASME water
A	23×10^{-4}	3.8×10^{-4}	21×10^{-4}
B	7.6×10^{-4}	$(3.2 - 5.6) \times 10^{-4}$	$(17 - 28) \times 10^{-4}$
Number N of cycles for crack extension			
	experiment	calculated: $\sum \Delta a / C\Delta K^n$ $C = 1.65 \times 10^{-11}$ $n = 5$	ASME water
D	2400	2600	231
E	2400	15400	1450

Fig. 9 Comparison of experimentally observed and calculated crack growth phenomena in model vessel MB 1

References

- [1] JANSKY, J.; SAUTER, A.; BEISSWÄNGER, H.: "Crack Initiation and Crack Growth at the Inner Nozzle Corner Surface Under Thermal Shock Loading " IAEA CSNI Specialists' Meeting on Subcritical Crack Growth, Freiburg May 1981
- [2] JANSKY, J.; SAUTER, A.: Thermoschock-Berechnung an Platten-Unterprogramm 1 MPA 815 103 a
- [3] KOBAYASHI, A.S. et al.: "A Procedure for Estimating the Stress Intensity Factor of a Flattened Surface Crack at a Nozzle Corner", Joint ASME/CSME Press. Vessel and Piping Conference, Montreal, June 25-30, 1978
- [4] PETERS, W.H.; BLAUDEL, J.G.: "A Study of Part Through Cracks in a Reactor Beltline Subjected to Thermal Shock", in: "Thermal Stresses in Severe Environments" ed. by Hasselman and Heller, Plenum Press, New York, London 1980
- [5] TADA, H.; PARIS, P.; IRWIN, G.: "The Stress Analysis of Cracks" Handbook, Del. Research Corporation, Hellertown, 1973
- [6] KOBAYASHI, A.S.; ENETANYA, A.N.; SHAH, R.C.: "Stress Intensity Factors of Elliptical Cracks", Proc. of the Conference on the Prospects of Advanced Fracture Mechanics, Delft, 24-28 June, 1974
- [7] HAYASHI, K.; ABE, H.: "Stress Intensity Factors for a Semi-Elliptical Crack in the Surface of a Semi-Infinite Body Subjected to Linearly Varying Pressure on the Crack Surface", Int. J. Fracture 15 (1979), R 171-174
- [8] PROMMER, R.; BLAUDEL, J.G.; KOFLER, E.: "Rißausbreitungsverhalten unter wiederholter Thermoschockbeanspruchung" IFKM-Zwischenbericht V 9/79, Juli 1979
- [9] ASME Boiler and Pressure Vessel Code, Sec. XI. 1974
- [10] BLAUDEL, J.G.; HODULAK, L.: "Rißwachstumsanalyse in einem Druckbehälterstutzen unter Thermoschockbeanspruchung", 4. Statusbericht des Projektes HDR-Sicherheitsprogramm, Karlsruhe, December 10, 1980

SUBCRITICAL CRACK GROWTH IN UNDERCLAD REGION

by

Milan BRUMOVSKY 1), Vaclav LINHART 2), Jan RUDA 3)

1) SKODA Concern, Power Machinery Plant, Plzen, CSSR

2) State Institute of Materials, Praha, CSSR

A b s t r a c t

Paper deals with the problem of subcritical crack growth in the transition zone between base material and austenitic stainless steel cladding. As a material under the study steel of Cr-Mo-V type (15Kh2MFa) has been chosen.

Crack growth rate as a function of stress intensity factor has been measured for pure base and clad materials likewise for the transition zone, too. In the latter case, cracks started both from the surface (cladding materials) and from the base material. For base and cladding materials threshold stress intensity factors have been determined as a function of stress asymmetry.

Results received in this study show to the decelerating effect of the boundary base material/cladding material which is explained by the role of this boundary.

Discussion of these results is made with respect to the other literature results, and to the reactor pressure vessel lifetime and safety.

1. INTRODUCTION

Defects in nuclear reactor pressure vessels, clad by austenitic stainless steel and situated near the boundary between base material and stainless steel cladding, could be the source of a substantial decrease of pressure vessel wall strength, especially from the following points of view:

- pressure vessel wall strength (decrease of net section),
- pressure vessel fatigue (decrease in endurance limit of material),
- brittle fracture initiation from this defect that can substantially increase during vessel lifetime.

Last problem becomes the most important because necessity of ensuring practically 100 % pressure vessel safety from the point of view of brittle fracture is required.

At this time only one method of defect evaluation including calculation of its allowability in reactor pressure vessel wall exists in codes [1]. This method is prepared only for types of steels, used for the

PWR, resp. BWR type of reactors in western countries, i.e. for steels of ASTM A 533B and ASTM A 508 types. Moreover, this method explicitly does not contain necessary material constants for underclad defects, only characteristics of base material are presented, without the effect of stainless steel cladding and its heat affected zone.

This work has been aimed to the determination of the most important material characteristics of 15Kh2MFA type of steel and the influence of austenitic stainless steel cladding on the subcritical crack growth rate in the transition zone between base material and stainless steel.

2. MATERIALS AND EXPERIMENTAL METHODS

Crack growth rate under cyclic loading has been measured in the 15Kh2MFA type steel, manufactured for nuclear reactor pressure vessels; specimens were cut off from the base material, stainless steel cladding and bimetal junction of base material-stainless steel cladding. All materials and cladding were manufactured by SKODA CONCERN, Plzen, CSSR.

Austenitic stainless steel cladding were prepared by automatic welding of steel strip under flux; first pass by Sv07Kh25N13, other three by Sv08Kh19N10G2B types of steel; the whole thickness of cladding in maximum reaches 10 mm.

Crack growth rates in base material have been measured in flat specimens of net section equal to 80 x 8 mm with side cracks. The same type of specimens has been used also for measurements in separated austenitic stainless steel cladding and in the transition zone between base material and stainless cladding in both directions of crack growth. For this purpose specimens with side crack or inner throughcrack (centric or excentric position) have been used, too. In all cases specimens have been loaded in tension with coefficient of asymmetry in the range of 0.1 to 0.9, small part also with $R = -1$. Loading frequency has been chosen equal to 35 and for comparison 0.2 Hz, too. Part of the experimental programme has been carried out with specimens under three-point bending loading with crack situated in outer surface; crack has propagated into base material or into stainless steel, depending on specimen cutting orientation.

Crack growth has been evaluated from gradual crack length measurements. This measurement has been carried out using special prepared measuring microscope (accuracy equal to 0.01 mm) and with resistometric method.

3. METHOD OF EXPERIMENT EVALUATION

Evaluation of crack growth measurement has been carried out using known Paris-Erdogan equation of type

$$\frac{da}{dN} = C_0 \cdot (\Delta K)^n \quad (1)$$

where a - crack length,

N - Number of cycles,

C_0, n - material constants,

K - amplitude of stress intensity factor.

For evaluation of measured values statistics methods have been used - regression analysis with determination of mean curve of scattering band and bilateral tolerance band (probability of values equal to 90 % with 0.5 % risk).

Moreover, threshold conditions for crack growth have been studied, too. This threshold value is determined for zero crack growth rate in 10^6 loading cycles. These threshold values are determined by gradual increases or decreases of cyclic loading in a very narrow interval. Dependence of threshold values of stress intensity factor amplitude on coefficient of asymmetry can be written as

$$(\Delta K_{Ts} - \Delta K_{Ts,0}) \cdot (1 - R)^A = B \quad (2)$$

where $\Delta K_{Ts,0}$, A, B - material constants,
R - coefficient of cycle asymmetry.

4. EXPERIMENTAL RESULTS

Experimental results can be divided into three groups depending on studied materials:

- base material,
- austenitic stainless steel cladding (separated),
- transition from base material to cladding (heat affected zone and fusion line).

Moreover, according to the planning of experiments our results can be evaluated also from the point of view of:

- threshold values for crack growth,
- crack growth rate.

4.1. Threshold conditions

Threshold conditions for crack growth have been evaluated according to equation (2).

Threshold values of stress intensity factor amplitudes, ΔK_{Ts} , are lower for austenitic stainless steel cladding in comparison with base material, independently of larger scattering of results. The largest difference, according to the equation (2) is received for coefficient of asymmetry $R = 0$, when ΔK_{Ts} for base material is equal to $15 \text{ MPa}\cdot\text{m}^{1/2}$, while for stainless steel cladding is equal only to $6 \text{ MPa}\cdot\text{m}^{1/2}$: it means approximately 2.5 smaller.

According to the equation (2) received results show a sharp hyperbolic dependence on coefficient of asymmetry. Decrease of threshold stress intensity factor values is more pronounced for base material in comparison with stainless cladding - for both material and coefficient asymmetry equal to $R = 0.9$ threshold values of stress intensity factors are close to $2 \text{ MPa}\cdot\text{m}^{1/2}$.

4.2. Crack growth rate

Crack growth rate has been measured in all three mentioned materials, received results are summarized in fig.1.

Results, measured in separated austenitic stainless steel cladding are represented by scatter band 1 (loading frequency equal to 35 Hz) and band 2 (loading frequency equal to 0.2 Hz). It is seen that decrease in loading frequency has positive influence on decrease of crack growth rate.

At lower loading frequencies very frequently the initiation of repeated crack branching has been observed by microscope. This branching occurs in the crack tip, after some parallel growth of both branches only one branch remains as dominant and the growth of the second one stops. Very early after this situation new branching in the crack tip is observed again and the process is going on in the same way. It is possible to suppose that this dividing of deformation energy is a reason for lower crack growth rates in the interval of low stress intensity factors. This effort in these conditions probably overbalances the effect of increased cyclic plastic strain and cyclic creep that must play some role in crack tip at lower loading frequencies. For bainitic materials, as studied steel is, this difference in cyclic strain effects in crack tip is probably of lower pronounced, thus practical no difference on the effect of loading frequency for base material is observed.

Scatter band of experimental results for base material is also shown in fig.1 as band 3.

Application of Paris-Erdogan equation to the results, shown in fig.1, given the following dependencies for upper band boundaries:
- base material:

$$\frac{da}{dN} [\text{mm.cycl}^{-1}] = 4.8 \times 10^{-9} (\Delta K)^{2,78} \quad (3)$$

- austenitic stainless steel cladding:

$$\frac{da}{dN} [\text{mm.cycl}^{-1}] = 4,8 \times 10^{-8} (\Delta K)^{2,62} \quad (4)$$

Examples from the study of crack growth through the boundary between austenitic cladding and base material are shown in fig.2. In two cases cracks grew from the austenitic cladding into the base material, in one case in opposite direction (in all cases accordance to increasing K values).

Summarized results show that these crack growth rates, determined for the bimetallic materials, are in a good agreement with results, received in pure base or cladding materials.

For comparison equation (3) and (4), i.e. for base and cladding materials, are also shown. Crack growth rates in stainless steel cladding are in cases lower than in pure, separated stainless steel cladding - see fig.1.

Before the crack penetrates from the cladding into the zone near the boundary cladding-base material the crack growth rate is substantially decelerated. These results are very clearly seen in fig.2. Nevertheless the crack growth rates in the heat affected zone closely under the cladding are higher than in base, nonaffected material.

Observed deceleration of crack growth rate in the neighbourhood of the fusion line cladding-base material is probably connected with the deceleration of plastic zone growth and cyclic strain processes in the front of the crack tip at the moment, when this plastic zone reaches the fusion line with higher hardness (approximately by 100 HV). Only after breaking of this fusion line further, normal crack growth can take place. With respect to some degradation of heat affected zone properties the crack growth rate is still higher than in base materials. Only after reaching the non-affected zone in base material by the front of plastic zone at the crack tip, this crack growth rate is fully close to the rate in normal base material. This distance is equal to approximately 10 to 15 mm from fusion line.

More pronounced changes in crack growth rate have been observed in specimens, loading by tension-compression. During this type of loading the plastic zone dimension in the front of crack tip is limited; in this case crack growth rate in heat affected zone decreased to the values very close to the base material.

Very similar picture has been observed also in the opposite case, when crack has propagated from the base material into the cladding, as it is also shown in fig.2. Crack growth rate in base material is practically equal to the rate, determined in pure base material. In this case some plateaus near the fusion line can be also observed. As in the previous case, a partial deceleration of crack rate takes place which means that the crack plastic zone reaches the heat affected zone. After the crack penetrates into the cladding material and acceleration of crack is again observed. This acceleration is supported by free growth of a large plastic zone in the front of crack tip and by a nonfavourable casting morphology of cladding. Fast acceleration of crack growth in cladding leads to the sudden breaking of the material bridge to the surface after relatively low number of cycles - in this case low-cycle fatigue loading takes place as plastic zone dimensions reach the outer surface of cladding.

Another two cases of results from three point bend tests are shown in fig.3. Even though larger scattering near the fusion line is seen, very similar dependencies in both base material and cladding have been also observed. The most characteristic effect in all cases is the plateau, situated in the region with thickness of several mm in front of the fusion line.

Comparing the dimensions of plateaus a very good agreement with calculated plastic zone sizes is received - for higher stress intensity factor this zone size is larger and thus the plateau dimension, too. Difference in these zone sizes is seen also in base material and in the cladding, in the dependence of their yield strength values.

5. DISCUSSION OF RESULTS

Experimental study of the crack growth rate under cyclic loading is very important for the evaluation of allowability of cracks, resp. of other type of defects especially from the point of view of the reactor pressure vessel safety and lifetime. These values of crack growth rates are authoritative for the evaluation of real or hypothetical crack "life" in different places of pressure vessel.

Comparison of received results with known information from world literature shows to the very good agreement, resp. to the some stock of safety with respect to the existing codes, containing design curves and formulas.

Thus in fig.4 curves 1 and 2 represent the reference curves according to 1 for the crack growth rate in pressure water of PWR (WWR) type reactors (curve 1) and for the air atmosphere (curve 2).

Curve 3 in the same fig. represents experimentally determined scattering band of results, received in this work for austenitic stainless steel cladding, while curve 4 represents the same results for base material of 15Kh2MFA steel.

For comparison the crack growth rate in austenitic stainless steel cladding as curve 6 according to [3] is also shown. Curve 6 has been proposed as a design curve for AISI 316 austenitic stainless steel that is very similar to stainless cladding. It is seen that experimentally determined values lie lower than the design curve 6.

Similarly curve 5 according to [2] and [4] is added - this dependence was received for the 15Kh2MFA steel. It is also very nice seen a very good agreement with results received in this work - our experimental ones are in the whole interval of stress intensity factors smaller than the design curve 2 that was evaluated, likewise curve 1, for the ASTM A 533 B and A 508 type steels. Thus it can be mentioned the 15Kh2MFA steel and its austenitic stainless steel cladding do not substantially differ from materials, being used in western countries for the manufacture of nuclear reactor pressure vessels, comparing their crack growth rates under cyclic loading. In some cases and for the larger part of loading interval these crack growth rates are substantially lower than design curves for ASTM and AISI type steels according to [1,2,3,4].

Using all aforementioned results the calculations of the allowable sizes of defects in the underclad region of the most exposed parts in reactor pressure vessel have been performed. It can be shown that the hypothetical elliptical defect 10 mm deep and 60 mm long practically during its lifetime (40 years) would not become critical, moreover it practically does not change its dimensions: the whole growth represents less than 0.1 mm which can be neglected. Similar results are received also for defects, situated in the most stress exposed place - for defects in nozzle ring. Results of such a calculation is seen in fig.5 for different defect sizes having shape factor equal to 1:6. It is shown how initially inner, underclad defect will grow during the whole reactor lifetime. It is again seen that defect that is 10 mm deep practically

does not change its dimensions - only a defect with initial size $a_0 = 25$ mm could grow in such a way to penetrate the stainless steel cladding and thus it will change into surface type defect, even though not yet critical.

Thus, all received results in this work, in a good agreement with other ones [2,4] show to the high resistivity of the 15Kh2MFA type steel and its cladding against subcritical crack propagation under cyclic loading; and at the same time to the high exploitation safety of the whole reactor pressure vessel.

6. CONCLUSIONS

In the framework of the summarization of material characteristics for the evaluation of the WWER-440 reactor pressure vessel safety and reliability very important results of subcritical crack growth rates have been received for base material and for material with stainless steel cladding, all under cyclic loading.

The main results received in our experimental study of the 15Kh2MFA type steel and its austenitic stainless steel cladding and discussed earlier, are:

1. Threshold values of stress intensity factors have been determined; for base material lie in interval between $15 \text{ MPa}\cdot\text{m}^{1/2}$ for $R=0$, and $3 \text{ MPa}\cdot\text{m}^{1/2}$ for $R=0.9$, while for austenitic stainless steel cladding lie between 2.5, resp. $2 \text{ MPa}\cdot\text{m}^{1/2}$. Dependence of these values of coefficient of asymmetry, R , is more pronounced for base material as for cladding, in both cases it has an hyperbolic type.
2. Statistically evaluated dependence of crack growth rates using Paris-Erdogan formula has been received for base material and stainless cladding of the 15Kh2MFA steel:
 - base material (upper boundary curve)

$$\frac{da}{dN} [\text{mm}\cdot\text{cycl}^{-1}] = 4.8 \times 10^{-9} (\Delta K)^{2,78}$$

- austenitic stainless steel cladding (dtto)

$$\frac{da}{dN} [\text{mm}\cdot\text{cycl}^{-1}] = 4.8 \times 10^{-8} (\Delta K)^{2,62}$$

Crack growth rate in cladding is approximately 4-to 5-times larger as in base material, in the whole studied interval of loading.

3. For cladding material the effect of loading frequency has been observed. Comparing crack growth rates for frequency equal to $f = 35$ Hz and 0.2 Hz we can observe that lower frequency is characterized with higher steepness (i.e. larger exponent in Paris-Erdogan formula). On the contrary

at lower values of stress intensity factors lower absolute values of crack growth rates have been received for lower frequencies, i.e. $f = 0.2$ Hz. This effect is probably connected with the branching of cracks in their tips - this phenomenon was observed especially at lower frequencies. In base material no similar effect has been found.

4. In specimens with stainless steel cladding (bimetal) and surface crack three different stages in growth dependencies have been found. In surface region subcritical crack growth runs with high rate, practically equal to the rate in austenitic steel. Reaching the crack tip to called fusion line, i.e. boundary between base material and cladding characterized by higher hardness, in crack growth rate some plateau (at $R = 0$) or decrease (at $R = -1$) is observed. Further crack growth rate under the cladding, i.e. in the heat affected zone, does not substantially differ from the results of base material, even though this rate is somewhat higher than in base material (approximately in distance of about 10 mm from fusion line).
5. In the case of crack growth from the underclad region the crack growth rate is firstly controlled by the dependence, determined for pure base material. At the fusion line again some plateau is observed, probably from the same reason, as in the aforementioned case. After overcoming this barrier of higher hardness a very fast crack growth starts; its rate is similar to the rate determined for pure separated stainless steel cladding material.
6. On the basis of received results some model of this effect has been proposed - decreasing of the crack growth rate in the neighbourhood of fusion line can be explained by the process of touching and penetrating this fusion line of higher hardness by the plastic zone in front of the crack tip. Overcoming this line somewhat slows down growth rate of the crack, nevertheless this crack penetrates from cladding to base material or in the opposite direction.
7. Comparison of received results in this work with literature values for the same steel shows to a very good agreement. Similarly, comparison of subcritical crack growth rates for the 15Kh2MFA steel and its cladding with literature values for steels, used in PWR pressure vessels [1,3] shows that studied material is in agreement with design curves, in most cases even with some stock of safety. This fact shows to a good resistivity of studied steel against crack growth under cyclic loading and thus also to the sufficiently high exploitation safety and reliability of WWER type nuclear reactor pressure vessels, manufactured in SKODA Concern.
8. Calculation of the growth of hypothetical underclad cracks shows to the fact that their growth is practically negligible for the whole reactor lifetime: crack growth is practically equal to about 0.1 mm for the initial dimension equal to 10 mm. This result is from the point of view of calculation accuracy and non-destructive methods possibility naturally negligible. Such a growth cannot affect the reactor pressure vessel lifetime, nor its reliability.

7. LITERATURE

- [1] - ASME Boiler and Pressure Vessel Code, Section XI, Appendix A
- [2] - Rahka K. - Fatigue crack growth characteristics of a Cr-Mo-V steel 12Kh2MFA in air. Report VTT-RMR-49 (1975)
- [3] - Flaw Evaluation Procedures. Background and Application of ASME Section XI, Appendix A. ASTM Special Report, NP-719-SR, edited by T.U. Marston (1978)
- [4] - Rahka K., Forsten J. The growth of underclad flaws in fatigue loading. Report VTT-RMR-64 (1976).

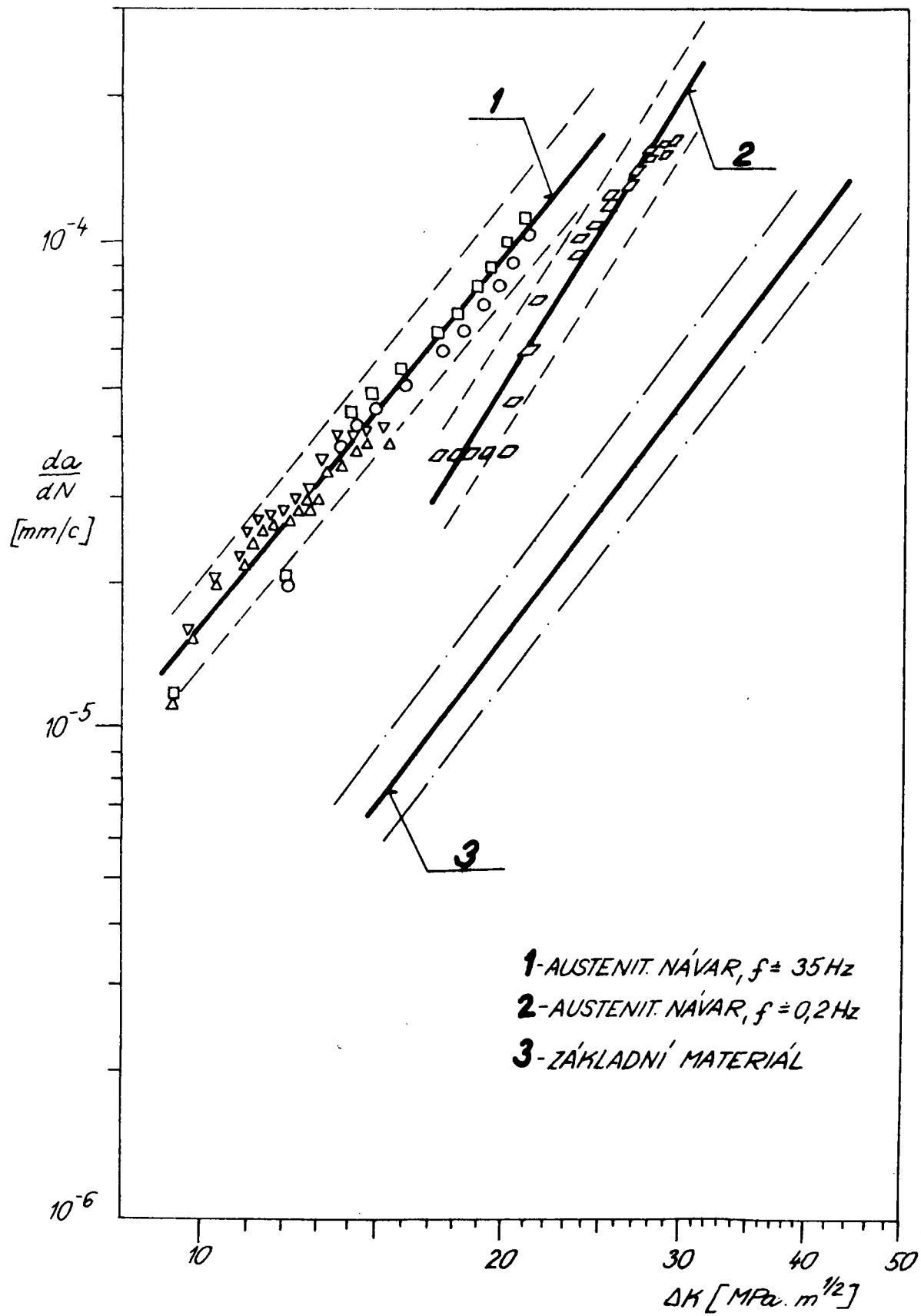
8. DIAGRAMS

Fig.1. Crack growth rate in base material, 3, austenitic stainless steel cladding at loading frequency $f=35$ Hz, 1, and at $f=0.2$ Hz, 2.

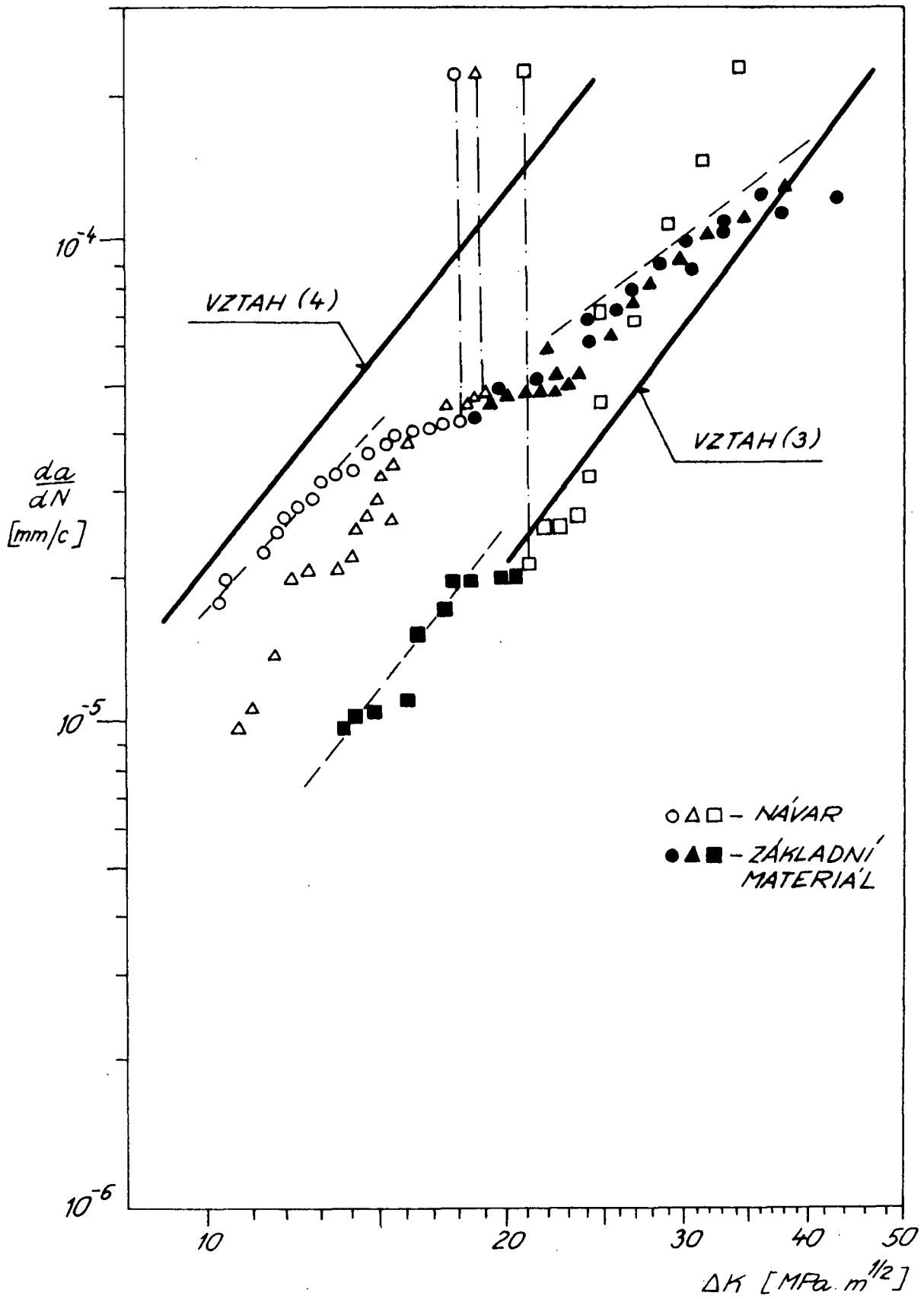
Fig.2. Crack growth rate during penetration of fusion line (vertical dashed line)
open symbols - cladding
solid symbols - base material

Fig.3. Crack growth rate during penetration of fusion line (vertical dashed line)
open symbols - cladding
solid symbols - base material

Fig.4. Comparison of crack growth rates in base material of the 15Kh2MFA steel and in the austenitic stainless steel cladding with literature values for the same steel [2,4] and with design curve for low-alloyed steels [1]
curve 1 - ASME XI - water
curve 2 - ASME XI - air
curve 3 - austenitic stainless steel cladding
curve 4 - base material
curve 5 - base material [2]
curve 6 - austenitic stainless steel [3]



Obr. 1



Obr. 2

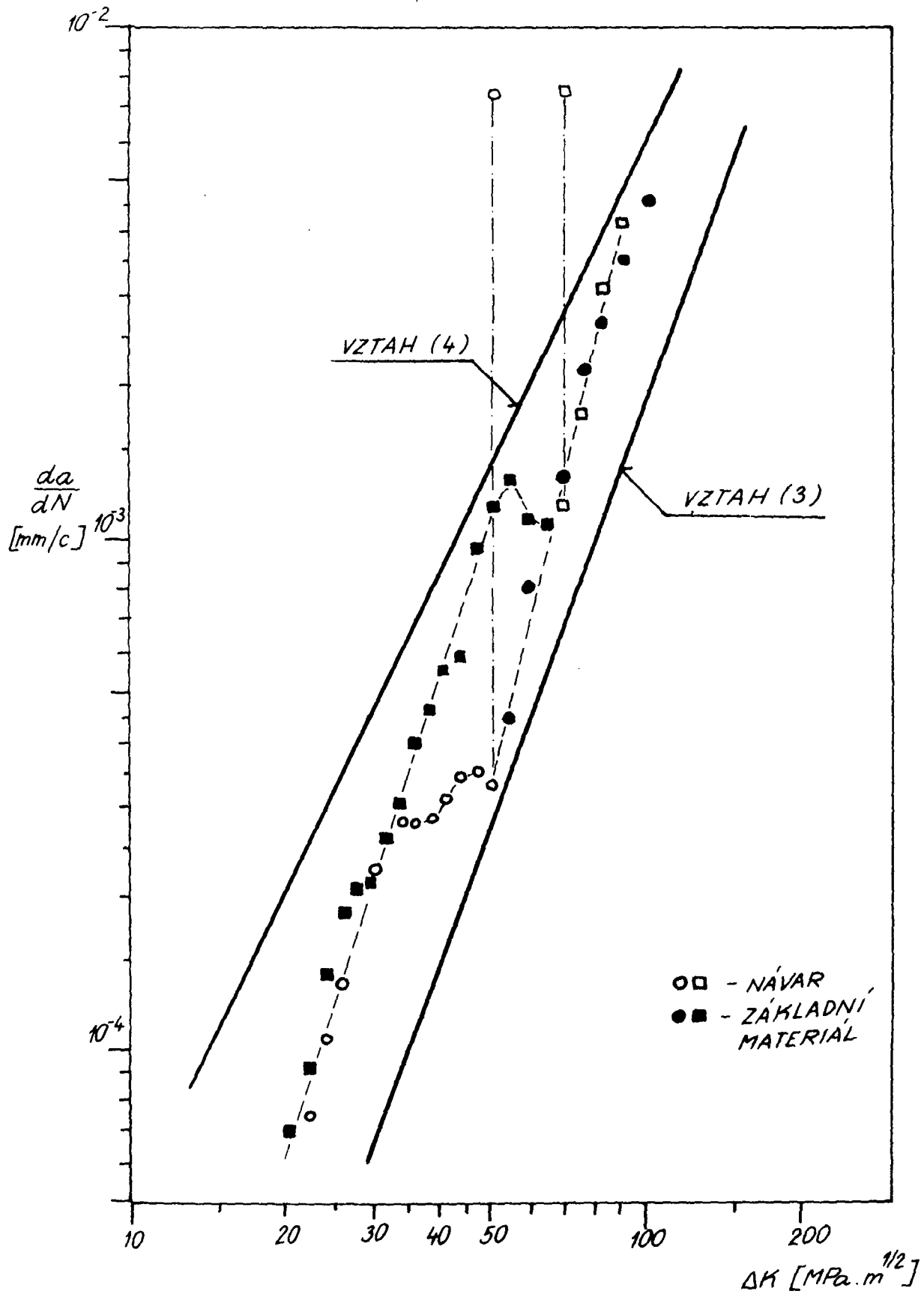
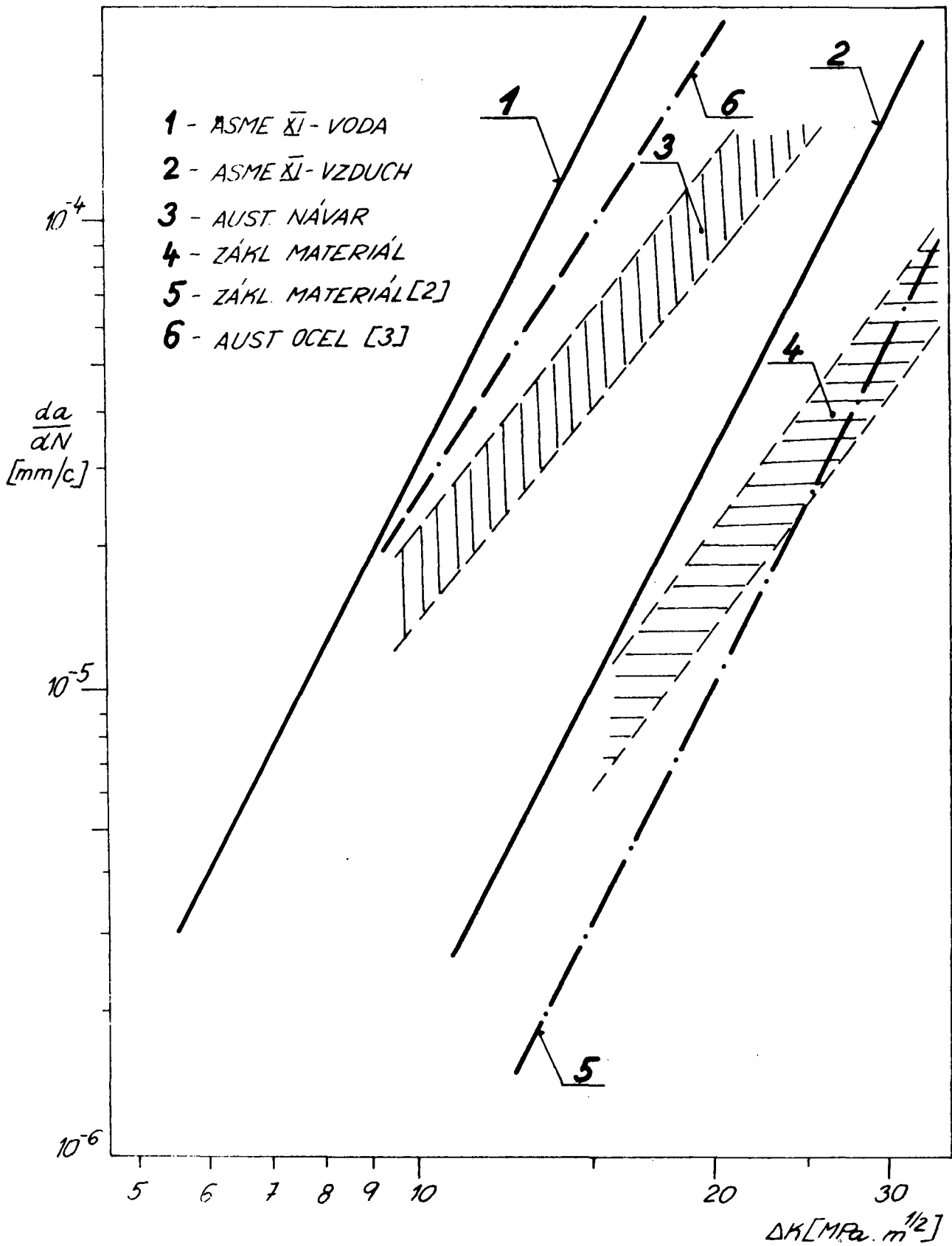


Fig. 3



Obr. 4

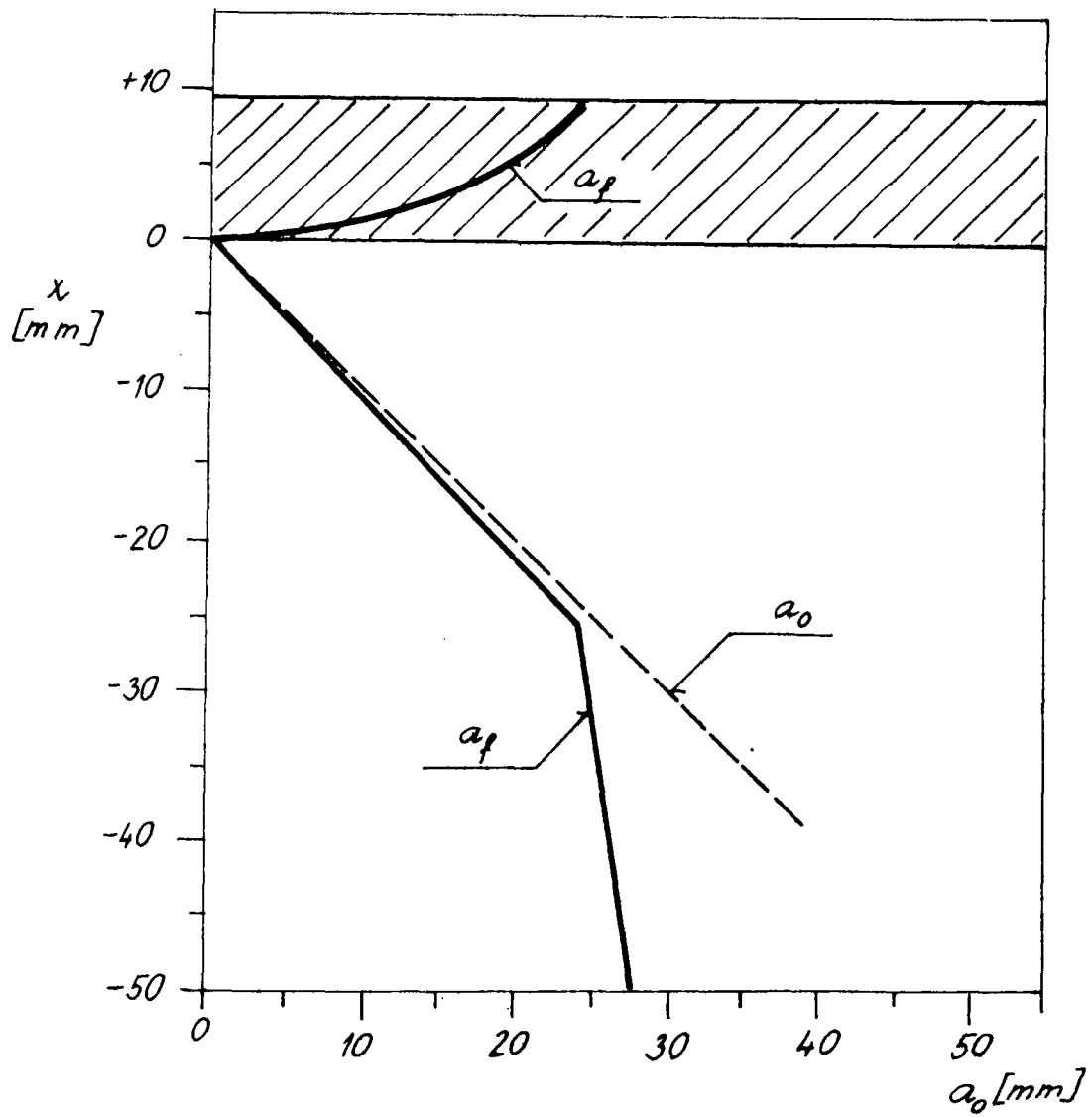


Fig.5

FREIBURG 13/15 MAY 1981

CONCLUSIONS

Reproducible crack growth data can be obtained in RPV steels in an inter-laboratory test programme when the effects of the environment are minimised eg high cyclic rate. However in order to obtain reproducible results in an aqueous environment the test conditions must be controlled within narrow experimental limits.

Factors which have been shown to influence crack growth rates are:

- frequency
- loading variables eg 'R ratio'
- wave form
- material variables
- water chemistry

Increases in growth rate are obtained when the cyclic frequency is below 0.1 Hz, the R ratio $\frac{K_{min}}{K_{max}}$ is increased, the wave form is sinusoidal rather

than saw tooth, and the sulphur content of the steel is increased (>0.010%). These factors are inter-related thus the bulk of the data on low sulphur steel (ie < 0.010%) is bounded within the ASME XI 74 wet line. Sodium and chloride contamination does not significantly increase the growth rate and additionally does not enhance the effect of oxygen. However oxygen contamination has been shown to increase the cyclic growth rate by a factor of 10 at low ΔK values.

Within the limits of the variables discussed above there does not appear to be a significant difference in growth rate between RPV quality plate, forging, weldmetal or HAZ material. Experiments on simulated HAZ material have shown an acceleration in growth rate but all the data available is contained within the ASME 74 wet line. It should be noted that this data was obtained on 0.006% S material. The effect of residual stress should be included in determining the growth rate when testing weldments.

Tests on irradiated material do not shown an enhancement in growth rate, compared with the unirradiated material. However, there are some indications that under the particular cyclic condition examined that the fracture surfaces differ between the irradiated and the unirradiated tests. It is noted that the FRG intend to carry out an experiment in 1981/82 to determine the effect of simultaneous irradiation on the growth rate in the KAHL reactor,

The bulk of the data has been obtained in tests where the stress intensity at the tip of the crack varies continuously during the test. Data is now becoming available under constant ΔK test conditions. The growth rates are comparable under both test conditions at low R (R = 0.2) but the constant ΔK tests do not show a large acceleration in growth rate under high R conditions (R = 0.7).

Tests in SA533 Gr B in high temperature oxygenated water have shown that the use of the Neuber notch stress amplitude based on the worse case NDTCH have a better approximation to initiating conditions than an elastic analysis. To minimise crack growth K_{max} must be kept below K_{ISC} .

Pipes with flaws were subjected to both primary and secondary stresses in order to determine crack growth. To a first approximation it was found that the secondary stresses should be added to the primary stresses in the fatigue analysis.

The effect of thermal shock on the RPV and piping system has been investigated. Crack initiation based on ASME III was marginally unconservative, but the maximum growth rates are comparable with the ASME 74 wet curve. The analysis emphasised the need for an accurate determination of the stress intensity at the crack tip and the ability to apply this data at complex geometries.

Studies have been made on the growth of cracks in the zone between the base metal and the stainless steel cladding. As the crack progresses there is a de-acceleration in growth rate at the base metal/cladding interface. This is thought to be due to an inter-action of the plastic zone with the fusion line. The residual stress pattern would also be expected to reduce the crack growth rate.

Recommendations

1. Consideration should be given to separating the crack growth curves in aqueous environments in the ASME XI/80 code for low and high sulphur steels. The existing curves are not thought to be representative of current steel making practice.
2. The attention of the appropriate standards and coding authorities should be drawn to the uncertainties in crack length measurements associated with the autoclave experiments.
3. The use of potentiometric measurements is advised for all experimental rigs.
4. Several models are now available to explain the observed growth phenomena. There is a need for some critical experiments to define the limits of application of these models and their validation to reactor operation. It would assist in this task if the problem areas could be clearly identified. Work in this area is to be encouraged.

Test data on RPV steels under the high oxygen conditions relevant to a BWR indicate that an oxygen effect exists but the upper bound of all the data is almost identical to that obtained under PWR conditions. There is evidence that under high oxygen conditions oxide entrapment within the crack can influence the growth rate.

Crack growth studies on sensitised stainless steel under cyclic and static loading indicate that environmentally controlled cracks under static loading will be the most important contributor to crack extension in the weld HAZ of BWP piping. Microstructural changes during service (low temperature sensitization) do not seem to lead to any substantial increase of growth rate in environmentally controlled cracking although crack initiation times are greatly reduced. Tests on stainless steel in PWR environment under cyclic conditions have not shown an enhancement in growth rate compared with data in air. Some enhancement was observed in high Nickel alloys but this was small compared with that obtained in RPV steels.

Attention was drawn to the uncertainties in the measurement of crack length using compliance techniques. An additional source of uncertainties is noted in processing the experimental a versus n data to obtain a da/dn versus K plot of data. The ASTM criteria needs to be re-assessed in the context of autoclave testing.

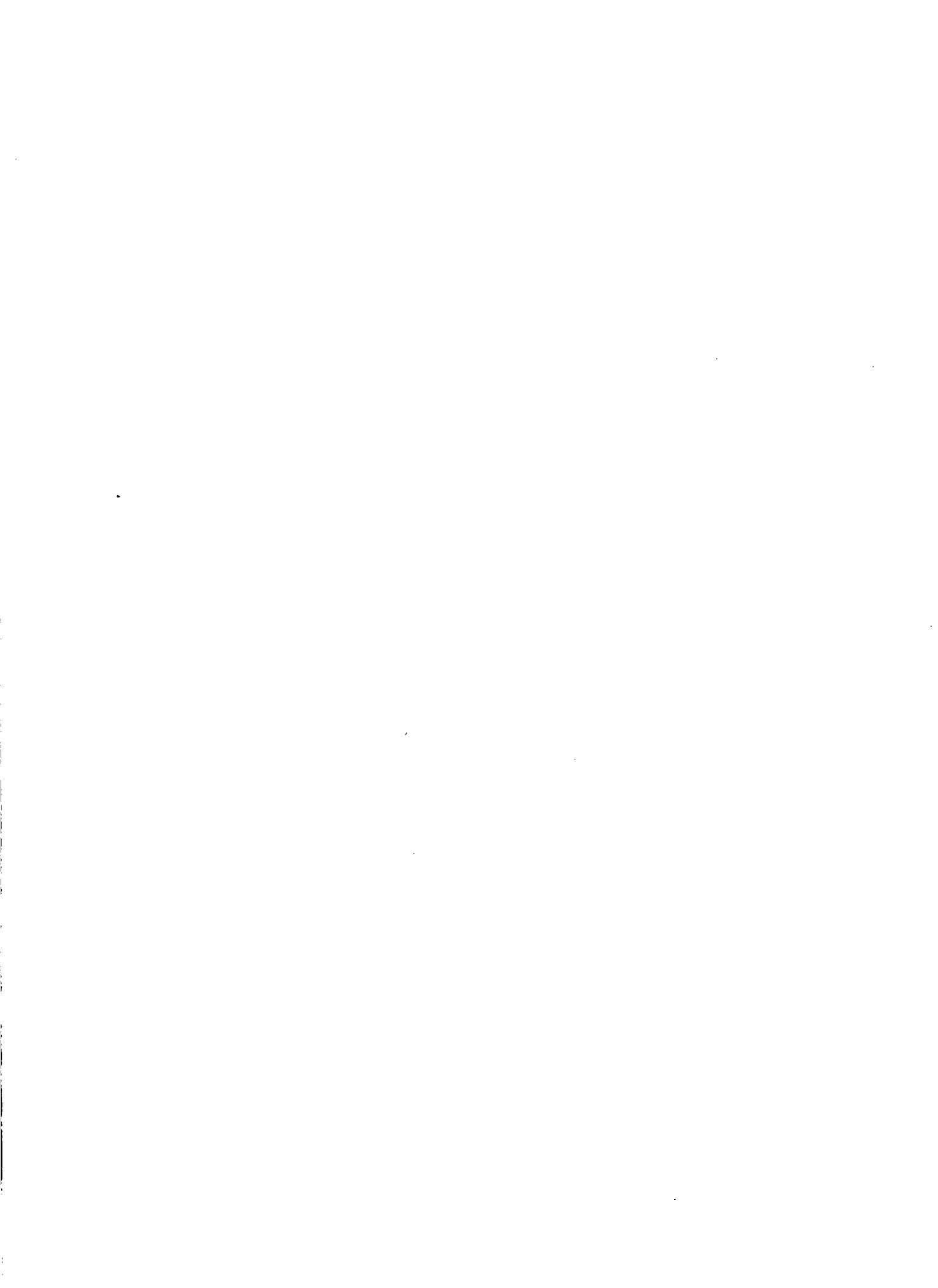
Fractographic studies of specimens tested at room temperature have shown evidence for both ductile and brittle crack advancement mechanisms. Tendency to brittle fracture advance is related to microstructure environment and frequency. For specimens tested at 280°C there is evidence of quasi cleavage facets associated in particular with regions of high manganese sulphide inclusion content but there is no general agreement that this indicates a brittle crack advance mode. Although brittle fractographic features indicate a role of hydrogen in crack advance the mechanism is unclear. The effect of local areas of hydrogen influenced crack advance on the overall crack growth rate is also unclear.

A model to explain the different behaviour observed in water environment was proposed on the basis of crack tip strain rate. The influence of flow rate and its effect on corrosion potential was emphasised. Without supporting potentiometric measurements the relevance of low flow rate tests to reactor conditions was questioned. It is clear that electro chemical potential consideration could explain many of the anomalies observed in the experimental data.

A mechanism based on slip dissolution gives good agreement at low temperature between theory and experimental data covering both static and dynamic loading conditions. At higher temperatures qualitative agreement between theory and experiment is not yet established. Under high crack propagation rates liquid diffusion in the crack seems to be the rate controlling factor.

A model was proposed which showed that at any ΔK value the maximum growth rate in a da/dn versus ΔK plot could be parallel to the growth rate in air.

In order to increase confidence in applying experimental data to reactor plant operation it is necessary to have a good understanding of the basic mechanism, with an ability to define the limits and rates of the controlling processes.



UNITED STATES
NUCLEAR REGULATORY COMMISSION
WASHINGTON, D.C. 20555

OFFICIAL BUSINESS
PENALTY FOR PRIVATE USE, \$300

FOURTH CLASS MAIL
POSTAGE & FEES PAID
USNRC
WASH. D.C.
PERMIT No. G-67